

BOSTON UNIVERSITY
GRADUATE SCHOOL OF ARTS AND SCIENCES

Dissertation

**CHEMICAL DESIGN OF SINGLE MOLECULE ELECTRONIC COMPONENTS
AND QUASI-1D CHAINS**

by

HANNAH E. SKIPPER

B.A., Skidmore College, 2017

Submitted in partial fulfillment of the
requirements for the degree of
Doctor of Philosophy

2023

© 2023 by
Hannah E. Skipper
All rights reserved

Approved by

First Reader

Linda H. Doerrer, Ph.D.
Professor of Chemistry
Professor of Material Science and Engineering

Second Reader

Maria Kamenetska, Ph.D.
Assistant Professor of Chemistry
Assistant Professor of Physics
Assistant Professor of Material Science and Engineering

ACKNOWLEDGMENTS

I would like to thank my advisors, Prof. Linda Doerrer and Prof. Masha Kamenetska. Thank you for taking me on as a joint student. I am grateful to have been mentored by both of you and feel very fortunate to have been a member of the Doerrer and Kamenetska Labs. Thank you for all the opportunities you have provided me. It has been a privilege to be your student.

Thank you to my dissertation thesis committee, Prof. Sahar Sharifzadeh, Prof. Björn Reinhard and Prof. Eric Cueny, for your valuable input. I would also like to thank and acknowledge the contributions from collaborators: Prof. Arnold Rheingold (University of California San Diego) and Dr. Jeff Bacon (Boston University) for crystallography, Prof. Mark Turnbull (Clark University) for magnetism measurements, and Prof. Sebastian Stoian and Adam Valaydon-Pillay (University of Idaho) for Mössbauer measurements. I would also like to thank Prof. Polly Arnold for hosting my DOE SCGSR fellowship as well as Dr. Rachel Meyer and the other members of the Arnold group for welcoming me into the lab.

I have had the pleasure of working with many wonderful people in the Doerrer and Kamenetska labs. Thank you to the current members of the Doerrer lab: Léa Toubiana, Shawn Moore, Cathlene Del Rosario, Thor Mdalel, Mary Bussiere, John Cerritelli, Alaina Minarik and Parnian Asgari. I also want to say thank you to past members of the Doerrer Lab: Dr. Stephanie Beach-Molony, Dr. Sarah Brazeau, Dr. Jessica Elinburg, Dr. Ariel Hyre, Dr. Nate Harmann, Dr. Jordan Aguirre, Sikung Choi, Lihao Feng, Linda Zuckerman,

Claire May, Gear Khuichad, Alice Fan, Paul Homuth, Ana Herning, Caroline Sabanos and Gigi Bao. Thank you to the members of the Kamenetska Lab, both past and present: Brent Lawson, Xiaoyun Pan, Daniel Jackson, Brian Dawes, Zelin Miao, Favian Liu, Freddy Luna, Nick Miller, Vera Degtiareva, Regal Jiang, Elizabeth Nevins, Faisal Halabeya, Hanil Chung and Maitreya Rose. I would like to say an extra thank you to Brent, Xiaoyun, Steph, Léa, Claire, Vera and Gigi for contributing to the work presented in this thesis.

Finally, a big thank you to my family and friends. Mum, Dad and Tom, thank you for all your love, support and encouragement over the past five years and throughout my life. Andy, thank you for everything.

**CHEMICAL DESIGN OF SINGLE MOLECULE ELECTRONIC COMPONENTS
AND QUASI-1D CHAINS**

HANNAH E. SKIPPER

Boston University, Graduate School of Arts and Sciences, 2023

Major Professors: Linda Doerrer, Professor of Chemistry and Material Science and Engineering
Maria Kamenetska, Assistant Professor of Chemistry, Physics, and Material Science and Engineering

ABSTRACT

A series of heterobimetallic lantern complexes of the form $[\text{PtFe}(\text{SOCR})_4(\text{pyX})]$ ($\text{R} = \text{Me}$, $\text{X} = \text{H}$ (**1**), $\text{X} = \text{NH}_2$ (**2**), $\text{X} = \text{SMe}$ (**3**); $\text{R} = \text{Ph}$, $\text{X} = \text{H}$ (**4**), $\text{X} = \text{NH}_2$ (**5**), $\text{X} = \text{SMe}$ (**6**)) have been synthesized and characterized, including ^{57}Fe Mössbauer spectroscopy. The synthesis of the new complexes in this family (**1**, **4**, **5**, **6**) are reported along with a detailed structure-property comparison across the entire series. Substitutions made on the thiocarboxylate backbone (R) and the pyridine axial ligand (X) significantly affect the quadrupole splitting (ΔE_Q) in the Mössbauer measurements. The quasi-1D chain $[\text{PtCo}(\text{SAc})_4(4,4'\text{-bipy})]_\infty$ (**7**) has been synthesized via bottom-up assembly of individual lantern units coupled by 4,4'-bipyridine bridging ligands. Synthesis and characterization, including magnetic studies are reported.

A new series of heterobimetallic lantern complexes $[\text{PtM}(\text{tba})_4(\text{pySMe})]$ ($\text{M} = \text{Mn}$ (**10**), Fe (**6**), Co (**11**), Ni (**12**), Zn (**13**)) and homobimetallic lantern complexes $[\text{Cu}_2(\text{OAc})_4(\text{pySMe})_2]$ (**14**) and $[\text{Co}_2(\text{esp})_2(\text{pySMe})_2]$ (**15**) have been synthesized and characterized. These complexes were utilized to study the incorporation of coordination

complexes into metal-molecule-metal junctions via the Scanning Tunneling Microscope Break Junction (STMBJ) technique. Single molecule conductance measurements reveal that intramolecular metal-ligand bonding is vulnerable to rearrangement on Au electrodes and competition from Au-ligand binding is consistent with empirical hard-soft acid-base principles. Single molecule conductance measurements in the presence of $[\text{KM}(\text{CN})_2]$ ($\text{M} = \text{Au}, \text{Ag}$) are reported, which produce numerous conductance features ranging from $10^{-1} - 10^{-6} G_0$ at distinct junction elongations. Some junction extensions are longer than predicted for a $[(\text{NC})\text{Au}(\text{CN})]^{1-}$ molecular bridge between Au electrodes, suggesting rearrangement and in situ formation of molecular wires.

Quantum interference effects between σ and π molecular orbitals have been identified in $\sim 4 \text{ \AA}$ pyrazine-based molecules, bridging source and drain electrodes. Destructive interference effects were modulated via external pH control, as demonstrated by single molecule conductance measurements and electronic transport calculations.

TABLE OF CONTENTS

ACKNOWLEDGMENTS	iv
ABSTRACT.....	vi
TABLE OF CONTENTS.....	viii
LIST OF TABLES	xii
LIST OF FIGURES	xiv
LIST OF SCHEMES	xxvi
LIST OF ABBREVIATIONS.....	xxviii
CHAPTER ONE: Introduction	1
1.1. Scanning Tunneling Microscope Break Junction (STMBJ) Technique	2
1.2. Transition Metal Complexes for Functional Single Molecule Components	6
1.3. Quasi-1D Materials.....	8
1.4. {PtM} Lantern Complexes	11
1.5. Quantum Interference	15
1.6. Motivation and Outlook.....	18
CHAPTER 2: Determination of Ligand Substituent Effects in Pt-Fe Heterobimetallic Lantern Complexes via ⁵⁷ Fe Mössbauer Spectroscopy	20
2.1. Introduction.....	20
2.2. Results and Discussion	22
2.2.1. Synthesis and Structure.....	22

2.2.2. Electronic Spectroscopy.....	34
2.2.3. Magnetic Susceptibility	37
2.2.4. Mössbauer Spectroscopy	38
2.3. Conclusions.....	51
2.4. Experimental	52
2.4.1. Materials and Methods.....	52
2.4.2. X-ray Crystallography Methods	52
2.4.3. ⁵⁷ Fe Mössbauer Spectroscopy Methods.....	53
2.4.4. Synthetic Procedures.....	54
CHAPTER THREE: Synthesis and Characterization of a {PtCo} Quasi-1D Chain.....	57
3.1. Introduction.....	57
3.2. Results and Discussion	63
3.2.1. Synthesis and Structural Analysis.....	63
3.2.2. Electronic Spectroscopy.....	79
3.2.3. Magnetic Studies.....	81
3.3. Conclusions.....	89
3.4. Experimental	90
3.4.1. Materials and Methods.....	90
3.4.2. X-ray Crystallography Methods	90
3.4.3. Magnetic Measurements	90
3.4.4. Synthetic Procedures.....	91

CHAPTER FOUR: Hard-Soft Chemistry Design Principles for Predictive Assembly of Single Molecule Metal-Junctions	94
4.1. Abstract	94
4.2. Introduction.....	95
4.3. Results and Discussion	98
4.4. Conclusions.....	113
4.5. Experimental	115
4.5.1. Materials and Methods.....	115
4.5.2. X-ray Crystallography Methods	115
4.5.3. STMBJ Measurements.....	115
4.5.4. DFT Calculations	116
4.5.5. Synthesis and Structure.....	117
4.6. Additional Data	130
4.7. STMBJ Measurements of $[\text{Cu}_2(\text{pABA})_4(\text{DMF})_2]$	139
CHAPTER FIVE: Assembly and Electron Transport Properties of Metal-Cyanide Containing Wires in Single Molecule Junctions.....	144
5.1. Introduction.....	144
5.2. Results and Discussion	147
5.3. Conclusions.....	160
5.4. Additional Data	161
CHAPTER SIX: Manipulating Quantum Interference Between σ and π Orbitals in Single Molecule Junctions via Chemical Substitution and Environmental Control	162

6.1. Abstract	162
6.2. Introduction.....	163
6.3. Results and Discussion	165
6.4. Conclusion	180
6.5. Experimental	182
6.5.1. STMBJ Measurements.....	182
6.5.1. DFT Calculations.....	183
6.6. Additional Data	184
BIBLIOGRAPHY	196
CURRICULUM VITAE.....	217

LIST OF TABLES

Table 2.1. Selected bond distances and angles for the [PtFe(SOCR) ₄ (pyX)] series.....	28
Table 2.2. Intermolecular distances and angles for the PtFe(SOCR) ₄ (pyX)] series	32
Table 2.3. Vis-NIR comparison for the [PtFe(SOCR) ₄ (pyX) series.....	36
Table 2.4. Zero field Mössbauer parameters determined at 4.35 K for 1 - 6 simulating only a single quadrupole doublet. ^a	40
Table 2.5. Selected Mössbauer parameters for high spin Fe(II) octahedral complexes shown in Scheme 2.4.	42
Table 2.6. Zero-field Mössbauer parameters used to simulate the 4.35 K spectrum of 3 considering either a nested or an intercalated arrangement.....	44
Table 2.7. Zero-field Mössbauer parameters used to generate the two-component theoretical spectra of 3, 4 and 5 . The spectral components are labeled blue and red corresponding to how they are shown in Figures 2.7 - 2.10.	46
Table 2.8. Zero-field Mössbauer parameters used to simulate the 4.35 K spectra of 1, 2 and 6	50
Table 2.9. Crystal data collection and refinement parameters for 1, 4 and 5	56
Table 3.1. Selected bond lengths and angles for 8	66
Table 3.2. Selected bond lengths and angles for 9	69
Table 3.3. Selected bond distances and angles for [PtCo(SAc) ₄ (4,4'-bipy)] _∞ (7) compared to previously reported [PtCo(SAc) ₄ (pyz)] _∞ ⁷⁹ and {[PtCo(SAc) ₄ (pyz)](pyz)} _∞ ⁸² chains.	74
Table 3.4. Intramolecular Pt...Pt, Pt...S and S...S interactions and Co-Co distances.....	78

Table 3.5. Vis-NIR Comparison for [PtCo(SAc) ₄ L] Complexes.....	80
Table 3.6. Crystal data collection and refinement parameters for 7 , 8 and 9	93
Table 4.1. Single crystal X-ray diffraction collection parameters for 6 , 10-15	129
Table 4.2. DFT calculated binding energies of 13 and pySMe.....	136
Table 5.1. Experimental and calculated conductance and displacement information ...	152
Table 5.2. Conductance ratios within HG, MG and LG regions from measurements in the presence of [KAu(CN) ₂] in Figure 5.2A.....	158

LIST OF FIGURES

Figure 1.1. Conductance traces of clean Au (left, yellow) and 4,4'-bipy (right, red).....	5
Figure 1.2. A) 1D conductance histograms of clean Au (yellow) and 4,4'-bipy (red). B) 2D conductance histogram of 4,4'-bipy.....	5
Figure 1.3. STMBJ scheme depicting binding of typical organic molecules and generic M-L frameworks binding in the Au junction via linker groups (L).....	7
Figure 1.4. Design features for SCM behavior in 1D chains.....	11
Figure 1.5. A) Scheme depicting electrons tunneling through frontier MOs. B) Example transmission through a hypothetical one-orbital system, C) Example transmission through a hypothetical two-orbital system. D) Benzene-based molecule with generic linker groups (L) bound to Au leads. QI predictions (constructive vs destructive) are illustrated based on the relative phases of the MOs at L. The relative phases at L are indicated by the red/blue circles. E) Example transmission of CQI (green trace) and DQI (red trace).....	17
Figure 2.1. A) ORTEP of 1 . Ellipsoids are drawn at the 50% level and hydrogen atoms are omitted for clarity. B) Mercury representation of intermolecular Pt...Pt (4.338 Å, gray), Pt...S (3.109 Å, green) and S...S (3.362 Å, orange) contacts between individual complexes.....	25
Figure 2.2. A) ORTEP of 4 . Ellipsoids are drawn at the 50% level and hydrogen atoms are omitted for clarity. B) Mercury representation of intermolecular Pt...Pt (3.562 Å, gray), Pt...S (3.474 Å, green) and S...S (3.532 Å, orange) contacts between individual complexes.....	26

- Figure 2.3.** A) ORTEP of **5**. Ellipsoids are drawn at the 50% level and hydrogen atoms are omitted for clarity. B) Mercury representation of intermolecular Pt...Pt (5.410 Å, gray), Pt...S (3.847 Å, green) and S...S (3.336 Å, orange) contacts between individual complexes. 27
- Figure 2.4.** Plots of Pt-Fe (A) and Fe-N (B) distances (Å) as a function of axial ligand substituent (H, SMe, NH₂) and backbone R group (Me = red circles, Ph = blue squares). C) Comparison of Fe-N distance and the closest Pt...L contact (L = S for **1**, **2**, **4**, **5** and **6**, L = Pt for **3**). R = Me (red), R = Ph (blue); L = H (diamonds), L = NH₂ ("x"), L = SMe (triangles). 30
- Figure 2.5.** UV-Vis spectra of [PtFe(SAc)₄(py)] (**1**, green), [PtFe(tba)₄(py)] (**4**, red) and [PtFe(tba)₄(pyNH₂)] (**5**, blue) in CH₂Cl₂. Visible and visible-NIR regions are also shown in the left and right insets respectively. 35
- Figure 2.6.** Zero-field Mössbauer spectra recorded at 4.35 K for **1** – **6**. The solid red lines are theoretical curves obtained considering a single quadrupole doublet characterized by the parameters listed in Table 2.4. 39
- Figure 2.7.** Zero-field Mössbauer spectrum recorded at 4.35 K for **3**. A) The solid gray lines are simulations obtained from the sum of two nested (A) or two intercalated (B) components, shown in blue and red, obtained using the parameters listed in Table 2.6. 43
- Figure 2.8.** Zero field Mössbauer spectra recorded at 4.35 K for two different samples of **4**. A) Spectra of **4** at t = 0 (initial) of sample 1 (top), sample 2 (middle) and the difference spectrum (bottom). Time –dependent Mössbauer spectra recorded for two

different samples of 4 . B) sample 1 after 9 months (bottom) compared to the initial measurement (top). C) sample 2 after 3 months (bottom) compared to the initial measurement (top). The solid gray lines are simulations derived from the sum of two components obtained using the parameters listed in Table 2.7.	45
Figure 2.9. Time-dependent zero-field Mössbauer spectra recorded for 3 at $t = 0$, initial (top) and after 12 months (bottom). Parameters for the blue and red spectral components are reported in Table 2.7.....	48
Figure 2.10. Time-dependent, zero-field Mössbauer spectra recorded at 4.35 K for 5 with parameters reported in Table 2.7.	49
Figure 3.1. ORTEP of $[\text{PtNi}(\text{SAC})_4(\text{pyz})]_\infty$ (top) ⁷⁹ and $\{[\text{PtNi}(\text{SAC})_4(\text{pyz})](\text{pyz})\}_\infty$ (bottom). ⁸² Ellipsoids are drawn at the 50 % level. Hydrogen atoms are omitted for clarity.	62
Figure 3.2. A) ORTEP of $[\text{PtNi}(\text{SAC})_4(2,5\text{-Me}_2\text{pyz})_{0.5}]_\infty$ (8). Ellipsoids are drawn at the 50 % level. Hydrogen atoms and solvent molecules (3 CHCl_3) are omitted for clarity. B) Mercury representation showing the packing of the individual chains. Solvent and Hydrogen atoms omitted.....	65
Figure 3.3. A) ORTEP of $[\text{PtNi}(\text{SOCR})_4(\text{OH}_2)](\text{phz})$ (9). Ellipsoids are drawn at the 50 % level. Hydrogen atoms are omitted for clarity. B) Mercury representation showing the packing and intermolecular interactions. H atoms omitted.....	68
Figure 3.4. ORTEP of $[\text{PtCo}(\text{SAC})_4(4,4'\text{-bipy})]_\infty$ (7). Ellipsoids are drawn at the 50% level. Hydrogen atoms and solvent molecules (2 equivalents of disordered PC) are omitted for clarity.	73

Figure 3.5. Packing diagrams of individual $[\text{PtCo}(\text{SAc})_4(4,4'\text{-bipy})]_\infty$ (7) chains with one molecule of PC per $\{\text{PtCo}(\text{SAc})_4(4,4'\text{-bipy})\}$ unit viewed down the <i>a</i> -axis (top) and along the <i>a</i> -axis (bottom). H atoms omitted.	75
Figure 3.6. Mercury representations displaying intermolecular Pt...Pt (gray), Pt...S (green) and S...S (orange) contacts in complexes $[\text{PtCo}(\text{SAc})_4(\text{py})]$ (A), $[(\text{py})\text{PtCo}(\text{SAc})_4(\text{py})]$ (B), $[\text{PtCo}(\text{SAc})_4(\text{pyz})_{0.5}]$ (C) and $[\text{PtCo}(\text{SAc})_4(4,4'\text{-bipy})]_\infty$ (7) (D). The purple arrows indicate the Co-Co distances reported in in Table 3.4. H atoms removed for clarity.	77
Figure 3.7 Diffuse reflectance spectrum of $[\text{PtCo}(\text{SAc})_4(4,4'\text{-bipy})]_\infty$. The inset includes only the near-IR region.	80
Figure 3.8. Magnetization as a function of applied magnetic field (M(H)) for $[\text{PtCo}(\text{SAc})_4(4,4'\text{-bipy})]_\infty$ (7) collected at 1.8 K.	82
Figure 3.9. Temperature dependence of $\chi_M T$ collected between 1.8 and 300 K at an applied dc field of 1000 Oe for $[\text{PtCo}(\text{SAc})_4(4,4'\text{-bipy})]_\infty$ (7).	82
Figure 3.10. Temperature dependence of $\chi_M T$ collected between 1.8 and 300 K at an applied dc field of 1000 Oe for $[\text{PtCo}(\text{SAc})_4(\text{py})]$ (blue), $[(\text{py})\text{PtCo}(\text{SAc})_4(\text{py})]$ (red), $[\text{PtCo}(\text{SAc})_4(\text{pyz})_{0.5}]$ (green, plotted per mol of dimer) and $[\text{PtCo}(\text{SAc})_4(4,4'\text{-bipy})]_\infty$ (black).	85
Figure 3.11 UV-vis-NIR spectrum $[\text{PtNi}(\text{SAc})_4(2,5\text{-Me}_2\text{pyz})_{0.5}]_\infty$ (8).	92
Figure 4.1. (A) Hard-soft trends of donor atoms apply for the synthesis of Au complexes, (B) effective linkers groups to Au in single molecule measurements arranged	

approximations according to binding strength,^{5, 6, 34, 104-106, 109, 110} and (C) the stability of metal complexes studied in this work on Au electrodes. 99

Figure 4.2. (A) Schematics of heterobimetallic lantern frameworks with SC(O)R backbone ligands R = Ph (B) homobimetallic lantern frameworks with OC(O)R backbone ligands, R = Me (**14**), for (**7**) OC(O)R= esp (**15**). All complexes have pySMe (L) axial ligands. (C) Molecular structures of the individual ligands. (D) Conductance histograms and sample traces (inset) of 1 mM measurements of SC(O)R as thiobenzoic acid and of **12** in TCB. (E) Conductance histograms and sample traces (inset) of 1mM OC(O)R as benzoic acid, pySMe, and **14** in TCB. Additional linear-binned conductance histograms are shown in Figure 4.13..... 102

Figure 4.3. Logarithmically-binned 1D conductance histogram of pySMe and heterobimetallic complexes **10** and **13** measured at ~ 0.01 mM (A). 2D histograms of the pySMe axial ligand at 1 mM (B), **13** at 0.01 mM (C) and **14** at 1 mM (D). Peak height as a function of 3d metal for the SC(O)R complexes Mn (gray), Fe (yellow), Co (red), Ni (green), Zn (blue), R = Ph (squares), R = Me (circles) (E). The average over all experiments for each M is designated by an X. 109

Figure 4.4. (A) Relaxed structures and (B) transmission spectra of pySMe (red) and the entire lantern complex **13** with R = Me bound through the Pt (blue) or S of backbone (green) to Au₃₇ electrodes. 112

Figure 4.5. ORTEP of [PtMn(tba)₄(pySMe)] (**10**). Ellipsoids are drawn at the 50% probability level and hydrogen atoms are omitted for clarity..... 121

Figure 4.6. ORTEP of [PtFe(tba) ₄ (pySMe)] (6). Ellipsoids are drawn at the 50% probability level and hydrogen atoms are omitted for clarity.....	122
Figure 4.7. ORTEP of [PtCo(tba) ₄ (pySMe)] (11). Ellipsoids are drawn at the 50% probability level and hydrogen atoms are omitted for clarity. There are two independent molecules in the asymmetric unit.....	123
Figure 4.8. ORTEP of [PtNi(tba) ₄ (pySMe)] (12). Ellipsoids are drawn at the 50% probability level and hydrogen atoms are omitted for clarity. There are two independent molecules in the asymmetric unit.....	124
Figure 4.9. ORTEP of [PtZn(tba) ₄ (pySMe)] (13). Ellipsoids are drawn at the 50% probability level and hydrogen atoms are omitted for clarity. There are two independent molecules in the asymmetric unit.....	125
Figure 4.10. ORTEP of [Cu ₂ (OAc) ₄ (pySMe) ₂] (14). Ellipsoids are drawn at the 50% probability level and hydrogen atoms are omitted for clarity. An inversion center relates the two halves of this compound.....	126
Figure 4.11. ORTEP of [Co ₂ (esp) ₂ (pySMe) ₂] (15). Ellipsoids are drawn at the 50% probability level and hydrogen atoms are omitted for clarity. An inversion center relates the two halves of the molecule.....	127
Figure 4.12. UV-vis-NIR spectra of compounds 6 , 10-15 in CH ₂ Cl ₂	128
Figure 4.13. (A) Schematics of heterobimetallic lantern frameworks with SC(O)R backbone ligands R = Ph (B) homobimetallic lantern frameworks with OC(O)R backbone ligands, R = Me (14), for (7) OC(O)R= esp (15). All complexes have pySMe (L) axial ligands. (C) Molecular structures of the individual ligands. (D)	

Conductance histograms and sample traces (inset) of 1 mM measurements of SC(O)R as thiobenzoic acid and of 12 in TCB. (E) Conductance histograms and sample traces (inset) of 1mM OC(O)R as benzoic acid, pySMe, and 14 in TCB. .	130
Figure 4.14 1D conductance histograms of heterobimetallic lantern complexes 13 , 12 , 11 , 6 , 10 (left to right) at 1 mM concentrations compared to the clean Au control.	131
Figure 4.15. Conductance histogram of 1 mM [Pt ₂ (mpy) ₄] homobimetallic lantern complex.....	132
Figure 4.16. Log-binned 1D (A) and 2D (B) conductance histograms of homobimetallic complex 15 compared to the individual axial ligand (pySMe). Structure for lantern complex (C).	133
Figure 4.17. Isosurface plots of PtZn(SAc) ₄ with SC(O)R backbone ligands and Cu ₂ (OAc) ₄ with OC(O)R backbone ligands at PBE/Def2-TZVP level of theory. .	134
Figure 4.18. Mercury representations of 10 , 13 , and 14 showing distances relative to pySMe. H atoms removed.....	134
Figure 4.19. Log-binned conductance histogram of SC(O)R complexes 6 , 10 – 13 (left) measured at ~ 0.01 mM and OC(O)R complexes 14 & 15 (right) measured at 1 mM in TCB.....	135
Figure 4.20. Measurements at different bias voltage of 11 at 0.01 mM (left) and 1 mM (right) concentrations in TCB.	137
Figure 4.21. Conductance histograms of OC(O)R (benzoic acid) and SC(O)R backbones (thioacetic acid, thiobenzoic acid and ethyl thioacetate) measured at 1 mM.	138

Figure 4.22. A) Conductance histograms recorded in the presence of DMF (yellow, 600 traces) and ~ 1 mM pABA from either H ₂ O (green, 4000 traces), DMF (red, 1400 traces) or ethyl benzoate (EB, orange, 10,000 traces) solutions. B) Conductance histogram recorded in the presence of ~ 1mM [Cu ₂ (pABA) ₄ (DMF) ₂] from a DMF solution (blue, 10,000 traces). C) 2D histograms of pABA from a EB solution (top) and [Cu ₂ (pABA) ₄ (DMF) ₂] from a DMF solution (bottom).....	142
Figure 4.23. Mercury representation of [Cu ₂ (pABA) ₄ (DMF) ₂]. Solvent molecules and H atoms removed, Cu (green), O (red), N (blue), C (dark gray). Distances between the adjacent and opposite NH ₂ groups are reported.....	143
Figure 5.1. Depiction of Au-CN bonding within the [Au(CN) ₂] ⁻ anion (left). Hypothetical molecular junction with (NC)Au(CN) bridged between Au ₁₈ electrodes (cropped for clarity) and DFT predicted distances at PBE level of theory (right).	146
Figure 5.2 1D log-binned (A) and 2D (B) conductance histograms from measurements in the presence of 1 mM [KAu(CN) ₂].....	148
Figure 5.3. A) Conductance decay for peaks H1, M1 and L1 (red) and calculated transmission per {Au(CN)} _n unit (blue) versus the length of the {Au(CN)} _n junction, measured from edge to edge of the apex Au atoms of the electrode. B) Transmission curves for {Au(CN)} _n n = 1-3 and [(NC)Au(CN)] ⁻ C) DFT relaxed structures for {Au(CN)} _n n = 1-3 with Au ₃₄ electrodes. Au-Au displacements are reported in Table 5.1	153
Figure 5.4. 1D conductance histograms from measurements in the presence of [KAg(CN) ₂] (red) compared to [KAu(CN) ₂] (black).....	159

- Figure 5.5.** 1D linear-binned conductance histogram using bins of 1×10^{-4} (red) and 1×10^{-6} (blue). Different shades of red and blue indicate multiple data sets..... 161
- Figure 5.6.** Conductance histograms of $[\text{KAg}(\text{CN})_2]$ from measurements performed at 10 mM (green), 1 mM (yellow) and 0.1 mM (blue) concentrations..... 161
- Figure 6.1.** A) Frontier MOs of benzene (left), 1,4-benzenediamine (middle) and pyz (right) at B3LYP/Def2-TZVP level of theory. B) Relaxed geometries of pyz junctions at various junction extensions with Au₃₇ electrodes. Au-Au separation is reported from edge to edge of the apex Au atoms. C) Transmission spectra and binding energy (BE) per Au-N bond (inset) of pyz at various junction lengths. Transmission calculated using Equation 1 at the 5.7 Å Au-Au separation considering the HOMO and LUMO (green trace). The black vertical dashed line indicates the Fermi energy (E_F). Isosurface plots of the molecular orbitals in the 5.7 Å junction at -2.0 eV (HOMO) and 0.9 eV (LUMO) are shown above and indicated by the blue and red dashed lines respectively. Transmission of 1,2-diaminoethane (yellow trace).
..... 166
- Figure 6.2.** 1D conductance histograms of clean Au (yellow), pyrazine (green), pySMe (red) and pyzSMe (blue) at 1mM concentrations in TCB. Example traces are shown in the inset and structures are shown above..... 172
- Figure 6.3.** A) Frontier MOs of pyzOH at B3LYP/Def2-TZVP level of theory. B) Relaxed junction geometries from left to right of pyz, pyzOH, pyzO (para) and pyzO (meta) at the longest extension before Au rupture (5.7 Å, 5.3 Å, 5.1 Å and 5.5 Å respectively, reported from edge to edge of the apex Au atoms). C) Corresponding

calculated transmission spectra for the pyz-based junction geometries shown above. Transmission calculated using Equation 1 considering the HOMO-1, HOMO and LUMO for pyzOH (green trace). The vertical dashed line indicates E_F 176

Figure 6.4. A) Molecular structures for pyzOH with predicted junction geometries through the para and meta pathways. B) 1D Conductance histogram of pyzOH measured in neutral conditions, pH ~ 7 (gray) and in basic conditions, pH ~ 12 (blue). C) 2D conductance histogram of pyzOH measured in basic conditions. 179

Figure 6.5. Pyz junction geometries and relevant junction lengths. Au-Au junction lengths are reported from edge to edge of the apex Au atoms. Au-N and Au-O bond lengths are reported from the center of the Au. 184

Figure 6.6. Transmission spectra and binding energy (inset) for all sampled geometries of pyz bridged between Au₃₇ electrodes. 185

Figure 6.7. 2D conductance histograms of pyz, pySMe and pyzSMe (left to right). 185

Figure 6.8. Conductance histogram of quinazoline, with N atoms in the 1, 3 positions (meta) of the ring. Measurements performed in a ~1 mM solution in 1,2,4-trichlorobenzene (TCB). 186

Figure 6.9. Frontier MOs of pyz and pyzOH at PBE and B3LYP level of theory with a Def2-TZVP basis set. Energies are reported in eV..... 187

Figure 6.10. Junction geometries of pyzOH (top) and pyzSMe (top) and relevant junction lengths. Au-Au junction lengths are reported from edge to edge of the apex Au atoms. Au-N and Au-O bond lengths are reported from the center of the Au..... 188

- Figure 6.11.** Transmission spectra and binding energy (inset) for all sampled geometries of pyzOH (left) and pyzSMe (right) bridged between Au₃₇ electrodes. 189
- Figure 6.12.** Junction geometries for pyzO para (top) and pyzO meta (top) and relevant junction lengths. Au-Au junction lengths are reported from edge to edge of the apex Au atoms. Au-N and Au-O bond lengths are reported from the center of the Au.. 190
- Figure 6.13.** Transmission spectra and binding energy (inset) for all sampled geometries of pyzO para (left) and pyzO meta (right) bridged between Au₃₇ electrodes. 191
- Figure 6.14.** Calculated transmission at Fermi as a function of Au-Au distance, measured edge to edge, for pyz (green), pyzOH (gray), pyzO para (blue), pyzO meta (red). 192
- Figure 6.15.** Isosurface plots of eigenchannels for the transmission of pyzOH bridged between two Au₃₇ electrodes with an Au-Au separation of 5.3 Å measured edge to edge (contour level 0.01). 193
- Figure 6.16.** Conductance histogram for 3-hydroxypyridine (pyOH) in 1 mM aqueous solutions in pH ~7 (gray) and pH ~12 conditions (red) (right). 2D conductance histogram for pyzO (pyzOH measured in pH ~12 conditions (left). Measurements were performed from H₂O solutions using the dropcast method. 194
- Figure 6.17.** A) Single molecule conductance histogram of pyzOH in pH ~7 (gray) and pH ~12 conditions (blue), performed in H₂O solutions with a wax tip. B) 2D conductance histogram of pyzOH in pH ~7 conditions. C) Conductance histogram of pyzOH measurements in a H₂O solution with a wax-coated tip in acidic conditions (black) and after the addition of 30 μL 1 mM NaOH. D) Conductance histogram of

measurements of KpyzO, dropcast from a H₂O solution (green) compared to pyzO
(pyzOH in basic conditions) (blue)..... 195

LIST OF SCHEMES

Scheme 1.1. General frameworks for extended arrays. Metal centers can be linked via bridging backbone ligands and/or M-M interactions (left) or bridging axial ligands (right).....	9
Scheme 1.2. [PtM(SOCR) ₄ L] lantern scheme indicating areas where modifications have occurred.....	12
Scheme 1.3. Summary of structural motifs observed in {PtM} lantern complexes. Complexes in bold are reported in this thesis.	13
Scheme 1.4. Structural motifs with Pt-L coordination.	14
Scheme 2.1. Representation of possible inter- and intramolecular effects on the Fe(II) center.....	22
Scheme 2.2. The series of [PtFe(SOCR) ₄ (pyX)] (R = Me, X = H (1), X = NH ₂ (2), X = SMe (3); R = Ph, X = H (4), X = NH ₂ (5), X = SMe (6)) complexes studied in this work.	23
Scheme 2.3. Dimeric classifications for the [PtFe(SOCR) ₄ (pyX)] series.....	31
Scheme 2.4. Fe(II) high spin octahedral complexes in N, O and S donor environments.	41
Scheme 3.1. Intra- and inter-molecular assemblies of [PtM(SAc) ₄ (L)] units (M = Co, Ni, Zn).....	58
Scheme 3.2. Examples of bulkier bidentate ligands compared to pyrazine.	63
Scheme 3.3. Summary of motifs from attempts toward [PtM(SOCR) ₄ L] _∞ chains with bulkier axial ligands ([PtCo(SAc) ₄ (4,4'-bipy)] _∞ (7), [PtNi(SAc) ₄ (2,5-Me ₂ pyz) _{0.5}] _∞)	

(8) and [PtNi(SOCR)₄(OH₂)](phz) (9)) compared to the previously reported [PtM(SAc)₄(pyz)]_∞⁷⁹ (x = 0) and {[PtM(SAc)₄(pyz)](pyz)}_∞⁸² (x = 1) chains. 70

Scheme 3.4. Intermolecular connections and types of magnetic behavior in various {PtCo} lantern frameworks. A) dimers with Pt...Pt contacts and antiferromagnetic exchange coupling constant reported for [PtCo(SAc)₄(OH₂)]⁷⁸ B) dimers with Pt...S contacts C) dimers with a N, N' bidentate bridge (e.g. pyz) with antiferromagnetic coupling between Co centers D) chains with a N, N' bidentate bridge (e.g. DABCO) between Co centers of two adjacent lanterns and antiferromagnetic exchange coupling constant reported for [PtM(SAc)₄(DABCO)_{0.5}]_∞⁸² E) chains with a N, N' bidentate bridge (e.g. 4,4'-bipy) between Pt and Co of adjacent lanterns. Co centers in yellow indicate antiferromagnetic coupling through the indicated pathway (also in yellow). Co centers in green indicate no observed coupling. 88

Scheme 4.1. Proposed redesigning of lantern complexes for STMBJ measurements. .. 140

LIST OF ABBREVIATIONS

β	decay constant
δ	isomer shift
Γ	linewidth
ε	molar absorptivity
ΔE_Q	quadrupole splitting
λ	wavelength
μ_B	Bohr magneton
μ_{eff}	effective magnetic moment
μL	microliter
$\chi_M T$	temperature dependent molar magnetic susceptibility
1D	one dimensional
2D	two dimensional
2,5-Me ₂ pyz	2,5-dimethylpyrazine
4,4'-bipy	4,4'-bipyridine
Å	angstrom
bpte	<i>S,S'</i> -bis(2- pyridylmethyl)-1,2-thioethane
bim	2,2'-biimidazole
BJ	break junction
cm ⁻¹	inverse centimeter
CN-	cyanide
CSD	Cambridge structural database

CQI	constructive quantum interference
DACBO	1,4-diazabicyclo[2,2,2]octane
DCM	dichloromethane
dc	direct current
DFT	density functional theory
DMF	<i>N,N</i> -dimethylformamide
DMSO	dimethylsulfoxide
DQI	destructive quantum interference
E_F	Fermi energy
E	energy
e	electron charge
EMAC	extended metal atom chain
esp	$\alpha,\alpha,\alpha',\alpha'$ -tetramethyl-1,3 benzenedipropionate
eV	electron volts
G	conductance
G_0	quantum conductance
h	Planck's constant
HOMO	highest occupied molecular orbital
HSAB	hard soft acid base
I	current
K	Kelvin
LMCT	ligand to metal charge transfer

LUMO	lowest unoccupied molecular orbital
M	Molarity
Me	methyl
MHz	megahertz
mg	milligram
mL	milliliter
mm	millimeter
mM	millimolar
MO	molecular orbital
mpy	2-mercaptopyridine
mV	millivolt
NC-	isocyanide
NCS-	thiocyanate
NEGF	non-equilibrium Green's Function
NIR	near infrared
nm	nanometer
NMR	nuclear magnetic resonance
OAc	acetate
Oe	Oersted
OPE	oligo(phenylene ethylene)
ORTEP	Oak Ridge Thermal Ellipsoid Plot
PC	propylene carbonate

Ph	phenyl
phz	phenazine
py	pyridine
pyNH ₂	4-aminopyridine
pyNO ₂	3-nitropyridine
pyOH	3-hydroxypyridine
pySMe	thiomethylpyridine
pyz	pyrazine
pyzOH	2-hydroxypyrazine
QI	Quantum Interference
QIS	Quantum Information Science
s	seconds
<i>S</i>	<i>spin</i>
S	Siemens
SAc	thioacetate
SCM	single chain magnet
SCXRD	single crystal X-ray diffraction
SMe	thiomethyl
SMepyz	2-thiomethylpyrazine
SOCR	thiocarboxylate
STMBJ	scanning tunneling microscope break junction
T	temperature

<i>T</i>	transmission
tba.....	thiobenzoate
TCB.....	1,2,4-trichlorobenzene
TIM	bis[(imidazol-4-methyl)-4'-imidazol-2'-yl]methane
UV	ultraviolet
V.....	voltage
vis.....	visible
xbim	1,1'-(α,α' -oxylyl)-2,2'-biimidazole

CHAPTER ONE: Introduction

Engineering molecules that exhibit non-trivial electron transport behavior is essential for the development of next-generation electronics. Using molecular building blocks as electronic components provides a bottom-up strategy for further miniaturization of electronics and is further motivated by the fundamental interest in quantum transport and electronic properties of the molecule-metal interface.¹⁻⁴

Molecular junctions on the scale of a nanometer are formed as individual molecules are coupled to metal leads. The molecular backbone and chemical linker groups used to bind to the metal electrodes have critical influence on transport properties.⁵⁻⁷ Understanding structure-property relationships at the nanoscale is important for the chemical design of single molecule electronic components. Therefore, the precise compositional control of molecular systems in their syntheses makes them attractive material candidates.

In addition to the desire for highly conductive molecular wires, there is also interest in molecular components with switching or rectification behavior.⁸ The incorporation of metal centers within molecular components is predicted to provide additional functionality via redox or magnetic properties.⁹⁻¹¹ For example, molecular species with *d* or *f*-block metal ions are current targets for quantum information storage and spintronic applications.^{12, 13} Metal ions can be bridged by organic ligands to form extended materials such as quasi-1D chains and coordination polymers. These systems offer bottom-up strategies to prepare atomically precise molecular wires with non-trivial electronic and magnetic properties due to their reduced dimensionality.¹⁴⁻¹⁶

Other interests in the design of functional molecular components include harnessing quantum interference (QI) effects. At the single molecule level, electron transport is dominated by QI, which results from electrons tunneling across discrete electronic states and, if controlled, could enable the manipulation of conducting states from on to off.^{17, 18} This idea has potential applications for the design of insulating electronic components^{19, 20} and molecular switching behavior.^{21, 22}

1.1. Scanning Tunneling Microscope Break Junction (STMBJ) Technique

Developed by Xu and Tao in 2003, the Scanning Tunneling Microscope Break Junction (STMBJ) technique probes the binding and conductance of single molecules between metal electrodes, typically Au.²³ STMBJ measurements in this thesis were performed in ambient conditions on a homebuilt instrument previously described.^{24, 25} In a typical experiment, the Au electrodes are brought in and out of contact using a piezoelectric positioner under a constant applied bias (typically 100 - 500 mV). The current is measured as a function of Au tip to Au substrate displacement and the conductance (G) is recorded:

$$G = \frac{I}{V}$$

After the formation of an Au-Au contact between the tip and substrate, the junction is stretched. At this scale, transport is ballistic and follows the Landauer formalism,²⁶ which states that conductance scales with the number and transmittance (T_i) of the conducting channels i as:

$$G = \frac{2e^2}{h} \sum_i T_i$$

$$G_0 = \frac{2e^2}{h} = 77.5 \mu S$$

where G_0 is the quantum conductance, e is the electron charge, h is the Planck constant and S (Siemens) is the unit of conductance.²⁶

Conductance traces as a function of junction elongation in Figure 1.1 show stepwise plateaus at integer values of G_0 . These plateaus correspond to the formation of Au contacts with an integer number of Au atoms in the cross-section.²⁷ Eventually the Au contact is broken and a 0.5 – 1 nm nano-gap²⁸⁻³⁰ is formed, after which the conductance decays exponentially. When performed in the presence of molecules that can bind to Au, one or a few molecules can bridge the nano-gap to form a molecular junction with a conductance that is typically less than 1 G_0 . Molecules are functionalized with chemical linker groups (functional groups) with a high binding affinity for Au such as thiol (SH),^{31, 32} thioether (SMe),⁵ pyridyl (py)³³ and amine (NH₂).^{6, 34, 35} Measurements performed in the presence of 1 mM 4,4'-bipyridine (4,4'-bipy) in TCB (1,3,5-trichlorobenzene) feature a plateau around $10^{-3} G_0$ corresponding to conductance of the 4,4'-bipy molecule (Figure 1.1).³³ Thousands of individual conductance traces are compiled into histograms without data selection and normalized to enable comparison. Conductance histograms of clean Au and of 4,4'-bipy on Au in Figure 1.2A both display a peak at 1 G_0 while only 4,4'-bipy displays a conductance feature at lower conductance. Two dimensional (2D) histograms as shown in Figure 1.2B provide displacement information about the molecular junction formation. From Figure 1.2B, there is a conductance feature around $10^{-3} G_0$ which extends to ~ 0.4

nm. Taking into account the Au snapback which is typically 0.5 – 0.8 nm,^{28, 29} we expect the molecular junction to be ~ 1 – 1.2 nm in length. The length of 4,4-bipy is ~ 0.7 nm, and a typical Au-N contact is ~ 2.5 nm, therefore the expected length of an Au-4,4-bipy-Au junction would be ~ 1.2 nm, consistent with the displacement in the 2D histogram.

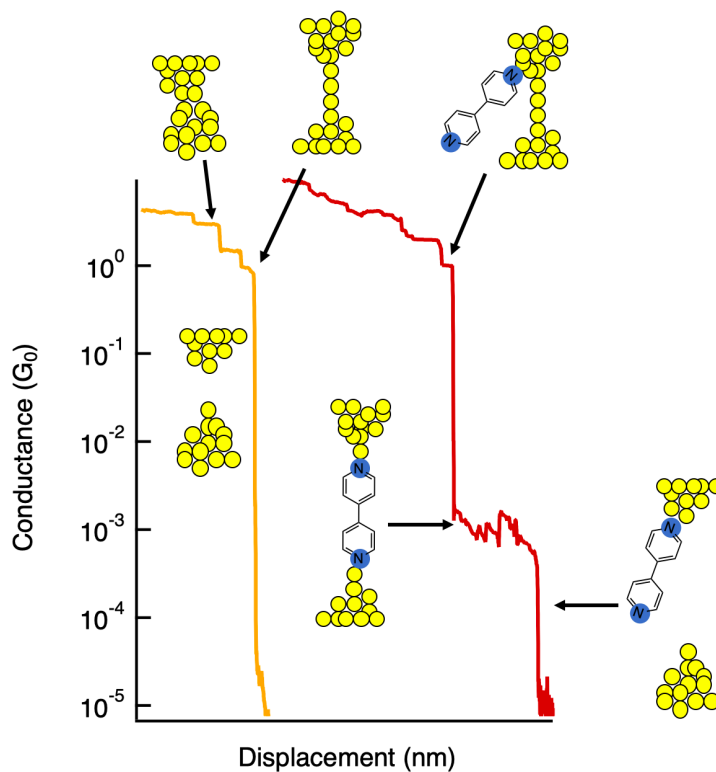


Figure 1.1. Conductance traces of clean Au (left, yellow) and 4,4'-bipy (right, red)

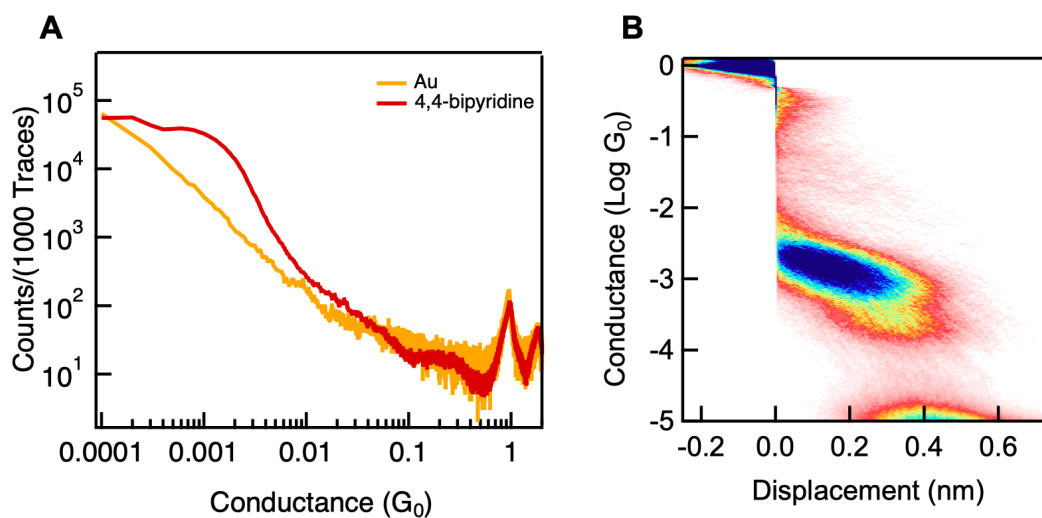


Figure 1.2. A) 1D conductance histograms of clean Au (yellow) and 4,4'-bipy (red). B) 2D conductance histogram of 4,4'-bipy.

1.2. Transition Metal Complexes for Functional Single Molecule Components

Single molecules are appealing material candidates because they can potentially serve as nanometer-sized, molecular electronic equivalents for wires and switches. In the field of single molecule electronics, electron transport has been explored through organic molecules from saturated alkanes,^{5,35} and small aromatic rings^{25,33,36,37} to oligo(phenylene ethynylene)s (OPEs).³⁸ These molecules are typically functionalized with linker groups on each end that can form donor-acceptor bonds to the Au electrodes.⁶ There is interest for incorporating metal centers into single molecule components for possible increased conductance³⁹ and additional functionality.⁹⁻¹¹ Yet, single molecule conductance studies of metal containing molecules are significantly less numerous, as will be described further below. Junctions of typical organic molecules and hypothetical junction geometries of generic mononuclear metal-ligand frameworks are represented in Figure 1.3.

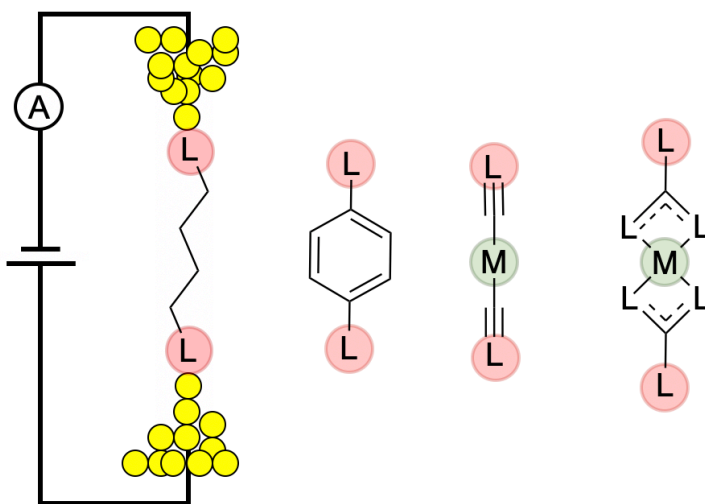


Figure 1.3. STMBJ scheme depicting binding of typical organic molecules and generic M-L frameworks binding in the Au junction via linker groups (L).

One possible implementation of a molecular wire is a linear chain of transition metal atoms brought in close contact via bridging ligands that span the length of the chain. The most well studied examples are the extended metal atom chains (EMACs), also referred to as homonuclear and heteronuclear metal string complexes.^{40, 41} As well as a potential framework for probing transport through metal-metal contacts, these wires can serve as molecular switches via redox mechanisms.⁴⁰

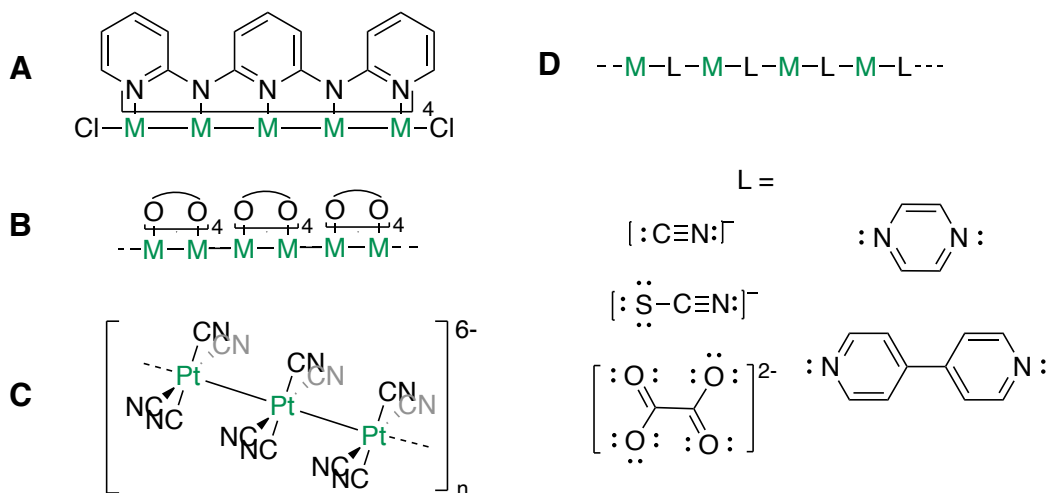
Somewhat surprisingly, existing experimental work on transition metal-containing complexes have yet to show significantly higher conductance compared to that of their organic counterparts at the single molecule level.^{42, 43} Nevertheless, behavior useful for switching and sensing applications has been established. For example, spin polarized

transport in paramagnetic junctions of vanadocene bridged between Ag electrodes has been reported.⁴⁴ Single molecule conductance studies of other metallocenes have demonstrated mechanically tunable conductance through SMe functionalized ferrocene-based junctions⁴⁵ as well as direct Au- π -ligand system links in ferrocene junctions at low temperature.⁴⁶ Spin-crossover complexes, where the spin state can be switched from a low-spin to a high-spin state, e.g. $S = 0$ to $S = 2$ in d^6 Fe(II) via external stimuli, are also appealing candidates for molecular switching applications.^{11, 47} However, fragmentation of Fe(II) spin-crossover complexes has been reported on Au(111) surfaces, raising questions about the degree of stability of metal complexes on Au electrodes,⁴⁸⁻⁵⁰ and what determines this stability. Few studies, if any, had been conducted to address these important questions prior to the work reported here. How to reliably incorporate coordination complexes into the current experimental break junction techniques such as STMBJ is an existing challenge that is addressed in this thesis.

1.3. Quasi-1D Materials

Quasi-1D materials, characterized by reduced dimensionality and high anisotropy which give rise to novel electronic and magnetic properties, are targets in next generation electronics and quantum information storage.^{14, 15, 51-56} Typical examples are 1D coordination polymers and arrays composed of repeating units of metal ions and bridging ligands (Scheme 1.1). One strategy to form molecular wires is to synthetically position metal centers in adjacent sites via bridging ligands to facilitate metal-metal interactions

such as with EMACs, shown in Scheme 1.1A.⁴¹ Chain formation can also be induced by bridging metal ions with bidentate ligands that allow for significant coupling and orbital delocalization across the chain. Unlike EMACs, these are often essentially infinite arrays instead of molecules with a discrete length. Infinite chains of $\{\text{Rh}_2(\text{O}_2\text{CR})_4\}$ units have been shown to form in the solid state with both bidentate O-donor and N-donor ligands as depicted in Scheme 1.1B.^{57, 58} Krogmann salts were one of the first examples of bottom-up molecular wires where chains form through Pt...Pt contacts in repeating units of partially oxidized $\{\text{Pt}(\text{CN})_4\}^{n-}$ (Scheme 1.1C).^{15, 59} Repeating units of metal ions and bidentate ligands as shown in Scheme 1.1D have been used to form 1D coordination polymers. Anionic ligands such as cyanide,^{60, 61} thiocyanate⁶² and oxalate,⁶³ as well as neutral ligands such as pyrazine⁶⁴ and 4,4-bipyridine⁶⁵ are a few examples of axial bridging ligands.



Scheme 1.1. General frameworks for extended arrays. Metal centers can be linked via bridging backbone ligands and/or M-M interactions (left) or bridging axial ligands (right).

The formation of 1D coordination polymers and chains is not only motivated by the desire for highly conductive molecular wires, but also by the search for non-trivial magnetic properties. Single chain magnets (SCM) are species with slow magnetic relaxation behavior.^{66, 67} This behavior is attributed to large uniaxial magnetic anisotropy, strong intra-chain interactions and minimal inter-chain interactions.⁶⁸ A synthetic approach to form 1D arrays with SCM behavior includes linking uniaxial anisotropic units, such as metal ions (M^{n+}), with ligands to form 1D chains (Figure 1.4). The functionality of SCMs depends critically on utilizing ligand systems that allow for strong magnetic coupling between metal centers (intra-chain) while providing magnetic isolation between the individual chains (inter-chain). For example, in $[Mn_2Ni]$ SCMs reported by Clérac and Miyasaka et al, $Ni^{2+} \dots Mn^{3+}$ antiferromagnetic and $Mn^{3+} \dots Mn^{3+}$ ferromagnetic interactions are observed along the chains, isolated by long Mn-Ni inter-chain distances that preclude π -stacking between the organic ligands.⁶⁹ Paramagnetic metal centers can also be coupled with diamagnetic metals through M-M contacts; this strategy has been shown to allow for antiferromagnetic interactions, comparable to and often stronger than those with organic bridges or halides.⁷⁰

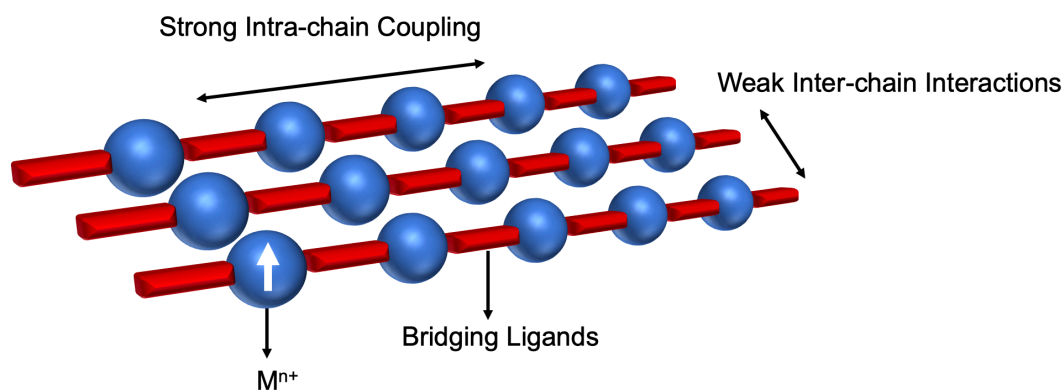
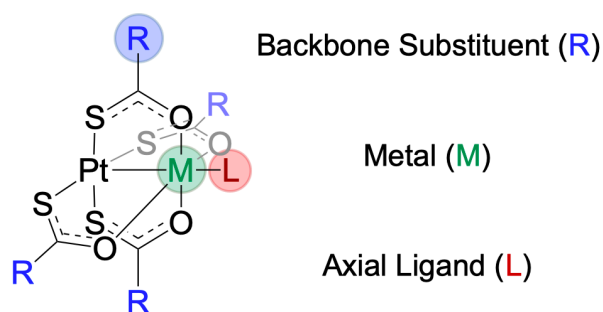


Figure 1.4. Design features for SCM behavior in 1D chains.

1.4. {PtM} Lantern Complexes

An important approach to forming quasi-1D structures is to synthetically assemble pre-designed anisotropic building blocks. The Doerrer group has designed an asymmetric {MM'} heterobimetallic core consisting of Pt and a 3d metal {PtM'} (Scheme 1.2). Hard-soft acid base interactions favor the homoleptic coordination of the thiocarboxylate backbone ligands (SOCR) forming {PtS₄} and {MO₄} coordination environments.⁷¹ Synthetically changing the 3d M(II) in a high spin pseudo-octahedral ligand environment allows for tuning the overall spin of the complex: M = Mn (d^5 , $S = 5/2$), Fe (d^6 , $S = 2$), Co (d^7 , $S = 3/2$), Ni (d^8 , $S = 1$), Zn (d^{10} , $S = 0$). The individual complexes have been isolated with solvent (H₂O, DMSO, DMF) in the terminal axial position on the 3d metal, which can also be exchanged for terminal ligands such as pyridine.⁷² A sizeable family of [PtM(SOCR)₄L] complexes has been synthesized thus far, varying the bulk on the

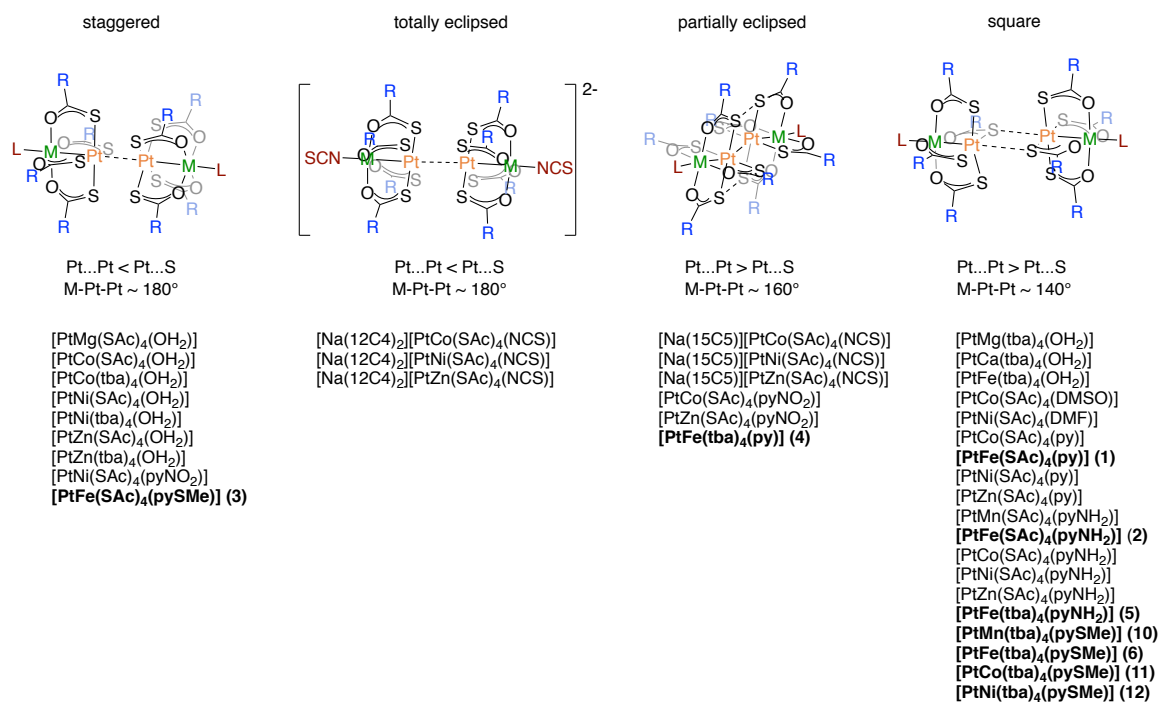
thiocarboxylate backbone ligand (R = Me, Ph), the metal (M = Mg, Ca, VO, Cr, Mn, Fe, Co, Ni, Zn) and the axial ligand (L = terminal or bridging, neutral or anionic), as shown in Scheme 1.2.⁷³⁻⁷⁶



Scheme 1.2. [PtM(SOCR)₄L] lantern scheme indicating areas where modifications have occurred.

Several of these complexes form dimers in the solid state through noncovalent Pt...Pt interactions that exhibit antiferromagnetic coupling between the 3*d* metals.^{77, 78} Four distinct structural motifs (Scheme 1.3) have been identified based on the structures of the solid-state dimers. These categories have distinct magnetic behaviors in the solid state, and the associated magnetic couplings have been quantized between the 3*d* metals,⁷²⁻⁷⁴ while all complexes behave as isolated high spin M(II) centers in solution.^{72, 75, 77, 79} Heterobimetallic lantern complexes with “staggered” backbones have shorter Pt...Pt interactions than Pt...S interactions and near linear M-Pt-Pt angles. These structures typically have ~ 3 Å Pt...Pt interactions that allow for antiferromagnetic coupling between

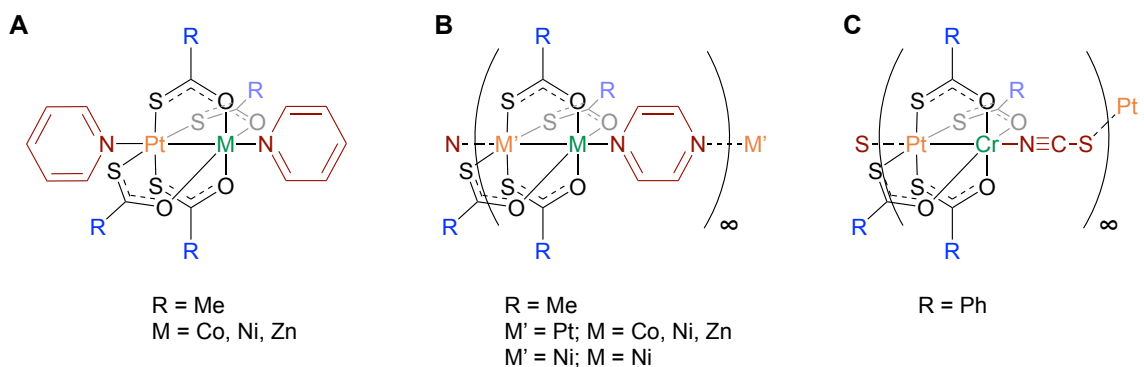
the open shell 3*d* metals of the two heterobimetallic lantern complexes.⁸⁰ In “square” confirmations, Pt...S interactions dominate, and magnetic communication between the 3*d* metals is not observed.⁷²



Scheme 1.3. Summary of structural motifs observed in {PtM} lantern complexes. Complexes in bold are reported in this thesis.

Another structural motif, [(py)PtM(SAc)₄(py)], was isolated from reactions of [PtM(SAc)₄(OH₂)] (M = Co, Ni, Zn) and an excess of pyridine (Scheme 1.4A).⁷² These species contain an unusual six-coordinate pseudo octahedral Pt(II). While six-coordinate Pt(IV) species are common, they are rare for Pt(II).⁸¹ It was hypothesized that this Pt-N binding could be used to form extended arrays, or quasi-1D chains of lantern complexes.

Pyrazine, a bidentate ligand structurally similar to pyridine, was used to bridge individual lantern complexes. An excess of pyrazine induces the formation of essentially infinite chains, where pyrazine forms a bridge between the $3d$ metal and Pt center of adjacent complexes as shown in Scheme 1.4B.^{79, 82} The Doerrer group has also utilized this bottom-up approach to form $\{\text{Ni}_2\}$ quasi-1D chains bridged with N,N'-donor bridging ligands (Scheme 1.4B)⁶⁴ and a $[\text{PtCr}(\text{tba})_4(\text{NCS})]_\infty$ (NCS = thiocyanate) coordination polymer where $\{\text{PtCr}\}^+$ units are bridged by $(\text{NCS})^-$ in a zigzag formation (Scheme 1.4C).⁶²



Scheme 1.4. Structural motifs with Pt-L coordination.

1.5. Quantum Interference

At the single molecule level, electron transport is dominated by quantum interference (QI). To understand how QI dominates transport through single molecule junctions, we consider electrons as waves. In a molecular junction where a molecule is bound between two Au leads, electrons tunnel from the source to the drain electrodes across the occupied and unoccupied frontier molecular orbitals (MOs) of the molecule as depicted in Figure 1.5A. The energies of these MOs are the resonances of the junction. At both molecule-metal interfaces where a mismatch of energies occurs, some fraction of the electronic waves will be reflected. An analogy can be made to an optical system cavity, with electromagnetic waves incident from the left on a pair of parallel, partially transmitting windows located at the two metal-molecule interfaces. The transmission probability in both cases is dependent on the energy of the incident wave relative to the resonances of the cavity. In the case of the molecular junction, it also depends on the relative phases of the molecular orbitals involved in transmission.

There are two important phase changes to consider, the phase change of the transmitted electrons and the phase changes of the frontier orbitals relative to each other. The first phase change is dependent on the energy at which the wave is transmitting and is fully analogous to the optical cavity analogy with resonances located at energies ϵ_i . If we consider a theoretical system with only a single resonance (ϵ_i) contributing to transport and E_F being the energy of the injected electrons from Au, one can show mathematically that on either side of the resonance at energy ϵ_i the phase of the transmitted electron will be

flipped by π (Figure 1.5B). Figure 1.5C shows a system where two orbitals with energies ϵ_i and ϵ_j , the HOMO and LUMO respectively, contribute to transport and E_F is within the HOMO-LUMO gap. The phase of the transmitting wave through ϵ_i will be the opposite of the phase of the transmitting wave through ϵ_j . This is because E_F is above the energy of the ϵ_i resonance and below the energy of the ϵ_j resonance. In other words, there is a phase shift of $\sim \pi$ between electrons transmitting through the HOMO and LUMO at the drain electrode.

The other phase change to consider is due to the symmetry of the transmitting MOs. For simplicity, we consider only the HOMO and LUMO since they contribute the most to transport. Figure 1.5D shows an example of a molecular junction with a benzene backbone and unspecified linker groups (L) bridged between two Au electrodes. The electronic wave transmitting through the orbital experiences whatever phase change exists, if any, between the two opposing ends of the MO at the Au connections. The relative phases of each end of the MOs at the source (bottom) and the drain (top) are indicated with red and blue circles on the L groups in Figure 1.5D. Therefore, for the HOMO on the left, the phase of the electronic wave changes by π over this orbital, as indicated by the change from red on one end and blue on the other. The corresponding LUMO above does not change phase, therefore we have an *overall* phase change of π between the HOMO and LUMO. Considering the additional phase change of π in the electron wave between the HOMO and LUMO discussed above, there is an overall phase change of $\sim 2\pi$, equivalent to no overall phase change and we expect constructive quantum interference (CQI) for an electron wave tunneling across these two orbitals. A qualitative transmission spectrum with CQI between the HOMO and LUMO at -1 eV and 1 eV respectively is shown in green in Figure 1.5E.

For the HOMO and LUMO on the right in Figure 1.5D, we see that there is no orbital phase change. Therefore, considering the electron phase change discussed above, there is an *overall* phase change between the HOMO and LUMO of π and we would predict destructive quantum interference (DQI), shown in the transmission spectrum in red.

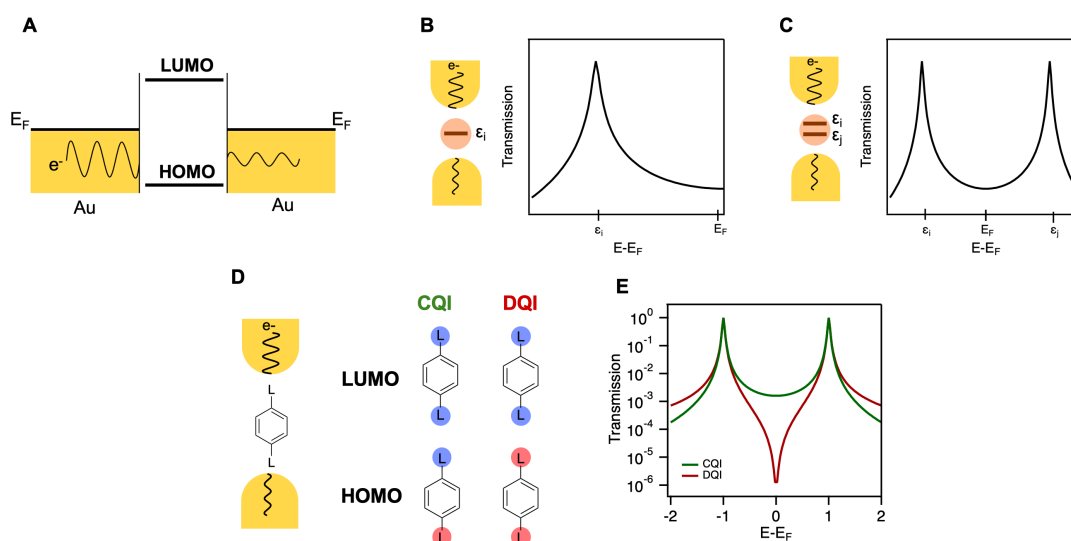


Figure 1.5. A) Scheme depicting electrons tunneling through frontier MOs. B) Example transmission through a hypothetical one-orbital system, C) Example transmission through a hypothetical two-orbital system. D) Benzene-based molecule with generic linker groups (L) bound to Au leads. QI predictions (constructive vs destructive) are illustrated based on the relative phases of the MOs at L. The relative phases at L are indicated by the red/blue circles. E) Example transmission of CQI (green trace) and DQI (red trace).

1.6. Motivation and Outlook

This thesis explores the design, synthesis and measurement of single molecule electronic components and quasi-1D structures. The subject of Chapter 2 is synthesis and characterization of individual {PtM} lantern units using ^{57}Fe Mössbauer spectroscopy to understand the effect of intra- and inter-molecular interactions on the electronic environment of the $3d$ metal ($M = \text{Fe}$). In Chapter 3, {PtM} quasi-1D chain formation with N,N' -donor bridging ligands is investigated where we report the synthesis and magnetic characterization of a $[\text{PtCo}(\text{SAc})_4(4,4'\text{-bipy})]_{\infty}$ ($4,4'$ -bipy = $4,4'$ bipyridine) chain.

Chapters 4 and 5 focus on developing synthetic strategies for robust incorporation of transition metal complexes into molecule-metal junctions using STMBJ measurements supplemented by density functional theory (DFT) calculations. In Chapter 4, we utilize the synthetically tunable framework of the heterobimetallic lantern complexes $[\text{PtM}(\text{SOCRL})]$ to study the stability of intramolecular metal-ligand bonding within the context of the Au junction. We perform break-junction measurements on individual lantern complexes and establish chemical design principles identifying the competition between the *intramolecular* metal ligand bonding within the complex and the *intermolecular* molecule-metal (Au electrode) interaction. Our insight is that metal-molecule junction assembly and disassembly trends are consistent with hard-soft acid-base chemistry, empirical observations used to rationalize and predict atomic arrangements of coordination complexes.⁷¹

Based on the above chemical design principles, we explore other metal-containing units with organometallic intramolecular metal-ligand bonding. In Chapter 5, the binding and conductance of $[M(CN)_x]^{n-}$ cyanometalate complexes is investigated, inspired by their use in the formation of 1D coordination polymers and chains.^{59, 60} The complex $[KAu(CN)_2]$, features a two-coordinate Au center with a linear $[(NC)Au(CN)]^{1-}$ unit and π backbonding from d^{10} Au(I) to the $C\equiv N$ π^* bonds. From STMBJ measurements, we observe rearrangement in the junction and formation of robust molecular bridges with conductance features ranging from $\sim 10^{-1} - 10^{-6} G_0$.

In Chapter 6, destructive QI between σ and π orbitals in single pyrazine-based junctions is identified for the first time. We then demonstrate how small changes in electronic structure via chemical substitution and environmental control can be leveraged to manipulate QI.

This work highlights how insights from transition metal coordination chemistry can be leveraged to further understand molecule-metal binding and to inform the design of molecular candidates for STMBJ experiments. In turn, electron transport properties at the single molecule level can feed back to inform synthetic choices of the design of molecular electronic components such as quasi-1D geometries. Single molecule electronic conductance measurements via the STMBJ method can probe conductance and binding of molecules on metal surfaces, as well as quantum transport behavior and interference effects. QI effects are potentially relevant for quasi-1D systems and could provide design considerations when choosing bridging ligands.

CHAPTER 2: Determination of Ligand Substituent Effects in Pt-Fe Heterobimetallic Lantern Complexes via ^{57}Fe Mössbauer Spectroscopy

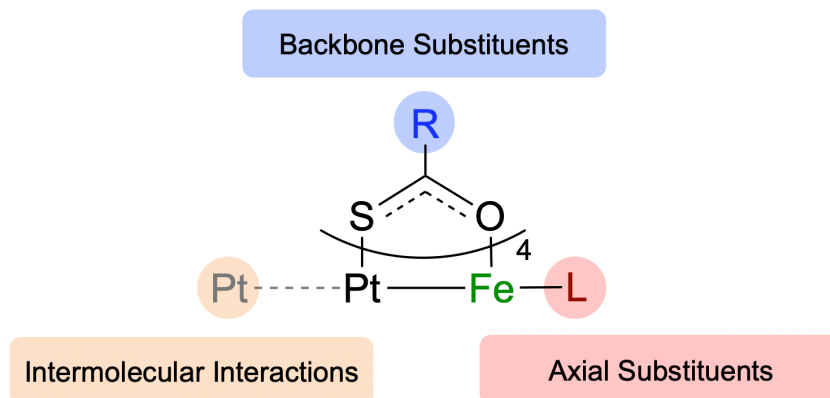
2.1. Introduction

Quasi-1D materials such as 1D arrays and coordination polymers have been recognized for their unusual electronic and magnetic properties due to their reduced dimensionality and high anisotropy.¹⁵ One approach to form quasi-1D materials is to assemble individual anisotropic units designed to bond to each other directly or linked via bridging groups. We employ this bottom-up approach using heterobimetallic complexes coupled by bridging ligands to form atomically precise quasi-1D chains. The individual heterobimetallic units themselves are synthetically tunable allowing for the study of structure-property relationships. A family of heterobimetallic complexes of the form $[\text{PtM}(\text{SOCR})_4(\text{L})]$ ($\text{M} = \text{Mg}, \text{Ca}, \text{VO}, \text{Cr}, \text{Mn}, \text{Fe}, \text{Co}, \text{Ni}, \text{Zn}$; $\text{R} = \text{Ph}$ (tba = thiobenzoate), Me (SAC = thioacetate); $\text{L} =$ neutral or anionic ligand) have been synthesized thus far by the Doerrer lab.^{73, 74, 76}

Synthetic control of the backbone ligands (SOCR), axial ligands (L), and two different metal centers (Pt and M) allows for local, intramolecular electronic and magnetic property tuning of the entire complex. Changes in the ligands via R and L also affect the intermolecular structural and magnetic properties and several structural motifs have been identified with varying assemblies depending on M, L and R (Scheme 1.3). Synthetically

tuning the electronic effects of the ligand framework within the individual lantern units is important for the design of these quasi-1D structures.

In this work, we develop our understanding of these structure-property relationships by investigating the effect on intra- and inter-molecular interactions of the electronic environment at the 3d metal (M = Fe) using ^{57}Fe Mössbauer spectroscopy (Scheme 2.1). A series of lantern complexes of the form $[\text{PtFe}(\text{SOCR})_4(\text{pyX})]$ (R = Me, Ph; X = H, NH_2 , SMe) were prepared (Scheme 2.2). Ligand substituents were varied in the R group on the thiocarboxylate bridge (SOCR) and in the *para* position of the axial (pyX) ligand while keeping the metal coordination environment constant. These complexes form intermolecular interactions in the solid state, dominated by either Pt...Pt or Pt...S interactions as seen in previous studies.^{73, 74} Mössbauer spectroscopy, sensitive to small changes in chemical environment, was used to probe the inter- and intramolecular effects on the Fe center. We find that substitutions made on the backbone carboxylate ligand (R = Me or Ph) and the pyridine axial ligand (pyX = H, NH_2 , SMe) significantly affect the quadrupole splitting (ΔE_Q) in the Mössbauer measurements. The degree of variation between the different {PtFe} derivatives is sizeable considering the distance of the substituents from the Fe(II) center (5 – 6 Å). This study expands our understanding of structure-property relationships in the context of the ligand framework and highlights the ability to tune the electronic properties of the individual {PtFe} heterobimetallic lantern complexes.



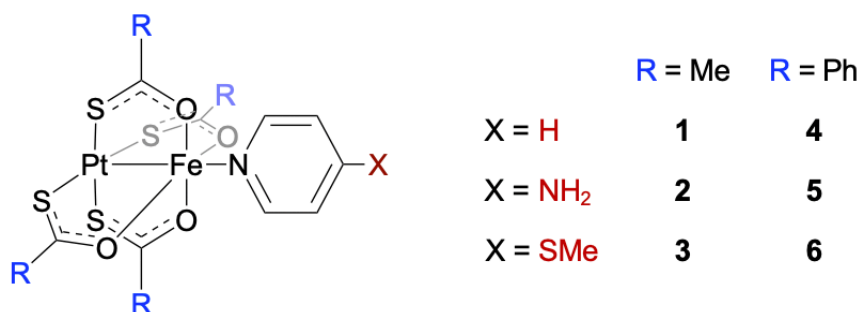
Scheme 2.1. Representation of possible inter- and intramolecular effects on the Fe(II) center.

2.2. Results and Discussion

2.2.1. Synthesis and Structure

A series of lantern complexes of the form $[\text{PtFe}(\text{SOCR})_4(\text{pyX})]$ ($\text{R} = \text{Me, Ph}$); $\text{X} = \text{H, NH}_2$ and SMe , were prepared (Scheme 2.2). The complexes were prepared with either a thioacetate (SAc, $\text{R} = \text{Me}$) or thiobenzoate (tba, $\text{R} = \text{Ph}$) backbone and a pyridine (py, $\text{X} = \text{H}$), 4-aminopyridine (pyNH_2 , $\text{X} = \text{NH}_2$) or 4-thiomethylpyridine (pySMe , $\text{X} = \text{SMe}$) axial ligand to form: $[\text{PtFe}(\text{SAc})_4(\text{py})]$ (**1**), $[\text{PtFe}(\text{SAc})_4(\text{pyNH}_2)]$ (**2**), $[\text{PtFe}(\text{SAc})_4(\text{pySMe})]$ (**3**) $[\text{PtFe}(\text{tba})_4(\text{py})]$ (**4**), $[\text{PtFe}(\text{tba})_4(\text{pyNH}_2)]$ (**5**) and $[\text{PtFe}(\text{tba})_4(\text{pySMe})]$ (**6**). Complexes **2** and **3**, with SAc backbones and pyNH_2 and pySMe axial ligands respectively were the first examples of $\{\text{PtFe}\}$ containing lantern complexes with a pyridine-based axial ligand and were prepared from reported procedures.⁷⁵ Complex

6, with a tba backbone and a pySMe axial ligand, was also reported previously⁸³ and synthetic details are provided in Chapter 4. In this work, the unsubstituted pyridine derivatives with a SAc (**1**) and tba (**4**) backbone as well as the tba derivative of the pyNH₂ version (**5**) were prepared to complete a series of {PtFe} lanterns with each variation of R and X. Complexes **1**, **4** and **5** were synthesized via modification of previously developed procedures.^{75, 77}



Scheme 2.2. The series of [PtFe(SOCR)₄(pyX)] (R = Me, X = H (**1**), X = NH₂ (**2**), X = SMe (**3**); R = Ph, X = H (**4**), X = NH₂ (**5**), X = SMe (**6**)) complexes studied in this work.

Complex **1** was synthesized from the addition of pyridine to freshly prepared [PtFe(SAc)₄(OH₂)] in acetone. The resulting orange precipitate was isolated via filtration and orange crystals were obtained from a CH₂Cl₂ solution layered under hexanes. Complex **4** was synthesized from the addition of pyridine to freshly prepared [PtFe(tba)₄(OH₂)] in acetone. The reaction mixture was dried and washed with water and hexanes. The

remaining red solid was dissolved in CH_2Cl_2 and layered under hexanes to obtain dark red crystals suitable for X-ray analysis. Complex **5** was prepared using the same procedure with pyNH_2 . Dark red crystals suitable for X-ray analysis were obtained from a CH_2Cl_2 solution layered under hexanes. All three complexes have been crystallographically characterized and ORTEPs for **1**, **4** and **5** are shown in Figures 2.1, 2.2 and 2.3 respectively. Selected bond distances and angles are reported in Table 2.1 along with selected bond lengths and angles for the previously published **2**, **3** and **6**.^{75, 83} Complex **3** has four independent lantern units in the asymmetric unit and bond lengths for all units are reported.

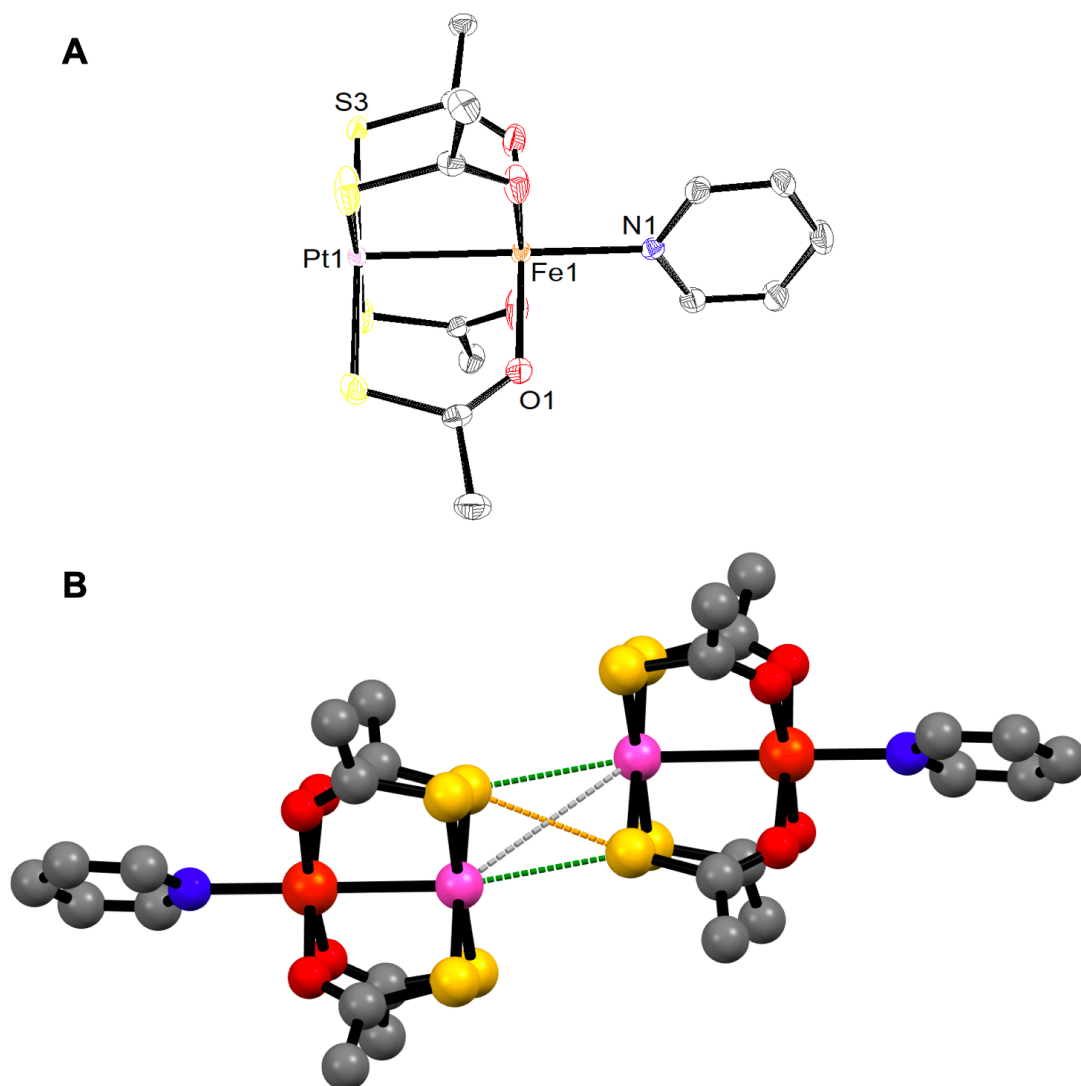


Figure 2.1. A) ORTEP of **1**. Ellipsoids are drawn at the 50% level and hydrogen atoms are omitted for clarity. B) Mercury representation of intermolecular Pt...Pt (4.338 Å, gray), Pt...S (3.109 Å, green) and S...S (3.362 Å, orange) contacts between individual complexes.

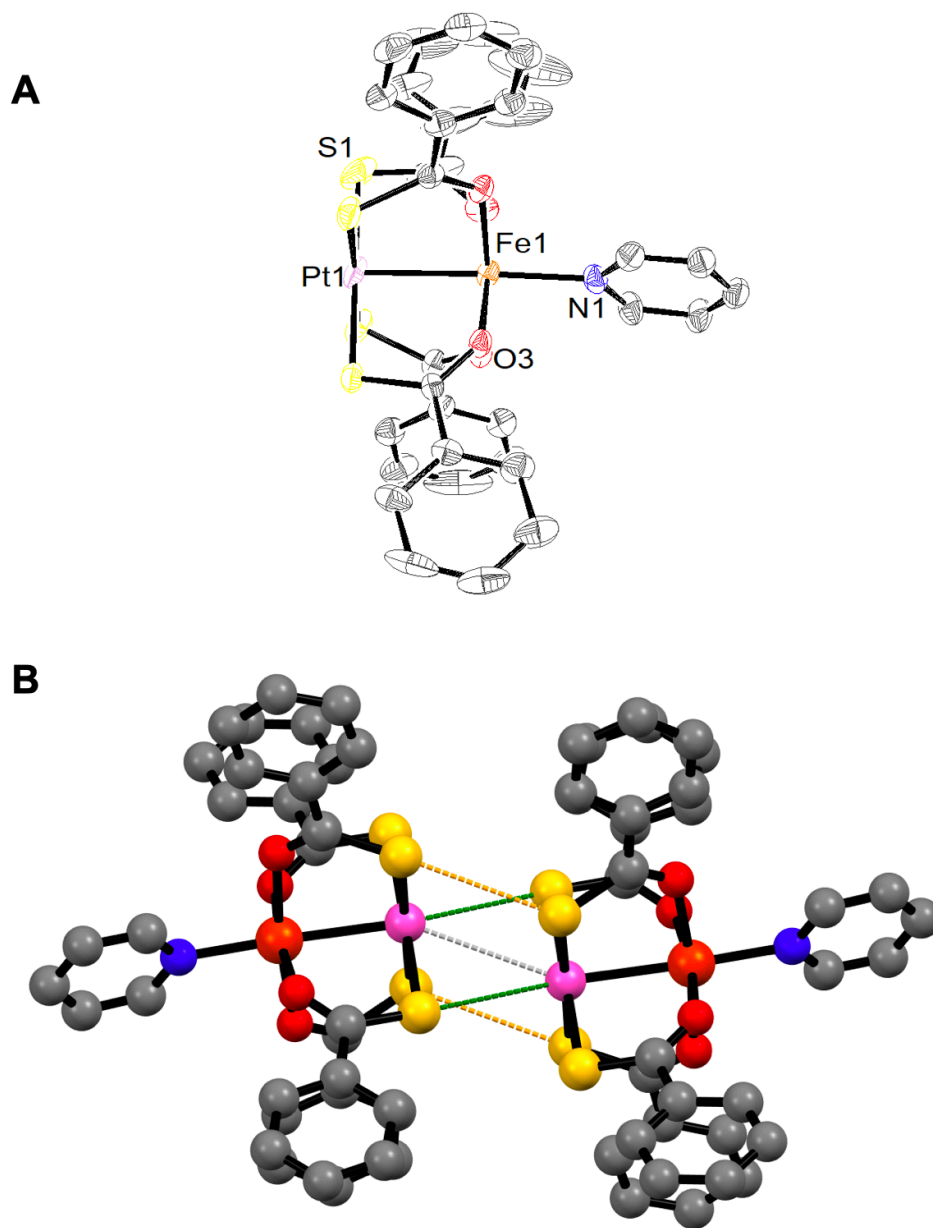


Figure 2.2. A) ORTEP of **4**. Ellipsoids are drawn at the 50% level and hydrogen atoms are omitted for clarity. B) Mercury representation of intermolecular Pt...Pt (3.562 Å, gray), Pt...S (3.474 Å, green) and S...S (3.532 Å, orange) contacts between individual complexes.

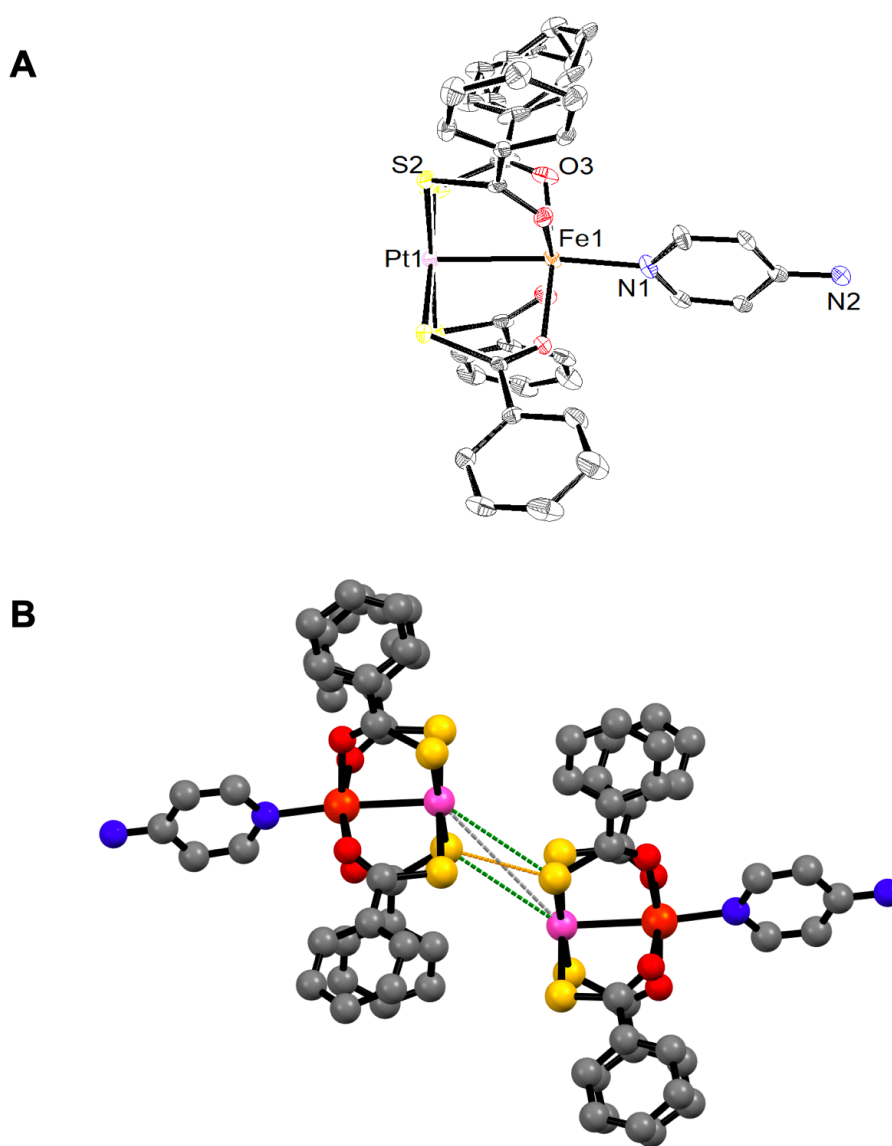


Figure 2.3. A) ORTEP of **5**. Ellipsoids are drawn at the 50% level and hydrogen atoms are omitted for clarity. B) Mercury representation of intermolecular Pt...Pt (5.410 Å, gray), Pt...S (3.847 Å, green) and S...S (3.336 Å, orange) contacts between individual complexes.

Table 2.1. Selected bond distances and angles for the [PtFe(SOCR)₄(pyX)] series

Complex	R	X	Pt-Fe (Å)	Fe-N (Å)	Average Pt-S (Å)	Average Co-O (Å)	Reference
1	Me	H	2.6610(6)	2.144(2)	2.320(1)	2.108(2)	this work
2	Me	NH ₂	2.6788(5)	2.105(2)	2.3263(9)	2.110(4)	75
3^a	Me	SMe	2.6633(6)	2.121(3)	2.324(1)	2.100(4)	75
	Me	SMe	2.6737(6)	2.131(3)	2.322(1)	2.079(4)	75
	Me	SMe	2.6848(6)	2.132(3)	2.328(1)	2.087(4)	75
	Me	SMe	2.6762(6)	2.127(3)	2.329(1)	2.094(4)	75
4	Ph	H	2.6449(8)	2.141(4)	2.319(2)	2.106(4)	this work
5	Ph	NH ₂	2.6686(7)	2.100(4)	2.322(1)	2.116(3)	this work
6	Ph	SMe	2.6538(9)	2.144(5)	2.322(2)	2.127(5)	83

^a Bond lengths reported for each of the four independent lantern units in the asymmetric unit.

As reported in Table 2.1 and shown in Figure 2.4, the Pt-Fe and Fe-N distances are relatively consistent, varying by ~ 0.04 and 0.05 Å across the series respectively. The SAc (SOCMe) derivatives have longer Pt-Fe distances than their tba (SOCPh) counterparts (Figure 2.4A). There is a decrease in Fe-N distance as the *para* substituent on the axial pyridine ligand becomes a stronger π -donor from H to SMe to NH₂. This is consistent with previous observations where M-N distances (M = Co, Ni, Zn) decrease with increasing basicity of the pyridine N from pyNO₂ to py to pyNH₂.⁷² As the *para* substituent on the axial pyridine ligand becomes a stronger π -donor from H to SMe to NH₂, the Pt-Fe distance increases (Figure 2.4B). There is no clear trend between the Pt-Fe distance and the closest Pt...L (L = Pt or S) intermolecular contact across the series (Figure 2.4C).

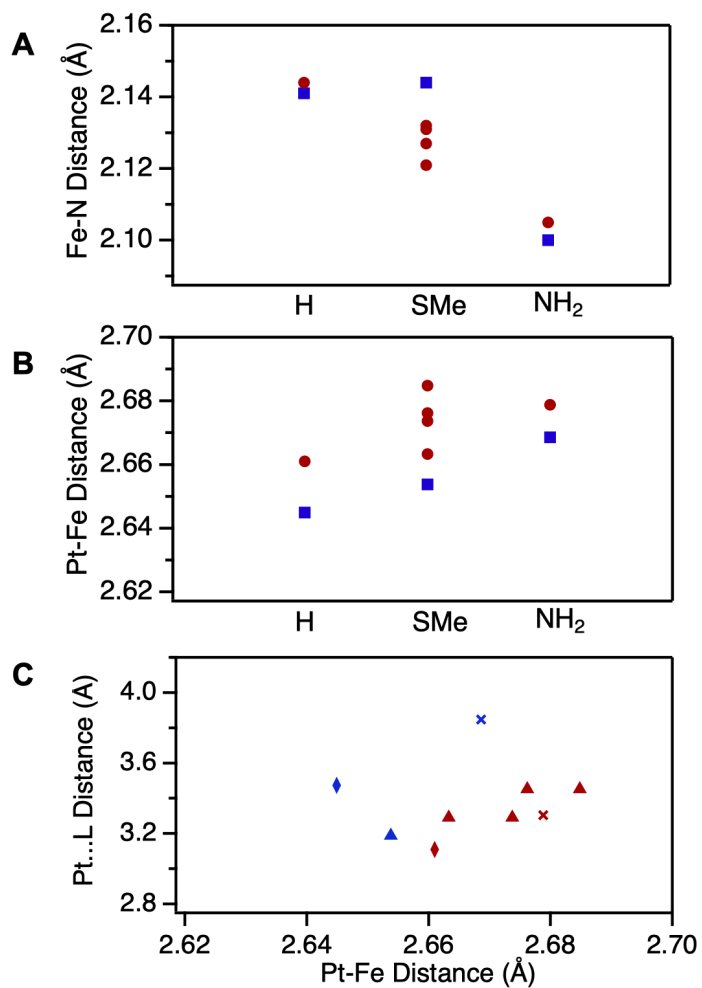
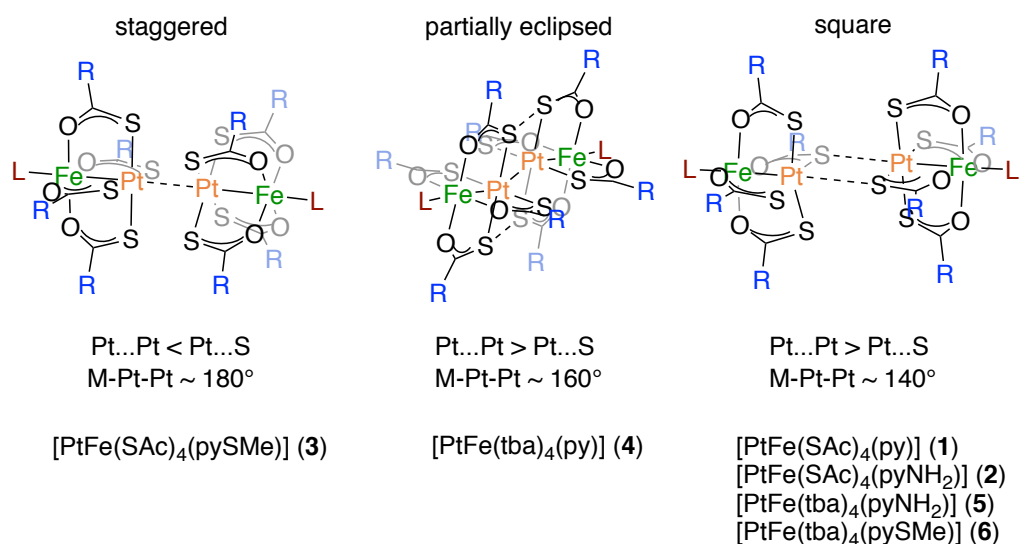


Figure 2.4. Plots of Pt-Fe (A) and Fe-N (B) distances (Å) as a function of axial ligand substituent (H, SMe, NH₂) and backbone R group (Me = red circles, Ph = blue squares). C) Comparison of Fe-N distance and the closest Pt...L contact (L = S for **1**, **2**, **4**, **5** and **6**, L = Pt for **3**). R = Me (red), R = Ph (blue); L = H (diamonds), L = NH₂ ("x"), L = SMe (triangles).

As shown in Figures 2.1 – 2.3 and summarized in Scheme 2.3, **1 - 6** form dimeric structures in the solid-state dominated by intramolecular interactions between the {PtS₄} faces. The shortest Pt...Pt, Pt...S and S...S intermolecular interactions are reported in Table 2.2. As discussed in Scheme 1.3 and shown in Scheme 2.3, these structures have been categorized into groups based on the relative distances of the Pt...Pt and Pt...S intermolecular interactions and the M-Pt-Pt angle between the monomers. This categorization emphasizes the effect of intermetallic structure on the coupling between the 3*d* metals. For example, dimers dominated by short (~ 3 Å) Pt...Pt interactions exhibit antiferromagnetic coupling between the open shell 3*d* metals, while dimers dominated by Pt...S interactions do not.^{72, 78}



Scheme 2.3. Dimeric classifications for the [PtFe(SOCR)₄(pyX)] series

Table 2.2. Intermolecular distances and angles for the $\text{PtFe}(\text{SOCr})_4(\text{pyX})$ series

Complex	R	X	Pt...Pt (Å)	Pt...S (Å)	S...S (Å)	M-Pt- Pt (°)	Dimer Category	Reference
1	Me	H	4.338	3.109	3.362	133.49	square	this work
2	Me	NH ₂	4.128	3.305	3.896	143.77	square	75
3^a	Me	SMe	3.291	3.884	3.430	177.63	staggered	75
	Me	SMe	3.453	3.942	3.496	175.01	staggered	75
4	Ph	H	3.562	3.474	3.532	152.41	partially eclipsed	this work
5	Ph	NH ₂	5.410	3.847	3.336	123.89	square	this work
6	Ph	SMe	3.747	3.189	3.376	143.39	square	83

^a Intermolecular distances and angles for each of the two dimers in the asymmetric unit.

Focusing first on the complexes with the SAc backbone, **1** has Pt...S and Pt...Pt interactions of 3.109 Å and 4.338 Å respectively with a M-Pt-Pt angle of ~ 133 °. This structure falls in the “square” category, where Pt...S interactions dominate. Complex **2** can also be described at “square” with the shortest contacts being Pt...S intermolecular interactions (Table 2.2). Based on this structural information, we would not expect magnetic communication between the monomers. Complex **3** has two independent solid-

state dimers with Pt...Pt interactions of ~ 3.2 Å and ~ 3.4 Å. The dominant Pt...Pt contacts and M-Pt-Pt angles nearing $\sim 180^\circ$ is consistent with the “staggered” category. In this configuration, the short Pt...Pt contacts forces staggering of the backbone ligands when viewed down the M-Pt-Pt axis. Despite the relatively long Pt...Pt interactions (> 3.1 Å), magnetic studies of these solid state dimers revealed magnetic coupling between the Fe(II) centers, consistent with other staggered lantern dimers.⁷⁵

In the group of three complexes with the tba backbone, **5** and **6** are “square.” The Pt...Pt, Pt...S and S...S intermolecular interactions of **6** are most comparable to those of **1** as reported in Table 2.2, while **5** has longer Pt...S and Pt...Pt distances of 3.847 Å and 5.410 Å respectively and a narrower M-Pt-Pt angle of $\sim 124^\circ$. The 3.336 Å S...S interaction forms the shortest contact between the individual units. Complex **4** has Pt...S (3.474 Å) and Pt...Pt (3.562 Å) interactions of similar distances and a M-Pt-Pt angle of $\sim 152^\circ$. This structure is most consistent with the “partially eclipsed” motif. Other “partially eclipsed” solid-state dimers have M-Pt-Pt angles closer to $\sim 160^\circ$. While a Pt-M-M angle of $\sim 152^\circ$ falls in between the “partially eclipsed” and “square” categories, the Pt...Pt and Pt...S interaction distances are more consistent to those in the partially eclipsed than the square category.^{73, 74}

2.2.2. Electronic Spectroscopy

UV-vis-NIR spectra for **1**, **4** and **5** are shown in Figure 2.5 and are consistent with previously reported heterobimetallic lantern complexes.⁷³⁻⁷⁵ All three complexes display LMCT from the thiocarboxylate backbone S to the Pt center around 260 nm. The two different backbones give rise to distinctive features. The tba derivatives have a feature in UV assigned to the $\pi-\pi^*$ of the aryl ring in the thiobenzoate backbone ligands. The SAc derivatives have a charge transfer feature at 361 nm, 359 nm and 380 nm for **1**, **2**, and **3** respectively (Table 2.3). Complexes **4**, **5** and **6** have features at 480 nm, 490 nm and 486 nm respectively corresponding to Fe(II) *d-d* transitions (Figure 2.5 inset (left) and Table 2.3). The inset (right) in Figure 2.5 shows a weak NIR peak around 960 nm for all complexes. This absorbance was observed for the other complexes in this series and assigned to intermetallic *d-d* transitions, except in **2** where this region was not measured.⁷⁵

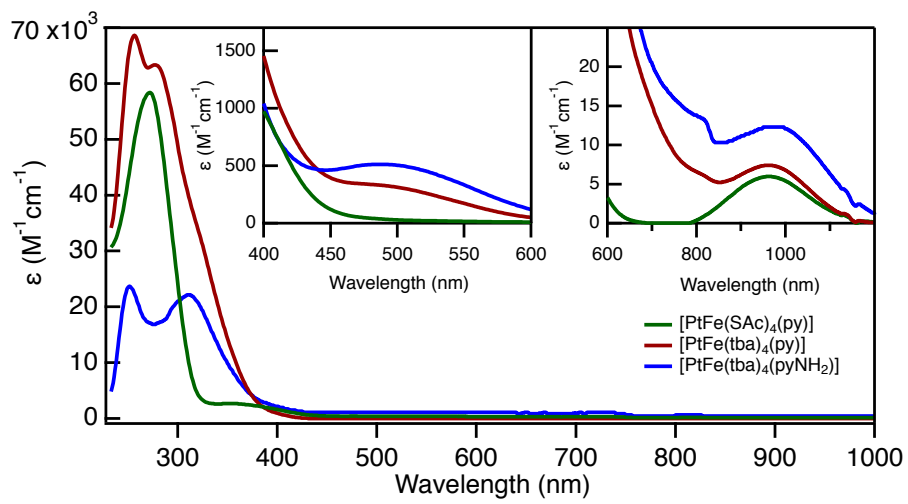


Figure 2.5. UV-Vis spectra of $[\text{PtFe}(\text{SAc})_4(\text{py})]$ (**1**, green), $[\text{PtFe}(\text{tba})_4(\text{py})]$ (**4**, red) and $[\text{PtFe}(\text{tba})_4(\text{pyNH}_2)]$ (**5**, blue) in CH_2Cl_2 . Visible and visible-NIR regions are also shown in the left and right insets respectively.

Table 2.3. Vis-NIR comparison for the [PtFe(SOCR)₄(pyX)] series.

Complex	R	X	λ , nm (ϵ , cm ⁻¹ M ⁻¹)	λ , nm (ϵ , cm ⁻¹ M ⁻¹)	Reference
			visible	near-IR	
1	Me	H	361 (1,404)	960 (6)	this work
2	Me	NH ₂	359 (15,900)	-	⁷⁵
3	Me	SMe	380 (3,060)	970 (8)	⁷⁵
4	Ph	H	480 (336)	959 (7)	this work
5	Ph	NH ₂	490 (511)	980 (12)	this work
6	Ph	SMe	486 (356)	966 (7)	⁸³

2.2.3. Magnetic Susceptibility

Solution magnetic susceptibility was measured via Evans' method for the new complexes of this series.⁸⁴ The predicted spin-only magnetic moment for a high spin octahedral Fe(II) complex is $4.90 \mu_B$.⁸¹ Complexes **1**, **4** and **5** have μ_{eff} values of 5.52, 5.71 and $5.17 \mu_B$ respectively, consistent with monomeric species in solution. These are in the typical range for Fe(II) high spin complexes that also have spin-orbit coupling contributions and are comparable to those of the previously reported complexes **2** ($4.41 \mu_B$),⁷⁵ **3** ($6.06 \mu_B$)⁷⁵ and **6** ($5.51 \mu_B$).⁸³ All complexes, with the exception of **2** have higher experimental susceptibilities than the predicted spin-only value and are in the typical range observed for Fe(II) high spin complexes. In general, the thiobenzoate derivatives tend to have higher magnetic susceptibilities than their thioacetate counterparts, but there are no clear trends with axial ligand substituent across the series.

2.2.4. Mössbauer Spectroscopy

Mössbauer measurements were utilized to evaluate the effects of ligand differences on the Fe center within the {PtFe} heterobimetallic lantern complexes, and possible intermolecular effects as well. The data were collected and analyzed by Prof. Sebastian Stoian and Adam Valaydon-Pillay at the University of Idaho.

To evaluate the electronic structure of the Fe sites, an initial survey of the entire series [PtFe(SOCR)₄(pyX)] series was performed. Figure 2.6 displays the Mössbauer spectra obtained in zero-field at 4.35 K. The parameters derived from the spectra considering only a quadrupole doublet are listed in Table 2.4. Inspection of Table 2.4 shows that the isomer shift values observed for these species are essentially constant, $\delta \sim 1.2$ mm/s. This value is typical of high-spin Fe(II) sites and demonstrates that the Fe sites adopt a quintet ground state. However, a much larger variation in quadrupole splitting is observed such that one of the smallest values is determined for **1**, $\Delta E_Q = 1.426$ mm/s, and the largest is determined for **6**, $\Delta E_Q = 2.415$ mm/s, and encompass a range of 1.1 mm/s. Moreover, the compounds supported by the thiobenzoate backbone ligands have a consistently larger quadrupole splitting than the thioacetate counterparts.

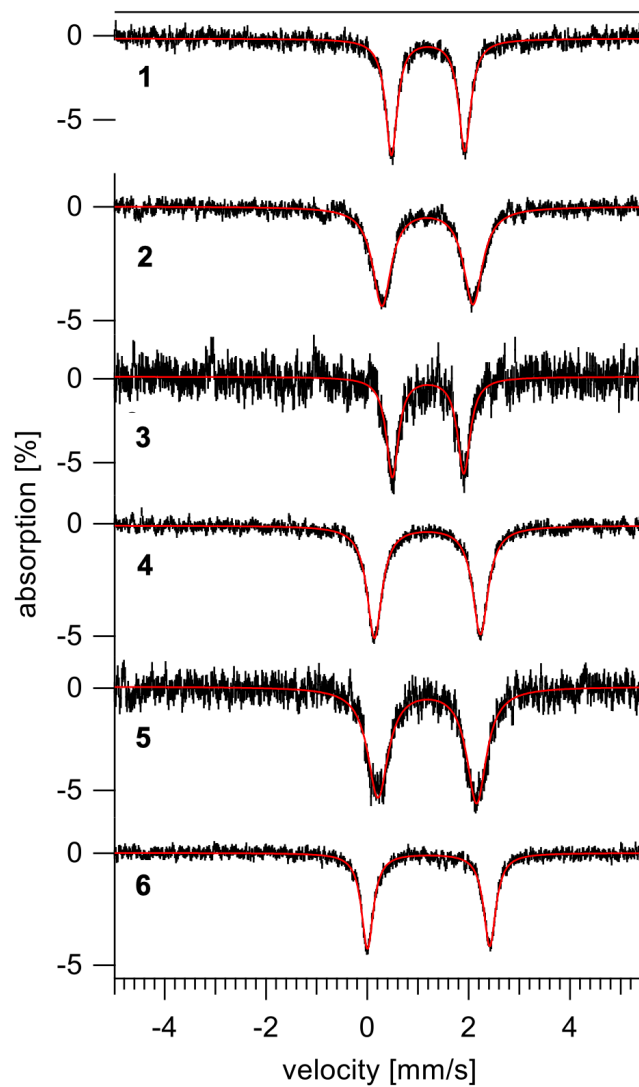


Figure 2.6. Zero-field Mössbauer spectra recorded at 4.35 K for **1** – **6**. The solid red lines are theoretical curves obtained considering a single quadrupole doublet characterized by the parameters listed in Table 2.4.

Table 2.4. Zero field Mössbauer parameters determined at 4.35 K for **1** - **6** simulating only a single quadrupole doublet.^a

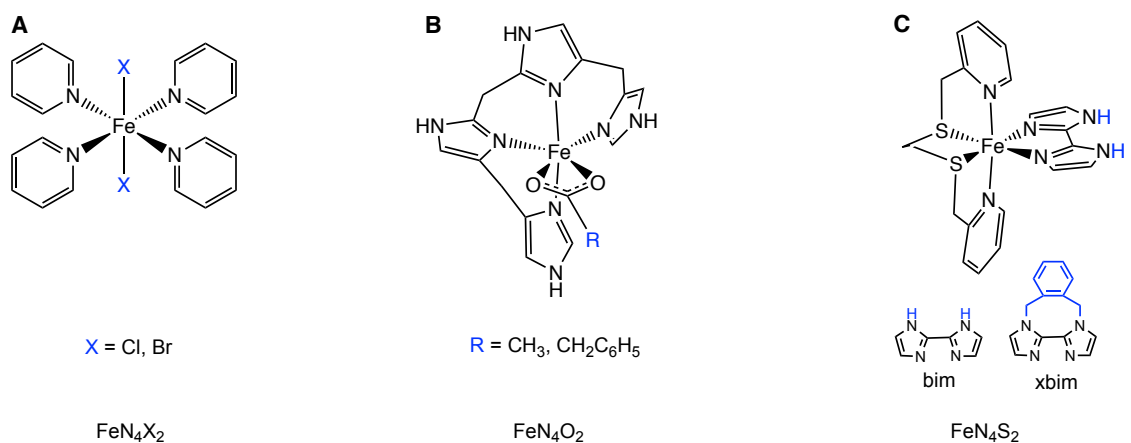
Complex	R	X	δ [mm/s]	ΔE_Q [mm/s]	Γ^b [mm/s]
1	Me	H	1.186(4)	1.426(4)	0.28(1)
2	Me	NH ₂	1.174(6)	1.296(8)	0.29(2)
3	Me	SMe	1.184(8)	1.947(7)	0.49(3)
4	Ph	H	1.187(8)	1.796(7)	0.44(4)
5	Ph	NH ₂	1.187(7)	2.091(1)	0.36(2)
6	Ph	SMe	1.210(4)	2.415(5)	0.28(2)

a) The values in parentheses are the estimated uncertainty of the last significant digit.

b) These simulations were obtained considering an asymmetric doublet. The value listed here is obtained by taking the average between the widths of the two lines.

The degree of variation between the different {PtFe} derivatives **1** - **6** is sizeable considering the differences are on the thiocarboxylate backbone and the *para* position of the axial pyridine ligands, 4.5 – 6 Å from the Fe center, and not directly coordinated to Fe. For comparison, the δ and ΔE_Q values for a selection of other Fe(II) high spin octahedral complexes in N, O and S donor environments shown in Scheme 2.4 are reported in Table 2.5.⁸⁵⁻⁸⁷ The isomer shifts range from 1 – 1.25 mm/s, consistent with high spin Fe(II) sites

and the δ for **1-6**. The ΔE_Q parameters are generally higher than those of **1 - 6** at about ~ 3 mm/s. The ΔE_Q differs by 0.56 mm/s for the FeN_4X_2 tetrakis(pyridine)Fe(II) *trans*-complexes $[\text{Fe}(\text{py})_4\text{Cl}_2]$ and *trans*- $[\text{Fe}(\text{py})_4\text{Br}_2]$ (Scheme 2.4A). Smaller differences in ΔE_Q of ~ 0.2 mm/s are observed for the FeN_4O_2 complexes, $[\text{Fe}(\text{TIM})(\text{C}_6\text{H}_5\text{CH}_2\text{CO}_2)](\text{ClO}_4)$ and $[\text{Fe}(\text{TIM})(\text{CH}_3\text{CO}_2)](\text{ClO}_4)$, which consist of an Fe(II) center coordinated by a tetraimidazole ligand (TIM = bis[(imidazol-4-methyl)-4'-imidazol-2'-yl]methane) and a carboxylate with varying degrees of bulk (Scheme 2.4B).⁸⁶ FeN_4S_2 complexes $[\text{Fe}(\text{bpte})(\text{bim})](\text{ClO}_4)_2$ and $[\text{Fe}(\text{bpte})(\text{xbim})](\text{ClO}_4)_2$ (bpte = *S,S'*-bis(2-pyridylmethyl)-1,2-thioethane) with a bidentate imidazole ligand (bim = 2,2'-biimidazole) or the alkylated derivative (xbim = 1,1'-(α,α' -o-xylyl)-2,2'-biimidazole) (Scheme 2.4C) have similar ΔE_Q differences of ~ 0.3 mm/s.⁸⁷ The variation in ΔE_Q observed across the $[\text{PtFe}(\text{SOCR})_4(\text{pyX})]$ series in **1 - 6** is over 1 mm/s whereas that observed among the species in Table 2.5, is only ~ 0.5 mm/s, regardless of the position of the ligand substitution relative to the Fe center (e.g. directly coordinated to the Fe or on the backbone of a ligand).



Scheme 2.4. Fe(II) high spin octahedral complexes in N, O and S donor environments.

Table 2.5. Selected Mössbauer parameters for high spin Fe(II) octahedral complexes shown in Scheme 2.4.

Complex	Coordination Environment	T [K]	δ [mm/s]	ΔE_Q [mm/s]	Reference
<i>trans</i> -[Fe(py) ₄ Cl ₂]	FeN ₄ Cl ₂	4.2	1.10	3.42	85
<i>trans</i> -[Fe(py) ₄ Br ₂]	FeN ₄ Br ₂	4.2	1.09	2.86	85
[Fe(TIM)(C ₆ H ₅ CH ₂ CO ₂)](ClO ₄)	FeN ₄ O ₂	4	1.128(1)	3.059(1)	86
[Fe(TIM)(CH ₃ CO ₂)](ClO ₄)	FeN ₄ O ₂	4	1.134(2)	3.291(3)	86
[Fe(bpte)(bim)](ClO ₄) ₂	FeN ₂ S ₂	298	1.00(1)	3.30(1)	87
[Fe(bpte)(xbim)](ClO ₄) ₂	FeN ₂ S ₂	298	1.25(1)	3.00(2)	87

The spectra for **1**, **2** and **6** exhibit relatively narrow resonances with linewidths $\Gamma \sim 0.28$ mm/s (Table 2.4). These values are typical of well-defined chemical species and indicates that the Fe sites of these compounds are structurally homogeneous. In contrast, the linewidths of **3** and **4** are significantly larger, a feature which is suggestive of an increased degree of structural heterogeneity. Indeed, the spectrum of **3** is better reproduced with two distinct quadrupole doublets with typical linewidths and a 1:1 relative ratio. These doublets can be organized either in a nested or in an intercalated arrangement (Figure 2.7 and Table 2.6). It is not typically possible to distinguish between these two possibilities, although in this case, the nested arrangement yields δ values which are similar to each other

and comparable to those obtained for the other complexes in this series (see Table 2.4). The similarity of the δ values suggests that the nested assignment is more likely to be correct with ΔE_Q of 1.71 mm/s and 2.17 mm/s for the two spectral components plotted in blue and red respectively in Figure 2.7. Interestingly, the crystal structure of **3** reveals that there are structurally distinct Fe sites with two independent Pt-Fe dimers per unit cell, providing a clear justification for the increased linewidth observed for this species (Tables 2.1 and 2.2).

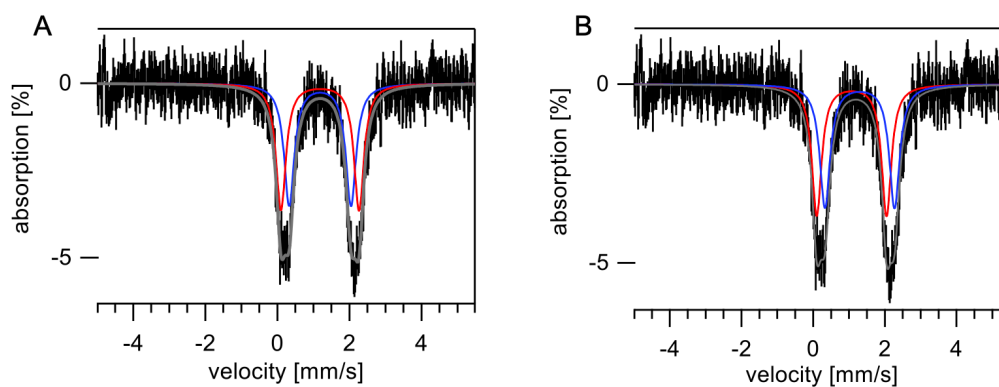


Figure 2.7. Zero-field Mössbauer spectrum recorded at 4.35 K for **3**. A) The solid gray lines are simulations obtained from the sum of two nested (A) or two intercalated (B) components, shown in blue and red, obtained using the parameters listed in Table 2.6.

Table 2.6. Zero-field Mössbauer parameters used to simulate the 4.35 K spectrum of **3** considering either a nested or an intercalated arrangement.

Simulation		δ [mm/s]	ΔE_Q [mm/s]	Γ [mm/s]	Area [%]
Nested	blue	1.18	1.71	0.34	50
Nested	red	1.18	2.17	0.33	50
Intercalated	blue	1.07	1.95	0.33	50
Intercalated	red	1.30	1.94	0.35	50

Analysis of the spectra recorded for **4** in Figure 2.8A, which also has an unusually large linewidth of 0.44 mm/s as reported in Table 2.4, reveals that while using two doublets leads to a better representation of the experimental spectrum, the individual spectral components have unequal spectral areas. As reported in Table 2.7, the two spectral components have ΔE_Q of 1.74 mm/s and 2.22 mm/s with spectral areas of 85 % and 15 % respectively. Investigation of a repeat sample shown in Figure 2.8A (middle) has different relative ratios of the two components, now 45 % and 55 %. The individual spectral components can be “isolated” and made more visible by taking the difference between the spectra of the two samples. This difference spectrum is shown at the bottom of Figure 2.8C and reveals that, just like for **3**, we observe two doublets with similar isomer shifts but different quadrupole splitting values, see Table 2.7.

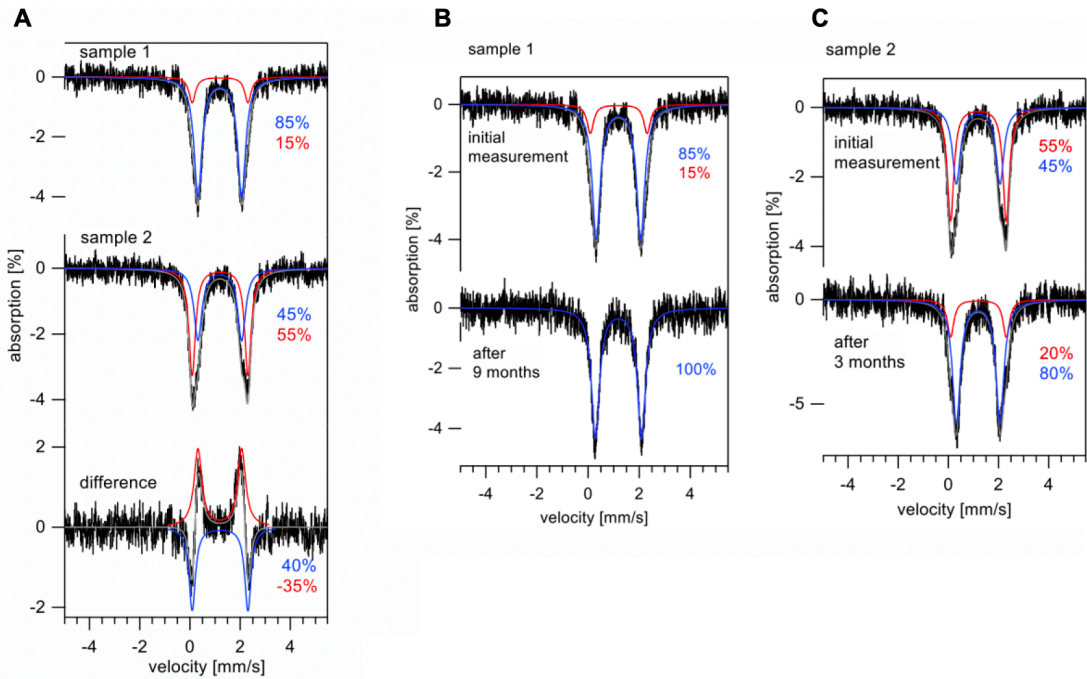


Figure 2.8. Zero field Mössbauer spectra recorded at 4.35 K for two different samples of **4**. A) Spectra of **4** at $t = 0$ (initial) of sample 1 (top), sample 2 (middle) and the difference spectrum (bottom). Time –dependent Mössbauer spectra recorded for two different samples of **4**. B) sample 1 after 9 months (bottom) compared to the initial measurement (top). C) sample 2 after 3 months (bottom) compared to the initial measurement (top). The solid gray lines are simulations derived from the sum of two components obtained using the parameters listed in Table 2.7.

Table 2.7. Zero-field Mössbauer parameters used to generate the two-component theoretical spectra of **3**, **4** and **5**. The spectral components are labeled blue and red corresponding to how they are shown in Figures 2.7 - 2.10.

Complex	Component	t= 0 (initial)				Component	t = 12 months (3), 9 months (4-sample 1, 5), 3 months (4-sample 2)			
		δ [mm/s]	ΔE_Q [mm/s]	Γ [mm/s]	Area [%]		δ [mm/s]	ΔE_Q [mm/s]	Γ [mm/s]	Area [%]
3	blue	1.18	1.71	0.34	50	blue	1.19	1.75	0.3	100
	red	1.18	2.17	0.33	50					
4 (sample 1)	blue	1.19	1.74	0.32	85	blue	1.20	1.80	0.38	100
	red	1.20	2.22	0.32	15					
4 (sample 2)	blue	1.19	1.74	0.38	45	blue	1.19	1.74	0.38	80
	red	1.20	2.22	0.31	55	red	1.20	2.22	0.31	20
5		1.18	2.091	0.36	100	blue	1.17	1.23	0.35	54
						red	1.18	2.33	0.36	46

We observe that the relative ratio of the spectral components of **4** changes over time. The linewidths of the spectra recorded for sample 1 decrease over time as the minor spectral component in red (15 %) disappears. After 9 months, there is only one component consistent with the smaller quadrupole doublet plotted in blue from the initial spectrum (Figure 2.8B). Inspection of the time-dependent spectra recorded for sample 2 in Figure 2.8C, shows that after three months the fraction of the red spectral component, with the larger quadrupole doublet, decreases from 55 % to 20 %, while the blue spectral component increases from 45 % to 80 % (Table 2.7). We note that the calculated spectrum of sample 1 recorded after 9 months was obtained using $\Delta E_Q = 1.80$ mm/s. All other fittings shown in blue in Figure 2.8 were obtained using $\Delta E_Q = 1.74$ mm/s. This difference is most likely due to a change in the calibration constant of the spectrometer.

While the nature of this transformation is yet to be established, we note that the isomer shift is conserved. Since the ΔE_Q sensitive to both changes in the coordination number, and to the nature of the ligands, it is most likely that we observe a change in the geometry of the Fe sites. Unlike for **3**, the SCXRD data for **4** do not substantiate the presence of distinct multiple Fe sites per unit cell. Remarkably, our re-investigation of the sample for which the spectrum of Figure 2.6 was recorded shows that **3** undergoes a similar time-dependent transformation. Inspection of Figure 2.9 shows that after twelve months, the apparent broadness of the original quadrupole doublet decreases from $\Gamma = 0.49$ mm/s to 0.30 mm/s (Table 2.7). As shown in Figure 2.9, the initial spectrum of **3** which has two spectral components (red and blue), contains just one component (blue) after 12 months. The fitted spectrum of **3** recorded after 12 months was obtained using $\delta = 1.19$ mm/s, ΔE_Q

= 1.75 mm/s, and $\Gamma = 0.30$ mm/s. These values are, within uncertainties, virtually identical to those used to derive the spectrum shown in blue of the initial spectrum (Table 2.7). Analogous to 4, there is no change in δ .

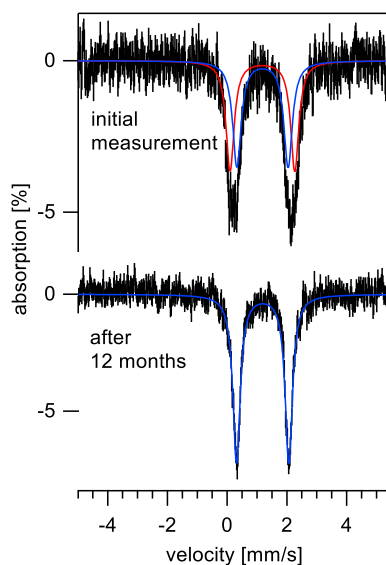


Figure 2.9. Time-dependent zero-field Mössbauer spectra recorded for **3** at $t = 0$, initial (top) and after 12 months (bottom). Parameters for the blue and red spectral components are reported in Table 2.7.

Changes in the spectral components over time was also observed for **5** shown in Figure 2.10. Over nine months the initial doublet of **5** ($\delta = 1.18$ mm/s, $\Delta E_Q = 2.091$ mm/s, and $\Gamma = 0.36$ mm/s) breaks apart into two distinct spectral components. The two doublets have similar δ and Γ but distinct ΔE_Q parameters of 1.23 mm/s and 2.33 mm/s, similar to

patterns observed in initial measurements of **3** and **4**. The similarity of these spectral parameters suggests that the mechanism for the speciation of the Fe sites is likely common to all three samples. Finally, the spectra recorded for **1**, **2**, and **6** seem to be time independent. For these samples, the small changes in parameter values determined for spectra recorded several months apart may be traced to either differences in the signal to noise levels of the corresponding data sets or to instrumental errors (Table 2.8).

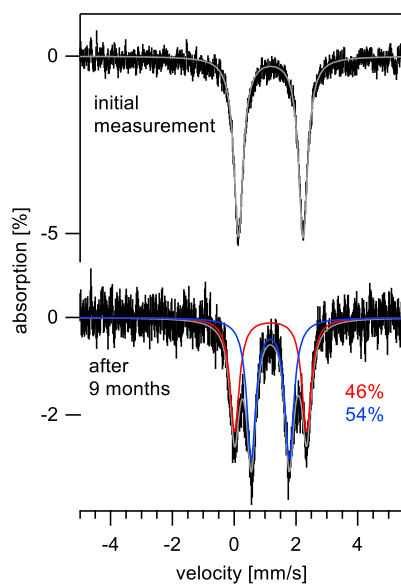


Figure 2.10. Time-dependent, zero-field Mössbauer spectra recorded at 4.35 K for **5** with parameters reported in Table 2.7.

Table 2.8. Zero-field Mössbauer parameters used to simulate the 4.35 K spectra of **1**, **2** and **6**.

Complex	t = 0 (initial)			t = 9 months (1), 11 months (2), 11 months (6)		
	δ [mm/s]	ΔE_Q [mm/s]	Γ [mm/s]	δ [mm/s]	ΔE_Q [mm/s]	Γ [mm/s]
1	1.18	1.42	0.27	1.20	1.45	0.28
2	1.17	1.30	0.29	1.20	1.41	0.29
6	1.21	2.42	0.29	1.22	2.42	0.32

To summarize, the isomer shift values observed for **1** - **6** are essentially identical to one another and demonstrate the presence of high-spin, $S = 2$ Fe(II) sites. In contrast, the magnitude of the quadrupole splitting, $|\Delta E_Q|$, exhibits a dramatic variation as function of the ligand substituents (R and X, Scheme 2.2). Furthermore, the zero-field spectra recorded for **3**, **4**, and **5** reveal the presence of two spectral components characterized by distinct ΔE_Q values with a surprising time dependent relative ratio. For **3** two initial components transform into one component, for **4** we observe the conversion of one species into another and for **5** one component differentiates into two species. We have shown that these changes are not due to the chemical decomposition of these compounds due to the consistent isomer shifts. Instead, they are likely caused by minute structural variations which in the case of **3**, **4**, and **5** occur over time. Unlike for the vast majority of Fe(II) complexes, in this case

the spectroscopic ΔE_Q parameter is strongly coupled to the structure of the Fe sites. Attempts to find a correlation between experimental or DFT-predicted metric parameters and the experimental quadrupole splitting values are on-going.

2.3. Conclusions

In this work, a series of $[\text{PtFe}(\text{SOCR})_4(\text{pyX})]$ lantern complexes were synthesized varying the lantern backbone (R) and the *para* substituent on the axial position (X). Complexes **2** and **3** were previously reported, with **3** displaying antiferromagnetic coupling across relatively long Pt...Pt contacts.⁷⁵ Complexes **1**, **4**, **5** and **6** were synthesized to complete the series with all combinations of R (Me, Ph) and X (H, NH₂, SMe) in order to compare backbone and terminal ligand effects. Structurally, these complexes are consistent with other lanterns in the $[\text{PtM}(\text{SOCR})\text{L}]$ family. UV-vis measurements are consistent across the series and solution magnetic measurements support isolated Fe(II) high spin complexes. Mössbauer measurements reveal a strong effect on the quadrupole splitting with changes in ligand substitutions (R and X). Varying the R and X substituents leads to changes in ΔE_Q over 1 mm/s across the series. This variation is significant considering the coordination environment of the Fe remains constant. Investigation of the species with larger linewidths (**3** and **4**) reveals multiple spectral components with similar δ and distinct ΔE_Q . Furthermore, we observe changes in the relative ratios of the spectral components in **3**, **4** and **5** with time, with **5** splitting into two distinct components. While the specific nature of this transformation is not clear, we do not attribute the changes to decomposition or

oxidation due to the consistent isomer shift ($\delta \sim 1.2$ mm/s) across the series and over time. The ΔE_Q is sensitive to changes in the coordination number and nature of the ligands, therefore this behavior it is most likely caused by small structural changes at the Fe site.

2.4. Experimental

2.4.1. Materials and Methods

Complexes [PtFe(SAc)₄(OH₂)] and [PtFe(tba)₄(OH₂)] were prepared via previously reported methods.^{75, 77} Other reagents were obtained commercially and used without further purification. Elemental analysis was performed by Atlantic Microlab Inc. (Norcross, GA). UV-vis-NIR spectra were collected on a Shimadzu UV-3600 spectrometer. Evans' method solution magnetic susceptibility measurements were performed using ¹H-NMR measurements recorded on a Varian 500 MHz spectrometer.⁸⁴

2.4.2. X-ray Crystallography Methods

X-ray crystallography, including data collection, solution and refinement, were performed by Professor Arnold Rheingold (University of California San Diego). Crystals of **1**, **4** and **5** were mounted on a cryoloop with Paratone N oil and data were collected at 100 K on a Bruker Proteum-R with a CCD using Mo K α radiation. Data were corrected for absorption with SADABS and structures were solved by direct method. All non-hydrogen

atoms were refined anisotropically by full matrix least-squares on F^2 . Data collection and refinement parameters are reported in Table 2.9.

2.4.3. ^{57}Fe Mössbauer Spectroscopy Methods

Mössbauer data were collected and analyzed by Prof. Sebastian Stoian and Adam Valaydon-Pillay at the University of Idaho. Nuclear Gamma Resonance (Mössbauer) spectra were recorded using a spectrometer operated in constant acceleration mode. This instrument was equipped with a Janis 8DT cryostat cooled with liquid helium and fitted with an 8 T American Magnetics superconducting coil. The cryostat was connected to a Cryomech liquid helium recovery system which pressurized the helium bath to ~ 1.8 psi increasing its temperature to 4.35 K. The applied magnetic field was oriented parallel to the direction of propagation of the 14.4 keV γ -ray used to detect the Mössbauer effect. Spectra were recorded at 4.35 K by submerging the sample in liquid helium. The sample temperature was measured using a calibrated Cernox sensor. The absorbers were contained in custom polyethylene containers and were prepared by dispersing 25 - 50 mg ground polycrystalline powders in eicosane which functioned as an inert support matrix. Between measurements absorbers were stored in regular vials open to the atmosphere. The theoretical spectra were obtained using both the WMOSS software (See Co., formerly known as Web Research Co., Edina MN) and C-based, Igor Pro codes developed in-house. Isomer shift values are reported against the center of a spectrum recorded at room temperature for a foil of α -Fe metal.

2.4.4. Synthetic Procedures

Synthesis of [PtFe(SAc)₄(py)] (1). Freshly prepared [PtFe(SAc)₄(OH₂)] (109 mg, 0.192 mmol) was dissolved in ~ 5 mL of acetone. While stirring, excess pyridine (py, ~ 0.1 mL) was added. After stirring for ~ 2 hours the orange precipitate was collected via vacuum filtration. Orange crystals (37 mg, 31 % yield) were obtained from CH₂Cl₂ solutions layered with hexanes. Anal. Calc'd. for PtFeC₁₃H₁₇NO₄S₄: C, 24.77; H, 2.72; N, 2.22%. Found: C, 24.77; H, 2.57; N, 2.19%. UV-vis-NIR (CH₂Cl₂) (λ_{max} , nm (ϵ_{M} , cm⁻¹ M⁻¹)): 272(58,409), 361(1,404), 960(6). Evans method (CD₂Cl₂): 5.52 μ_{B} .

Synthesis of [PtFe(tba)₄(py)] (4). Freshly prepared [PtFe(tba)₄(OH₂)] (157 mg, 0.192 mmol) was dissolved in ~ 15 mL of acetone. While stirring, excess py (~ 0.1 mL) was added. After stirring for ~ 2 hours the clear red solution was dried and washed with water and hexanes 3x each. Dark red crystals (74 mg, 44 % yield) were obtained from CH₂Cl₂ solutions layered with hexanes. Anal. Calc'd. for PtFeC₃₃H₂₅NO₄S₄: C, 45.11; H, 2.87; N, 1.59%. Found: C, 44.42; H, 2.85; N, 1.61%. UV-vis-NIR (CH₂Cl₂) (λ_{max} , nm (ϵ_{M} , cm⁻¹ M⁻¹)): 255(68,627), 277(63,273), 480(336), 953(7). Evans method (CD₂Cl₂): 5.71 μ_{B} .

Synthesis of [PtFe(tba)₄(pyNH₂)] (5). Freshly prepared [PtFe(tba)₄(OH₂)] (157 mg, 0.192 mmol) was dissolved in ~ 15 mL of acetone. While stirring, a slight excess of 4-aminopyridine (pyNH₂, 25 mg, 0.27 mmol) was added dropwise in ~ 5 mL of acetone. After stirring for ~ 2 hours the clear red solution was dried and washed with water and hexanes 3x each. Dark red crystals (82 mg, 48 % yield) were obtained from CH₂Cl₂ solutions layered with hexanes. Calc'd. for PtFeC₃₃H₂₆N₂O₄S₄: C, 44.35; H, 2.93; N, 3.13%. Found: C, 42.41; H, 2.79; N, 2.90%. Found: C, 42.48; H, 2.84; N, 3.02%. UV-vis-NIR (CH₂Cl₂)

(λ_{max} , nm (ϵ_{M} , $\text{cm}^{-1} \text{M}^{-1}$): 251(23,684), 310(22,149), 490(511), 980(12). Evans method (CD_2Cl_2): 5.17 μ_{B} .

Complexes $[\text{PtFe}(\text{SAc})_4(\text{pyNH}_2)]$ (**2**) and $[\text{PtFe}(\text{SAc})_4(\text{pySMe})]$ (**3**) were prepared from established protocols.⁷⁵ Complex $[\text{PtFe}(\text{tba})_4(\text{pySMe})]$ (**6**) was prepared from previously reported methods and synthetic details are also provided in Chapter 4.⁸³ Initial sample of **1** was prepared for crystallography by Ariel Hyre.

Table 2.9. Crystal data collection and refinement parameters for **1**, **4** and **5**.

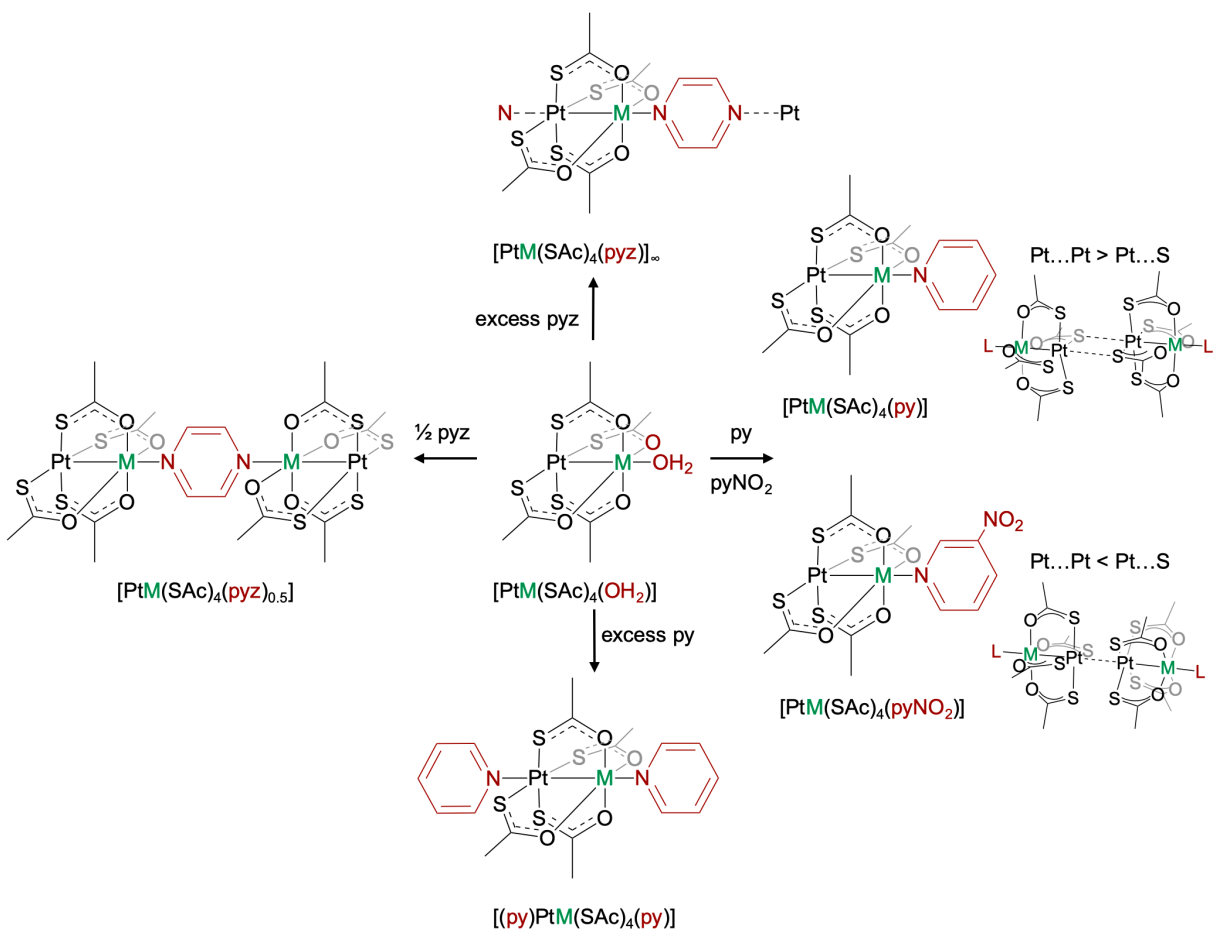
Compound	1	4	5
Formula	C ₁₃ H ₁₇ FeNO ₄ PtS ₄	C ₃₃ H ₂₅ FeNO ₄ PtS ₄	C ₃₃ H ₂₆ FeN ₂ O ₄ PtS ₄
Formula weight	630.46	878.72	893.74
Crystal system	Triclinic	Monoclinic	Triclinic
Color	Orange	Red	Red
Space group	<i>P</i> -1	<i>P</i> -2 ₁ / <i>n</i>	<i>P</i> -1
<i>a</i> , Å	8.4910(19)	11.1644(4)	11.3435(9)
<i>b</i> , Å	10.669(2)	21.2256(8)	11.9454(10)
<i>c</i> , Å	11.710(3)	14.7762(5)	12.5212(10)
<i>α</i> , deg	74.585(7)	90	74.064(2)
<i>β</i> , deg	76.402(7)	92.503(2)	85.560(2)
<i>γ</i> , deg	71.617(5)	90	84.018(2)
<i>V</i> , Å ³	957.105	3498.2(2)	1620.5(2)
<i>Z</i> , <i>Z'</i>	2	4	2
<i>ρ</i> (calcd), mg/cm ³	2.188	1.668	1.832
Absorption coefficient mm ⁻¹	604	4.684	5.058
<i>temp</i> , K	100	100	100.0
Final R indices [<i>I</i> > 2σ(<i>I</i>)]	R1 = 0.0192, wR2 = 0.0421	R1 = 0.0395, wR2 = 0.0881	R1 = 0.0313, wR2 = 0.0674
R indices (all data)	R1 = 0.0216, wR2 = 0.0431	R1 = 0.0565, wR2 = 0.0989	R1 = 0.0392, wR2 = 0.0715

CHAPTER THREE: Synthesis and Characterization of a {PtCo} Quasi-1D Chain

3.1. Introduction

Quasi-1D materials are promising candidates for nanoscale electronic and magnetic applications, from conductive wires to magnetic storage devices.^{15, 53, 54, 56, 69, 88} A bottom-up strategy to design such materials is to synthetically assemble predesigned anisotropic building blocks. We employ this approach by bridging individual heterobimetallic complexes of the form $[\text{PtM}(\text{SOCR})_4]$ with bidentate ligands (L) having two Lewis basic donor atoms on opposite ends of the molecule forming essentially infinite arrays, $\{[\text{PtM}(\text{SOCR})_4](\text{L})\}_\infty$.^{62, 64, 79, 82} Important factors and requirements for magnetic communication in quasi-1D structures include (1) the structural connectivity between molecular building blocks, (2) a viable orbital pathway for communication and (3) a sufficiently short distance between the molecular building blocks. Therefore, the choice of the organic bridge (L) between the $[\text{PtM}(\text{SOCR})_4]$ units is critical.

The Doerrer group has previously synthesized a large family of heterobimetallic lantern complexes, demonstrating structure-property relationships and control over the individual building blocks.^{73, 74} The use of an asymmetric thiocarboxylate backbone ligand (SOCR) allows for the selective coordination of the Pt and 3d metal (M) to the S and O respectively due to hard-soft acid-base principles. Changing the R group (R = Me, Ph) on the backbone ligand varies the level of bulk separating the individual chains, potentially important for minimizing inter-chain coupling. Incorporation of different 3d metals allows for control of the overall spin of the complex (e.g. M = Co(II) $S = 3/2$). Various intra- and intermolecular assemblies have been identified, examples of which are shown in Scheme 3.1.^{72, 78, 79, 82}



Scheme 3.1. Intra- and inter-molecular assemblies of $[PtM(SAc)_4(L)]$ units ($M = Co, Ni, Zn$).

As shown in Scheme 3.1, addition of a terminal axial ligand (L) such as pyridine (py) or 3-nitropyridine (pyNO₃) to the aquo adduct, [PtM(SAc)₄(OH₂)] (SAc = thioacetate), leads to the formation of [PtM(SAc)₄(py)]⁷² and [PtM(SAc)₄(pyNO₂)]⁷⁸ respectively, where the pyridine N (N_{py}) coordinates to the 3d metal. In the solid state, the individual lantern units form dimeric species via Pt...Pt or Pt...S interactions. For example, [PtM(SAc)₄(py)] (M = Co, Ni, Zn) have shorter Pt...S intermolecular interactions⁷² while [PtM(SAc)₄(pyNO₂)] (M = Ni) have shorter Pt...Pt interactions.⁷⁸ Other categories based on the intramolecular dimeric structures have been identified as previously described in Chapter 1 (Scheme 1.3). The assembly of distinct dimeric species with Pt...Pt, Pt...S, or S...S intermolecular interactions allows for comparison between different pathways for possible magnetic communication. For example, the Doerrer group has previously demonstrated that complexes with Pt...Pt interactions (~ 3 Å) exhibit antiferromagnetic coupling, suggesting that the Pt *d_z²* orbitals can serve as a pathway for magnetic communication between the paramagnetic 3d metal centers.^{77, 78}

The addition of a large excess py forms the species [(py)PtM(SAc)₄(py)] (M = Co, Ni, Zn) in which py coordinates to both the 3d metal and the Pt(II) center (Scheme 3.1).⁷² These complexes are unusual due to the pseudo octahedral coordination environment of the Pt(II) center. While six-coordinate Pt(IV) species are common, six-coordinate Pt(II) species are quite rare.⁸¹ The Pt-N_{py} distances are ~ 0.5 Å longer than typical Pt-N_{py} bond lengths in Pt(II) square planar complexes.⁸⁹⁹⁰ The coordination of the N_{py} to the Pt center prevents the formation of solid state dimers through Pt...Pt or Pt...S interactions, providing an important comparison for exploring potential pathways for magnetic communication. Based on the presence of Pt-N_{py} binding in these complexes, it was hypothesized that the Pt-N_{py} interaction could be used form extended arrays of lantern complexes. Pyrazine (pyz), a bidentate ligand structurally similar to pyridine was used as a bridging ligand to

form linkages between individual lantern complexes.^{79, 82} Combining half an equivalent of pyz with the in situ generated aquo adduct [PtM(SAc)₄(OH₂)] forms the dimer [PtM(SAc)₄(pyz)_{0.5}] (R = Me, M = Co, Ni, Zn) where one pyz coordinates to the 3*d* metals of two different lantern complexes, forming a bridge between them (Scheme 3.1).⁷⁹ These complexes exhibit antiferromagnetic coupling due to magnetic communication between the 3*d* metal centers across the pyz bridge.⁷⁹

An excess of pyz induces the formation of essentially infinite chains where one N_{pyz} coordinates to the 3*d* metal and the other links to the *d*⁸ Pt(II) center of an adjacent complex forming [PtM(SAc)₄(pyz)]_∞ (M = Co, Ni, Zn)⁷⁹ or {[PtM(SAc)₄(pyz)](pyz)}_∞ (M = Co, Ni, Zn)⁸² (Scheme 3.1). The Pt-N_{pyz} bond lengths of these species are comparable to that of the of the Pt-N_{py} distances. These materials were not reproducible for elemental analysis or magnetic measurements due to excess and volatile pyz in the crystal lattice, which is necessary for crystal formation, but not chain assembly (Figure 3.1).⁸² Therefore, in this work, the use of bulkier bridging ligands and less volatile solvents were explored. Attempts were made with 2,5-dimethylpyrazine (2,5-Me₂pyz), phenazine (phz), and 4,4'-bipyridine (4,4'-bipy), all of which have two N lone pairs pointing in opposite directions. The structures with [PtNi(SAc)₄(2,5-Me₂pyz)_{0.5}]_∞ (**8**) and [PtNi(SOCR)₄(OH₂)](phz) (**9**) did not have the correct connectivity to investigate the potential coupling patterns that we are interested in, or to be compared with the previous work. Success was achieved with the third bridge, namely 4,4'-bipy, in that [PtCo(SAc)₄(4,4'-bipy)]_∞ grown from PC (4,4'-bipy = 4,4'-bipyridine, PC = propylene carbonate) (**7**) was appropriate for SCXRD studies and was robust for magnetism measurements. We report the magnetic properties of **7** in the context of the individual {PtCo} building blocks with terminal ligands, [PtCo(SAc)₄(py)]⁷² and [(py)PtCo(SAc)₄(py)],⁷² and the dimer [PtCo(SAc)₄(pyz)_{0.5}]⁷⁹

shown in Scheme 3.1, which have distinct magnetic behavior, in order to explore the pathways that allow for magnetic communication in this family of {PtM} heterobimetallic lantern complexes. A structural comparison of **7** and previously reported pyz chains $[\text{PtCo}(\text{SAc})_4(\text{pyz})]_\infty$ ⁷⁹ and $\{[\text{PtCo}(\text{SAc})_4(\text{pyz})](\text{pyz})\}_\infty$ ⁸² is also included.

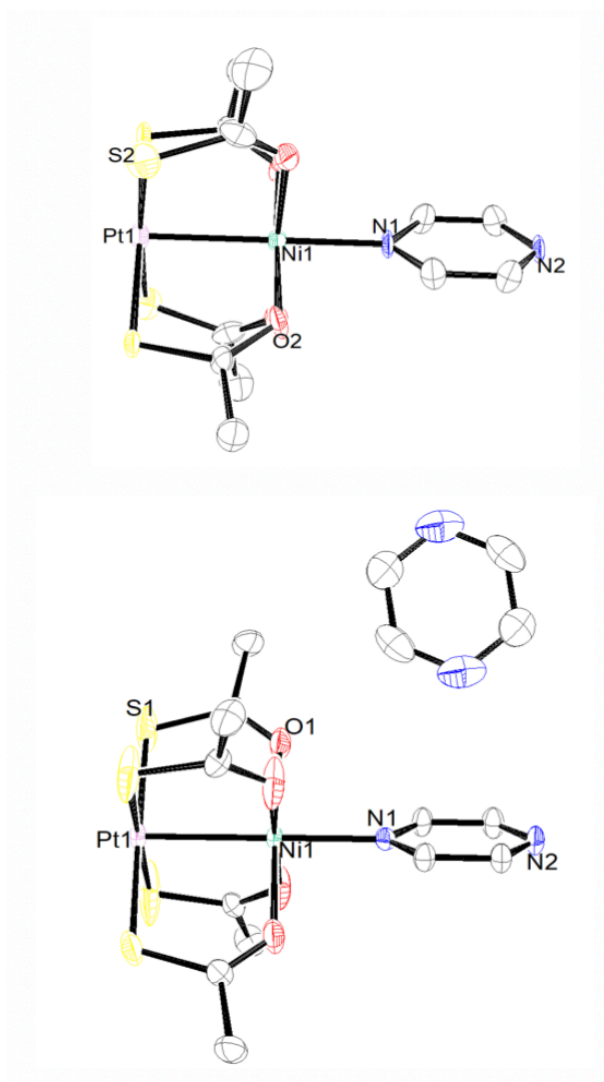


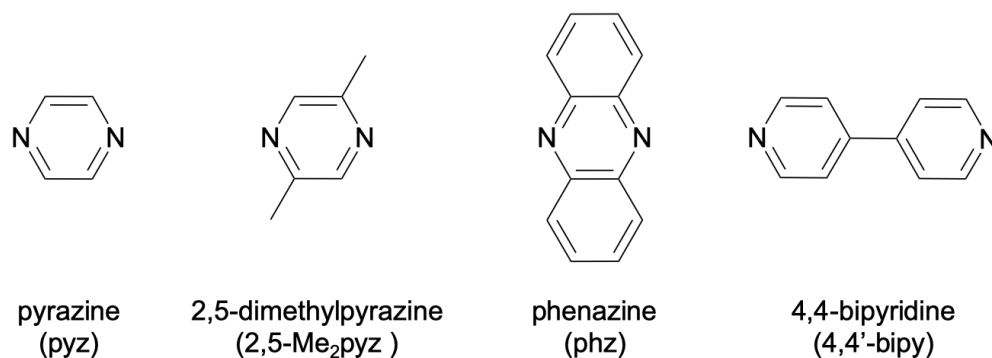
Figure 3.1. ORTEP of [PtNi(SAc)₄(pyz)]_∞ (top)⁷⁹ and {[PtNi(SAc)₄(pyz)](pyz)}_∞ (bottom).⁸²

Ellipsoids are drawn at the 50 % level. Hydrogen atoms are omitted for clarity.

3.2. Results and Discussion

3.2.1. Synthesis and Structural Analysis

The synthesis of quasi-1D chains of the form $[\text{PtM}(\text{SOCR})_4\text{L}]_\infty$ was explored using bulkier axial ligands and less volatile solvents to achieve a reproducible material for magnetic measurements as discussed above. Bulkier bidentate ligands, with similar binding motifs as pyz were tested for chain formation (Scheme 3.2).



Scheme 3.2. Examples of bulkier bidentate ligands compared to pyrazine.

Chain formation with the methyl substituted 2,5-dimethylpyrazine (2,5-Me₂pyz) leads to $[\text{PtNi}(\text{SAC})_4(2,5\text{-Me}_2\text{pyz})_{0.5}]_\infty$ (**8**) without excess 2,5-Me₂pyz in the crystal lattice as revealed by SCXRD (Figure 3.2). This chain is structurally distinct from the pyz chains. The repeating unit of the chain is composed of two $\{\text{PtNi}(\text{SAC})_4\}$ lantern cores and one 2,5-Me₂pyz bridging ligand as shown in Figure 3.2A. One 2,5-Me₂pyz is bound to the 3d metals (M = Ni) of two individual lantern complexes, linked by 3.071(1) Å Pt...Pt contacts, so that dimers formed by metallophilic interactions, $[(\text{SAC})_4\text{NiPt} \dots \text{PtNi}(\text{SAC})_4]$, are made into chains with 2,5-Me₂pyz. Selected bond distances and angles are reported in Table 3.1.

This chain motif has been observed previously with the saturated ligand 1,4-diazabicyclo[2.2.2]octane (DABCO), which forms the chain $[\text{PtM}(\text{SAc})_4(\text{DABCO})_{0.5}]_\infty$. (M = Co, Ni, Zn).⁸² Magnetic studies of $[\text{PtM}(\text{SAc})_4(\text{DABCO})_{0.5}]_\infty$ (M = Co, Ni) revealed that antiferromagnetic coupling between the M centers is best described by magnetic exchange across Pt...Pt interactions with a 8.306(3) Å Ni...Ni intrachain distance, as opposed to across the DABCO ligand (6.843(2) Å Ni...Ni intrachain distance) or between individual chains (9.835(3) Å interchain Ni...Ni distance).⁸² These studies indicate that the communication path is structurally dependent, with the Pt...Pt pathway being more favorable for magnetic communication than across the DABCO ligand in this case. The intermolecular and intramolecular Ni...Ni distances in **8** are similar to the previously reported DABCO chains. The shortest Ni...Ni interchain distance is 9.582(4) Å and the intrachain Ni...Ni distances are 8.278(4) Å through Pt...Pt pathway and 6.986(3) Å through the 2,5-Me₂pyz ligand (Table 3.1). Both DABCO and pyz have two lone pairs on the N separated by three σ bonds, and pyz also has a π system. The intramolecular N...N distances through DABCO in $[\text{PtNi}(\text{SAc})_4(\text{DABCO})_{0.5}]_\infty$ and 2,5-Me₂pyz in **8** are 2.697 Å and 2.79(2) respectively. Although the chains formed with DABCO and 2,5-Me₂pyz are structurally similar, there is a different orbital pathway through the 2,5,Me₂pyz.

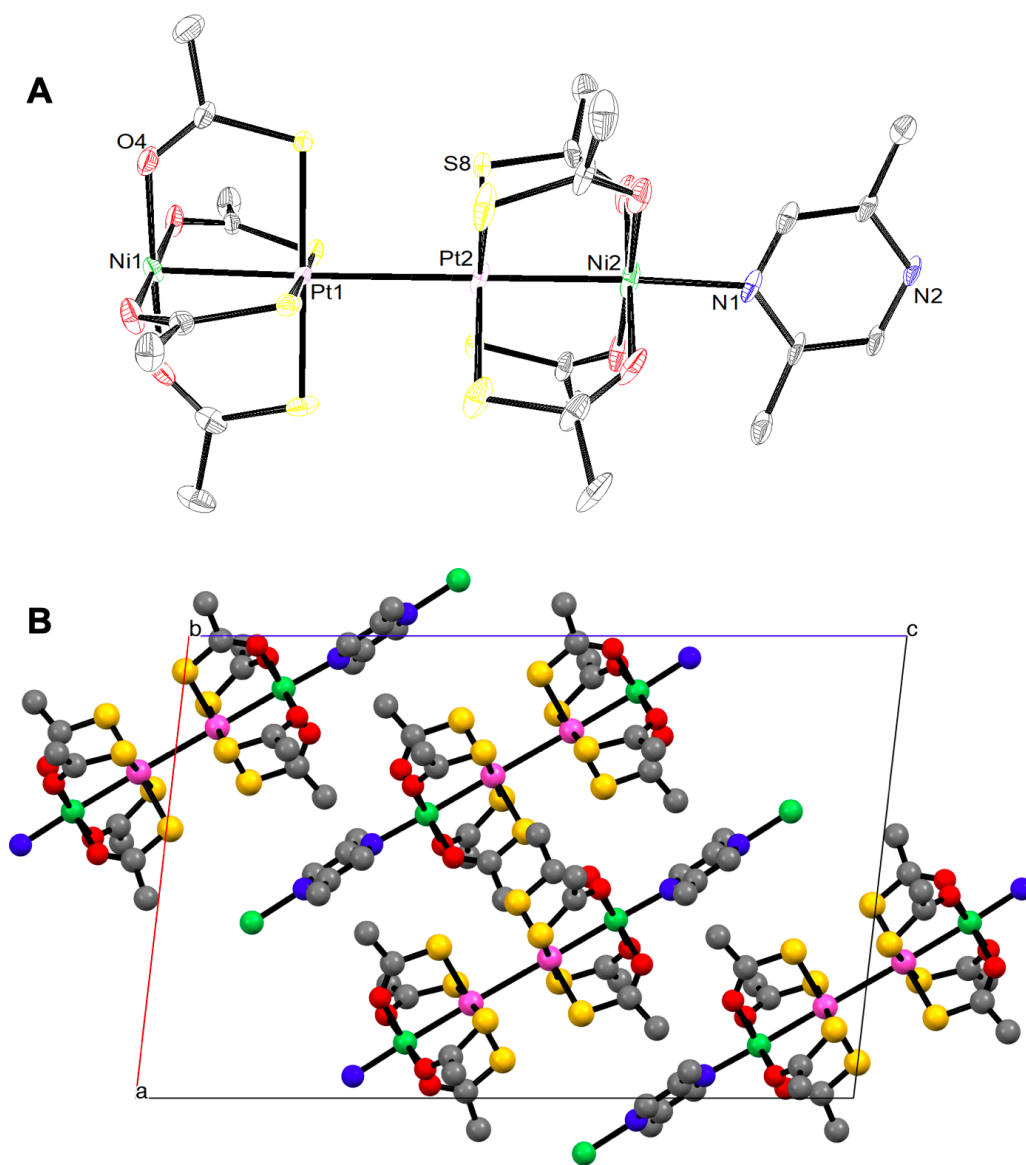


Figure 3.2. A) ORTEP of [PtNi(SAc)₄(2,5-Me₂pyz)_{0.5}]_∞ (**8**). Ellipsoids are drawn at the 50 % level. Hydrogen atoms and solvent molecules (3 CHCl₃) are omitted for clarity. B) Mercury representation showing the packing of the individual chains. Solvent and Hydrogen atoms omitted.

Table 3.1. Selected bond lengths and angles for **8**

Parameter	Distance (Å) / Angle (°)
Pt1-Ni1 (Å)	2.603(2)
Pt2-Ni2 (Å)	2.606(2)
Ni1-N2 (Å)	2.10(1)
Ni2-N1 (Å)	2.12(1)
Pt...Pt (Å)	3.071(1)
Pt...S (Å) ^a	3.853(4)
Pt1-Pt2-N2 (°)	179.42(5)
Pt2-Ni2-N1 (°)	177.3(4)
Pt2-Ni2-N2 (°)	177.6(2)
Intramolecular Ni...Ni (Å) via Pt...Pt pathway	8.278(4)
Intramolecular Ni...Ni (Å) via 2,5-Mepyz pathway	6.986(3)
Intermolecular Ni...Ni (Å)	9.582(4)

^a Shortest Pt...S contact reported

Synthetic attempts to form a chain with phenazine (phz) yielded the complex $[\text{PtNi}(\text{SOCR})_4(\text{OH}_2)](\text{phz})$ (**9**). Instead of displacing the donor solvent (H_2O) and coordinating to the $3d$ metal, each N of the phz ligand forms a hydrogen bond to the H_2O of separate lantern complexes as shown in the crystal structure (Figure 3.3). Selected bond lengths and angles are reported in Table 3.2. As shown in the packing diagram, the individual lantern units form Pt...Pt and Pt...S interactions in the solid state. The 3.4109(7) Å Pt...Pt interactions are slightly shorter than the 3.457(1) Å Pt...S distances with a Pt-Pt-M angle of 160 °. This intermolecular structure is best described by the “partially eclipsed” category previously established for this family of heterobimetallic lantern complexes.^{73, 74}

Chain formation with the bidentate ligand 4,4'-bipy was explored due to the structural similarity to pyz near the N coordination site but overall longer structure, expected to prevent excess 4,4'-bipy ligand from residing in the crystal lattice. This approach was successful, leading to $[\text{PtCo}(\text{SAC})_4(4,4'\text{-bipy})]_\infty$ (**7**), which has a similar chain motif to the $[\text{PtM}(\text{SAC})_4(\text{pyz})]_\infty$ chains (Figure 3.4). The resulting structures using these bulkier bridging ligands 2,5-Me₂pyz, phz and 4,4'-bipy compared to the previously reported pyz are summarized in Scheme 3.3. See the experimental section (3.4) for preparation details of **8** and **9**.

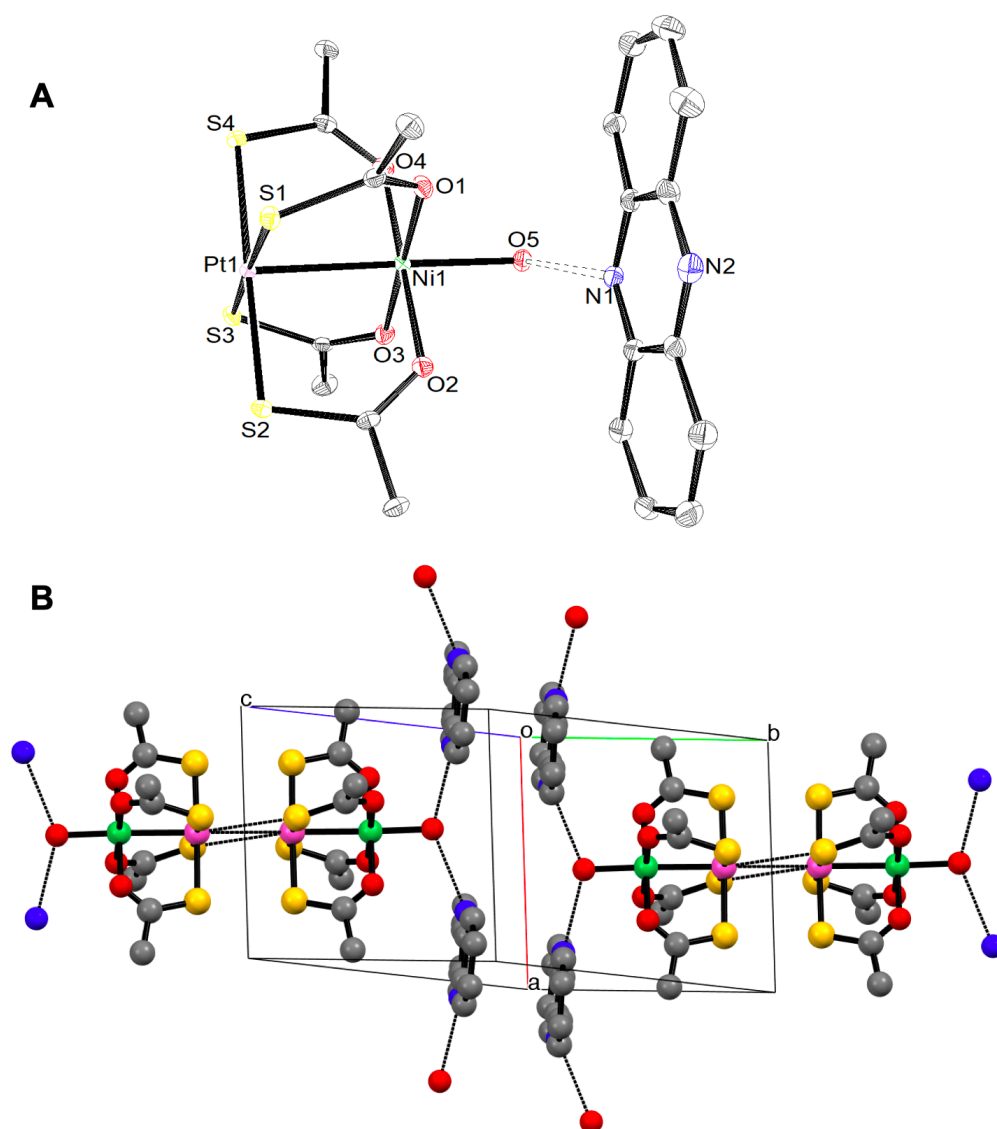
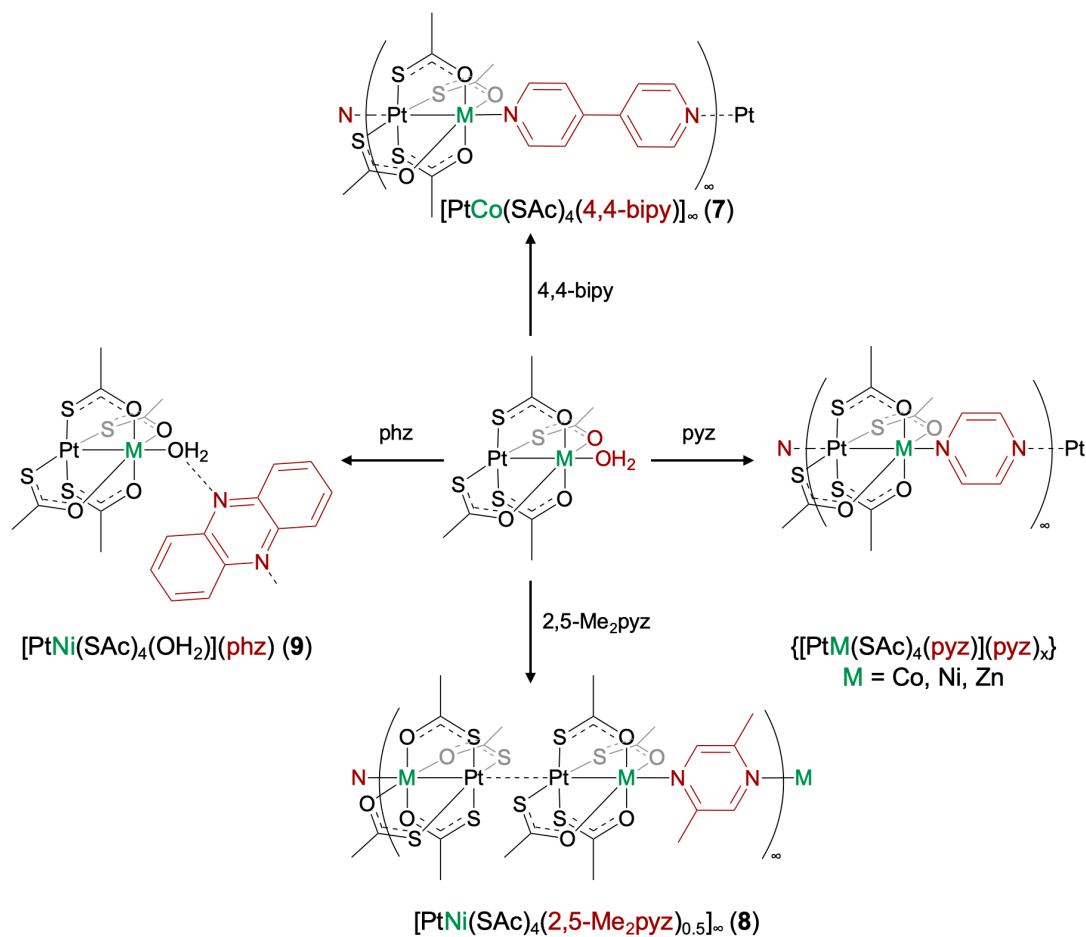


Figure 3.3. A) ORTEP of $[\text{PtNi}(\text{SOCR})_4(\text{OH}_2)](\text{phz})$ (**9**). Ellipsoids are drawn at the 50 % level. Hydrogen atoms are omitted for clarity. B) Mercury representation showing the packing and intermolecular interactions. H atoms omitted.

Table 3.2. Selected bond lengths and angles for **9**

Parameter	Distance (Å) / Angle (°)
Pt1-Ni1 (Å)	2.5806(6)
Ni1-O5 (Å)	2.050(2)
O5-N1 (Å)	2.893(4)
O5-N2 (Å)	2.990(4)
Pt...Pt (Å)	3.4109(7)
Pt...S (Å) ^a	3.457(1)
Pt-Pt-M (°)	160.77(1)

^a Shortest Pt...S contact reported



Scheme 3.3. Summary of motifs from attempts toward $[\text{PtM}(\text{SOCR})_4\text{L}]_\infty$ chains with bulkier axial ligands ($[\text{PtCo}(\text{SAC})_4(4,4'\text{-bipy})]_\infty$ (7), $[\text{PtNi}(\text{SAC})_4(2,5\text{-Me}_2\text{pyz})_{0.5}]_\infty$ (8) and $[\text{PtNi}(\text{SOCR})_4(\text{OH}_2)](\text{phz})$ (9)) compared to the previously reported $[\text{PtM}(\text{SAC})_4(\text{pyz})]_\infty$ ⁷⁹ ($x = 0$) and $\{[\text{PtM}(\text{SAC})_4(\text{pyz})](\text{pyz})\}_\infty$ ⁸² ($x = 1$) chains.

To obtain **7**, the $[\text{PtCo}(\text{SAc})_4(\text{OH}_2)]$ lantern was added to an excess of 4,4'-bipy in acetone and stirred for ~ 2 hours. The resulting pink powder was isolated by filtration and crystalline material was obtained from a dichloromethane (DCM) solution layered with hexanes at 5 °C. SCXRD reveals chain formation structurally consistent with the pyz version, with one N of the 4,4'-bipy coordinated to the Co and the other bound to the Pt of the neighboring complex. Crystals grown from both DCM and acetone solutions have volatile solvent (DCM or acetone) in the crystal lattice. Therefore, the synthesis was changed to use the less volatile solvents PC and toluene. In addition, since the solubility of the chain is limited and minimal, the chain was crystallized directly from the reaction mixture instead of recrystallization of the solid. Pink crystals were obtained from $[\text{PtCo}(\text{SAc})_4(\text{OH}_2)]$ in PC layered underneath 4,4'-bipy in toluene with a 1:1 mixture of PC and toluene layered in between. The resulting complex, $[\text{PtCo}(\text{SAc})_4(4,4'\text{-bipy})]_\infty$, (**7**) has been crystallographically characterized (Figure 3.4). Selected bond distances and angles are reported in Table 3.3 compared to the previously synthesized pyz chains $[\text{PtCo}(\text{SAc})_4(\text{pyz})]_\infty$ ⁷⁹ and $\{[\text{PtCo}(\text{SAc})_4(\text{pyz})](\text{pyz})\}_\infty$ ⁸².

The asymmetric unit of **7** contains two distinct $\{\text{PtCo}\}$ lantern units with 4,4'-bipy bound to the Co centers (Figure 3.4). Two molecules of PC are present in the crystal lattice, consistent with the elemental analysis. The Pt-Co distances are both 2.579(1) Å, which is comparable to the pyz lantern chain structures, with and without extra pyz in the lattice, which both have Pt-Co distances of 2.588 Å (L = pyz). The Co-N distances of 2.096(6) Å and 2.097(6) Å are slightly shorter than the Co-N distances of the pyz lanterns which are 2.155(6) Å and 2.111(5) Å for $[\text{PtCo}(\text{SAc})_4(\text{pyz})]_\infty$ and $\{[\text{PtCo}(\text{SAc})_4(\text{pyz})](\text{pyz})\}_\infty$ respectively, see Table 3.3. The Pt-N distances are ~ 0.5 Å longer than the Co-N distances and are 2.579(6) Å and 2.589(6) Å for **7**. The Pt-N distances in **7** are also slightly shorter than the 2.65(1) Å and 2.676(6) Å Pt-N distances

in the other two chain structures. In **7**, the Pt-Co-N and Co-N-Pt angles are just under 180° at $179.7(2)^\circ$ and $179.2(2)^\circ$. This is consistent for $\{[\text{PtCo}(\text{SAc})_4(\text{pyz})](\text{pyz})\}_\infty$ which similar Pt-Co-N and Co-N-Pt angles,⁸² whereas for $[\text{PtCo}(\text{SAc})_4(\text{pyz})]_\infty$ these angles are $180.000(1)^\circ$ and $180.0(3)^\circ$ (Table 3.3).⁷⁹ For **7**, the intrachain distance between the two Co centers along the Pt-Co axis is $14.329(2) \text{ \AA}$.

Diagrams showing the crystal packing of the individual chains are shown in Figure 3.5, along the *a*-axis (top) and the *c*-axis (bottom). The chains run in alternating directions with one equivalent of PC per $\{\text{PtCo}(\text{SAc})_4(\text{bipy})\}$ unit between the individual chains. It was previously observed that $\{[\text{PtCo}(\text{SAc})_4(\text{pyz})](\text{pyz})\}_\infty$ chains with extra pyrazine in the crystal lattice had longer interchain Co...Co distances of $10.827(1) \text{ \AA}$ compared to chains without lattice pyrazine $[\text{PtCo}(\text{SAc})_4(\text{pyz})]_\infty$ ($7.965(2) \text{ \AA}$), indicating that the chains are more isolated from each other, with the additional pyrazine acting as a spacer.⁸² For **7**, the shortest Co-Co interchain distances are $6.646(2) \text{ \AA}$, suggesting that the individual chains are less isolated than the pyz derivatives even with the PC molecules in the crystal lattice.

Table 3.3. Selected bond distances and angles for $[\text{PtCo}(\text{SAC})_4(4,4'\text{-bipy})]_\infty$ (**7**) compared to previously reported $[\text{PtCo}(\text{SAC})_4(\text{pyz})]_\infty$ ⁷⁹ and $\{[\text{PtCo}(\text{SAC})_4(\text{pyz})](\text{pyz})\}_\infty$ ⁸² chains.

Parameter	Distance (Å) / Angle (°)		Atoms	Distance (Å) / Angle (°)
	$[\text{PtCo}(\text{SAC})_4(\text{pyz})]_\infty$	$\{[\text{PtCo}(\text{SAC})_4(\text{pyz})](\text{pyz})\}_\infty$		7
Pt-Co (Å)	2.588(2)	2.588(1)	Pt1 Co1 Pt2 Co2	2.579(1) 2.579(1)
Co-N (Å)	2.155(6)	2.111(5)	Co1 N1 Co2 N3	2.095(6) 2.097(6)
Pt-N (Å)	2.65(1)	2.676(6)	Pt1 N4 Pt2 N2	2.579(6) 2.589(6)
Pt-S (Å) ^a	2.3333(12)	2.309(2)	Pt1 S1-S4 Pt2 S5-S8	2.329(2) 2.328(2)
Co-O (Å) ^a	2.059(3)	2.312(3)	Co1 O1-O4 Co2 O5-O8	2.107(6) 2.102(7)
Pt-Co-N (°)	180.000(1)	179.8(17)	Pt1 Co1 N1 Pt2 Co2 N3	178.8(2) 179.1(2)
Co-Pt-N (°)	180.0(3)	179.69(16)	Co1 Pt1 N4 Co2 Pt2 N2	179.7(2) 179.2(2)
Intrachain Co...Co (Å)	10.236	10.1348(4)	Co1 Co2	14.329(2)
Interchain Co...Co (Å)	7.965(2)	10.827(1)	Co1 Co1	6.646(2)

^a The average Pt-S and Co-O bond lengths are reported for **7** and one example of a Pt-S and Co-O distance is reported for both

$[\text{PtCo}(\text{SAC})_4(\text{pyz})]_\infty$ and $\{[\text{PtCo}(\text{SAC})_4(\text{pyz})](\text{pyz})\}_\infty$

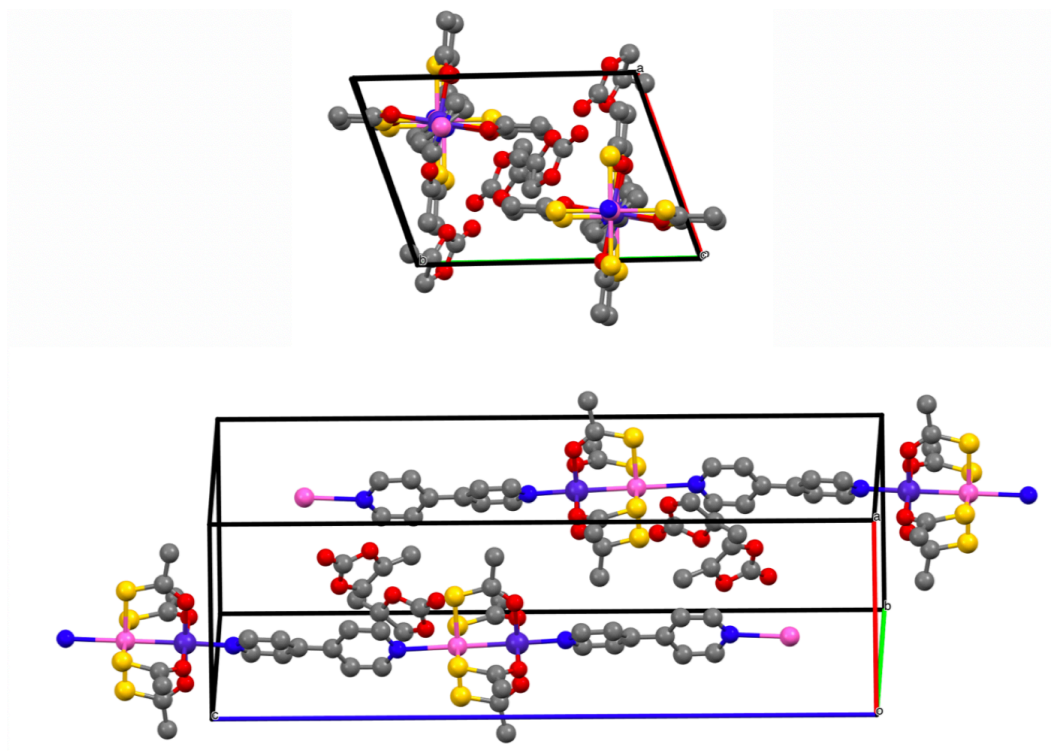


Figure 3.5. Packing diagrams of individual $[\text{PtCo}(\text{SAc})_4(4,4'\text{-bipy})]_{\infty}$ (7) chains with one molecule of PC per $\{\text{PtCo}(\text{SAc})_4(4,4'\text{-bipy})\}$ unit viewed down the *a*-axis (top) and along the *a*-axis (bottom). H atoms omitted.

Next we compare the inter- and intra-molecular Co...Co, Pt...Pt, and Pt...S distances in the chain, **7**, to those of the individual {PtCo} building blocks with terminal ligands, [PtCo(SAc)₄(py)]⁷² and [(py)PtCo(SAc)₄(py)],⁷² and the dimer [PtCo(SAc)₄(pyz)_{0.5}].⁷⁹ These structural parameters determine whether or not there is magnetic coupling, and the type of magnetic coupling seen.

Figure 3.6 shows the shortest Pt...Pt (gray), Pt...S (green) and S...S (orange) interactions which are collected for comparison in Table 3.4. Intra- or inter-molecular Co...Co distances through these contacts or through the N, N' bidentate ligands as indicated with purple arrows in Figure 3.6 and are reported in Table 3.4. The monomeric species, [PtCo(SAc)₄(py)] (Figure 3.6A) forms intermolecular 3.0774(9) (Å) Pt...S interactions in the solid state, shorter than the Pt...Pt and S...S interactions between the {PtS₄} faces (Table 3.4). The [(py)PtCo(SAc)₄(py)] species in Figure 3.6B has pyridine coordinated to both the Co and the Pt, preventing close Pt...Pt or Pt...S interactions in the solid state. The closest intramolecular interaction between individual lantern complexes is a S...S interaction of 3.923(1) Å. The dimer, [PtCo(SAc)₄(pyz)_{0.5}] (Figure 3.6C) has a Co-Co distance 6.9779(6) (Å) through the pyz bridge. The interactions distances between the {PtS₄} faces in [PtCo(SAc)₄(pyz)_{0.5}] are most comparable to [PtCo(SAc)₄(py)] with the 3.3232(7) Pt...S interactions bring the shortest contacts. The Co...Co distance between individual complexes across the Pt...S interactions is 8.5925(5) Å, and longer than the Co...Co distance between individual complexes across the pyz bridge as reported in Table 3.4. In the chain, [PtCo(SAc)₄(4,4'-bipy)]_∞ (Figure 3.6D) 4,4'-bipy coordination to Pt

prevents any close Pt...Pt or Pt...S solid state interactions. The solid-state S...S interactions of 4.289(4) Å are comparable but slightly longer to those of [(py)PtCo(SAc)₄(py)].

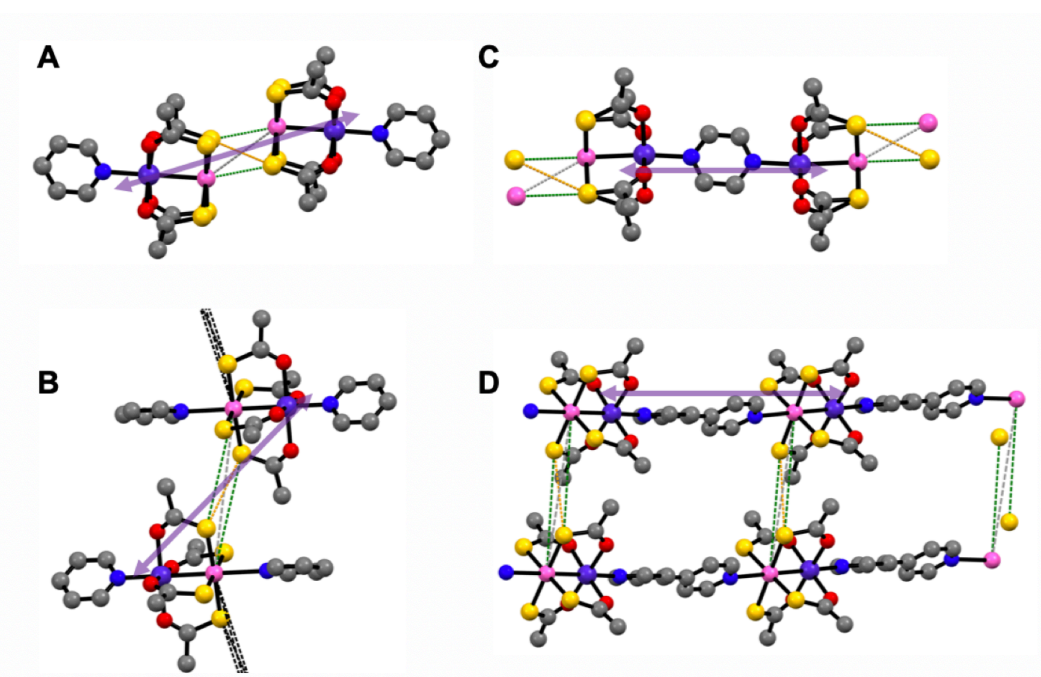


Figure 3.6. Mercury representations displaying intermolecular Pt...Pt (gray), Pt...S (green) and S...S (orange) contacts in complexes [PtCo(SAc)₄(py)] (A), [(py)PtCo(SAc)₄(py)] (B), [PtCo(SAc)₄(pyZ)_{0.5}] (C) and [PtCo(SAc)₄(4,4'-bipy)]_∞ (7) (D). The purple arrows indicate the Co-Co distances reported in in Table 3.4. H atoms removed for clarity.

Table 3.4. Intramolecular Pt...Pt, Pt...S and S...S interactions and Co-Co distances

Complex	Pt...Pt (Å)	Pt...S (Å)	S...S (Å)	Co...Co (Å)	Reference
[PtCo(SAc) ₂ (py)]	4.3042(3)	3.0774(9)	3.656(1)	8.7797(7)	⁷²
[(py)PtCo(SAc) ₄ (py)]	7.8759(2)	5.7699(8)	3.923(1)	10.2357(8)	⁷²
[PtCo(SAc) ₂ (pyz) _{0.5}]	3.6682(2)	3.3232(7)	3.703(1)	6.9779(6)	⁷⁹
[PtCo(SAc) ₂ (bipy)] _∞ (7)	8.4032(6)	6.252(3)	4.289(4)	14.328(2)	this work

3.2.2. Electronic Spectroscopy

Diffuse reflectance UV-vis-NIR absorption data were collected for $[\text{PtCo}(\text{SAc})_4(4,4\text{'-bipy})]_\infty$ (**7**) and the spectrum, in Figure 3.7, is generally consistent with other $[\text{PtCo}(\text{SAc})_4(\text{L})]$ lanterns.⁷² Features around 234 nm and 309 nm and a shoulder ~ 400 nm are assigned to the 4,4-bipy $\pi \rightarrow \pi^*$ transition and LMCT from the thioacetate backbone. The broad feature in the visible region at 502 nm is assigned to Co(II) $d-d$ transitions and is consistent with other $[\text{PtCo}(\text{SAc})_4(\text{L})]$ complexes (Table 3.5).^{72, 78} There is evidence of intermetallic Pt...Co $d-d$ charge transfer in the near-IR region at 1238 nm. Similar features have been identified for monomeric $\{\text{PtCo}\}$ complexes (L = OH₂, py, pyNO₂, pyNH₂) reported in Table 3.5 as evidence of a Pt-Co interaction. The $[\text{PtCo}(\text{SAc})_4(\text{pyz})]_\infty$ chain has a feature 1269 nm, consistent with the monomeric complexes, while the near-IR feature for the $[\text{PtCo}(\text{SAc})_2(\text{pyz})_{0.5}]$ dimer is the most blue shifted at 1162 nm.⁷⁹ The transition at 1238 nm for the chain falls within the previously observed range 1233-1324 nm for monomeric species. The UV-vis-NIR spectrum for $[\text{PtNi}(\text{SAc})_4(2,5\text{-Me}_2\text{pyz})_{0.5}]_\infty$ (**8**) is reported in Figure 3.11 and is consistent with other $[\text{PtNi}(\text{SAc})_4(\text{L})]$ derivatives.⁷²

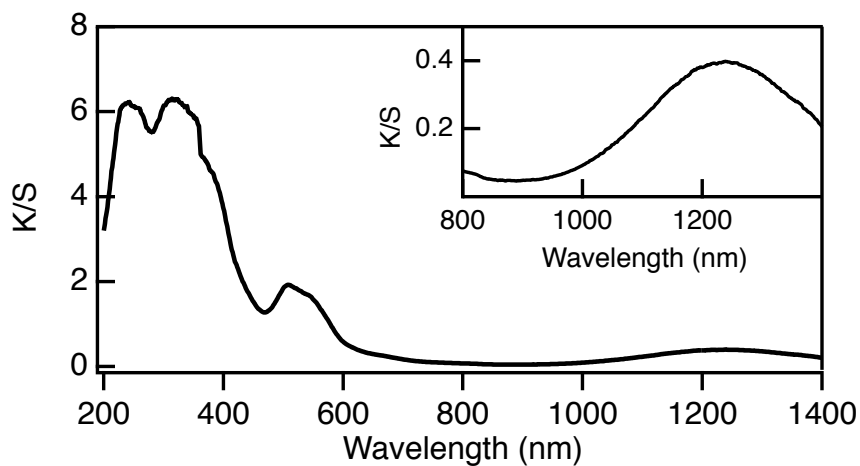


Figure 3.7 Diffuse reflectance spectrum of $[\text{PtCo}(\text{SAc})_4(4,4'\text{-bipy})]_\infty$. The inset includes only the near-IR region.

Table 3.5. Vis-NIR Comparison for $[\text{PtCo}(\text{SAc})_4\text{L}]$ Complexes

Complex	λ visible (nm) ^a	λ near-IR (nm)	Reference
$[\text{PtCo}(\text{SAc})_4(\text{OH}_2)]$	492	1284	78
$[\text{PtCo}(\text{SAc})_4(\text{py})]$	497	1284	72
$[\text{PtCo}(\text{SAc})_4(\text{pyNO}_2)]$	487	1233	78
$[\text{PtCo}(\text{SAc})_4(\text{pyNH}_2)]$	504	1324	72
$[\text{PtCo}(\text{SAc})_2(\text{pyz})_{0.5}]$	463	1162	79
$[\text{PtCo}(\text{SAc})_4(\text{pyz})]_\infty$	491	1269	79
$[\text{PtCo}(\text{SAc})_4(4,4'\text{-bipy})]_\infty$, 7	502	1238	this work

^a The feature with the lowest wavelength in the visible region is reported for each.

3.2.3. Magnetic Studies

Magnetic susceptibility measurements of **7** were performed Prof. Mark Turnbull at Clark University. Magnetization was measured as a function of applied magnetic field at 1.8 K as shown in Figure 3.8 where no hysteresis is observed. Solid state temperature-dependent magnetic susceptibility measurements were performed for **7** between 1.8 and 300 K. As shown in Figure 3.9, the room temperature $\chi_{\text{M}}T$ value is $3.30 \text{ cm}^3 \cdot \text{K} \cdot \text{mol}^{-1}$ ($\mu_{\text{eff}} = 5.14$). This value is higher than the calculated spin-only value of $1.875 \text{ cm}^3 \cdot \text{K} \cdot \text{mol}^{-1}$ ($\mu_{\text{eff}} = 3.87$) for an isolated $S = 3/2$ ion with $g = 2$, consistent with many known high spin Co(II) complexes with significant spin-orbit coupling contributions. As the temperature is decreased, $\chi_{\text{M}}T$ remains generally constant until ~ 200 K after which $\chi_{\text{M}}T$ decreases to $1.86 \text{ cm}^3 \cdot \text{K} \cdot \text{mol}^{-1}$ at 1.8 K. This behavior is consistent with high spin Co(II) single ion anisotropy and indicates no magnetic coupling between the Co centers,⁹¹ demonstrating that while the bipy ligand promotes the formation of a structural chain, the Co centers within the chain are magnetically isolated. We hypothesize that this could be due to the long Co-Co intrachain distance of 14.328(2) nm and many diamagnetic interactions (4,4'-bipy and Pt) between the Co centers.

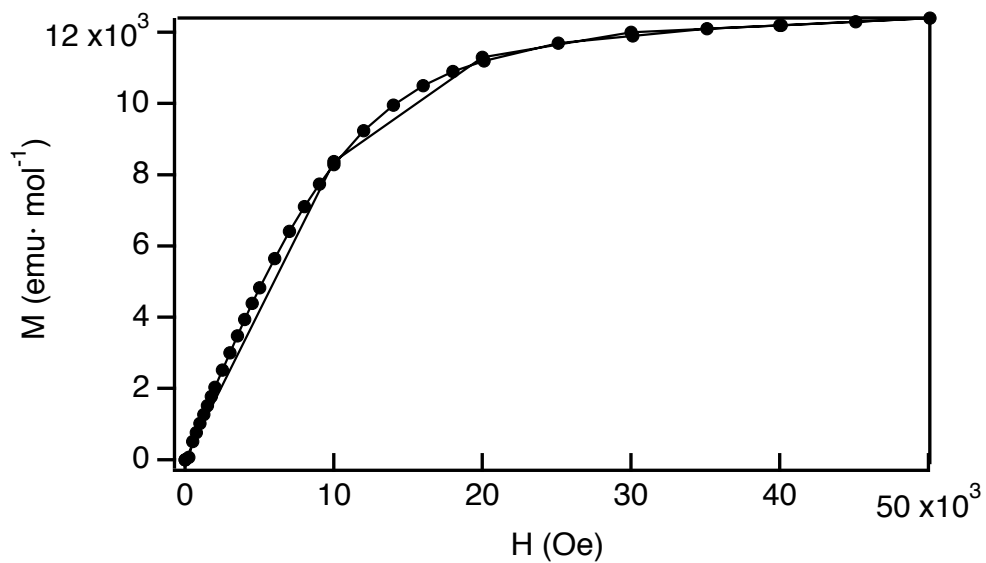


Figure 3.8. Magnetization as a function of applied magnetic field ($M(H)$) for $[\text{PtCo}(\text{SAc})_4(4,4'\text{-bipy})]_\infty$ (**7**) collected at 1.8 K.

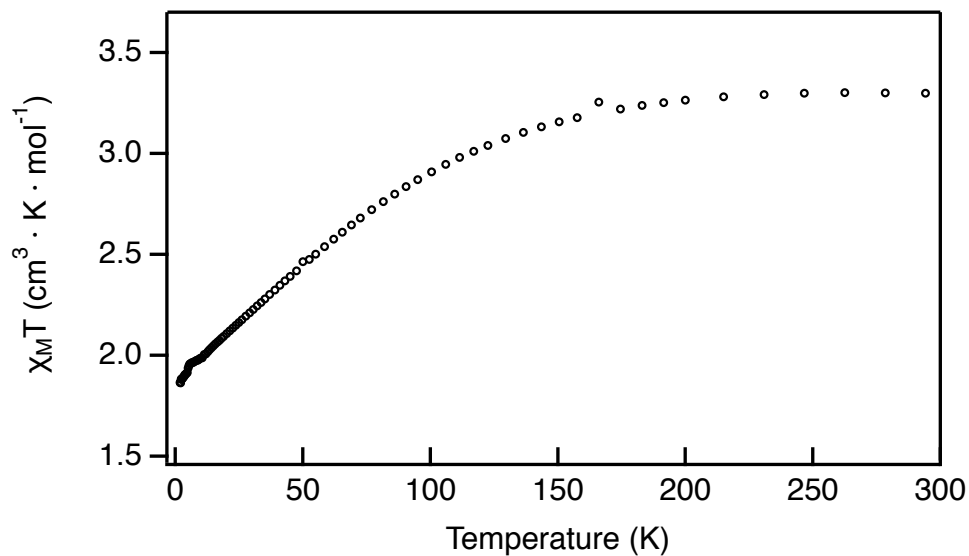


Figure 3.9. Temperature dependence of $\chi_M T$ collected between 1.8 and 300 K at an applied dc field of 1000 Oe for $[\text{PtCo}(\text{SAc})_4(4,4'\text{-bipy})]_\infty$ (**7**).

In Figure 3.10, we compare the temperature dependent magnetic susceptibility measurements of **7** to the previously reported complexes $[\text{PtCo}(\text{SAC})_4(\text{py})]$ ⁷² $[(\text{py})\text{PtCo}(\text{SAC})_4(\text{py})]$ ⁷² and $[\text{PtCo}(\text{SAC})_4(\text{pyz})_{0.5}]$ ⁷⁹ shown in Scheme 3.1 and Figure 3.6. The room temperature $\chi_{\text{M}}T$ values for $[\text{PtCo}(\text{SAC})_4(\text{py})]$ (blue), $[(\text{py})\text{PtCo}(\text{SAC})_4(\text{py})]$ (red) and $[\text{PtCo}(\text{SAC})_4(4,4'\text{-bipy})]_{\infty}$ (black) are all $\sim 3.0 - 3.3 \text{ cm}^3 \cdot \text{K} \cdot \text{mol}^{-1}$ ($\mu_{\text{eff}} = 4.89 - 5.14$), consistent with high spin Co(II) and its spin-orbit coupling and unquenched angular momentum contributions. The $[\text{PtCo}(\text{SAC})_4(\text{pyz})_{0.5}]$ complex, (plotted per mole of dimer, green) has a room temperature $\chi_{\text{M}}T$ value of $5.91 \text{ cm}^3 \cdot \text{K} \cdot \text{mol}^{-1}$ ($\mu_{\text{eff}} = 6.87$), consistent with two magnetically isolated $S = 3/2$ Co (II) centers. As the temperature decreases, there is an obvious decrease in $\chi_{\text{M}}T$ attributed to antiferromagnetic coupling between the Co(II) centers which yields an $S = 0$ ground state at low temperature.⁷⁹ For the other complexes, $\chi_{\text{M}}T$ begins to gradually decrease around 200 K. After 10 K, $[(\text{py})\text{PtCo}(\text{SAC})_4(\text{py})]$ (red) and $[\text{PtCo}(\text{SAC})_4(\text{py})]$ (blue) decrease sharply, reaching $1.5 \text{ cm}^3 \cdot \text{K} \cdot \text{mol}^{-1}$ and $0.21 \text{ cm}^3 \cdot \text{K} \cdot \text{mol}^{-1}$ at ~ 2 K respectively.

From Figure 3.10 we observe that for $[\text{PtCo}(\text{SAC})_4(\text{pyz})_{0.5}]$ (green) and $[\text{PtCo}(\text{SAC})_4(\text{py})]$ (blue), $\chi_{\text{M}}T$ decreases to $0 \text{ cm}^3 \cdot \text{K} \cdot \text{mol}^{-1}$ and $0.21 \text{ cm}^3 \cdot \text{K} \cdot \text{mol}^{-1}$ respectively. We note the similarity of the solid-state Pt...Pt and Pt...S intramolecular interactions of $[\text{PtCo}(\text{SAC})_4(\text{pyz})_{0.5}]$ and $[\text{PtCo}(\text{SAC})_4(\text{py})]$ as reported in Table 3.4 and shown in Figures 3.6C and 3.6A respectively, suggesting that these interactions should not be ruled out for promoting coupling. Previous attempts to fit the magnetic data for $[\text{PtCo}(\text{SAC})_4(\text{py})]$ and $[(\text{py})\text{PtCo}(\text{SAC})_4(\text{py})]$ revealed these complexes cannot be modeled as “dimers” unlike complexes with closer ($\sim 3.0 \text{ \AA}$) Pt...Pt interactions,^{77,78} suggesting that

the closest solid-state interactions between the monomers (Pt...S or S...S) cannot explain the downturn of $\chi_M T$ at low temperature. Therefore, this magnetic behavior was attributed to zero-field splitting, as opposed to antiferromagnetic coupling. These interpretations were also corroborated with the Ni derivatives, $[\text{PtNi}(\text{SAc})_4(\text{py})]^{72}$ and $[(\text{py})\text{PtNi}(\text{SAc})_4(\text{py})]^{72}$, where reasonable fits for the magnetic data were achieved.⁷² Therefore, in $[\text{PtCo}(\text{SAc})_4(\text{pyz})_{0.5}]$, we hypothesize that the orbital interactions across the pyrazine bridge are the dominant exchange pathway, rather than via the Pt...S contacts. In addition, the Co...Co distances across the pyrazine bridge are shorter than those across the Pt...S interactions.⁷⁹

The chain, **7** (black), does not display a sharp decrease in $\chi_M T$ at low temperature. This magnetic behavior is also attributed to single ion anisotropy of the Co(II) high spin centers. The $\chi_M T$ temperature dependence is most comparable to the $[(\text{py})\text{PtCo}(\text{SAc})_4(\text{py})]$ complex, which also has no solid-state interactions between the $\{\text{PtS}_4\}$ faces of individual complexes. The magnetic behavior is not identical, for the $[(\text{py})\text{PtCo}(\text{SAc})_4(\text{py})]$ complex has a significant decrease in $\chi_M T$ below 10 K. Although there is no evidence for magnetic communication across the 4,4'-bipy bridge, the magnetic behavior is distinct from a monomeric analogue ($[(\text{py})\text{PtCo}(\text{SAc})_4(\text{py})]$).

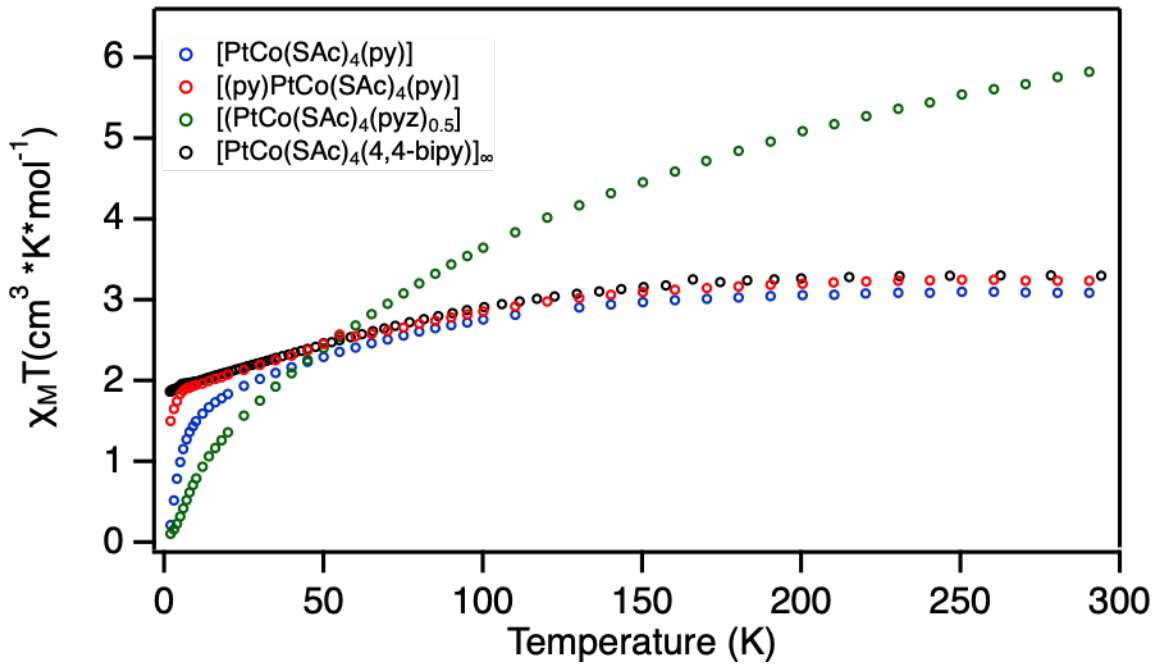
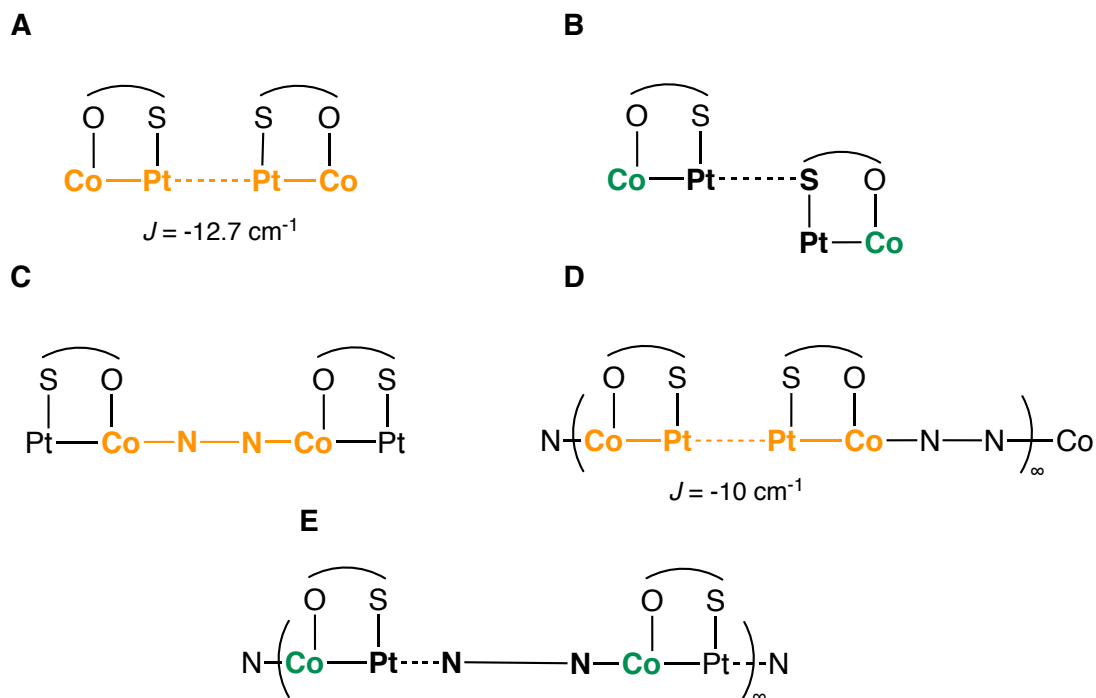


Figure 3.10. Temperature dependence of $\chi_M T$ collected between 1.8 and 300 K at an applied dc field of 1000 Oe for $[\text{PtCo}(\text{SAc})_4(\text{py})]$ (blue), $[(\text{py})\text{PtCo}(\text{SAc})_4(\text{py})]$ (red), $[\text{PtCo}(\text{SAc})_4(\text{pyz})_{0.5}]$ (green, plotted per mol of dimer) and $[\text{PtCo}(\text{SAc})_4(4,4'\text{-bipy})]_\infty$ (black).

Scheme 3.4 summarizes the pathways for communication between Co centers in various intra- and intermolecular frameworks studied previously and presented in this work. The Pt...Pt bridges (A) have been shown to facilitate antiferromagnetic coupling between Co centers,^{77, 78} while Pt...S contacts (B) do not.⁷² The Co centers of individual lanterns bridged by bidentate N, N' ligands such as pyrazine (C) also exhibit antiferromagnetic coupling, which yields an $S = 0$ ground state at low temperature ([PtCo(SAc)₄(pyz)_{0.5}] as shown in Figure 3.10).⁷⁹ The N, N' bidentate ligands DABCO⁸² and 2,5-Mepyz promote chain formation through short Pt...Pt contacts while the ligand bridges the Co centers of two adjacent lantern complexes (D). Magnetic studies of the DABCO chains revealed antiferromagnetic coupling between the M (M = Co, Ni) centers best described by magnetic exchange across Pt...Pt interactions with insignificant interactions across the DABCO ligand. While DABCO and 2,5-Mepyz produce chains with the same connectivity, the potential orbital pathways for magnetic exchange via each bridging ligand are distinct.⁹²

Similar antiferromagnetic exchange coupling constants have been reported for [PtCo(SAc)₄(OH₂)]⁷⁸ (Scheme 3.4A) and [PtCo(SAc)₄(DABCO)_{0.5}]_∞⁸² (Scheme 3.4D), which are $J = -12.7 \text{ cm}^{-1}$ and $J = -10 \text{ cm}^{-1}$ respectively and where magnetic exchange is facilitated by the Pt...Pt contacts. Although a reasonable fit for the [PtCo(SAc)₄(pyz)_{0.5}] dimer was not achieved, the Ni derivative has been reported as $J = -7.1 \text{ cm}^{-1}$, where magnetic exchange is facilitated by the pyrazine bridge.⁷⁹ This value and pathway is distinct from [PtNi(SAc)₄(OH₂)]⁷⁸ and [PtNi(SAc)₄(DABCO)_{0.5}]_∞, which have J values of -50.8 cm^{-1} and -32 cm^{-1} , respectively, and magnetic exchange is facilitated by the Pt...Pt

contacts. Magnetic measurements of **7** reported here, are consistent with high spin Co(II) single ion anisotropy, indicating that there is no magnetic coupling between the Co centers in the repeating units of {Co-Pt-L-Co} (L = 4,4'-bipy) (E). While 4,4'-bipy provides a similar possible magnetic exchange pathway through the π^* orbitals as pyrazine, we hypothesize that the intramolecular distance between the Co centers is too long. In addition, the antiferromagnetic exchange across the pyrazine in [PtNi(SAc)₄(pyz)_{0.5}]⁷⁹ is already relatively weak compared to the Pt...Pt contacts, consistent with relatively weak magnetic exchange reported for pyrazine bridges in other systems.⁹²



Scheme 3.4. Intermolecular connections and types of magnetic behavior in various {PtCo} lantern frameworks. A) dimers with Pt...Pt contacts and antiferromagnetic exchange coupling constant reported for $[\text{PtCo}(\text{SAC})_4(\text{OH}_2)]$ ⁷⁸ B) dimers with Pt...S contacts C) dimers with a N, N' bidentate bridge (e.g. pyz) with antiferromagnetic coupling between Co centers D) chains with a N, N' bidentate bridge (e.g. DABCO) between Co centers of two adjacent lanterns and antiferromagnetic exchange coupling constant reported for $[\text{PtM}(\text{SAC})_4(\text{DABCO})_{0.5}]_{\infty}$ ⁸² E) chains with a N, N' bidentate bridge (e.g. 4,4'-bipy) between Pt and Co of adjacent lanterns. Co centers in yellow indicate antiferromagnetic coupling through the indicated pathway (also in yellow). Co centers in green indicate no observed coupling.

3.3. Conclusions

Earlier work had produced quasi-1D chains in $[\text{PtM}(\text{SAc})_4(\text{pyz})]_\infty$ with $M = \text{Co}$, Ni , Zn , but the material properties were unsuitable for magnetization studies. Here we explore chain formation between $[\text{PtM}(\text{SOCR})_4]$ units with bulkier bridging ligands L , relative to pyrazine, and less volatile solvents to achieve a reproducible material for magnetic studies.^{79, 82} Complexes **8** and **9** exhibit chain formation, with bridging ligands 2,5-Me₂pyz and phz, but did not have the correct connectivity to compare the potential magnetic coupling pathways with the previous pyrazine chains. Attempts with 4,4'-bipy produced the desired structural chain (**7**). Magnetic studies of **7** reveal that although the bridging ligand 4,4'-bipy achieves a structural chain, there is no evidence for magnetic communication between Co centers. These results are reported in the context of other $\{\text{PtCo}\}$ species including a pyrazine bridged dimer $[\text{PtCo}(\text{SAc})_4(\text{pyz})_{0.5}]$ ⁷⁹ and a DABCO chain $[\text{PtM}(\text{SAc})_4(\text{DABCO})_{0.5}]_\infty$ ⁸² in order to compare and identify the pathways that allow for magnetic communication. Since DABCO bridges have only a σ framework, this ligand does not provide a low-energy orbital pathway for communication. Pyrazine bridges in the dimeric species $[\text{PtCo}(\text{SAc})_4(\text{pyz})_{0.5}]$ ⁷⁹ appear to promote antiferromagnetic coupling across the N...N bridge via the π^* orbital. The lack of coupling in the 4,4'-bipy chain suggests that magnetic coupling through aromatic imines is only present across shorter distances. Therefore, using aromatic imines with short N...N pathways may promote coupling in these quasi-1D chains.

3.4. Experimental

3.4.1. Materials and Methods

The $[\text{PtM}(\text{SAc})_4(\text{OH}_2)]$ ($\text{M} = \text{Co}, \text{Ni}$) lanterns were prepared from previously reported methods.⁷⁸ Other reagents were obtained commercially and used without further purification. Elemental analysis was performed by Atlantic Microlab Inc. (Norcross, GA). UV-vis-NIR spectra were collected on a Shimadzu UV-3600 spectrometer using a Harrick Praying Mantis Diffuse Reflection accessory and were analyzed using the Kubelka Munk transformation.⁹³

3.4.2. X-ray Crystallography Methods

X-ray crystallography, including data collection, solution and refinement, were performed by Léa Toubiana and Jeff Bacon (BU). Single-crystal X-ray diffraction of $[\text{PtCo}(\text{SAc})_4(4,4'\text{-bipy})]_{\infty}$ was collected using a Bruker X8 Proteum-R diffractometer by using $\text{Cu}_{\text{K}\alpha}$ radiation in an N_2 gas stream at 100(2) K with phi and omega scans. Data were refined using SHELXL 2018/3 and Olex2 1.5 was used for molecular graphics and preparation of materials for publication. Data collection and refinement parameters are reported in Table 3.6.

3.4.3. Magnetic Measurements

Magnetic measurements were performed by Prof. Mark Turnbull at Clark University. Data for **7** were collected on a Quantum Design MPMS SQUID

magnetometer. Crystals were powdered, packed into a gelatin capsule and mounted in a plastic straw. The magnetization of the sample was measured as a function of field from 0 – 50 kOe at 1.8 K. Several data points were recollected as the field returned to 0 Oe to check for hysteresis effects; none were observed. The magnetization of the sample was then measured in a 1 kOe applied field from 1.8 – 310 K. Data were corrected for the diamagnetic contributions of the constituent atoms as estimated from Pascal's constants,⁹⁴ the contributions from the sample holder (measured independently) and the temperature independent paramagnetism of the Cu(II) ion.

3.4.4. Synthetic Procedures

Synthesis of $\{[PtCo(SAc)_4(bipy)](PC)\}_\infty$ (7). The complex $[PtCo(SAc)_4(OH_2)]$ (110 mg, 0.192 mmol) was freshly prepared via previously reported methods⁷⁸ and dissolved in minimal propylene carbonate (PC) (~ 5-10 mL). The pale pink solution was layered underneath a ~ 2 mL mixture of 1:1 PC and toluene. A toluene solution of 4,4-bipyridine (75 mg, 0.48 mmol) was layered on top of the solvent layer. Dark pink crystals (65 mg, 42 % yield) were obtained at 5 °C after one week. Anal. Calc'd. for $C_{22}H_{26}CoN_2O_7PtS_4$: C, 32.51; H, 3.22; N, 3.45%. Found: C, 32.61; H, 3.19; N, 3.47%. UV-vis-NIR (Diffuse Reflectance) (λ_{max} , nm (k/s)): 234 (6.2), 309 (6.3), 502 (1.9), 1238 (0.4).

Synthesis of $[PtNi(SAc)_4(2,5-Me_2pyz)_{0.5}]_\infty$ (8) The complex $[PtNi(SAc)_4(OH_2)]$ (55 mg, 0.096 mmol) was freshly prepared via previously reported methods⁷⁸ and dissolved in ~ 5 mL acetone. While stirring, 2,5-Me₂pyz was added to the green solution in minimal

acetone. After stirring for ~ 12 hours a green precipitate was isolated via vacuum filtration and dissolved in chloroform. Green crystals were obtained from slow diffusion with hexanes. Anal. Calc'd. for $C_{22}H_{32}Ni_2N_2O_8Pt_2S_8$: C, 21.72; H, 2.65; N, 2.30%. Found: C, 21.46; H, 2.60; N, 2.27%. UV-vis-NIR (CH_2Cl_2) (λ_{max} , nm (ϵ_M , $cm^{-1} M^{-1}$)): 247 (926640), 275 (542360), 359 (84817), 685 (16), 1377 (15).

Synthesis of $[PtNi(SAc)_4(OH_2)](phz)$ (9). The complex $[PtNi(SAc)_4(OH_2)]$ (55 mg, 0.096 mmol) was freshly prepared and dissolved in ~ 5 mL of acetone. The solution was added slowly to an excess of phenazine (36 mg, 0.2 mmol) and stirred for ~ 12 hours. The clear green solution was layered under hexanes and yielded green crystals. Anal. Calc'd. for $C_{20}H_{21}NiN_2O_5PtS_4$: C, 31.97; H, 2.82; N, 3.73%. Found: C, 31.95; H, 2.81; N, 3.65%.

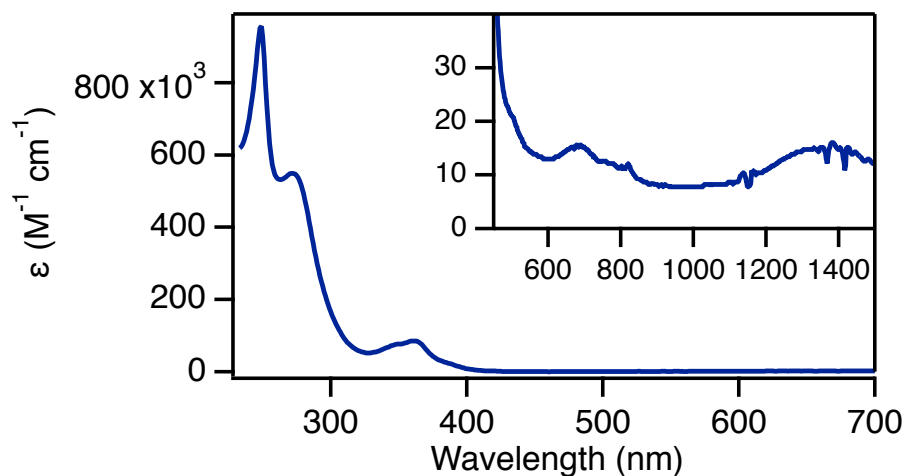


Figure 3.11 UV-vis-NIR spectrum $[PtNi(SAc)_4(2,5-Me_2pyz)_{0.5}]_{\infty}$ (**8**).

Table 3.6. Crystal data collection and refinement parameters for **7**, **8** and **9**.

Compound	7	8	9
Formula	C ₁₈ H ₂₀ CoN ₂ O ₄ PtS ₄ , C ₄ H ₆ O ₃	C ₂₅ H ₃₅ Cl ₉ N ₂ Ni ₂ O ₈ Pt ₂ S ₈	C ₈ H ₁₃ NiO ₅ PtS ₄ C ₁₂ H ₈ N ₂
Formula weight		1574.68	752.43
Crystal system	Triclinic	Monoclinic	Triclinic
Color	Dark pink	Green	Green
Space group	<i>P</i> -1	<i>P</i> -2 ₁ /n	<i>P</i> -1
<i>a</i> , Å	8.4032(4)	15.763(6)	8.3354(17)
<i>b</i> , Å	12.0997(6)	14.166(5)	10.644(2)
<i>c</i> , Å	28.6580(13)	24.323(9)	13.618(3)
<i>α</i> , deg	89.768(2)	90	92.888(2)
<i>β</i> , deg	89.743(2)	96.596(7)	97.607(3)
<i>γ</i> , deg	71.677(2)	90	90.044(2)
<i>V</i> , Å ³	2766.06	5396(3)	1196.1(4)
<i>Z</i> , <i>Z'</i>	4	4	2
<i>temp</i> , K	100	100	100.0
Final R indices [I > 2σ(I)]	R1 = 0.0537 wR2 = 0.1400	R1 = 0.0848, wR2 = 0.1952	R1 = 0.0267, wR2 = 0.0616

CHAPTER FOUR: Hard-Soft Chemistry Design Principles for Predictive Assembly of Single Molecule Metal-Junctions

4.1. Abstract

Achieving atomic control over the organic-inorganic interface is key to engineering electronic and spintronic properties of molecular devices. We leverage insights from inorganic chemistry to create hard-soft acid-base (HSAB) theory-derived design principles for incorporation of single molecules onto metal electrodes. Typically, a single molecule circuit assembles via a bond between an organic backbone and an under-coordinated metal atom of the electrode surface, typically Au. Here, we establish that the observed trends in the robustness and chemical selectivity of single molecule junctions formed with a range of linkers correlate with HSAB principles, which have traditionally been used to guide atomic arrangements in the synthesis of coordination complexes. We find that this similarity between the intermolecular electrode-molecule bonding in a molecular circuit and the intra-molecular bonds within a coordination complex have implications for the design of metal-containing complexes compatible with electrical measurements on metal electrodes. Our results here show that HSAB principles determine which intramolecular interactions can be compromised by inter molecule-electrode coordination; in particular, on Au electrodes, soft-soft metal-ligand bonding is vulnerable to competition from soft-soft Au-linker bonding in the junction. Neutral donor-acceptor intramolecular bonds can be tuned by the Lewis acidity of the transition metal ion, suggesting future synthetic routes

towards incorporation of transition metal atoms into molecular junctions for increased functionality of single molecule devices.

4.2. Introduction

The most promising route to further miniaturization of electronic components is through the design of functional molecular devices. In this scheme, molecules are wired into nanoscale circuits to replace bulk silicon as an active component. Indeed, single molecule junctions that exhibit transport phenomena such as high conductance, switching, or rectification have already been demonstrated and are appealing material candidates for next generation electronics and spintronic applications.^{7,13} These functionalities have been achieved primarily by forming single molecule junctions with organic molecules coordinating to metallic electrodes through donor-acceptor or covalent bonds.⁶ In donor-acceptor metal-molecule linking, a Lewis-basic electron lone-pair on the molecule coordinates to a Lewis-acidic undercoordinated atom, typically gold, on the metal electrode. This approach has proven effective at assembling chemically selective organic molecule-metal junctions with robust electronic properties.⁹⁵ However, there is a dispersion in the performance and robustness of different linker groups on gold; to our knowledge, no overarching theoretical framework has been developed to explain and predict the success of some, but not other, donor atoms for molecular electronics applications.

Compared to organic molecular wires, molecules containing transition metal centers have the potential for enhanced conductance^{39,96} and increased functionality via

redox or magnetic properties which can be leveraged to create components such as molecular switches^{8, 11, 97} and memory storage devices.^{10, 44} Metal-centered electronic states or nuclear spin states of molecules containing one or more transition metals can be synthetically tuned and manipulated in situ,^{50, 98-100} for potential applications in spintronics and quantum information science (QIS).^{9, 12, 76, 101} Synthetic efforts to form molecular metal wires include coordination polymers, extended metal atom chains (EMACs), and infinite one-dimensional (1D) chains.^{62, 102, 103}

Many of the transition-metal containing molecular candidates mentioned above are coordination complexes where the organic ligands are bound to the transition metal atom centers via Lewis acid-base donor-acceptor interactions. The field of inorganic chemistry has developed qualitative principles to guide the synthesis of compounds with predictable internal arrangements of transition metal atoms and *p*-block elements. In particular, the hard-soft acid base theory (HSAB) establishes the preferential coordination of “hard” (“soft”) Lewis acidic transition metal ions to “hard” (“soft”) ligands and is used successfully for selective synthesis of coordination complexes.⁷¹

Here, we draw a parallel between HSAB principles guiding coordination complex synthesis on the one hand and trends in the formation of molecular junctions using break junction (BJ) techniques on the other. In typical BJ experiments, corrugated electrodes are repeatedly brought into physical contact and then broken in the presence of molecules which can bind to undercoordinated atoms at the interface and bridge the inter-electrode gap. In particular, the scanning tunneling microscopy BJ (STM-BJ) technique can probe the conformation and electronic properties of a single molecule on metal electrodes in a

statistically meaningful way.^{5, 23, 24} Here, we observe that in such experiments, synthetically “soft” donor atoms on organic molecules can coordinate selectively to the “soft” Au adatoms on the electrode surface; importantly, this bonding scheme can result in reproducible molecular junctions because covalent intramolecular bonds in organic molecules, e.g. C-C, C-N, C-S bonds in α,ω diamines or dithiols, are stronger (~ 4 eV) than the molecule-gold interactions (~ 0.5 - 1.5 eV) or the Au-Au bonds (~ 1.5 eV).¹⁰⁴⁻¹⁰⁶ In contrast, we hypothesize that the intramolecular donor-acceptor bonds of coordination complexes are similar in character to inter electrode-molecule links and may be compromised by competition from under-coordinated Au atoms on the electrode surface present in these experiments. We perform STMBJ measurements and DFT calculations to test the HSAB principles in the context of molecular junctions and to investigate the compatibility of metal ion-containing coordination complexes with the molecular junction environment. To test a range of hard-soft intramolecular interactions, we use hetero- and homobimetallic lantern complexes, which provide a synthetically tunable ligand framework and independent choice of two metal atoms, in the heterobimetallic case.⁷³ By synthetically varying different components of the lanterns and performing STMBJ conductance measurements, we systematically identify which intramolecular metal-ligand bonding schemes are compatible with Au electrodes. Our combined conductance and DFT calculations show that Lewis acid-base design principles used in synthesis also govern stability of complexes on Au; specifically, since Au is a soft metal, soft-soft interactions are prone to competition from the Au surface, while hard-hard interactions remain intact. In addition, we find that certain intramolecular neutral donor-acceptor interactions

rearrange in the junction to form donor-acceptor bonds to the Au electrodes; by synthetically tuning the intramolecular acid-base interactions, we can affect the stability of the overall complex on Au. Recognition of HSAB principles in single molecule electronics and transition metal-containing molecule-metal junctions lay the foundation for significantly improved future design of functional molecular components for electronics, spintronics and other applications.

4.3. Results and Discussion

To establish the rules governing the formation of single molecule junctions on Au electrodes, we first compare the prevalence of donor atoms in structurally characterized¹⁰⁷ Au-containing coordination complexes (Figure 4.1A) and single molecule junctions assembled (Figure 4.1B) with a range of donor atoms. In both panels, the ligands are arranged from soft (left) to hard (right).^{71, 108} In Figure 4.1B, we also indicate the relative strength of the Au-ligand bonds based on previous single molecule force spectroscopy studies and binding energy calculations.^{5, 6, 34, 104-106, 109, 110} The qualitative similarity of the trends between the two series is critical. In both cases, the softest thiols/thiolates on the left are the most commonly observed ligands in Au-containing coordination complexes; they also form the strongest Au-molecule linkages and result in junctions with multiple binding configurations, resulting in a wider dispersion of conductance values observed in experiment.^{31, 32} In contrast, the hardest O-donor ligands are rarely used in synthesis of Au complexes or for linking molecule-metal junctions because of poorer interaction. The

amines and pyridines are intermediate along this continuum and have been used in single molecule measurements for forming sufficiently robust but chemically selective metal-molecule bonds. These observations suggest that HSAB theory can be used as a guiding principle not only for synthesis of atomically-defined complexes, but also for predictable assembly and robustness of single molecule-metal junctions.

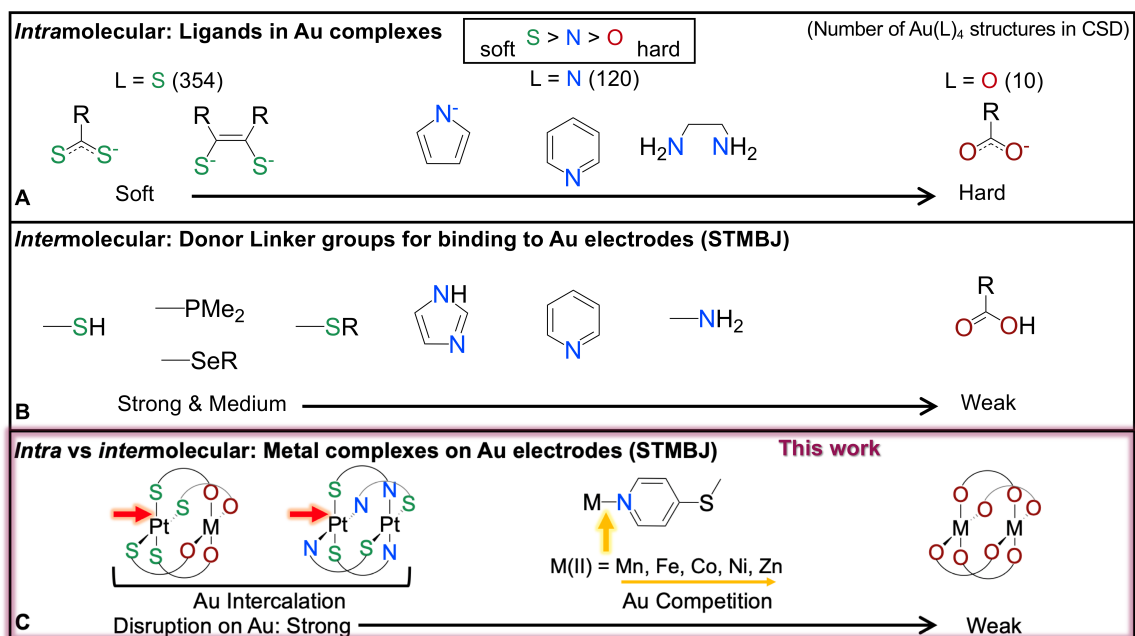


Figure 4.1. (A) Hard-soft trends of donor atoms apply for the synthesis of Au complexes, (B) effective linker groups to Au in single molecule measurements arranged according to binding strength,^{5, 6, 34, 104-106, 109, 110} and (C) the stability of metal complexes studied in this work on Au electrodes.

We further test these observations by probing the junction-formation behavior of organic ligands and coordination complexes on gold using STMBJ experiments and DFT theoretical calculations. We use the lantern framework and systematically vary its components to probe the robustness of different intramolecular interactions on Au electrodes.⁷³ As shown in Figure 4.1C, we propose that intramolecular soft-soft interactions within coordination complexes become disrupted in favor of coordination of soft donor ligands to gold, while the hard-hard interactions stay intact. We show that we can tune the stability of the pyridine N-M interaction by changing the Lewis acidity of the $3d$ metal (M). We hypothesize that the HSAB principles established here for lanterns on gold are applicable in general to conductance measurements of coordination complexes in metal-molecule junctions.

Schematics of the hetero- and homobimetallic lanterns are shown in Figure 4.2A and 4.2B, respectively, emphasizing their various synthetically tunable aspects. Molecular structures of the ligand backbones and the axial linker (L) used in this study are shown in Figure 4.2C. Varying the donor atoms of the organic backbones from sulfur to oxygen allows us to compare the effect of hard-soft acid-base interactions on the behavior of the Au-lantern junctions. The thiocarboxylate backbone (SC(O)R), shown in blue in Figure 4.2C, allows for selective coordination of the Pt and $3d$ metal (M) within the heterobimetallic complex in Figure 4.2A. During synthesis, the Pt preferentially coordinates to sulfur (soft-soft interaction), while the $3d$ metal preferentially coordinates to oxygen (hard-hard interaction). Homobimetallic lantern complexes in Figure 4.2B, with carboxylate (OC(O)R) backbones, shown in green in Figure 4.2C, contain only hard-hard

metal-ligand interactions, which enables comparison of hard-soft metal-ligand interactions in the junction. We also systematically vary the 3*d* metal (M and M' in Figures 4.2A and 4.2B) to probe the effect of the 3*d* metal Lewis acidity on the robustness of the neutral donor-acceptor metal ligand bonding between the 3*d* metal and the axial linker (L) through the pyridine nitrogen. The axial linker used for this study is 4-thiomethylpyridine (pySMe), shown in red in Figure 4.2C. To summarize, we synthesize and compare the behavior in the Au junction of organic ligands with different donor groups and of a series of new heterobimetallic lantern complexes of the form [PtM(tba)₄(pySMe)] M = Mn (**10**), Fe (**6**), Co (**11**), Ni (**12**), and Zn (**13**) (tba = thiobenzoate) and two new homobimetallic lantern complexes [Cu₂(OAc)₄(pySMe)₂] (**14**) (OAc = acetate) and [Co₂(esp)₂(pySMe)₂] (**15**) (esp = $\alpha,\alpha,\alpha',\alpha'$ -tetramethyl-1,3 benzenedipropionate) (pySMe = 4-thiomethylpyridine).

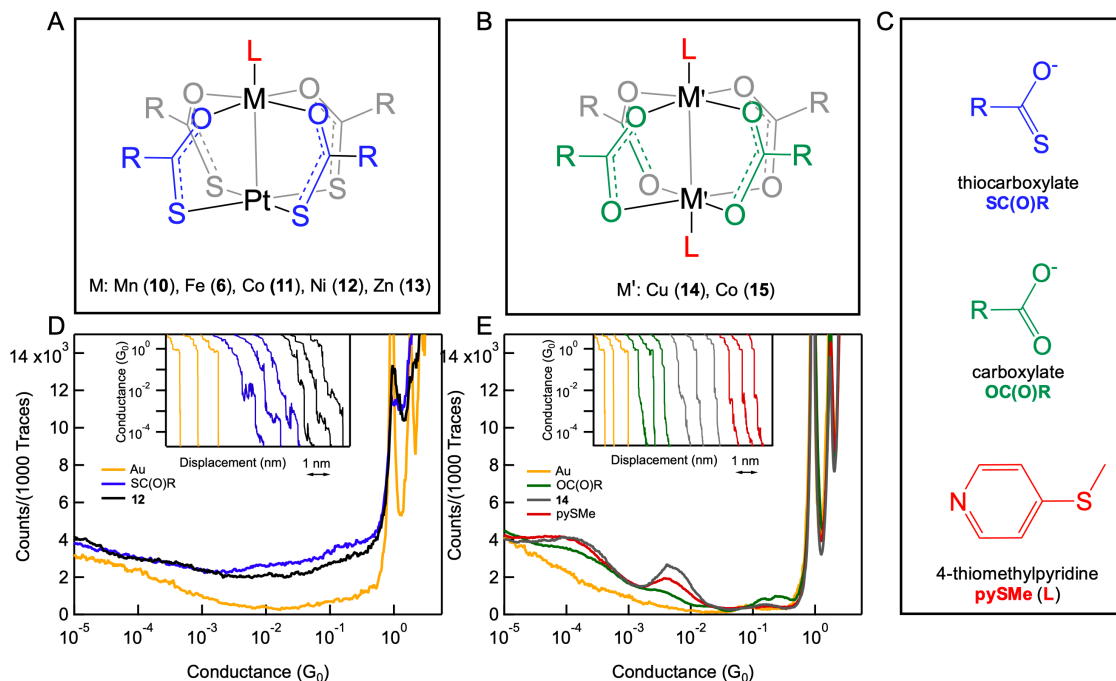


Figure 4.2. (A) Schematics of heterobimetallic lantern frameworks with SC(O)R backbone ligands R = Ph (B) homobimetallic lantern frameworks with OC(O)R backbone ligands, R = Me (**14**), for (7) OC(O)R= esp (**15**). All complexes have pySMe (L) axial ligands. (C) Molecular structures of the individual ligands. (D) Conductance histograms and sample traces (inset) of 1 mM measurements of SC(O)R as thiobenzoic acid and of **12** in TCB. (E) Conductance histograms and sample traces (inset) of 1mM OC(O)R as benzoic acid, pySMe, and **14** in TCB. Additional linear-binned conductance histograms are shown in Figure 4.13.

We first test the HSAB principles for binding organic molecular in the junctions by establishing conductance signatures of the individual backbone and axial ligands, the structures of which are shown in Figure 4.2C. We perform STMBJ measurements in the presence of these molecules using a home-built instrument and protocol as previously described.^{23-25, 29, 111} All conductance measurements are performed in 1,2,4-trichlorobenzene (TCB). As described in Figure 4.1B, previous studies have established that thiol-linked molecules form strong Au-S bonds ($\sim 1-1.5$ eV) that rival Au-Au (~ 1.5 eV) interactions and disrupt G_0 plateaus by weakening and intercalating into Au atomic chains.^{31, 32, 106} We measure the conductance signatures of the SC(O)R backbone ligand thiobenzoic acid (R=Ph) at a typical concentration of ~ 1 mM and plot example traces and a histogram of thousands of measurements in Figure 4.2D (blue). Thiobenzoic acid, like thiol linkers, binds to the Au electrodes through the Au-thiolate bond.^{32, 106, 112, 113} Numerous plateaus appear in the traces across the full range of conductance measured, confirming that the single thiol intercalates into the Au in multiple configurations, reducing the G_0 signature and raising the background compared to the clean Au as shown in Figure 4.2D.^{31, 32} We identify the reduction of the 1 G_0 peak observed in Figure 4.2D as a signature of the Au-thiolate interaction.

In contrast to thiols, linkers such as thioethers or pyridine, form donor-acceptor bonds which are weaker than the Au-Au interaction and do not disrupt 1 G_0 conductance signatures.^{6, 114, 115} Carboxylate ligands have been reported to form similarly weak Au-OC(O)⁻ bonds.^{34, 109} Our measurements of the OC(O)R backbone ligand as benzoic acid (R=Ph) are consistent with these reports and show no interference with the G_0 plateaus as

seen in Figure 4.2E (green). This result is consistent with hard-soft acid base principles we described in Figure 4.1A and B, in that the softer S intercalates with the softer Au, while the harder O does not. Next, we test the neutral lone-pair donors, such as N, which are neutral intermediate Lewis bases. The axial linker 4-thiomethylpyridine (pySMe) shown in Figure 4.2C contains an imine N and a thioether donor. Both types of donor groups have been studied previously in STMBJ experiments and demonstrated robust but selective binding to gold.^{5,28,33} Consequently, we observe here that the pySMe molecule can bridge the junction, resulting in reproducible conductance plateaus. The narrow peak in the conductance histogram observed for this molecule above a low background as shown in Figure 4.2E (red) is evidence of chemically selective and reproducible coordination between the lone-pairs of the Lewis basic donor and the under-coordinated Au atoms in the junction.^{23,24,111} By fitting a Gaussian to the histogram, the most likely conductance of pySMe is determined to be around $10^{-2} G_0$.^{5,33} This behavior is again distinct from the ligands containing the thiol, which binds to Au so strongly as to intercalate into the Au chains, disrupt the $1G_0$ plateaus and cause non-selective binding of the ligands in the junction. Summarizing these results, we formulate our *first* design rule: hard-soft acid base principles apply for both synthesis of transition metal complexes and binding of organic ligands in the Au junction. The binding strength of Lewis basic donors to the soft Au in single molecule junctions is predicted by the HSAB theory, which can serve as a useful guide to future engineering of robust but selective linkers for single molecule junctions.

We now test the consequence of HSAB principles for forming single molecule junctions with coordination complexes. We perform STMBJ conductance measurements

in the presence of lanterns at typical concentrations for such measurements, ~ 1 mM.^{23, 111,}
¹¹⁶ Standard protocols used for synthesis, purification and characterization of these complexes are detailed in the experimental section. The resulting traces and histograms for the heterobimetallic complex **12** and for the homobimetallic complex **14** are shown in black in Figure 4.2D and in gray in Figure 4.2E respectively. Compared to measurements of clean Au, the amplitude of the G_0 peak observed for **12** is diminished and the background at lower conductance values is increased due to conductance plateaus appearing at a broad range of values in individual traces as shown. This behavior is similar for all the heterobimetallic complexes **1-5** under these conditions (Figure 4.14). Notably, the resulting histogram shown in Figure 4.2D looks comparable to the histogram of the SC(O)R backbone plotted in blue, with no clear molecular signature below G_0 . The disruption of the $1G_0$ peak in the conductance histogram for the lantern containing the SC(O)R backbone is more consistent with the formation of a covalent S-Au bond in the junction, rather than a donor-acceptor R_2S -Au bond that we would expect if the S-Pt bond remained intact. This observation suggests that there may be competition between the soft-soft S-Pt and the soft-soft S-Au interactions. To confirm that this behavior is not specific to the SC(O)R backbone, measurements were repeated with $[Pt_2(mpy)_4]$ ($mpy = 2$ -mercaptopyridine), a homobimetallic lantern complex with S and N donor atoms, shown in Figure 4.15.¹¹⁷ A similar disruption of the Au surface was observed confirming the sulfur atoms of the backbone ligands as the source of the Au surface interference (Figure 4.15).

In contrast to lanterns formed with the sulfur-containing SC(O)R backbones discussed above, G_0 features measured in the presence of Cu(II) or Co(II) homobimetallic lantern complexes **14** and **15** with carboxylate backbone ligands are comparable to that of the bare Au control as shown in Figure 4.2E and 4.16. This comparison demonstrates that the O-donor backbone does not disrupt the Au signatures and does not interact strongly with the electrodes. A molecular conductance signature observed with these lanterns at $\sim 10^{-2} G_0$ indicates the formation of reproducible molecular junctions and overlaps with the conductance signature of the axial ligand pySMe as shown in Figure 4.2E and Figure 4.16.

The disruption of the Au electrodes with lanterns having SC(O)R backbones but not those with OC(O)R ligands is again consistent with the established HSAB principles. Measurements with the SC(O)R lanterns indicate that there is competition between the softer Pt and Au for binding to the softer sulfur; in contrast complexes held together via hard-hard interactions between oxygen and a $3d$ metal appear to remain intact. Isosurface plots of the frontier orbitals of the SC(O)R and the OC(O)R lanterns shown in Figure 4.17 reflect the difference in the behavior of these two compounds on Au. Whereas the HOMO of the SC(O)R heterobimetallic lantern is concentrated on the sulfur lone pairs, which are part of the conjugated π system, the HOMO of the OC(O)R lanterns are concentrated on the dz^2 orbital of the metal atom and are deeper in energy. This distinction may help explain the difference in the interaction of the Au with these two types of lantern backbones. Summarizing these results, we formulate our *second* design rule: transition metal complexes which rely on soft-soft intramolecular metal-ligand interactions are vulnerable

to competition from Au atoms on the electrode surface and are also likely to disrupt Au-Au junction formation. In the absence of sufficient steric or other protection, conductance measurements performed in the presence of such complexes may correspond to the intercalation of the soft moiety into the atomic contact.¹¹⁸

Next, we investigate the stability of the intramolecular neutral donor-acceptor bonding between the *3d* metal atoms and the pyridine N of the axial ligand (L). As shown in Figure 4.1, N is intermediate in its affinity for Au compared to the stronger S and the weaker O. Here, we examine the robustness of the pyridine N donor-acceptor bond to the *3d* metals (M(II) = Mn, Fe, Co, Ni, Zn) in the context of a single molecule BJ measurement on Au. Specifically, we explore whether the Lewis acidity of the *3d* metal can tune the intramolecular bond strength and improve the robustness of this interaction to outcompete the pyridine N donor-acceptor interaction with Au. We perform STMBJ conductance measurements at lower concentrations (< 0.01 mM) where the $1G_0$ disruption described above is minimized.

Log-binned conductance histograms from at least 5000 traces measured in these conditions for the heterobimetallic lantern series are plotted in Figure 4.3A.⁹⁵ A conductance peak at $\sim 10^{-2} G_0$ for all complexes was observed in this series, which coincides with the most likely conductance of pySMe. We note that the conductance histogram of the homobimetallic lanterns containing two axial ligands (Figure 4.2B) also displays a conductance signature at $10^{-2} G_0$ (Figure 4.2E and Figure 4.16). Next, we investigate whether the conductance signature is due to a junction with (1) the full lantern complex containing axial pySMe linkers or (2) the pySMe linker alone which detaches from the

lanterns and bridges the Au electrodes through the pyridine nitrogen and the thiomethyl linkers.

To distinguish between these two possibilities, we turn to two-dimensional (2D) conductance histograms. Such 2D histograms bin the log of the conductance versus electrode displacement relative to G_0 rupture, and can identify the length and binding geometry of the molecule in the junction.^{24, 29, 31} For example, the lengths of molecular signatures in 2D histograms have been shown to scale with the length of the molecular complex binding in the junction. Here, we compare the molecular plateau signatures measured in the presence of pySMe (N-S distance ~ 4.5 Å), a heterobimetallic compound containing one axial pySMe (**13**, Pt-SMe distance ~ 9 Å) and a homobimetallic complex containing two pySMe linkers (**14**, SMe-SMe distance ~ 16 Å) in 2D histograms plotted in Figure 4.3B, 4.3C and 4.3D respectively (see Figure 4.18 for length information). We observe that instead of scaling with molecular length, the maximal lengths of the plateaus for all three molecules are nearly identical, as marked by the dashed line. This close similarity of average conductance and plateau lengths across all measurements strongly suggests that the same molecule, the axial pySMe linker, is bridging the junction in all three cases.

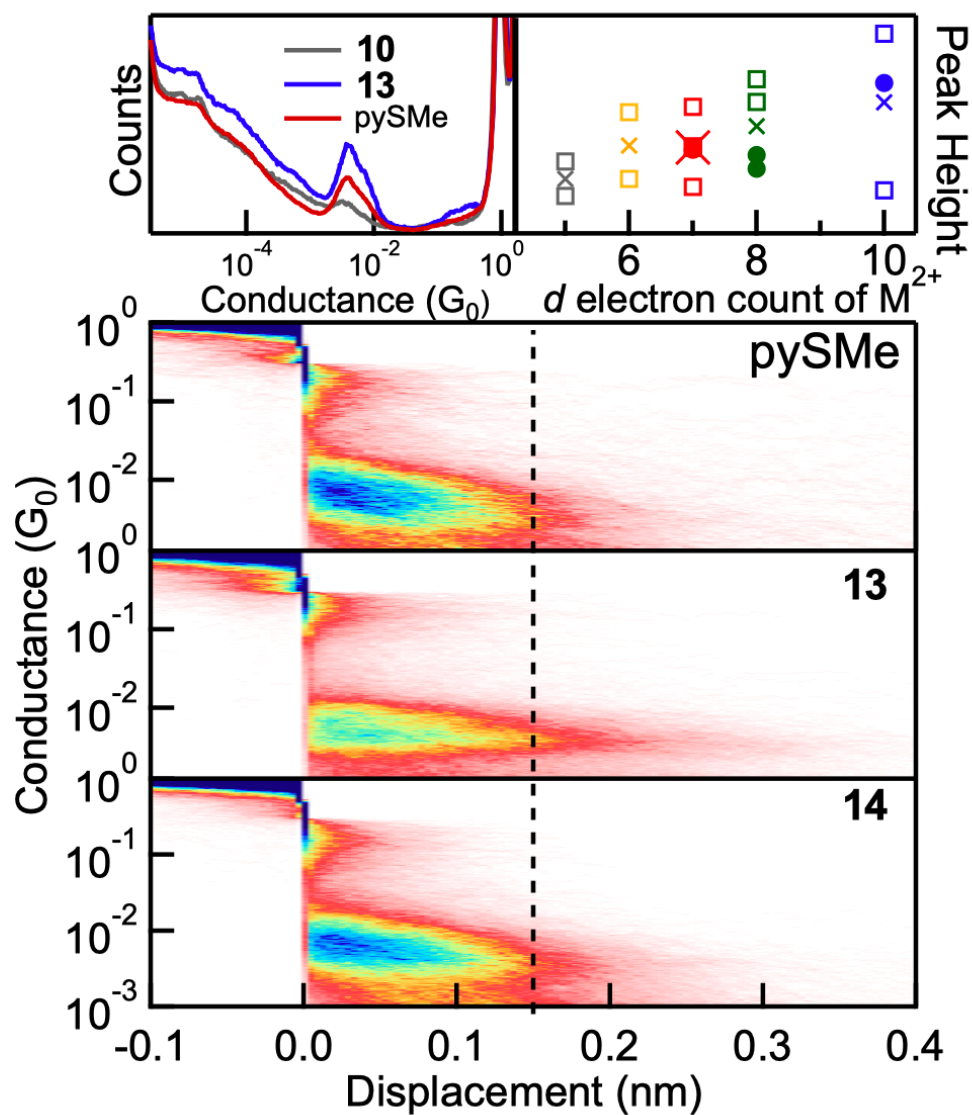


Figure 4.3. Logarithmically-binned 1D conductance histogram of pySMe and heterobimetallic complexes **10** and **13** measured at ~ 0.01 mM (A). 2D histograms of the pySMe axial ligand at 1 mM (B), **13** at 0.01 mM (C) and **14** at 1 mM (D). Peak height as a function of $3d$ metal for the SC(O)R complexes Mn (gray), Fe (yellow), Co (red), Ni (green), Zn (blue), R = Ph (squares), R = Me (circles) (E). The average over all experiments for each M is designated by an X.

To determine whether the synthetic tuning of the intramolecular $3d$ -M bond can strengthen the integrity of the complex on the Au electrodes, we examine the difference in the peak heights observed in the conductance histograms for this heterobimetallic lantern series (Figure 4.3A and Figure 4.19). To quantify the trend, we repeat measurements with each complex and measure the height of a signal obtained after 5000 or more traces by extracting the amplitude of a Gaussian fit. Measurements were also repeated with several previously synthesized SC(O)R lanterns, $[\text{PtM}(\text{SAc})_4(\text{pySMe})]$ ($M = \text{Co}, \text{Ni}, \text{Zn}$), differing only in the carboxylate R group ($R = \text{methyl}$).⁷⁵ As shown in Figure 4.3E, we observe that the height of the molecular conductance peak generally correlates with the d electron count of the $3d$ metal. This trend suggests that the variation in the number of counts observed is due to the relative Lewis acidity of the $3d$ metal and therefore the relative strength of the $3d$ metal-pyridine bond, where the complexes with the strongest link to the axial ligand result in fewer molecular plateaus, supporting hypothesis (2) above. We propose that the more electron deficient Mn(II), d^5 , is more strongly coordinated to the pySMe electron donor, leading to fewer pySMe-Au junctions measured than with Zn(II), d^{10} , as we observe here. These results point to the potential to synthetically tune the intramolecular interactions to increase the success rate of single molecule experiments with coordination complexes on metal electrodes.¹¹⁸

To further confirm that the conductance signature observed in Figure 4.3A corresponds to the pySMe axial linker alone, we perform DFT calculations to determine the binding interaction energies using Gaussian,¹¹⁹ and transport using FHI-Aims and AITRANSS (details in the experimental section).¹²⁰⁻¹²⁵ We determine binding energies of

the pySMe ligand to both the lantern complex and the Au electrodes (Table 4.2). Specifically, we find the binding energy of the M-pyridine bond, where M is either the 3*d* metal of the complex or the Au electrode, to be ~ 0.9 eV in both cases, confirming the similarity of these two bonds and the potential for ligand rearrangement in the junction. This binding energy is also comparable to that of M(II)-py bond dissociation energies.¹²⁶

DFT transport calculations can capture electron transport trends between molecules and distinguish the conductance signatures of the intact lantern from the axial ligand. We compare the transmission of the individual pySMe ligand and the closed-shell complex **5** (details in experimental section). We calculate transmission through the axial ligand bound to the Au electrodes through the pyridine N and the SMe group as shown in Figure 4.4A. The transmission, shown in red in Figure 4.4B, is consistent with the experimentally measured conductance $\sim 10^{-2} G_0$. To determine the transmission through the whole lantern complex we bind Au₃₇ pyramids to the S atom of the pySMe linker of the axial ligand on one side, and either the Pt or the S of the SC(O)R backbone on the other side as shown in Figure 4.3A. The relaxed structures of the molecular junctions with the lanterns and transmission through these junctions as a function of energy are shown in Figure 4.4A and 4.4B respectively. The transmission through the entire lantern complex **13**, with R = Me instead of Ph, bound through either the Pt or the S, is two to three orders of magnitude lower than that of the pySMe ligand at around $10^{-5} G_0$. This difference indicates that the conductance signature at $10^{-2} G_0$ observed is due to the individual pySMe molecule and not the intact lantern complex. It should be noted that we have not observed a convincing conductance feature at the $10^{-5} G_0$ conductance range, as can be seen in the log-binned

histograms in Figure 4.3A, further indicating that the pySMe ligand does not remain bound to the 3d metal in our experiments. These transport calculations support the hypothesis that the axial ligand comes off during break-junction measurements of the lanterns.

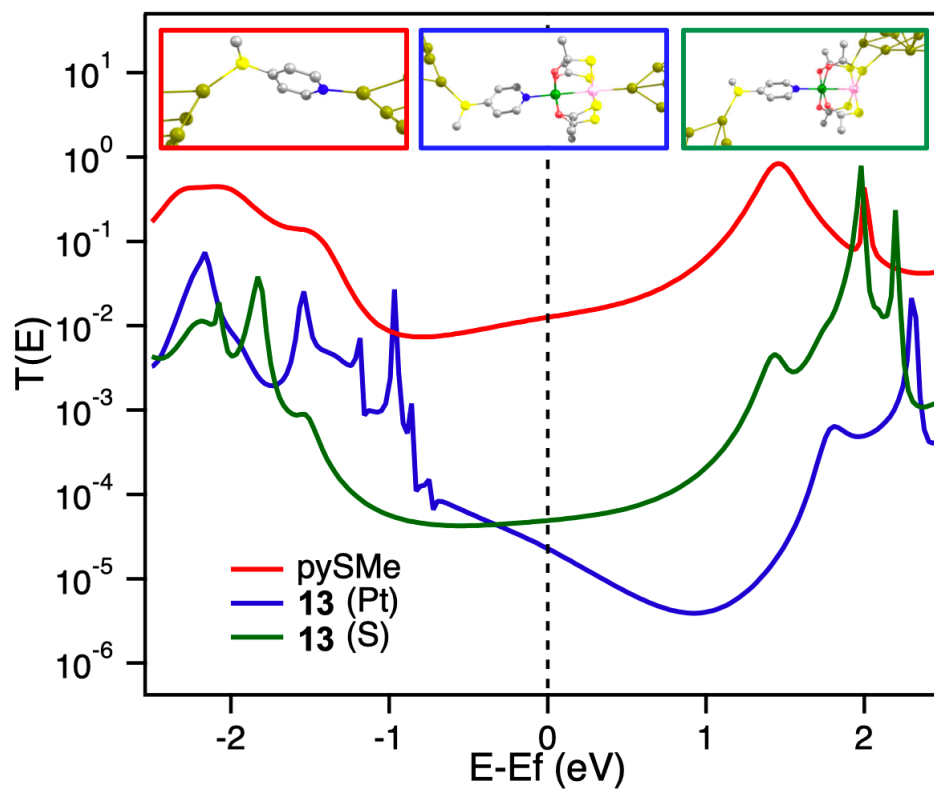


Figure 4.4. (A) Relaxed structures and (B) transmission spectra of pySMe (red) and the entire lantern complex **13** with R = Me bound through the Pt (blue) or S of backbone (green) to Au₃₇ electrodes.

Our measurements suggest that the Au-linker interactions, specifically the M-thioether and M-pyridine donor-acceptor bonds with under-coordinated Au in the electrodes, compete with the pyridine coordination to the 3d metal. Therefore, we formulate our *third* design rule: Au-linker interactions with the Lewis basic N-donor can outcompete intramolecular donor-acceptor metal ligand bonding in transition metal complexes. Nevertheless, we see evidence that increasing the Lewis acidity of the 3d metal can help stabilize the metal-linker bond relative to linker-Au bonds and propose that including an anionic axial ligand may further increase stability of coordination complexes in the Au junction.

4.4. Conclusions

Our results establish HSAB theory as a predictive framework for understanding the formation of molecule-metal junctions with various lone-pair donors on Au and the compatibility of coordination complex designs with gold electrodes. Specifically, we summarize our findings with three design rules for metal-molecule junction formation. First, (1) HSAB chemistry principles utilized for intramolecular binding in metal complexes can also govern the formation, robustness and selectivity of organic metal-molecule junctions formed on Au, which is a soft metal. This similarity between the intra and inter-molecular bonding of coordination complexes on Au electrodes, which is not present with organic molecular wires, results in competition by Au for organic ligands. Thus, (2) soft-soft metal ligand interactions, such as the Pt-S in the thiocarboxylate-based

lanterns, are vulnerable to competition from the soft Au which leads to the disruption of the complex and to the formation of Au-S bonds evident in conductance histograms as disruption of $1 G_0$ signatures; ultimately, this competition prevents reproducible conductance measurements of such complexes. Thirdly, (3) even for N which is a neutral Lewis basic donor intermediate on the hard-soft continuum, the Au-ligand bonding can outcompete intramolecular donor-acceptor M-N bonding in transitional metal complexes, though synthetic tuning does help stabilize the complex against competition from Au. These principles suggest several requirements for incorporating coordination complexes into molecular circuits. Careful design and selection of linker groups, donor atoms and metal ions is needed to ensure that Au interactions do not compete with the intramolecular bonding of the complex. We propose these design rules as guidance for the synthesis of coordination complexes for the robust assembly of molecular junctions for molecular electronics or spintronics.

4.5. Experimental

4.5.1. Materials and Methods

Complexes [PtM(tba)₄(OH₂)] were prepared via previously reported methods.⁷⁷ Elemental analyses were performed by Atlantic Microlab Inc. (Norcross, GA). UVvis-NIR spectra were measured with a Shimadzu UV-3600 spectrometer. ¹H-NMR measurements were recorded on a Varian 500 MHz spectrometer. Evans' method solution magnetic susceptibility measurements were performed for the paramagnetic compounds **6** and **10-12**.^{84, 127}

4.5.2. X-ray Crystallography Methods

Data collection, solution, and refinement were performed by Prof. Arnold Rheingold at the University of California-San Diego. Crystals of **6** and **10-15** were mounted on a Cryoloop with Paratone N oil, and data were collected at 100 K on a Bruker Proteum-R with a CCD detector using Mo K α radiation. Crystal data collection and refinement parameters for all compounds are reported in Table 4.1. Data were corrected for absorption with SADABS and structures were solved by direct methods. All non-hydrogen atoms were refined anisotropically by full matrix least-squares on F^2 .

4.5.3. STMBJ Measurements

Break junction measurements were performed using a home-built STMBJ and experimental protocols established previously.^{23, 24, 29, 128} A Au tip and substrate are brought

together, forming a metallic contact. The junction is then stretched apart at 16 nm/s, while current is recorded under a constant bias of 500 mV. Measurements on clean Au show steps at integer values of G_0 until contact is broken.²⁷ These steps correspond to the formation of Au contacts with integer number of Au atoms in the junction cross-section. Thousands of conductance traces showing the evolution of a junction as a function of displacement are compiled into histograms without data selection and normalized to enable comparison. After the Au contact is broken, a nano-gap is formed between two newly ruptured rough Au electrodes which can interact with molecules in solution.^{24, 129} To measure molecular conductance signatures, crystals of purified lantern complexes are dissolved in 1,2,4-trichlorobenzene (Sigma Aldrich #296104) and diluted to a range of concentrations of 1 mM and < 0.01 mM. The above STMBJ measurement protocol is then repeat in the presence of the molecular solution.

4.5.4. DFT Calculations

DFT calculations for binding energies with Au electrodes were performed with Gaussian with a PBE exchange correlation functional and a Def2-TZVP basis set.^{119, 130, 131} DFT transport calculations were performed with FHI-aims and AITRANS with a PBE exchange correlation functional under the “tight” level basis set.^{120-124, 130} The diamagnetic complex, **5** and the pySMe axial ligand, were each relaxed with various size Au electrodes to ensure convergence. Only the positions of the molecule and apex Au atoms (2 layers) were allowed to relax. After relaxation, interaction energies between the molecule and the

Au electrodes as well as transmission across the junction as a function of energy at zero bias were calculated with Nonequilibrium Greens Function using AITRANSS.

4.5.5. Synthesis and Structure

A new series of $[\text{PtM}(\text{tba})_4(\text{pySMe})]$ ($\text{M} = \text{Mn}$ (**10**), Fe (**6**), Co (**11**), Ni (**12**), Zn (**13**)) complexes with a thiobenzoate (tba) chelating backbone ligand and a thiomethylpyridine (pySMe) axial ligand has been synthesized using protocols established previously.^{73, 75} Briefly, we rely on hard-soft acid-base principles to selectively coordinate the soft S to the soft Pt, and the O to the harder $3d$ metal. Two new homobimetallic lantern complexes with carboxylate backbones and the same terminal linker group were synthesized to enable comparison between complexes with S and O donor atoms. These are $[\text{Cu}_2(\text{OAc})_4(\text{pySMe})_2]$ (**14**) (OAc = acetate) and $[\text{Co}_2(\text{esp})_2(\text{pySMe})_2]$ (**15**) (esp = $\alpha, \alpha', \alpha', \alpha'$ -tetramethyl-1,3 benzenedipropionate), an analogue of a $[\text{Co}_2(\text{esp})_2(\text{EtOH})_2]$ lantern previously reported.^{132, 133} Complexes $[\text{PtM}(\text{SAc})_4(\text{pySMe})]$ ($\text{M} = \text{Co}, \text{Ni}, \text{Zn}$) were previously published and synthesized from reported methods.⁷⁵

*Synthesis of $[\text{PtMn}(\text{tba})_4(\text{pySMe})]$ (**10**)*

$[\text{PtMn}(\text{tba})_4(\text{OH}_2)]$ (79 mg, 0.097 mmol) was prepared and dissolved in ~ 5 mL of acetone. While stirring, pySMe (12 mg, 0.097 mmol) was added dropwise in ~ 5 mL acetone. After stirring for 2 hours, the yellow precipitate was collected via vacuum filtration. Yellow crystals were obtained from CH_2Cl_2 and hexanes vapor diffusion. Yield 47%. Anal. Calc'd. for $\text{PtMnC}_{34}\text{H}_{27}\text{NO}_4\text{S}_5$: C, 44.20; H, 2.95; N, 1.52%. Found: C, 44.27;

H, 2.87; N, 1.55%. UV-vis-NIR (CH_2Cl_2) (λ_{max} , nm (ϵ_{M} , $\text{cm}^{-1} \text{M}^{-1}$): 249(136,740), 278(106,435), 315(79,087). Evans method (CD_2Cl_2): 5.92 μ_{B} .

Synthesis of [PtFe(tba)₄(pySMe)] (6)

The same procedure as **10** was used with corresponding starting complex [PtFe(tba)₄(OH₂)]. The dark red precipitate was collected via vacuum filtration. Dark red crystals were obtained from CH_2Cl_2 layered with hexanes. Yield 33%. Anal. Calc'd. for PtFeC₃₄H₂₇NO₄S₅: C, 44.16; H, 2.94; N, 1.51%. Found: C, 44.21; H, 2.88; N, 1.60%. UV-vis-NIR (CH_2Cl_2) (λ_{max} , nm (ϵ_{M} , $\text{cm}^{-1} \text{M}^{-1}$): 249(89,966), 275(68,659), 310(49,422), 486(356) 966(7). Evans method (CD_2Cl_2): 6.06 μ_{B} .

Synthesis of [PtCo(tba)₄(pySMe)] (11)

The same procedure as **10** was used with corresponding starting complex [PtCo(tba)₄(OH₂)]. Purple precipitate was collected via vacuum filtration. Purple crystals were obtained from CH_2Cl_2 layered with hexanes. When analyzed under high optical magnification, two highly dichroic polymorphs were observed: one (reported here) is yellow/blue, the other is pink/purple. The second polymorph was more disordered, but contains the same lantern structure, and is not included herein. (C_2 , $a = 24.5950(19) \text{ \AA}$, $b = 11.4980(7) \text{ \AA}$, $c = 26.8216(17) \text{ \AA}$, $\alpha = 90^\circ$, $\beta = 116.654(4)^\circ$, $\gamma = 90^\circ$, $V = 6778.9(8) \text{ \AA}^3$) Yield 70%. Anal. Calc'd. for PtCoC₃₄H₂₇NO₄S₅: C, 44.01; H, 2.93; N, 1.51%. Found: C, 43.96; H, 3.09; N, 1.54%. UV-vis-NIR (CH_2Cl_2) (λ_{max} , nm (ϵ_{M} , $\text{cm}^{-1} \text{M}^{-1}$): 252(51,625), 284(45,125), 319(30,250), 502(183) 1300(4). Evans method (CD_2Cl_2): 5.79 μ_{B} .

Synthesis of [PtNi(tba)₄(pySMe)] (12)

The same procedure as **10** was used with corresponding starting complex [PtNi(tba)₄(OH₂)]. Green precipitate was collected via vacuum filtration. Green crystals were obtained from CH₂Cl₂ and hexanes vapor diffusion. Yield 64 %. Anal. Calc'd. for PtNiC₃₄H₂₇NO₄S₅: C, 44.02; H, 2.93; N, 1.51%. Found: C, 43.83; H, 2.95; N, 1.54%. UV-vis-NIR (CH₂Cl₂) (λ_{max} , nm (ϵ_{M} , cm⁻¹ M⁻¹)): 246(82,893), 274(76,226), 316(38,867) 668(16) 1165(12). Evans method (CD₂Cl₂): 3.08 μ_{B} .

Synthesis of [PtZn(tba)₄(pySMe)] (13)

The same procedure as **10** was used with corresponding starting complex [PtZn(tba)₄(OH₂)]. White precipitate was collected via vacuum filtration. Off-white crystals were obtained from CH₂Cl₂ and hexanes vapor diffusion. Yield 32%. Anal. Calc'd. for PtZnC₃₄H₂₇NO₄S₅: C, 43.71; H, 2.91; N, 1.50%. Found: C, 43.66; H, 2.90; N, 1.50%. UV-vis-NIR (CH₂Cl₂) (λ_{max} , nm (ϵ_{M} , cm⁻¹ M⁻¹)): 247(50,377), 279(41,116), 316(30,884). ¹H NMR (δ , ppm {CD₂Cl₂}: 2.68 (s), 7.35 (t), 7.47 (t), 7.58 (d), 8.05 (d), 9.01 (d).

Synthesis of [Cu₂(OAc)₄(pySMe)₂] (14)

Cu(OAc)₂ hydrate (22 mg, 0.11 mmol) was dissolved in 10 mL 1:1 H₂O and acetonitrile mixture. The pySMe (14 mg, 0.11 mmol) was dissolved in 5 mL of methanol and added dropwise. After stirring for 24 hours, the solvent was removed. Blue-green needles suitable for X-ray analysis were obtained from CH₂Cl₂ layered with hexanes. Yield 61%. Anal. Calc'd. for Cu₂C₂₀H₂₆N₂O₈S₂: C, 39.15; H, 4.27; N, 4.57%. Found: C, 39.12;

H, 4.14; N, 4.57%. UV-vis-NIR (CH₂Cl₂) (λ_{max} , nm (ϵ_{M} , cm⁻¹ M⁻¹)): 266(438,982), 378(201), 720(586).

Synthesis of [Co₂(esp)₂(pySMe)₂] (15)

This complex was prepared by Claire May based on literature procedures for [Co₂(esp)₄(EtOH)₂].¹³² CoCO₃ hydrate (10 mg, 0.08 mmol), esp ($\alpha,\alpha,\alpha',\alpha'$ -tetramethyl-1,3 benzenedipropionate) (22.2 mg, 0.08 mmol) and pySMe (20 mg, 0.16 mmol) were dissolved in 10 mL ethanol and transferred to a Teflon container, sealed in an autoclave and heated in a programmable oven from RT to 75 °C over 1 hour, held for 8 hours, then cooled to RT over 48 hours, yielding to purple crystals. Yield 83%. Anal. Calc'd. for Co₂C₄₄H₅₄N₂O₈S₂: C, 57.39; H, 5.91; N, 3.04%. Found: C, 57.16; H, 5.90; N, 2.96%. UV-vis-NIR (CH₂Cl₂) (λ_{max} , nm (ϵ_{M} , cm⁻¹ M⁻¹)): 266(30,400) 444(333), 566(199) 1285(3).

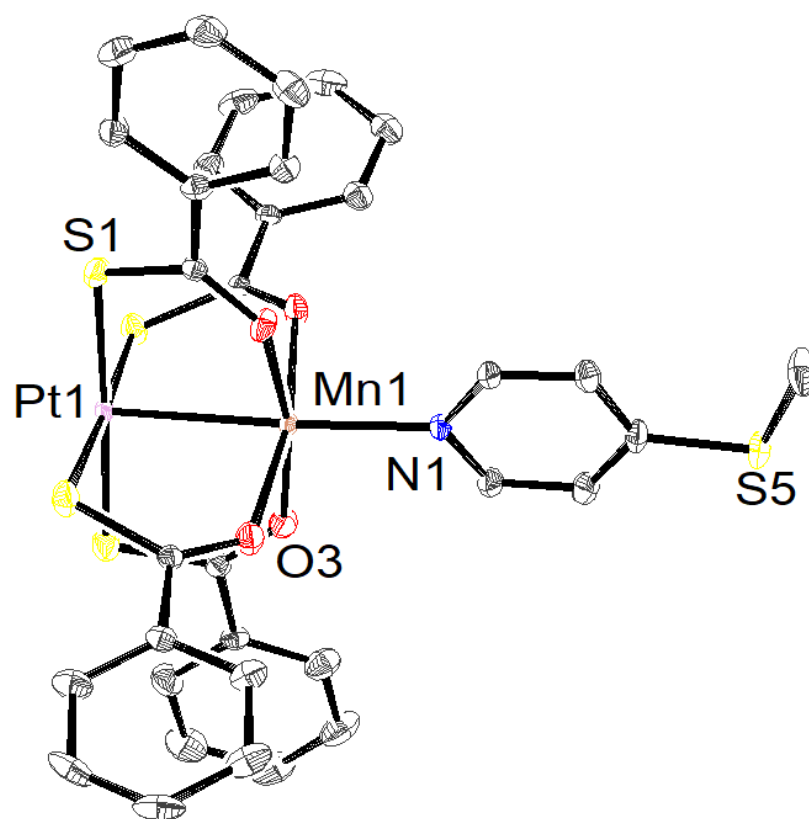


Figure 4.5. ORTEP of [PtMn(tba)₄(pySMe)] (10). Ellipsoids are drawn at the 50% probability level and hydrogen atoms are omitted for clarity.

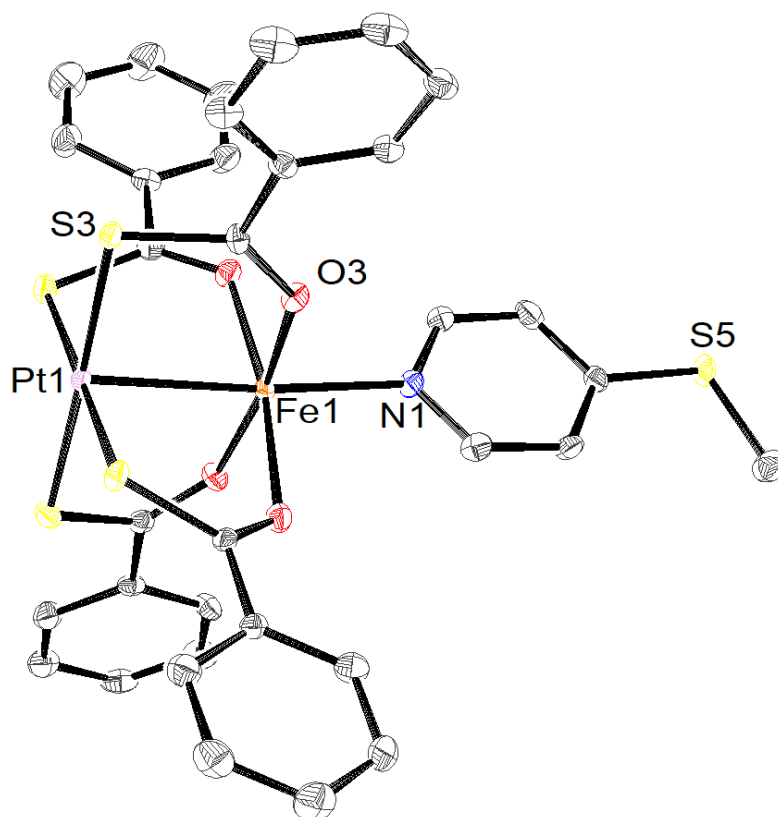


Figure 4.6. ORTEP of $[\text{PtFe}(\text{tba})_4(\text{pySMe})]$ (**6**). Ellipsoids are drawn at the 50% probability level and hydrogen atoms are omitted for clarity.

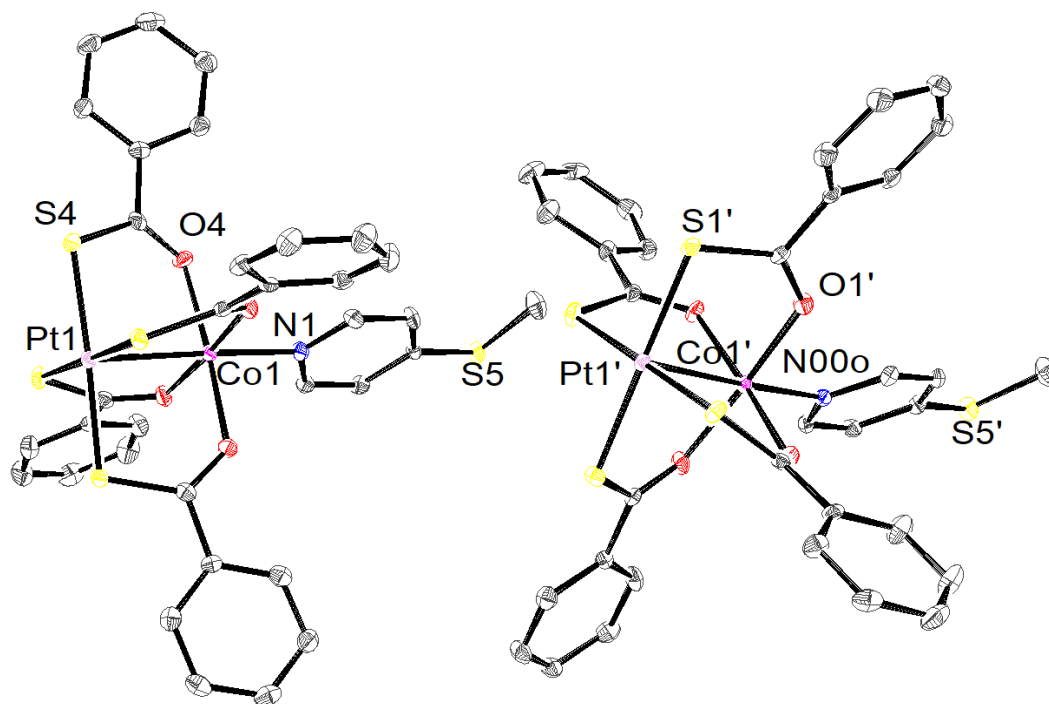


Figure 4.7. ORTEP of [PtCo(tba)₄(pySMe)] (**11**). Ellipsoids are drawn at the 50% probability level and hydrogen atoms are omitted for clarity. There are two independent molecules in the asymmetric unit.

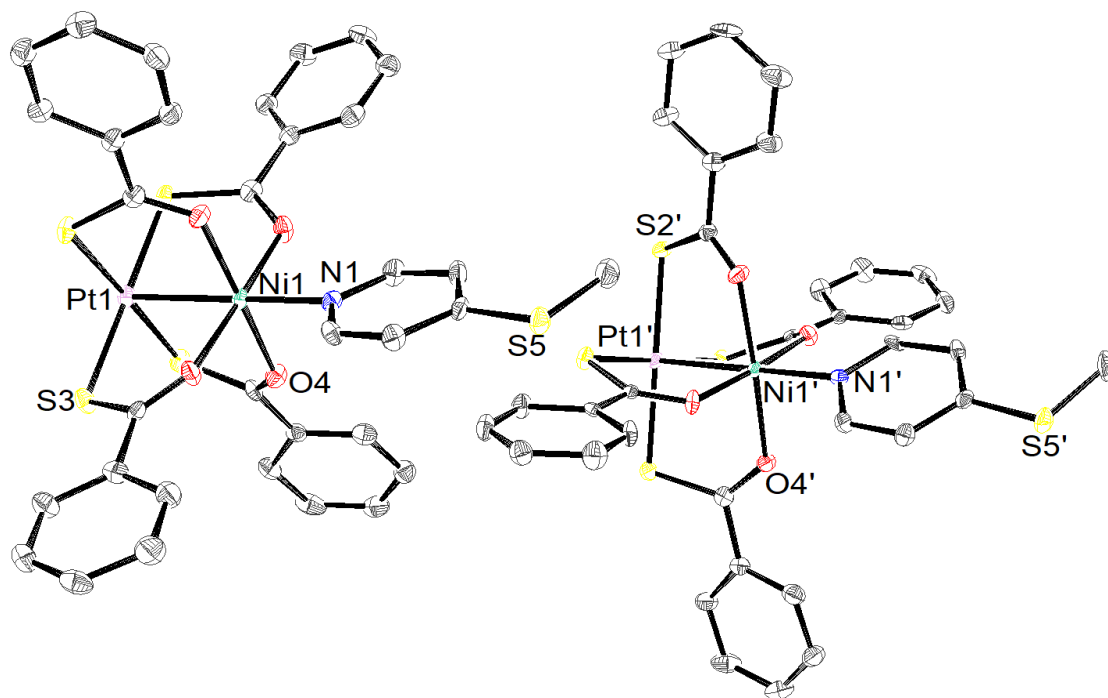


Figure 4.8. ORTEP of [PtNi(tba)₄(pySMe)] (**12**). Ellipsoids are drawn at the 50% probability level and hydrogen atoms are omitted for clarity. There are two independent molecules in the asymmetric unit.

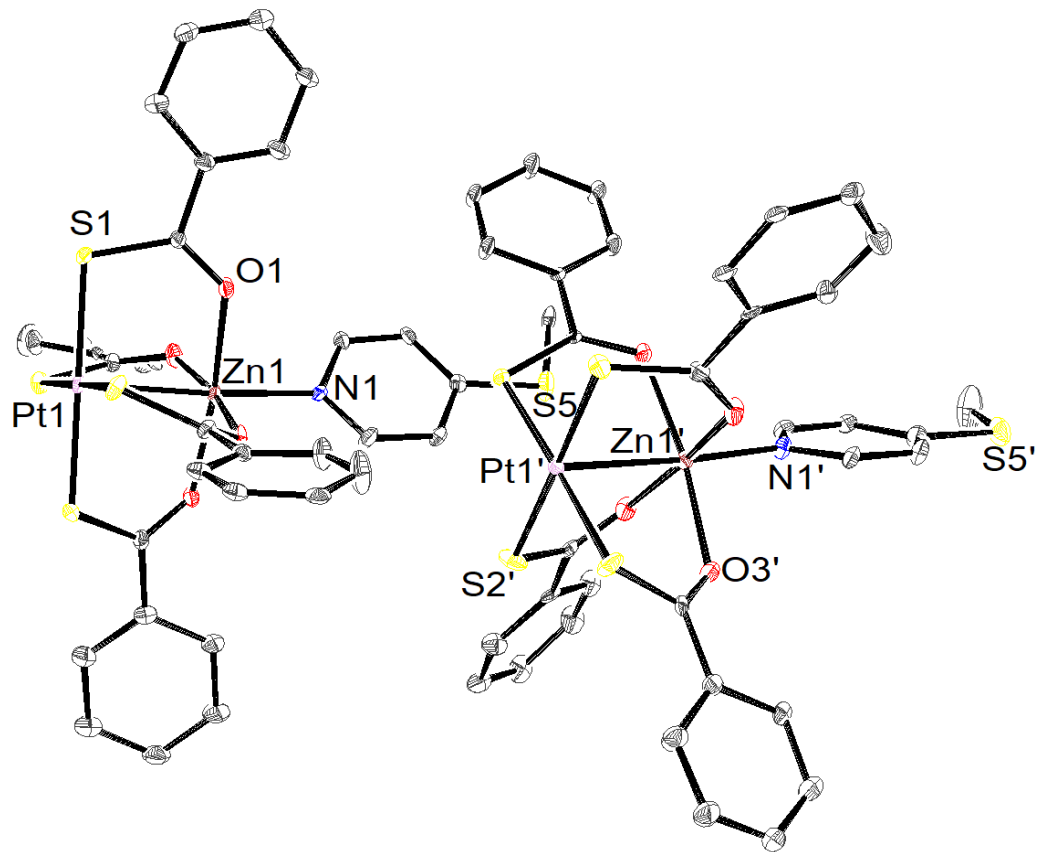


Figure 4.9. ORTEP of [PtZn(tba)₄(pySMe)] (13). Ellipsoids are drawn at the 50% probability level and hydrogen atoms are omitted for clarity. There are two independent molecules in the asymmetric unit.

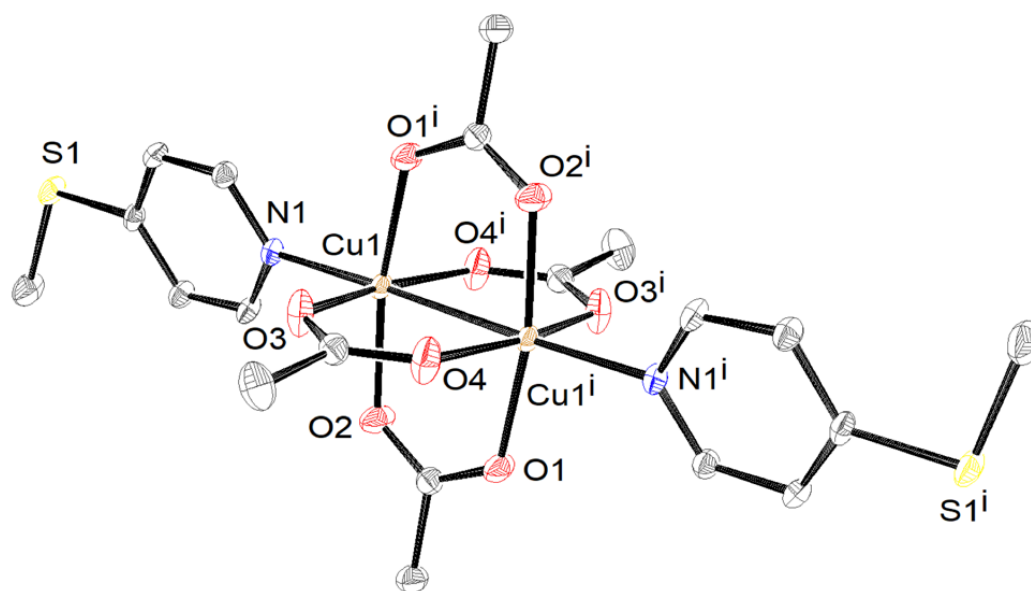


Figure 4.10. ORTEP of [Cu₂(OAc)₄(pySMe)₂] (**14**). Ellipsoids are drawn at the 50% probability level and hydrogen atoms are omitted for clarity. An inversion center relates the two halves of this compound.

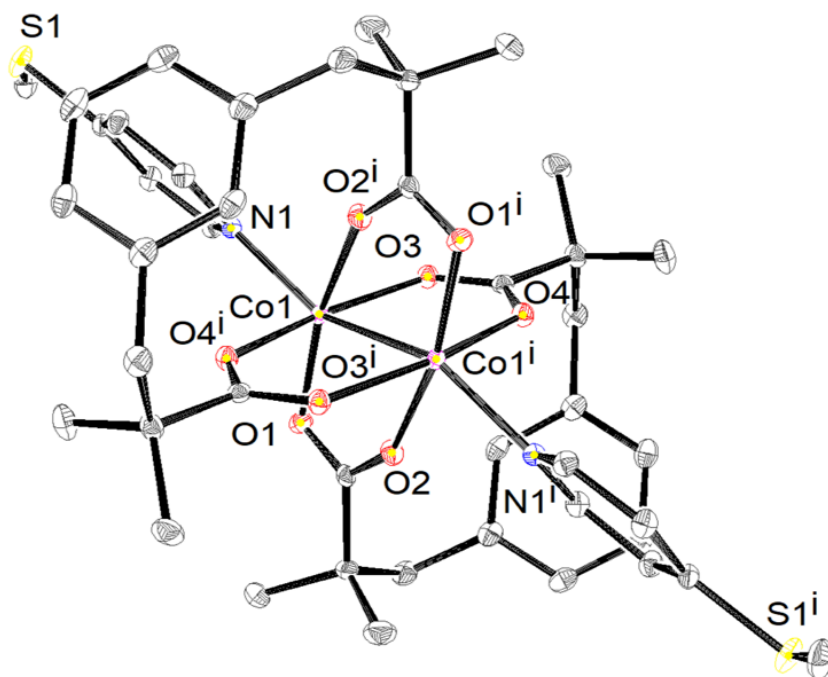


Figure 4.11. ORTEP of [Co₂(esp)₂(pySMe)₂] (**15**). Ellipsoids are drawn at the 50% probability level and hydrogen atoms are omitted for clarity. An inversion center relates the two halves of the molecule.

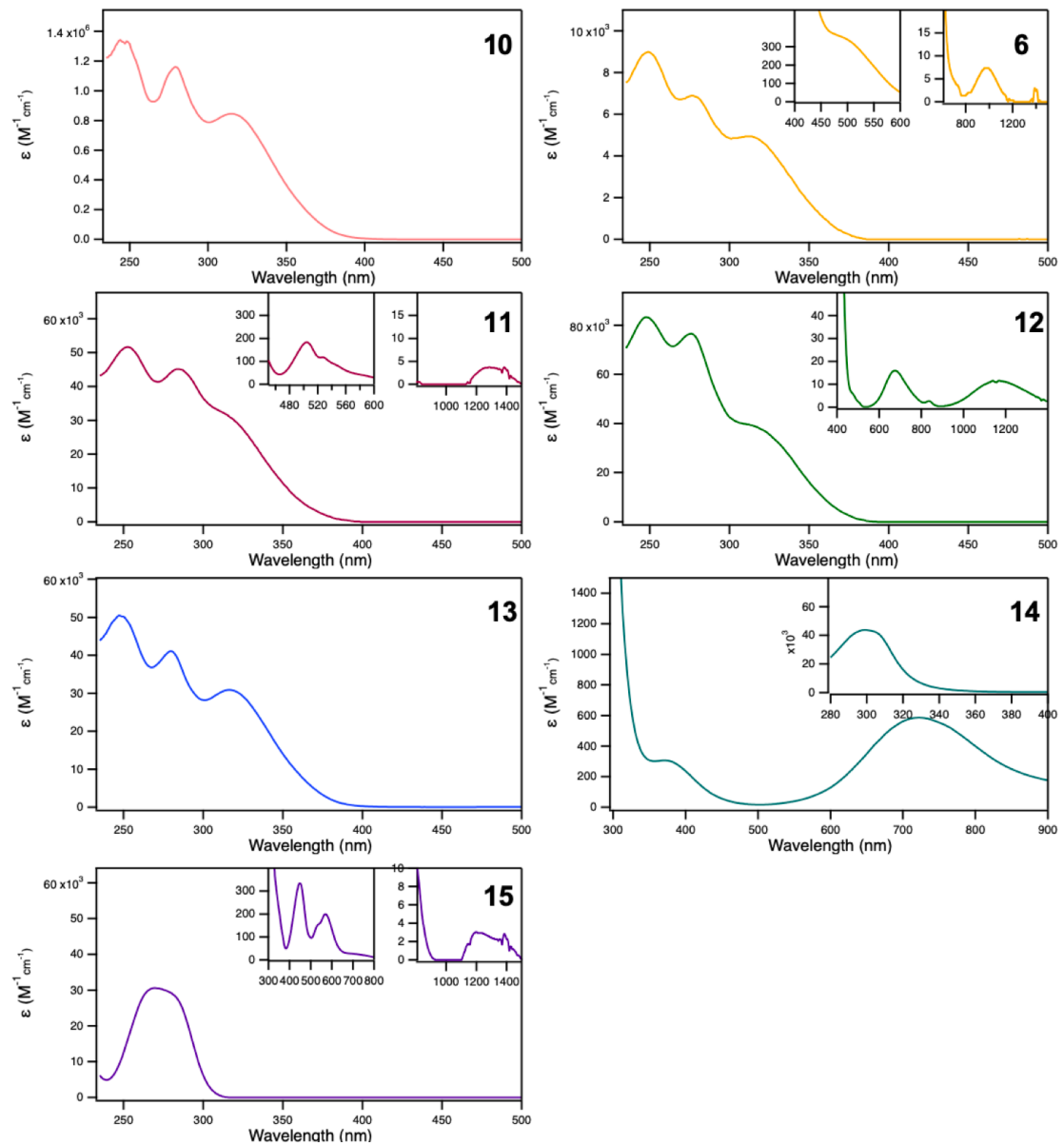


Figure 4.12. UV-vis-NIR spectra of compounds **6**, **10-15** in CH_2Cl_2 .

Table 4.1. Single crystal X-ray diffraction collection parameters for **6, 10-15**

Complex	10	6	11	12	13	14	15
Formula	C ₃₄ H ₂₇ MnNO ₄ PtS ₅	C ₃₄ H ₂₇ FeNO ₄ PtS ₅	C ₃₄ H ₂₇ CoNO ₄ PtS ₅	C ₃₄ H ₂₇ NiNO ₄ PtS ₅	C ₃₄ H ₂₇ ZnNO ₄ PtS ₅	C ₂₁ H ₂₈ Cl ₂ Cu ₂ N ₂ O ₈ S ₂	C ₄₄ H ₅₄ Co ₂ N ₂ O ₈ S ₂
Formula weight	923.89	924.80	927.88	927.66	934.32	698.55	920.87
Crystal system	Triclinic	Triclinic	Triclinic	Triclinic	Monoclinic	Triclinic	Triclinic
Color	Yellow	Red	Yellow/blue (dichroic)	Green	Off-white	Blue/green	Dark red
Space group	<i>P</i> -1	<i>P</i> -1	<i>P</i> -1	<i>P</i> -1	<i>C</i> ₂	<i>P</i> -1	<i>P</i> -1
<i>a</i> , Å	11.461(2)	11.3489(14)	11.1572(12)	11.162(2)	24.5369(16)	9.4266(5)	9.8093(7)
<i>b</i> , Å	12.282(2)	12.3796(18)	12.9913(14)	12.917(3)	11.5157(8)	12.0866(7)	10.1132(6)
<i>c</i> , Å	13.588(2)	13.5186(18)	24.488(3)	24.455(5)	26.5771(18)	13.06505(8)	12.6559(8)
<i>α</i> , deg	67.008(2)	67.501(4)	82.638(2)	82.593(4)	90	82.464(2)	112.795(2)
<i>β</i> , deg	74.931(2)	74.667(4)	81.849(2)	82.073(4)	115.422(3)	72.781(2)	106.901(2)
<i>γ</i> , deg	77.571(3)	76.735(5)	73.192(2)	73.647(3)	90	76.936(2)	94.678(2)
<i>V</i> , Å ³	1686.2(5)	1674.6(4)	3349.2(6)	3335.7(12)	6782.5(8)	1443.67(14)	1080.29(12)
<i>Z</i> , <i>Z'</i>	2, 1	2, 1	4, 2	4, 2	8, 1	2, 1	1, 1
<i>ρ</i> (calcd), mg/cm ³	1.820	1.834	1.840	1.847	1.830	1.607	1.415
Absorption coefficient mm ⁻¹	4.867	4.957	5.019	5.107	5.175	1.848	0.919
<i>temp</i> , K	100	100	100.0	100	100	100	100
<i>R</i> (<i>F</i>), % ^a	0.0464	0.0399	0.0370	0.0437	0.0567	0.0352	0.0255
<i>R</i> (<i>wF</i> ²), % ^b	0.1098	0.1094	0.0713	0.0798	0.1456	0.0927	0.0613

4.6. Additional Data

Linear binned conductance histogram of Figure 4.2:

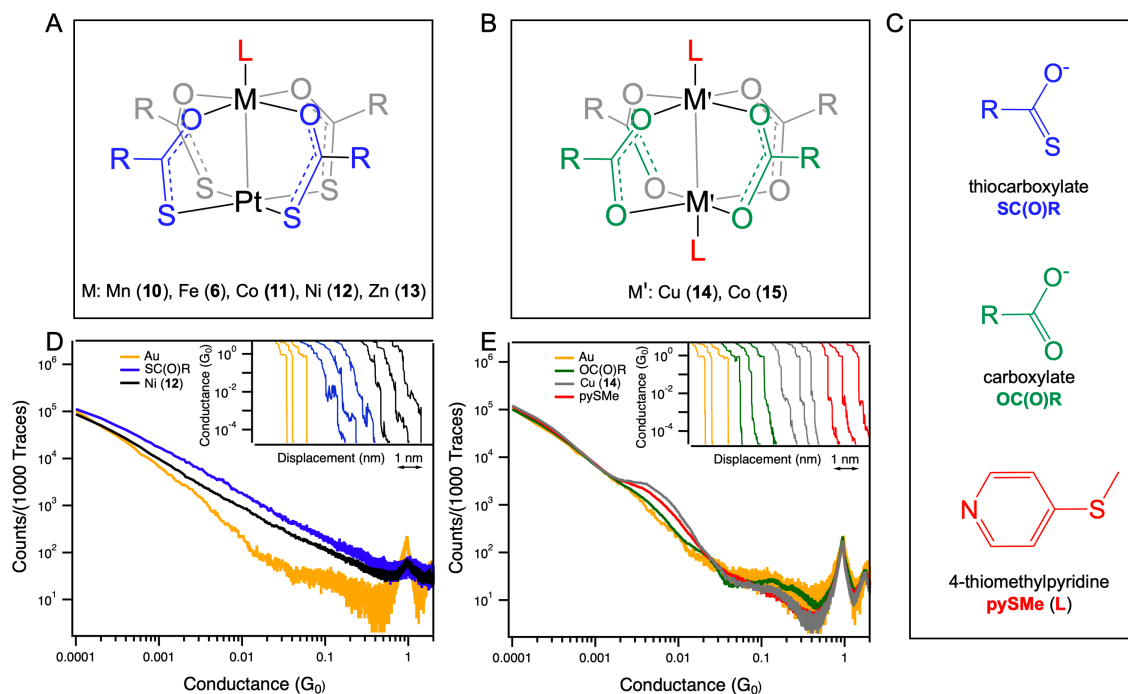


Figure 4.13. (A) Schematics of heterobimetallic lantern frameworks with SC(O)R backbone ligands R = Ph (B) homobimetallic lantern frameworks with OC(O)R backbone ligands, R = Me (14), for (7) OC(O)R= esp (15). All complexes have pySMe (L) axial ligands. (C) Molecular structures of the individual ligands. (D) Conductance histograms and sample traces (inset) of 1 mM measurements of SC(O)R as thiobenzoic acid and of 12 in TCB. (E) Conductance histograms and sample traces (inset) of 1mM OC(O)R as benzoic acid, pySMe, and 14 in TCB.

Measurements of SC(O)R lantern complexes (**6**, **10-15**) at 1 mM in TCB are shown in Figure 4.14. The amplitude of the G_0 peak is decreased compared to the Au control and the background at lower conductance values is increased as shown. The behavior of these SC(O)R lantern complexes at 1 mM concentrations is consistent and not dependent on the $3d$ metal.

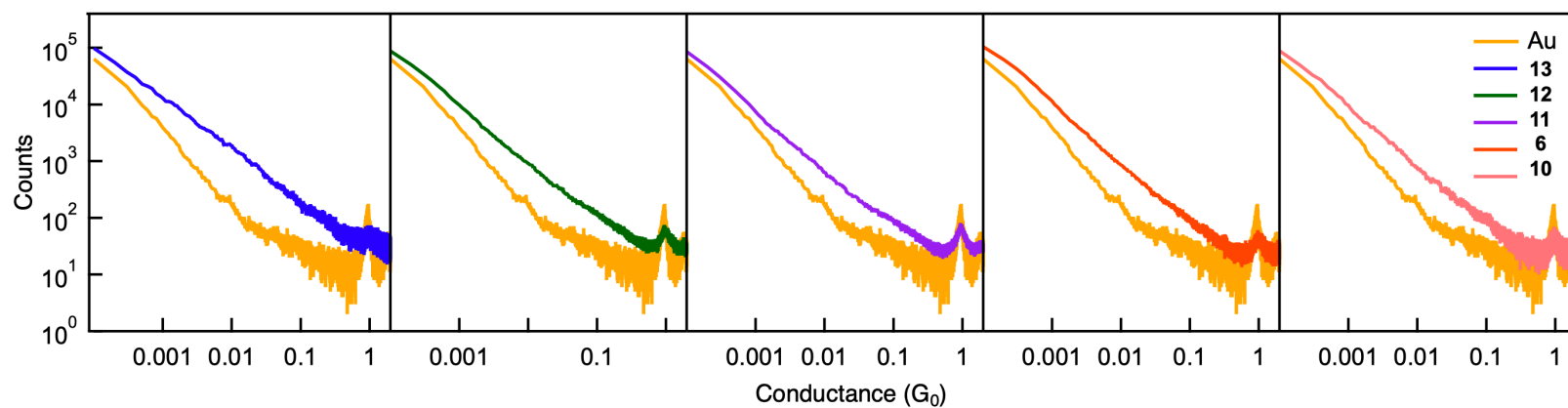


Figure 4.14 1D conductance histograms of heterobimetallic lantern complexes **13**, **12**, **11**, **6**, **10** (left to right) at 1 mM concentrations compared to the clean Au control.

To confirm that the S of the SC(O)R backbone ligands was the source of the G_0 inference and various conductance plateaus as a broad range of conductance values, another lantern complex with S donor backbone ligands was measured. The homobimetallic complex $[\text{Pt}_2(\text{mpy})_4]$ with S and N donor atoms was prepared from previously reported methods.¹¹⁷ The resulting histogram is shown in Figure 4.15. These complexes behave similarly behavior to the SC(O)R heterobimetallic complexes in that they diminish the G_0 plateaus.

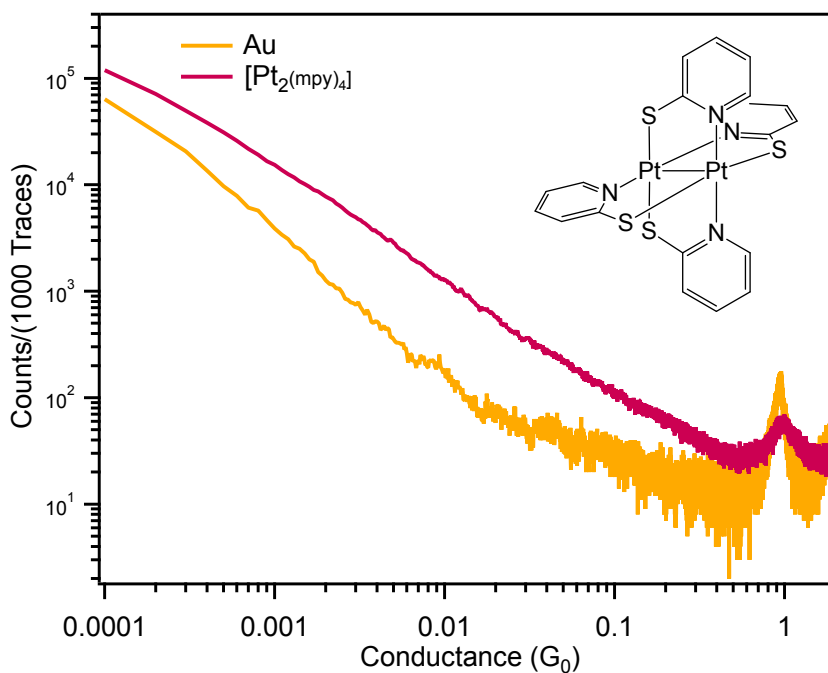


Figure 4.15. Conductance histogram of 1 mM $[\text{Pt}_2(\text{mpy})_4]$ homobimetallic lantern complex.

Conductance measurements of an additional homobimetallic lantern complex (**7**) are shown in Figure 4.17. The conductance of this complex is similar to that of the pySMe ligand, as observed for complex **15** and shown in the log-binned histogram (Figure 4.17A). The length of the conductance feature in the 2D histogram is also consistent with the axial ligand itself instead of the entire complex (Figure 4.17B). The structure of complex **15** is shown in Figure 4.17C.

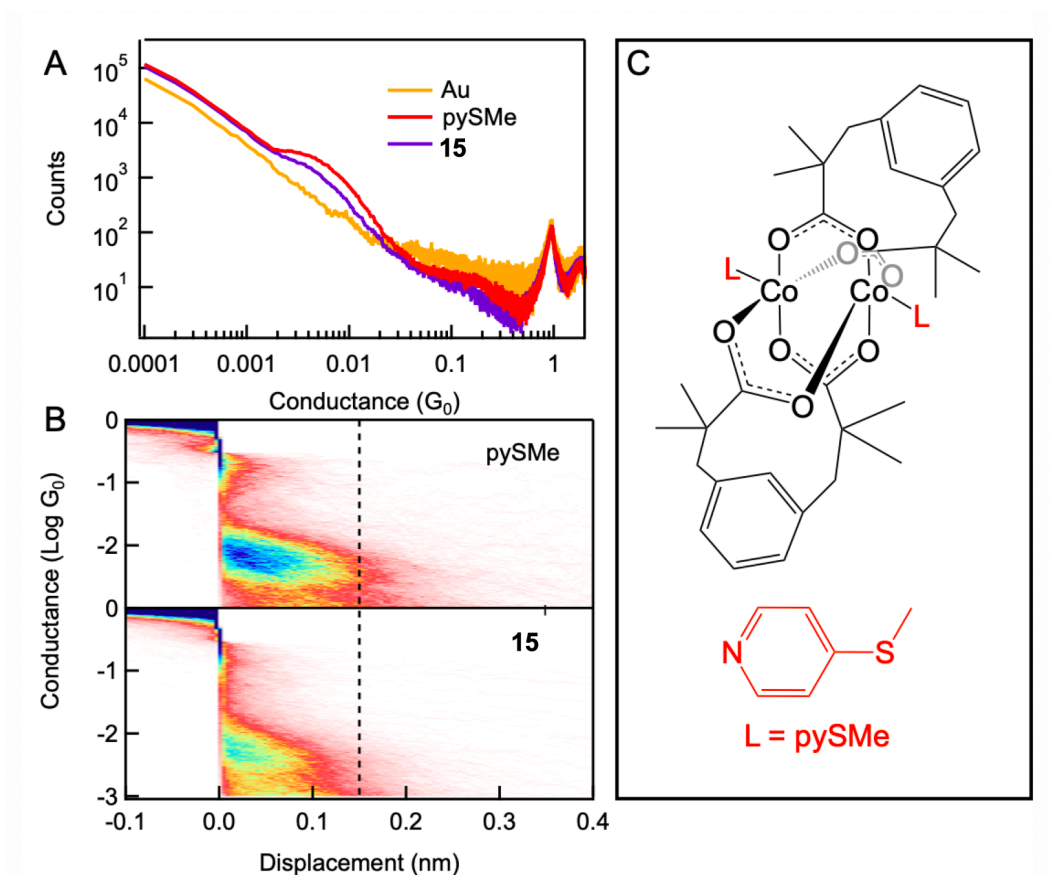


Figure 4.16. Log-binned 1D (A) and 2D (B) conductance histograms of homobimetallic complex **15** compared to the individual axial ligand (pySMe). Structure for lantern complex (C).

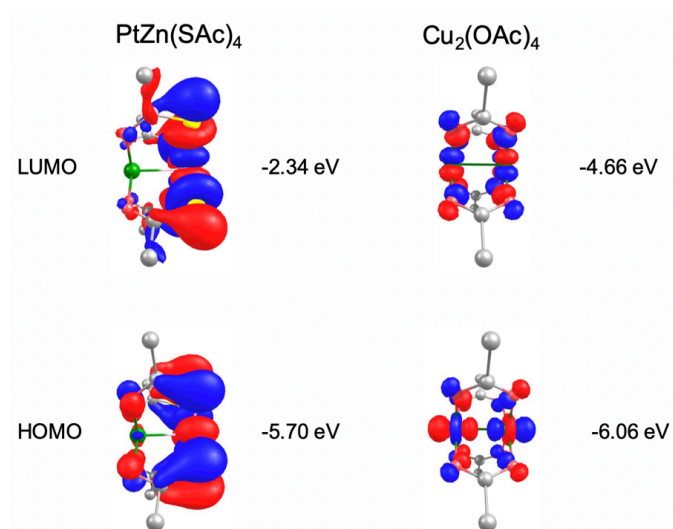


Figure 4.17. Isosurface plots of PtZn(SAc)_4 with SC(O)R backbone ligands and $\text{Cu}_2(\text{OAc})_4$ with OC(O)R backbone ligands at PBE/Def2-TZVP level of theory.

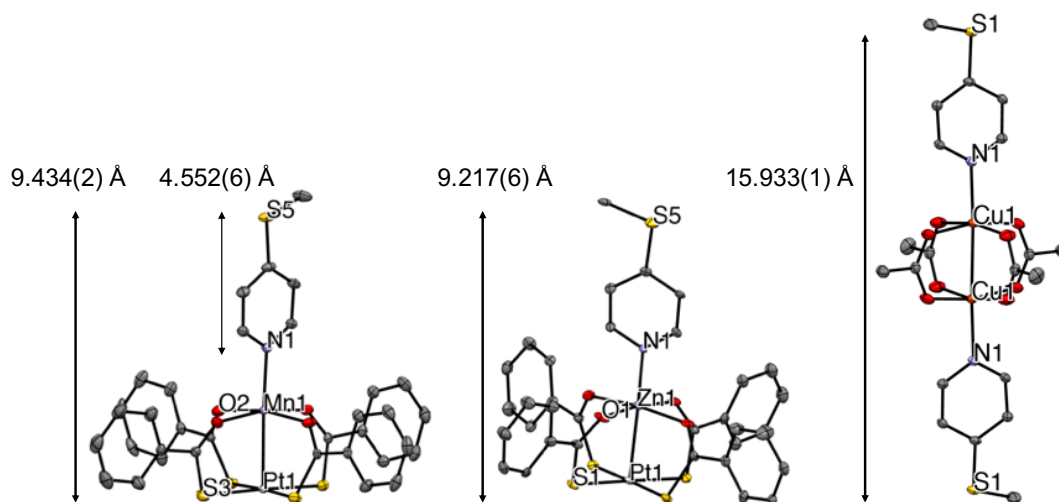


Figure 4.18. Mercury representations of **10**, **13**, and **14** showing distances relative to pySMe. H atoms removed.

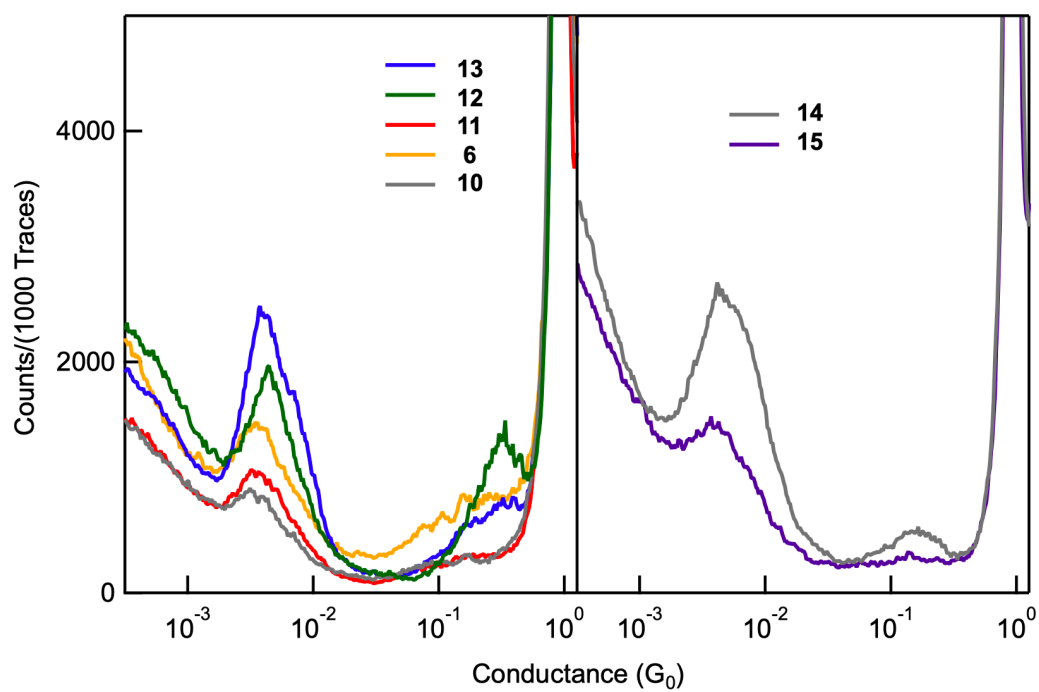


Figure 4.19. Log-binned conductance histogram of SC(O)R complexes **6**, **10** – **13** (left) measured at ~ 0.01 mM and OC(O)R complexes **14** & **15** (right) measured at 1 mM in TCB.

DFT calculated binding energies of the possible linker groups on **13** with R = Me and pySMe to Au₂₀ pyramids are shown in Table 4.2. The calculated binding energies of the pyridine N and SMe linkers on the pySMe ligand are comparable to those reported in the literature.^{5,95} These were also compared to the binding energy of the 3d M-N (pyridine) bond. Binding energy calculations were done with Au₂₀ pyramids using Gaussian (PBE/Def2-TZVP).^{119, 130, 131, 134}

Table 4.2. DFT calculated binding energies of **13** and pySMe

Linker to Au	Binding Energy (eV)
N of pySMe	0.9
SMe of pySMe	0.7
S of SC(O)R	1.0
Pt	0.6
3d M to N	0.9

Measurements of **11** at different bias voltage are shown in Figure 4.20. The conductance feature at $10^{-2} G_0$ (0.01 mM, left) does not depend on the bias voltage. The behavior of the SC(O)R lantern at higher concentrations (1 mM, right) does not dependent on the bias voltage either.

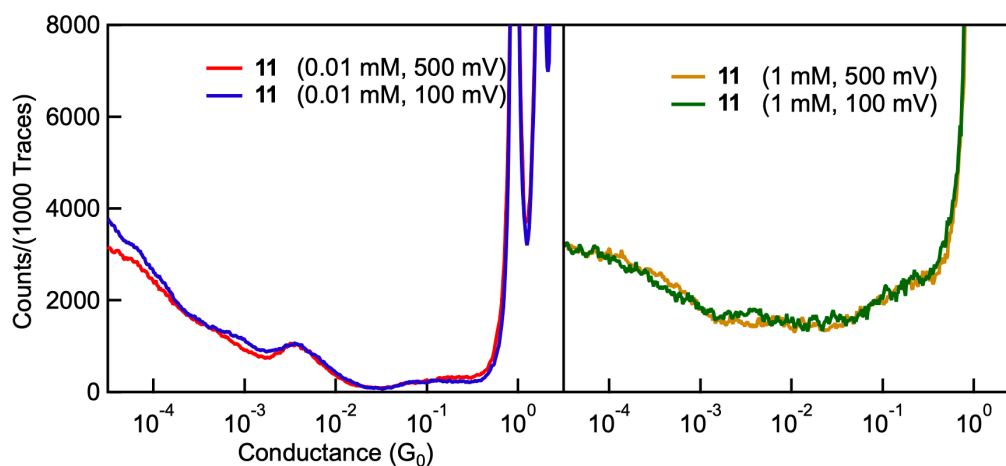


Figure 4.20. Measurements at different bias voltage of **11** at 0.01 mM (left) and 1 mM (right) concentrations in TCB.

The dampening of the G_0 peak with certain ligand backbones is shown in Figure 4.21. As reported in the main text, SC(O)R backbones such as thiobenzoic acid (Htba) and thioacetate (HSAc) contain thiol linkers that intercalate with the Au in various configurations. Carboxylate backbones (OC(O)R), measured as benzoic acid, do not have this effect. As shown in Figure 4.21, ethyl thioacetate does not disrupt the Au surface since now only R_2S -Au donor-acceptor interactions can occur.

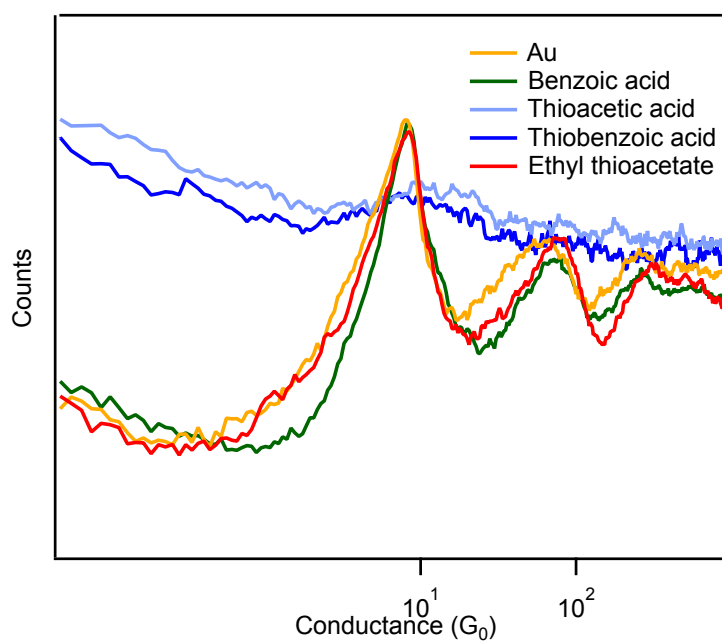


Figure 4.21. Conductance histograms of OC(O)R (benzoic acid) and SC(O)R backbones (thioacetic acid, thiobenzoic acid and ethyl thioacetate) measured at 1 mM.

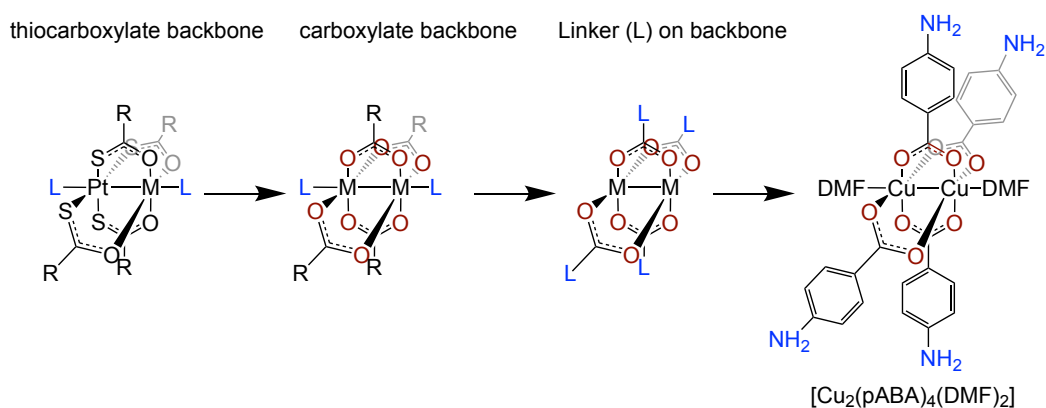
4.7. STMBJ Measurements of $[\text{Cu}_2(\text{pABA})_4(\text{DMF})_2]$

In this chapter, we have demonstrated that coordination complexes are vulnerable to rearrangement on Au during STMBJ measurements.⁸³ These rearrangements are consistent with hard-soft acid base principles in that soft-soft metal-ligand interactions such as the Pt-S in the thiocarboxylate-based lanterns, are vulnerable to competition from the soft Au. Measurements of the thiocarboxylate-based lanterns exhibit disruption of the G_0 signatures in the conductance histograms. This signature indicates the formation of Au-S bonds due to intercalation of the thiolate within the Au atomic contacts³² and prevents reproducible measurements of the complexes. This signature is not present in carboxylate-based ligands with hard-hard metal-ligand interactions such as Cu-O coordination environments as reported in Figure 4.2. Furthermore, Au-ligand bonding can outcompete neutral donor-acceptor M-N bonding within transition metal complexes, as observed with pyridine-based ligands in Figure 4.3.

Based on these observations, we propose a new lantern structure for STMBJ measurements in Scheme 4.1. First, we opt for a carboxylate backbone which contains O-donor atoms which do not intercalate into the Au chains. Next, instead of placing neutral linker groups (L) in the axial positions, as done previously with pySMe (see Figures 4.2 and 4.3), we incorporate the linker group on the carboxylate backbone, where electrostatic and chelating effects can potentially lead to more robust metal-ligand bonding.

We investigate the binding and conductance of $[\text{Cu}_2(\text{pABA})_4(\text{DMF})_2]$ (pABA = *para*-aminobenzoic acid, DMF = *N,N*-dimethylformamide), prepared from published methods.¹³⁵ As shown in Scheme 4.1, the $\{\text{Cu}_2\}$ homobimetallic complex has amine linkers

on the backbone ligands, known to bind to Au for junction formation.^{5, 28, 34, 37} The complex is crystallized from DMF solution, which coordinates to the axial position of each Cu(II) center.



Scheme 4.1. Proposed redesigning of lantern complexes for STMBJ measurements.

Single molecule conductance measurements were performed using the STMBJ technique as described above. Measurements were performed using a dropcast technique, where ~ 1 mM solutions of the molecule were deposited on the Au substrate.²⁵ Measurements in the presence of pABA from H₂O (green), DMF (red) and EB (ethyl benzoate, orange) solutions display a feature around $10^{-3} G_0$ in the conductance histograms (Figure 4.22A). This suggests that the backbone ligand itself can bind in the Au junction, coordinating to Au through the amine^{5, 28, 34, 37} and carboxyl groups.^{34, 109, 136} Measurements from EB and DMF solutions have an additional feature at lower conductance between 10^{-4} and $10^{-5} G_0$, that we hypothesize is due to a π - π stacked dimer which has been widely

reported in the literature.^{21, 137, 138} Measurements of DMF dropcast on an Au substrate do not display molecular conductance signatures as shown in the yellow trace of Figure 4.22C.

Conductance histograms from measurements performed in the presence of $[\text{Cu}_2(\text{pABA})_4(\text{DMF})_2]$ from DMF solutions in Figure 4.22B are consistent with the conductance histograms from pABA measurements in Figure 4.22A. 2D conductance histograms of pABA and $[\text{Cu}_2(\text{pABA})_4(\text{DMF})_2]$ reveal that the displacements of the conductance features are identical. The conductance features in Figure 4.22C for pABA (top) and $[\text{Cu}_2(\text{pABA})_4(\text{DMF})_2]$ (bottom) both extend to ~ 0.3 nm, while the lower conducting features extend slightly further to ~ 0.4 nm. Accounting for a snapback,^{28, 29} these features correspond to junction displacements of $\sim 1.1 - 1.2$ nm, comparable to the length of pABA which is 0.64 nm (from NH_2 to COOH) plus ~ 0.25 nm (the approximate length of an Au- NH_2 bond) per Au-linker contact. The length of $[\text{Cu}_2(\text{pABA})_4(\text{DMF})_2]$ between NH_2 groups in either adjacent or opposite backbone ligands is ~ 1.1 nm and 1.6 nm respectively (Figure 4.23). Considering the Au- NH_2 bonds, the hypothetical molecular junction for the entire $[\text{Cu}_2(\text{pABA})_4(\text{DMF})_2]$ complex is significantly longer than the conductance plateaus in Figure 4.22C.

Conductance measurements of the $[\text{Cu}_2(\text{pABA})_4(\text{DMF})_2]$ complex are consistent with junction formation of the backbone ligand pABA bridged between Au electrodes. Therefore, we conclude that rearrangement of the $[\text{Cu}_2(\text{pABA})_4(\text{DMF})_2]$ complex occurs during break junction measurements. Placing the NH_2 linker groups on the anionic chelating backbone ligand does not prevent rearrangement. This work demonstrates the complications of incorporating coordination complexes into STMBJ measurements.

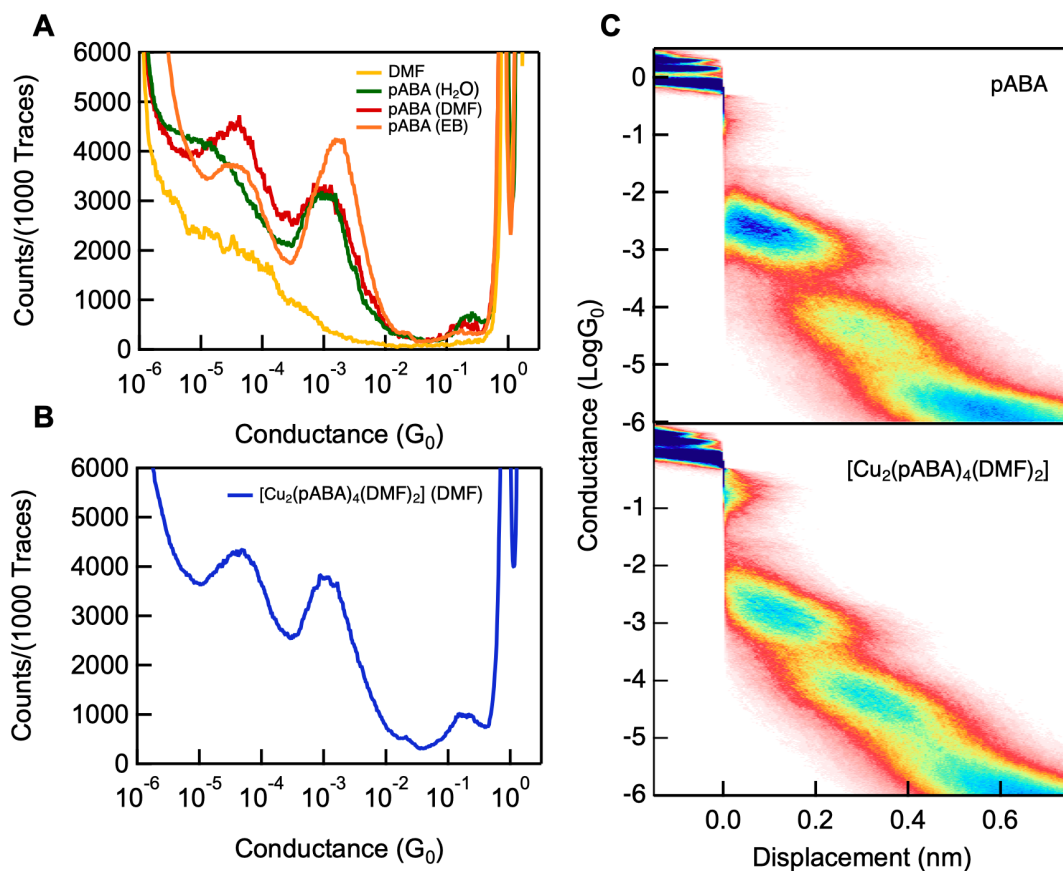


Figure 4.22. A) Conductance histograms recorded in the presence of DMF (yellow, 600 traces) and ~ 1 mM pABA from either H₂O (green, 4000 traces), DMF (red, 1400 traces) or ethyl benzoate (EB, orange, 10,000 traces) solutions. B) Conductance histogram recorded in the presence of ~ 1 mM $[\text{Cu}_2(\text{pABA})_4(\text{DMF})_2]$ from a DMF solution (blue, 10,000 traces). C) 2D histograms of pABA from a EB solution (top) and $[\text{Cu}_2(\text{pABA})_4(\text{DMF})_2]$ from a DMF solution (bottom).

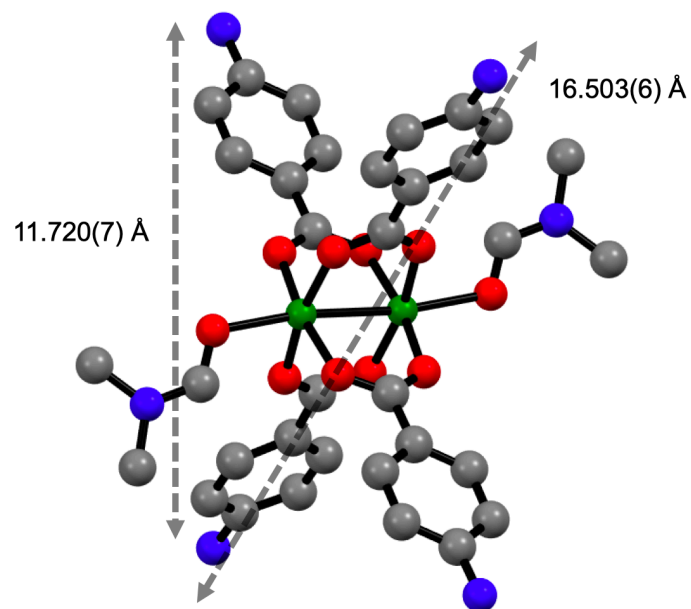


Figure 4.23. Mercury representation of [Cu₂(pABA)₄(DMF)₂]. Solvent molecules and H atoms removed, Cu (green), O (red), N (blue), C (dark gray). Distances between the adjacent and opposite NH₂ groups are reported.

CHAPTER FIVE: Assembly and Electron Transport Properties of Metal-Cyanide Containing Wires in Single Molecule Junctions

5.1. Introduction

Incorporating metal-containing complexes into molecular-scale devices is an important goal for next generation electronics and can lead to the design of functional molecular electronic components. Measuring conductance through complexes containing metal ions can help establish electronic properties and electron transport potential of individual metal ion-containing species. Yet, as demonstrated in Chapter 4, intramolecular metal-ligand bonding is often vulnerable to rearrangement on metal electrodes in break junction experiments.⁸³ Organometallic complexes such as metallocenes⁴⁴⁻⁴⁶ appear to remain intact in the junction environment during conductance measurements.¹³⁹⁻¹⁴¹ Together, these prior results suggest that strong intramolecular covalent metal-ligand interactions may be required for successful incorporation of transition metal centers into molecular electronic devices.

Cyanometallates are a class of anionic transition metal complexes coordinated by cyanide ligands (CN⁻) through covalent M-CN intramolecular bonding. The complex [KAu(CN)₂], for example, features a two-coordinate Au(I) center with a linear [(NC)Au(CN)]¹⁻ unit characterized by σ bonding and π backbonding from d^{10} Au(I) to the C \equiv N π^* bonds (Figure 5.1). Cyanometallates, including [Au(CN)₂]⁻, are common units in the formation of extended structures and 1D coordination polymers due to their ability to bridge to other metal centers through the N lone pair.⁶⁰ Separately, cyanide (CN⁻)^{142, 143}

and isocyanide (NC-) ¹⁴⁴ functional groups installed on short organic backbones have been previously reported to bind to Au electrodes and promote molecular junction formation. Here, we investigate whether the CN⁻ ligand within [M(CN)_n]^{m-} complexes provides a functional group for binding to Au electrodes in break-junction experiments and whether the complexes can remain intact to bridge the junction as illustrated in Figure 5.1. We probe the conductance and binding of the linear [Au(CN)₂]⁻ and [Ag(CN)₂]⁻ anions between Au electrodes using single molecule conductance measurements, performed with the Scanning Tunneling Microscope Break Junction (STMBJ) method, and density functional theory (DFT) calculations. We start with [Au(CN)₂]⁻ and find that when deposited in the junction, the molecule binds to produce numerous robust conductance features ranging from $\sim 10^{-1} - 10^{-6} G_0$. These conductance features cluster into three distinct groups which we are able to identify as junctions with one, two, or three {Au(CN)} units bridging the junction in series. Using DFT calculations, we show that multiple peaks within each cluster are likely signatures due to variations in the arrangement and binding orientations of the {Au(CN)} units within the chains bridging the Au electrodes. These results are reinforced by measurements of [Ag(CN)₂]⁻. Overall, our results suggest rearrangement of the {Au(CN)} units in the junction with respect to the original [Au(CN)₂]⁻ as well as formation of robust molecular bridges of varying length.

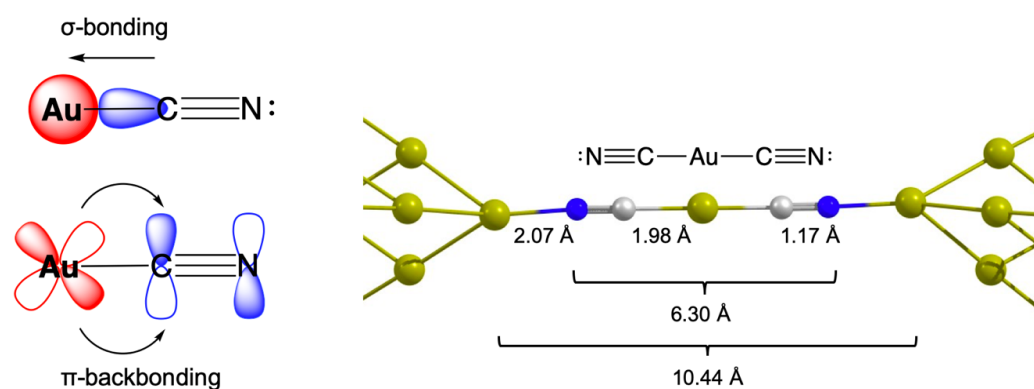


Figure 5.1. Depiction of Au-CN bonding within the $[\text{Au}(\text{CN})_2]^-$ anion (left). Hypothetical molecular junction with $(\text{NC})\text{Au}(\text{CN})$ bridged between Au_{18} electrodes (cropped for clarity) and DFT predicted distances at PBE level of theory (right).

5.2. Results and Discussion

Single molecule conductance measurements were performed using a home-built STMBJ as previously described.^{24, 25} Briefly, Au electrodes are brought in and out of contact under a constant bias of 500 mV and the conductance (current/voltage) is recorded. Conductance traces recorded during junction stretching show plateaus at integer values of G_0 which correspond to the formation of Au contacts with an integer number of Au atoms in the junction cross-section. After the Au contact is broken, a nano-gap forms between the electrodes and a molecule can bridge the electrodes to form a molecular junction. Measurements were performed in the presence of $[\text{KAu}(\text{CN})_2]$ deposited on Au substrates from a 1 mM aqueous solution.²⁵ We record 6000 thousand conductance-displacement traces in the presence of the molecule and compile them into linear or log-binned conductance histograms without data selection, shown in Figures 5.5 and 5.2A, respectively.

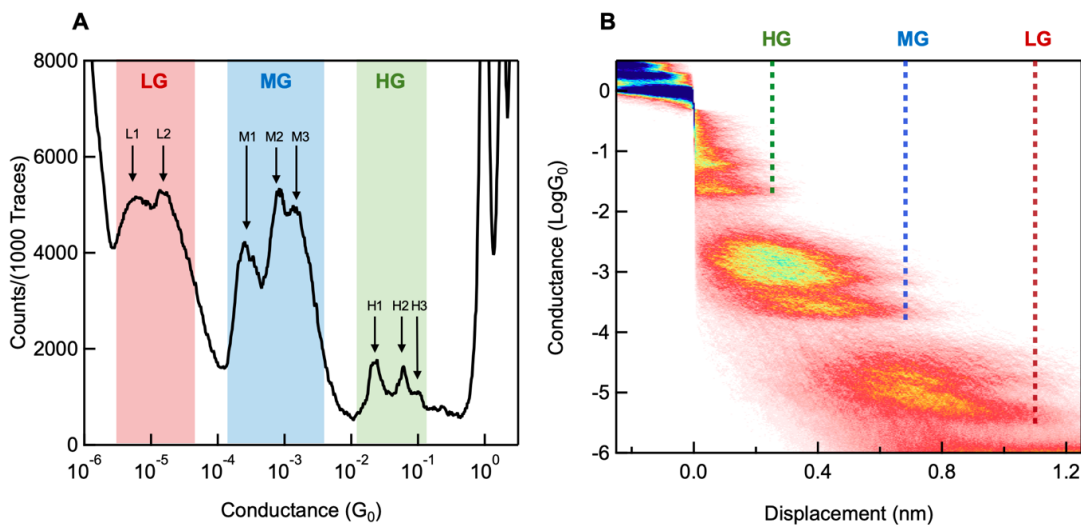


Figure 5.2 1D log-binned (A) and 2D (B) conductance histograms from measurements in the presence of 1 mM $[\text{KAu}(\text{CN})_2]$.

We observe that $[\text{KAu}(\text{CN})_2]$ on Au electrodes produces numerous conductance features ranging from $\sim 10^{-1} - 10^{-6} G_0$ as shown in the one-dimensional (1D) conductance histogram in Figure 5.2A. We hypothesize that the observed features are due to the bridging of the $[\text{Au}(\text{CN})_2]^-$ either through the cyanide π system, or through the lone pairs of the terminal nitrogen atoms, which are common donor linkers in single molecule break junction measurements.^{6, 33, 37} We identify eight distinct peaks, indicated by arrows in Figure 5.1A and group them into three conductance regimes of relative “high” conductance (HG) shaded in green, “medium” conductance (MG) shaded in blue and “low” conductance (LG) shaded in red. We label the distinct conductance features from the lowest to highest conductance within each regime as indicated in Figure 5.1A. The characteristic

conductance of each feature is determined by fitting multiple Gaussian curves to the linear-binned histogram of each region (Figure 5.5). For example, the three distinct conductance peaks in the HG region are identified as H1 at $2.2 \times 10^{-2} G_0$, H2 at $5.7 \times 10^{-2} G_0$ and H3 at $9.2 \times 10^{-2} G_0$. The conductance of each feature labeled in Figure 5.2A, including H1-H3, M1-M3 and L1-2 are listed in Table 5.1.

Two-dimensional (2D) histograms display conductance as a function of electrode displacement, which provide simultaneous length and conductance information. From the 2D histogram in Figure 5.2B it is apparent that the junction lengths of these three regions are distinct. First, we consider whether a single $[\text{Au}(\text{CN})_2]^-$ anion can generate all of the features observed. We identify a characteristic junction elongation length for the HG, MG and LG regions as marked in dashed green, blue and red vertical lines, respectively, in Figure 5.2B and listed in Table 5.1. The HG region has the highest conductance and shortest junction length with plateaus extending to ~ 0.2 nm, while the LG region has the lowest conductance and longest junction length with plateaus extending to ~ 1.1 nm. Accounting for the Au snapback distance of $\sim 0.5 - 0.8$ nm,²⁹ these features correspond to molecular junction lengths of ~ 0.7 nm – 1 nm and $\sim 1.6 - 1.9$ nm respectively. Importantly, the lengths of the LG molecular signatures are almost double the length of the entire complex shown in Figure 5.1. Therefore, we conclude that a single $[\text{Au}(\text{CN})_2]^-$ anion alone cannot generate features in the LG regime without rearrangement of the molecular units or appending of Au atoms from the electrodes into the molecular junction bridge.

The 2D histogram in Figure 5.2B also reveals that the conductance of the molecular features decreases with increasing length of the junctions. The distance between the dashed

lines in Figure 5.2B is $\sim 4.5 \text{ \AA}$, indicating that the characteristic length of each distinct region increases in multiples of this unit length. Therefore, we hypothesize that a discrete molecular unit $\sim 4.5 \text{ \AA}$ is repeatedly appended into the junction during elongation, increasing the length of the molecular chain spanning the Au-Au gap and the corresponding molecule signatures.¹⁴⁵ We consider the lengths of the molecular units present in the junction. The entire $[\text{Au}(\text{CN})_2]^-$ anion is $\sim 6.3 \text{ \AA}$ from N to N which is $\sim 40\%$ longer than the experimentally identified unit length of $\sim 4.5 \text{ \AA}$ as shown in Figure 5.1. The neutral unit $[\text{AuCN}]$ measures $\sim 3.2 \text{ \AA}$, and $\sim 5.2 \text{ \AA}$ including the Au-CN-Au(electrode) contact to the apex Au atom, providing a more reasonable structure for the $\sim 4.5 \text{ \AA}$ extension increase observed in Figure 5.2B. The increase in length coincides with a decrease in conductance as the junction evolves from the HG to the MG and LG regimes. The presence of numerous peaks within each conductance region (H1-H3, M1-M3, L1-L2) suggests that multiple molecular chains can span the junction in parallel as has been reported for other charged molecular bridges.²⁵ Another possibility is that a single molecular chain can bind in several junction geometries with distinct conductance signatures as has been reported for pyridyl linkers, for example.³³

We start by comparing the conductance evolution across regions by examining the lowest conductance signatures in each group (H1, M1 and L1). Based on literature precedent with similar conductance motifs, we interpret the lowest conducting signature within each conductance regime as the geometry which corresponds to a single molecular bridge fully stretched between electrodes and with no additional molecules bound in parallel.¹⁴⁵ To test the hypothesis that the distinct conductance regimes (HG, MG and LG)

correspond to integer multiples of a proposed molecular motif $\{\text{Au}(\text{CN})\}$ repeating in series, we determine the conductance decay rate between the molecular signatures H1, M1 and L1. In Figure 5.3A the conductance of H1, M1 and L1, reported in Table 1, is plotted against index n Figure 5.3A (top x axis), which identifies the number of repeating units assembled in series. The conductance decays exponentially with n , as expected from non-resonant tunneling through molecules with an integer number of repeating identical molecular units of length L_0 :

$$G \propto e^{-\beta L_0}$$

As shown in Figure 5.3A, we fit an exponential decay to the conductance trend as a function of molecular junction distance derived from DFT calculations, discussed further below and reported in Table 5.2, to determine a β decay value of 0.80 \AA^{-1} . Interestingly, the decay constant for the $\{\text{Au}(\text{CN})\}_n$ units is comparable to that of saturated molecular wires, such as alkanes (0.84 \AA^{-1}), suggesting these molecular wires containing Au^+ ions connected by short CN^- linkers are fairly insulating.⁶

Table 5.1. Experimental and calculated conductance and displacement information

		Experiment		Theory	
Region	Peak	Conductance (G_0)	Junction Lengths (nm) ^a	Transmission	Au-Au Displacement (nm) ^b
	H3	9.1×10^{-2}			
HG	H2	5.7×10^{-2}			
	H1	2.2×10^{-2}	0.7	7.0×10^{-2}	0.53
	M3	1.4×10^{-3}			
MG	M2	6.0×10^{-4}			
	M1	2.2×10^{-4}	1.1	7.4×10^{-4}	1.04
	L2	1.5×10^{-5}			
LG	L1	5.8×10^{-6}	1.5	1.3×10^{-5}	1.55

^a Experimental plateau lengths include snapback of ~ 0.5 nm

^b Measured edge to edge of the apex Au atoms

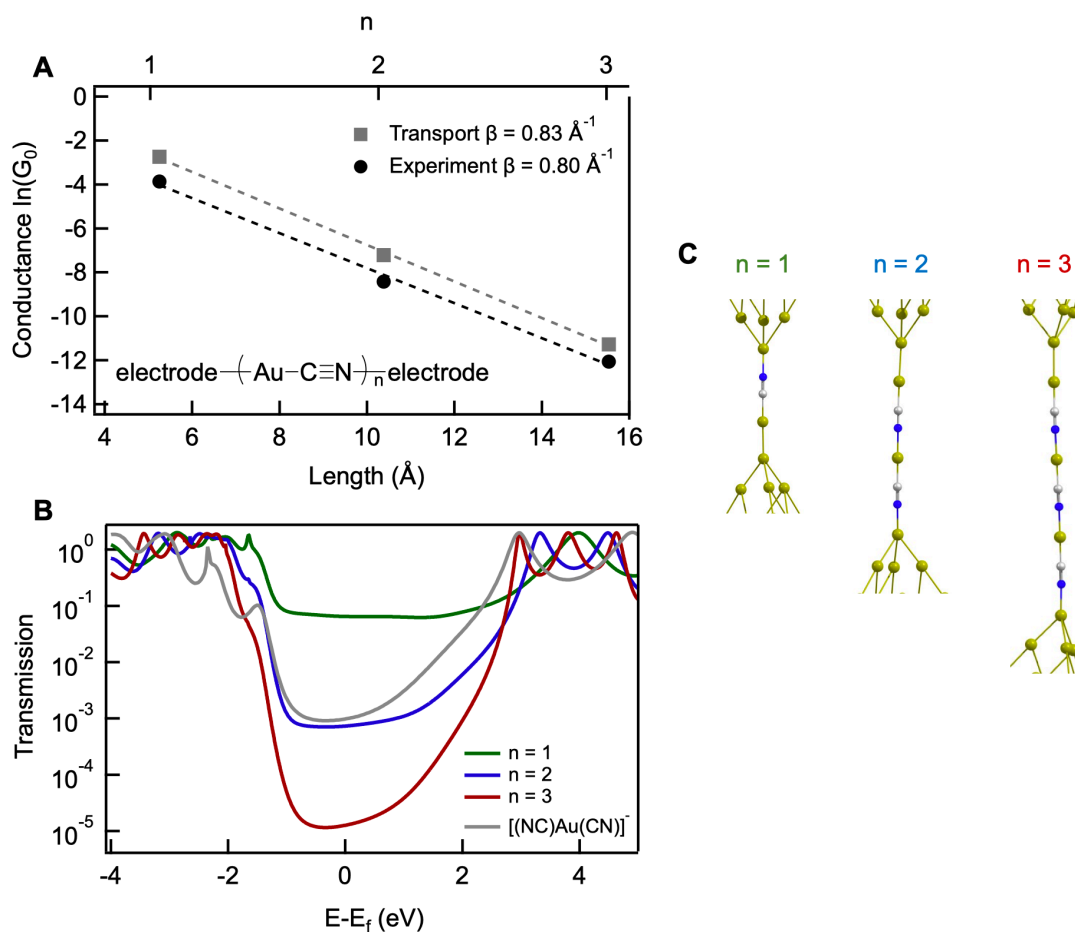


Figure 5.3. A) Conductance decay for peaks H1, M1 and L1 (red) and calculated transmission per $\{\text{Au}(\text{CN})\}_n$ unit (blue) versus the length of the $\{\text{Au}(\text{CN})\}_n$ junction, measured from edge to edge of the apex Au atoms of the electrode. B) Transmission curves for $\{\text{Au}(\text{CN})\}_n$ $n = 1-3$ and $[(\text{NC})\text{Au}(\text{CN})]^-$ C) DFT relaxed structures for $\{\text{Au}(\text{CN})\}_n$ $n = 1-3$ with Au_{34} electrodes. Au-Au displacements are reported in Table 5.1.

We use density functional theory (DFT) and non-equilibrium Green's Function (NEGF) transmission calculations to explore the possible junction geometries corresponding to conductance signatures observed in experiment. The DFT and transport

calculations reported here were performed by Brent Lawson, a graduate student in the Kamenetska Group and a co-author on the publication. We construct molecular bridges bound between Au(111) electrodes containing 34 Au atoms arranged in 3 layers with 4 apex Au atoms forming in an atomically sharp tip. Each candidate molecular junction geometry is relaxed by allowing the molecule and apex Au atoms to rearrange while the 3 back layers for each electrode are frozen. To determine the most likely inter-electrode distance for a given molecular chain configuration, the electrodes are systematically moved in and out in steps of 0.05 Å. At each step, the junction is re-relaxed as described above, and the total junction energy is calculated. The junction with the lowest total energy is taken as a representative geometry for a given molecular bridge configuration with the binding energy given by $[E_{\text{junction}} - (E_{\text{electrodes}} + E_{\text{molecule}})]$.

Guided by the experimental results described above, we first consider sharp-tip junctions of $\text{Au}_{34}\text{-[Au-C}\equiv\text{N]}_n\text{-Au}_{34}$ where $n = 1, 2$ or 3 . The representative junction geometries are shown in Figure 5.3C. We find that all three proposed molecular wires with $n = 1, 2$ or 3 repeating units form stable junctions with binding energies of 1.2, 1.5 and 1.6 eV per electrode-molecule contact, respectively. The calculated binding energies to the Au electrodes are significantly larger than typical donor acceptor binding energies in molecular junctions such as amine (0.6 eV), SMe (0.5 eV) and pyridyl (0.8 eV) groups,^{5, 146, 147} and are more consistent with reports of charged species bridging the junction, such as imidazolate²⁵ and 1,4-phenylene diisocyanide,¹⁴⁵ where the metal-molecule interaction may be enhanced by image-charge effects. These binding energies are also comparable to the inter-atom Au-Au binding within the electrodes which has previously been measured

to be ~ 1.5 eV.¹⁰⁶ In the case of anionic imidazolate²⁵ and zwitterionic 1,4-phenylene diisocyanide,¹⁴⁵ the anionic atoms are found to pull Au atoms into the junction during elongation forming chains containing repeating numbers of {AuL} units, analogous to the molecular chains formed here with (CN) $^-$. From the minimum energy DFT geometries shown in Figure 5.3C, we determine the distance between the apex Au atoms to be 5.1, 10.3, and 15.3 Å, for $n = 1-3$ respectively. These are measured from edge to edge of the apex Au atoms and are reported in Table 5.1. The difference in extension between these geometries is ~ 5 Å, which is in good agreement to the experimentally determined values of ~ 4.5 Å.

Next, we calculate the transmission spectra of these representative junction geometries shown in Figure 5.3B. Transmission at Fermi ($E-E_F = 0$) is extracted and plotted in Figure 5.3A in grey squares alongside the experimentally measured conductance, which is plotted in black circles. We note that the calculated transmission at E_F is $\sim 50\%$ higher than the experimentally determined conductance for H1, M1 and L1, consistent with other DFT-experiment comparisons and the established tendency of DFT to over-estimate conductance of metal-molecule junctions in the field of molecular electronics.^{3, 37} Importantly, while the absolute value of the DFT-calculated transmission is overestimated, the trends between junction geometries are representative and reliable. We find that the DFT-calculated conductance decays exponentially with n , or the number of incorporated {AuCN} units, with a molecular decay constant of $\beta = 0.83 \text{ \AA}^{-1}$, in excellent agreement with the experimentally determined molecular decay constant of $\beta = 0.80 \text{ \AA}^{-1}$ (Figure 5.3A). Again, the large decay constant across these metal-containing units, suggests that

these molecular wires are insulating. Existing reports of transition metal-containing complexes with closed shell or pseudo closed shell metal centers (e.g. Au(I) and Pt(II)) also demonstrate low conductance at the single molecule level.^{43, 139} In addition, transmission spectra of the $\{\text{Au}(\text{CN})\}_n$ chains in Figure 5.3B suggests that destructive quantum interference (DQI) is also a factor in the rapid decay. We see that even as the HOMO-LUMO gap narrows as the chains grow longer, the transmission at Fermi decreases. The characteristic dip in transmission in the HOMO-LUMO gap and the decrease in transmission at E_F is a signature of DQI that has been observed in alkanes and oligophenyls.¹⁷

To further confirm the assignment of these regions as $\{\text{Au}(\text{CN})\}_n$ with $n = 1, 2$, or 3 units, we calculate the transmission of the original $\{\text{Au}(\text{CN})_2\}^-$ anion. The hypothetical $[(\text{NC})\text{Au}(\text{CN})]^-$ junction bridged between two Au electrodes, shown in Figure 5.1, has a binding energy of ~ 1.7 eV per Au-N bond, suggesting that this molecule can form relatively robust molecular junctions, with comparable binding energies to those predicted for the $\{\text{Au}(\text{CN})\}_n$ chains above. The transmission through the $\{\text{Au}(\text{CN})_2\}^-$ anion shown in gray in Figure 5.3B, is comparable to that of the $n = 2$ system, assigned to the MG region. The calculated transmission through $[(\text{NC})\text{Au}(\text{CN})]^-$ is on the order of $\sim 10^{-3} G_0$ and is significantly lower than the measured conductance of the HG region ($n = 1$), which is on the order of 10^{-1} - $10^{-2} G_0$. This confirms that some degree of disassembly of the original complex into smaller units such as $\{\text{Au}(\text{CN})\}$ must be occurring.

In order to investigate the other conductance features in Figure 5.2 (H2, H3, M2, M3 and L2) we quantify the conductance ratios between the peaks in each conductance

region and report them in Table 5.2. Due to the small, linear structures of these units, we hypothesize that multiple molecules can bind in the junction in parallel. Typically, molecules bound in parallel result in the multiple conductance peaks at integer values.²⁵ From Table 5.2, we observe the conductance of peak 2 within each group is more than twice the conductance of peak 1. This pattern is contrary to the behavior of non-interacting molecules bound parallel in the junction with conductance corresponding to integer multiples. In addition, conductance measurements performed at lower or higher concentrations do not consistently affect the number of counts observed in the conductance histogram for peaks 2 and 3 of each region (Figure 5.6). The amplitude of distinct peaks varies with experiment, suggesting that the formation of these junctions is potentially sensitive to the measurement conditions or Au substrate surface.

Table 5.2. Conductance ratios within HG, MG and LG regions from measurements in the presence of $[\text{KAu}(\text{CN})_2]$ in Figure 5.2A.

Conductance features	Ratio
$G_{\text{H3}}/G_{\text{H1}}$	4.1
$G_{\text{H2}}/G_{\text{H1}}$	2.6
$G_{\text{M3}}/G_{\text{M1}}$	6.4
$G_{\text{M2}}/G_{\text{M1}}$	2.7
$G_{\text{L2}}/G_{\text{L1}}$	2.6

We also perform conductance measurements in the presence of the Ag analogue $[\text{KAg}(\text{CN})_2]$. Conductance histograms from 20,000 traces collected in the presence of $[\text{KAg}(\text{CN})_2]$ are shown in Figure 5.4. The conductance histogram of $[\text{KAg}(\text{CN})_2]$ has multiple conductance features which cluster into distinct groups analogous to the Au analogue. Notably, the conductance of peak H1 is the same for both complexes, supporting the assignment of this feature to $(\text{CN})^-$ bound to a gold apex atom which can extend into $\{\text{Au}(\text{CN})\}$ upon pulling. This result confirms that some disassembly and rearrangement of the complexes occurs in the junction. The MG region for $[\text{KAg}(\text{CN})_2]$ contains a broad molecular conductance feature consistent with the conductance of M1 in the $[\text{KAu}(\text{CN})_2]$ measurements. Overall, the conductance histogram for $[\text{KAg}(\text{CN})_2]$ features fewer peaks in the MG and LG regions compared to the $[\text{KAu}(\text{CN})_2]$ measurement. We conclude that the presence of the units $\{\text{Ag}(\text{CN})\}$ influences transport properties of the junctions. Further

studies to investigate the binding geometries and transport properties of these junctions are required.

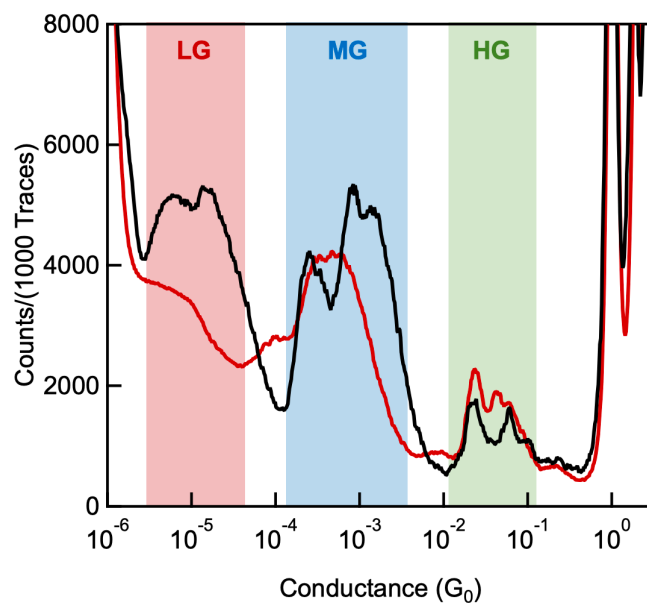


Figure 5.4. 1D conductance histograms from measurements in the presence of [KAg(CN)₂] (red) compared to [KAu(CN)₂] (black).

5.3. Conclusions

Single molecule conductance measurements in the presence of linear cyanometallate complexes, $[M(CN)_2]^{1-}$ ($M = Au$ or Ag) produce numerous conductance features ranging from $\sim 10^{-1} - 10^{-6} G_0$ at distinct junction elongations of $\sim 5 \text{ \AA}$ increments. Junction extensions in the LG region are longer than predicted for a $[(NC)Au(CN)]^-$ molecular bridge between Au electrodes, suggesting a certain degree of disassembly of the molecule and the formation of extended structures in the junction. The conductance of each region decays exponentially with integer $n = 1, 2, 3$. The extension of each region also increases in unit increments of $\sim 5 \text{ \AA}$, allowing us to assign the molecular units to $\{Au(CN)\}$ components. As the junction is stretched, an increasing number $n = 1, 2, 3$ of these are appended in series. The decay constant calculated from both experimental conductance and DFT is found to be $\sim 0.8 \text{ \AA}$ per $\{Au(CN)\}_n$ unit, characteristic of an insulating junction. Overall, this work demonstrates the in situ assembly of $\{M(CN)\}_n$ units in the junction environment and characterizes the electronic transport of these systems. Measurements in the presence of $[Ag(CN)_2]^{1-}$ preserve the conductance features corresponding to $\{M(CN)\}_1$ and $\{M(CN)\}_2$ molecular wires, but significantly impact the formation of more extended $n = 3$ structures. Further studies of $\{M(CN)\}_n$ transport is required to identify the influence of the metal center, its oxidation state and the coordination environment on transport properties.

5.4. Additional Data

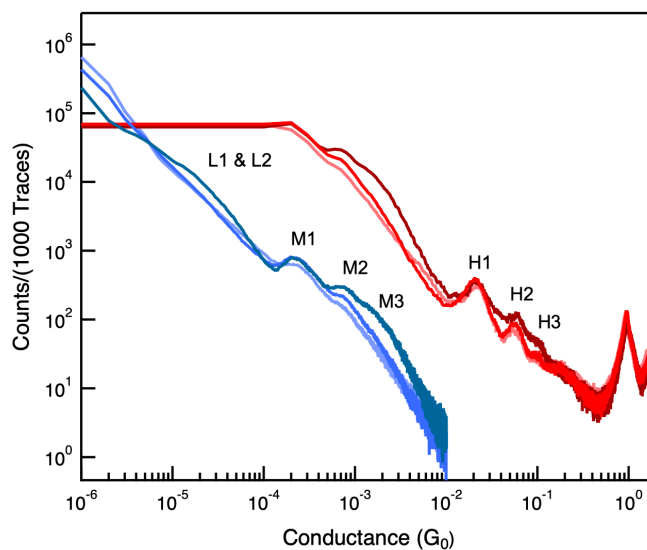


Figure 5.5. 1D linear-binned conductance histogram using bins of 1×10^{-4} (red) and 1×10^{-6} (blue). Different shades of red and blue indicate multiple data sets.

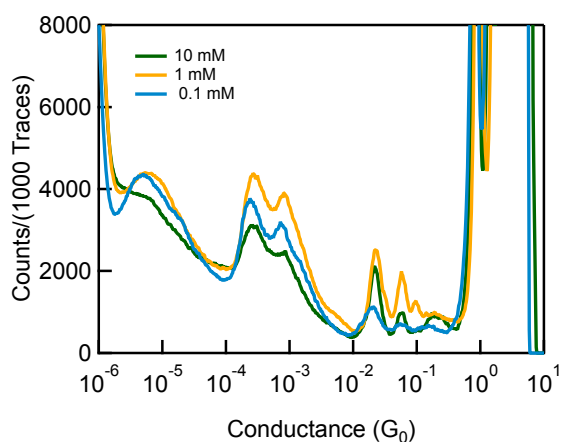


Figure 5.6. Conductance histograms of $[\text{KAg}(\text{CN})_2]$ from measurements performed at 10 mM (green), 1 mM (yellow) and 0.1 mM (blue) concentrations.

CHAPTER SIX: Manipulating Quantum Interference Between σ and π Orbitals in Single Molecule Junctions via Chemical Substitution and Environmental Control

6.1. Abstract

Understanding and manipulating quantum interference (QI) effects in single molecule junction conductance can enable design of molecular-scale devices. Here we demonstrate QI between σ and π molecular orbitals in a ~ 4 Å molecule, pyrazine, bridging source and drain electrodes. Using single molecule conductance measurements, first principles analysis and electronic transport calculations, we show that this phenomenon leads to new patterns of electron transport in nanoscale junctions, such as destructive interference through the para position. These QI effects can be tuned to allow conductance switching using environmental pH control. Our work lays out a conceptual framework for engineering QI features in short molecular systems through synthetic and external manipulation that tunes the energies and symmetries of the σ and π channels, opening the door to applications in molecular sensing, electronics and responsive nanoscale materials design.

6.2. Introduction

Quantum interference (QI) in nanoscale contacts can be harnessed to create new functionality in next generation electronic devices. In molecular circuits, QI has been shown to affect the conductance of a metal-molecule-metal junction, suggesting that controlled manipulation of QI can enable toggling of the conducting state from on to off.^{17, 18, 148, 149} Recent work has demonstrated mechanosensitive QI phenomena in molecular junctions, which result in variations in conductance during mechanical modulation experiments.^{21, 22, 45, 150} Other strategies to tune QI include synthetic modifications of the molecule and use of environmental stimuli such as electrode potential and cation-gating mechanisms.¹⁵¹⁻¹⁵⁶

QI results from electrons tunneling across two or more electronic states in the molecular junction as described in Chapter 1. These states derive from molecular orbitals (MOs) which impart distinct phases to the tunneling electrons at the Fermi energy. MOs are either π or σ —antisymmetric or symmetric relative to the internuclear axis of the molecule, respectively. Until now, all observed interference effects have been derived from π - π or σ - σ MO interactions. The reliance on orbitals with similar symmetry, like all π or all σ , limits the range of accessible QI phenomena. For example, most reported trends and modulation of destructive quantum interference (DQI) involve the π system of extended conjugated systems because the more conducting π system of these molecules dominates transport. In π orbital-mediated interference, para-linked species, which also bind more efficiently due to steric interactions, are better conducting than meta-linked analogues. The

presence of numerous frontier π -orbitals in large conjugated systems means that the on/off conductance ratio in these extended molecular systems is limited. In shorter, often saturated molecules, interference between σ channels has also been observed, but complete DQI where conductance is fully suppressed is rare in organic systems.^{19,20}

Here we demonstrate that QI between the π and σ channels can be harnessed in sub-nanometer molecules to create junctions with novel and adjustable interference phenomena with a high on/off ratio. We use the simple six-member conjugated rings to demonstrate that synthetic substitution can reorder the relative energies of σ and π MOs and introduce new QI trends between these transport channels. We demonstrate how single atom substitutions from carbon to nitrogen in the para position of benzene to yield pyrazine, shown in Figure 6.1A, creates a tunable and synthetically accessible molecular framework for QI manipulation and environmental control. First, through experiment, analysis and density functional theory calculations, we show that interference between σ and π channels determines transport in pyrazine. We demonstrate full suppression of conductance through the para channel of this molecule which is only possible through σ - π DQI. Then, by synthetically tuning the relative energy and symmetry between these MOs we adjust the QI phenomena through the molecule. Finally, we show experimentally and validate computationally that recovery of the conductance signal can be observed through environmental pH control. This is the first demonstration of QI environmental manipulation in a molecule shorter than ~ 4 Å and with a constructive QI (CQI) conductance as high as benzene at $\sim 1\%$ of a fully open quantum channel. Importantly, the restricted set of binding degrees of freedom that is characteristic of short molecular

junctions, allows us to achieve null conductance in the destructive QI state and high on/off ratios between states of the molecular circuit through environmental control.

6.3. Results and Discussion

Both benzene and pyrazine (pyz), shown in Figure 6.1A, are six-membered conjugated rings, but whereas benzene is composed of all sp^2 hybridized carbons, pyz contains two sp^2 hybridized nitrogen atoms in the 1 and 4 (para) positions. Benzene-based bridges, such as 1,4-benzenediamine shown in the middle column in Figure 6.1A are well-studied systems with a high molecular conductance approaching $\sim 1\%$ of $1G_0$, which depends slightly on the chemical linker, e.g. amine or thiol, used to bind it to Au electrodes.^{36, 37} Transport through these molecules is known to be strongly dependent on the position of the linker electrode contacts due to QI effects, with para and meta substitution resulting in CQI and DQI respectively.^{17, 153, 157}

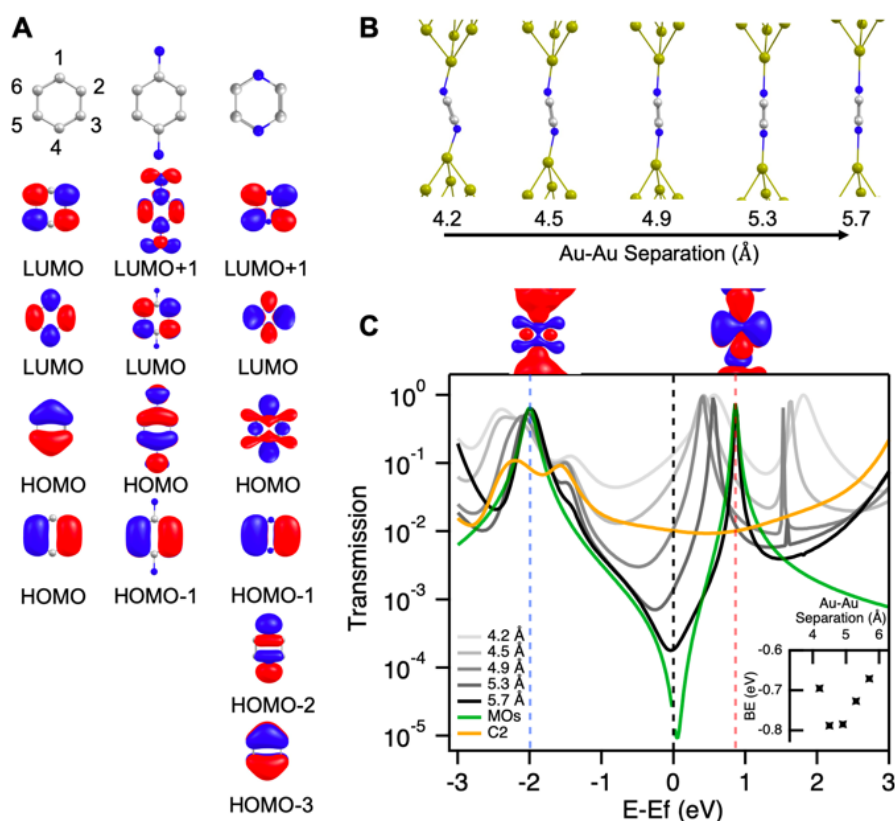


Figure 6.1. A) Frontier MOs of benzene (left), 1,4-benzenediamine (middle) and pyz (right) at B3LYP/Def2-TZVP level of theory. B) Relaxed geometries of pyz junctions at various junction extensions with Au₃₇ electrodes. Au-Au separation is reported from edge to edge of the apex Au atoms. C) Transmission spectra and binding energy (BE) per Au-N bond (inset) of pyz at various junction lengths. Transmission calculated using Equation 1 at the 5.7 Å Au-Au separation considering the HOMO and LUMO (green trace). The black vertical dashed line indicates the Fermi energy (E_F). Isosurface plots of the molecular orbitals in the 5.7 Å junction at -2.0 eV (HOMO) and 0.9 eV (LUMO) are shown above and indicated by the blue and red dashed lines respectively. Transmission of 1,2-diaminoethane (yellow trace).

Pyridine-type nitrogen atoms are robust and selective linker groups for binding to Au electrodes, suggesting that pyz which contains two pyridine N atoms in the para position of a six-membered ring, is an ideal candidate for junction bridging.³³ Yet few reports of pyrazine conductance are found in the literature and our own measurements show no discernible signal as we show further below.^{158, 159} We reason that the absence of a reliable pyrazine conductance signature is due to the reordering of frontier MOs in pyz compared to benzene as shown in Figure 6.1A. The highest occupied molecular orbital (HOMO) and lowest unoccupied molecular orbital (LUMO) of benzene consist of two degenerate MOs that all have π character, dominated by the six unhybridized C $2p_z$ orbitals. The HOMOs and LUMOs of 1,4-benzenediamine are largely the same as those of benzene. In the conductance of 1,4-benzenediamine, these π -based frontier MOs dominate transport at the Fermi energy (E_F), resulting in CQI through para- and DQI through meta-linked molecules.^{153, 157} In contrast, in pyz, the non-degenerate HOMO is dominated by the σ framework of bonding among the C/N sp^2 hybrids in the plane of the ring, and the LUMO retains the π character of the benzene LUMO. The HOMO-2 contains the σ framework and N lone pairs. The rest of the π -based MOs in pyz are shifted away from E_F to the LUMO+1, HOMO-1 and HOMO-3 (Figure 6.1A). MOs with nodes in the 1 and 4 positions where the molecule binds to the electrodes, such as the pyz HOMO-1, do not contribute to transport through the para channel. Thus, we predict that transport in pyz will be dominated by the σ HOMO and the π LUMO. Transport at E_F can then be approximated as the modulus squared of the sum of the individual transmission coefficients.¹⁷

$$T = |t_\sigma + t_\pi|^2 = |t_\sigma|^2 + |t_\pi|^2 + 2\text{Re}(t_\sigma^* t_\pi) \quad (1)$$

The last term above is the QI contribution between the two channels. Usually, σ and π channels do not both contribute to conductance or to QI. In conjugated systems, typically $t_\pi \gg t_\sigma$ and the π channel dominates the transmission. In saturated systems, only the σ channel is available. However, in a conjugated molecule as short as pyz, the σ and π transport channels are of similar amplitude. The conductance of saturated and conjugated molecules which are ~ 0.5 nm long, for example 1, 2- ethylenediamine and 1,4- benzenediamine has been determined to be $\sim 10^{-2} G_0$ in both cases.^{5, 36, 37} In other words, we can assume that in pyz, $t_\pi \approx t_\sigma$ so that the interference term can be pronounced.^{19, 160} Since the phase change in the HOMO and LUMO between the 1 and 4 positions is the same in Figure 6.1A, the *overall* phase difference between t_π and t_σ at E_F will be π (180°) assuming there is no tilting of the molecule relative to gold electrodes. In this situation, the last term of Equation 1 becomes negative and it predicts DQI through the para channel.¹⁷

We now turn to density functional theory (DFT) and non-equilibrium Green's Function (NEGF) transmission calculations of realistic pyz junction geometries.^{121, 125} The pyz molecule is relaxed with Au_{37} electrodes, which are frozen except for the four apex Au atoms on each electrode (see experimental section for more details). Each Au electrode is moved in or out in increments of 0.05 \AA . At each step, the junction geometry is relaxed and the binding energy and the transmission are calculated as detailed in the experimental section. A selection of relaxed junction geometries with increasing electrode distances from left to right are shown in Figure 6.1B (see Figure 6.5 and 6.6 for all geometries). Figure 6.1C reports the transmission spectra and binding energy per Au-linker bond (inset) of pyz junctions over various Au-Au distances. We note that no correction to the DFT-

calculated HOMO-LUMO gaps has been applied, so they are underestimated here, but the overall transport trends and symmetry arguments are representative and meaningful.³ As shown in Figure 6.1B, at shorter junction lengths, the pyz molecule tilts to fit in the junction. When the molecule is tilted, the π LUMO couples effectively to Au, and these tilted geometries have a relatively high transmission at E_F (indicated by the dashed black line), approximately $5 \times 10^{-2} G_0$ for the 4.5 Å geometry measured from edge to edge of the apex Au atoms, as shown by the lighter gray traces in Figure 6.1C. In these configurations, the LUMO peak at ~ 0.9 eV has more overlap at the E_F than the HOMO peak. We also see an emergent gateway state at ~ -1.5 eV which has a low amplitude and does not contribute significantly to conductance at Fermi.¹⁶¹⁻¹⁶³ From Figure 6.1A, we infer that the empty part of the spectrum is dominated by the π system. When the molecule is tilted, the π LUMO couples effectively to Au, resulting in a broader LUMO resonance with a large overlap at E_F ; $t_\pi \gg t_\sigma$ and transport is LUMO dominated at shorter junction lengths (< 5 Å). We note that in this tilted confirmation, when the Au electrodes bind to the opposite sides of the π system, the QI between σ and π is expected to be constructive because of the extra phase change in π MOs across the internuclear axis. In single molecule experiments in ambient conditions, geometries where Au-Au edge-to-edge distance is < 5 Å are not observed, so we do not expect these short geometries to contribute to measured conductance signatures.²⁸⁻³⁰

As the junction is elongated beyond 5.0 Å, the lone pairs of the N atoms, which are part of the σ framework, couple to the electrodes and the pyz molecule binds vertically in the junction (Figure 6.1B). In the transmission spectrum (Figure 6.1C) for the junction

fully extended to 5.7 Å, neither the full nor the empty part of the spectrum solely dominate transport at E_F . Instead, a typical DQI signature—a deep dip in the transmission spectrum—is observed around E_F and the transmission is lower by over 2 orders of magnitude, as shown by the solid black trace in Figure 6.1C. Isosurface plots of the 5.7 Å vertical junction geometry on top of Figure 6.1C show that the junction resonances closest to E_F in the full (left) and empty (right) part of the spectrum have σ and π character, respectively.

We emphasize that the transport predicted for the fully stretched pyz at E_F (black trace) is lower than of a typical sigma-conducting alkane of similar length, 1,2-diaminoethane (C2, yellow trace), as shown in Figure 6.1C. Therefore, the low transmission of pyz cannot be explained by a suppression of the π channel only due to a lack of coupling in the vertical geometry.¹⁹ Instead, we observe a situation where $t_\pi \approx t_\sigma$ and there is an overall phase change of π (180°) between the para positions in t_π and t_σ at the E_F .¹⁷ Using Equation 1 and plugging in the values of the frontier resonance positions and width from fits to the black curve in Figure 6.1C, we obtain an approximate transmission. This is plotted in green in Figure 6.1C and has excellent qualitative agreement with the DFT and NEGF-calculated transmission of the vertical geometry. Therefore, we conclude that the DQI predicted by DFT through the para channel of pyz in the vertical geometry is due to destructive interference between the σ and π channels, or HOMO and LUMO respectively.

We use single molecule conductance measurements to experimentally detect these predicted QI effects through both the para and meta pathways of the pyz ring. We perform

STMBJ measurements using a home-built instrument and protocol as previously described.^{24, 25} Briefly, we bring Au electrodes in and out of contact under a constant bias of 500 mV and record the conductance (current/voltage) during this junction-formation process. Conductance traces recorded during junction stretching show plateaus at integer values of G_0 which correspond to the formation of Au contacts with an integer number of Au atoms in the junction cross-section. Individual traces for clean Au are shown in the inset of Figure 6.2. Thousands of such conductance traces are compiled into histograms without data selection and normalized to enable comparison. An example of a clean Au histogram is shown in Figure 6.2 (yellow trace) where a pronounced peak at $1G_0$ is evident. After the Au contact is broken, a nano-gap forms between the Au electrodes and a molecule present can bridge the Au electrodes to form a molecular junction with a conductance that is typically less than $1G_0$.

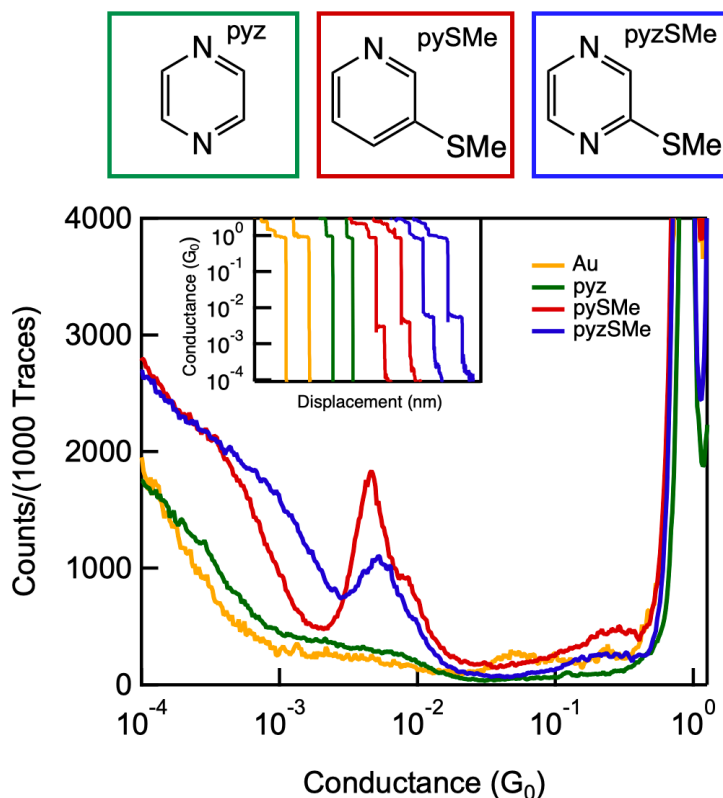


Figure 6.2. 1D conductance histograms of clean Au (yellow), pyrazine (green), pySMe (red) and pyzSMe (blue) at 1mM concentrations in TCB. Example traces are shown in the inset and structures are shown above.

Figure 6.2 demonstrates the experimentally determined conductance signatures of pyz-based molecules with linker groups (pyridine N, or SMe) which allow selective bridging of Au electrodes to either the para (1,4) or the meta (1,3) positions.^{5, 6, 33} We observe that pyz, with linkers only at the para positions, (in green) does not produce clearly identifiable molecular conductance signatures as seen in the individual experiment traces (Figure 6.2 inset) and the histogram (Figure 6.2) in green as predicted by our analysis

above. To eliminate the possibility that the pyz N atoms are not able to bind to Au, we perform measurements of 3-thiomethylpyridine (pySMe) and 2-thiomethylpyrazine (pyzSMe) both of which have an SMe linker in the 3 positions, meta to an imine N. The traces and histograms are shown in Figure 6.2 in red and blue for pySMe and pyzSMe respectively. For both molecules, we observe a clear conductance feature near $5 \times 10^{-3} G_0$, with a slight shoulder at higher conductance consistent with binding through pyridine linker groups.³³ Two-dimensional (2D) conductance histograms of pyz, pySMe and pyzSMe, which display conductance as a function of electrode displacement are included in Figure 6.7. We conclude that the pyrazine N is able to bind to Au and conduct when another linker group on the ring is present. Importantly, for pyzSMe, which contains both para (N-N) and meta (N-S) binding sites, we observe only a single conductance feature. The similarity in conductance values for pyzSMe and pySMe indicates that transport in pyzSMe occurs through the meta N-S pathway, rather than the para N-N pathway, of the pyrazine ring. Conductance through quinazoline, which has a meta N-N rather than a para N-N pathway also occurs (Figure 6.8). Additionally, the calculated binding energies of the Au-N bonds between pyz and the Au surface are $\sim 0.7 - 0.8$ eV, comparable to other linker groups such as NH_2 and SMe, suggesting that pyz should bind in the Au junction (Figure 6.1C inset).^{5, 143, 146} Therefore, we conclude that pyz, like pySMe and pyzSMe, is able to bind to Au through the N atoms, but that the conductance through the N-N para channel is suppressed due to DQI as we predicted.

To summarize our results so far, we find that substituting pyridine N atoms into the para positions of a benzene ring leads to a rearrangement of MOs that results in distinct QI

phenomena between the σ and π MOs. As a result, in pyz molecules, the para channel is non-conducting due to DQI. Interestingly, substitution at the 3 position with the SMe linker preserves the DQI through the 1,4 channel.

We perform calculations to understand the effect of π -donating substituents like SMe on the electronic structure of pyz derivatives and to gain insight into routes to turn on conductance through the para channel. We consider the effect of SMe as well as the OH substituent, which can influence the electronic structure of pyz, but which is not known to bind to Au in break junction experiments.⁸³ The gas phase MOs of pyzSMe and pyzOH are shown in Figure 6.9. Transport calculations are shown in Figure 6.3 for pyzOH and Figure 6.10 and 6.11 for pyzSMe. We observe that the features of the two molecules are similar (Figure 6.11) and we focus on the pyzOH results in Figure 6.3 as representative for both. The HOMO in pyzOH now has π symmetry while the σ MO is now the HOMO-1, which is the reverse of pyz. Furthermore, the π HOMO of pyzOH has non-zero weight on the N atoms and may contribute to transport through the para channel of pyzOH. The symmetries of the π HOMO and LUMO indicate that the relative phase between these MOs is zero at E_F and should result in CQI through the para pathway. We also note that the σ HOMO-1 retains the symmetry of the HOMO of pyz and is only ~ 0.3 eV below the π HOMO and can interfere destructively with the π LUMO (Figure 6.9).

To test these predictions, we now model the conductance of fully elongated geometries of pyzOH and the unsubstituted pyz shown in Figure 6.3B-C. These structures represent the junctions before Au rupture (for more details see Figures 6.5-6.6, 6.10-6.13). We observe that the transmission at E_F through the para pathway of pyzOH (gray) is higher

than that of unsubstituted pyz (black) and the DQI feature in transmission at E_F is diminished. We conclude that the nearly degenerate HOMO and HOMO-1 (Figure 6.9) of the gas-phase pyzOH both contribute to the broad peak in the filled part of the spectrum at $\sim -2\text{eV}$ in Figure 6.3C. This conclusion is confirmed by DFT-calculated isosurface plots of the eigenchannels in Figure 6.15. Using Equation 1 and including the relative symmetries of the HOMO-1, HOMO and LUMO seen in Figure 6.3A, we reproduce in green a qualitatively similar transmission to the DFT calculated result in grey. This result suggests that QI effects between these three MOs determine the conductance of pyzOH. We note that in pyzSMe transmission on the right of Figure 6.11, the DQI feature is more pronounced than in pyzOH (left of Figure 6.11) because the π -based HOMO has less weight on the N atoms and therefore contributes less to CQI (Figure 6.9). Apparently, the inclusion of the OH group, and SMe to a lesser extent, in the meta position mitigates, but does not eliminate, the DQI through the para channel due to the reordering of frontier MOs as discussed above.

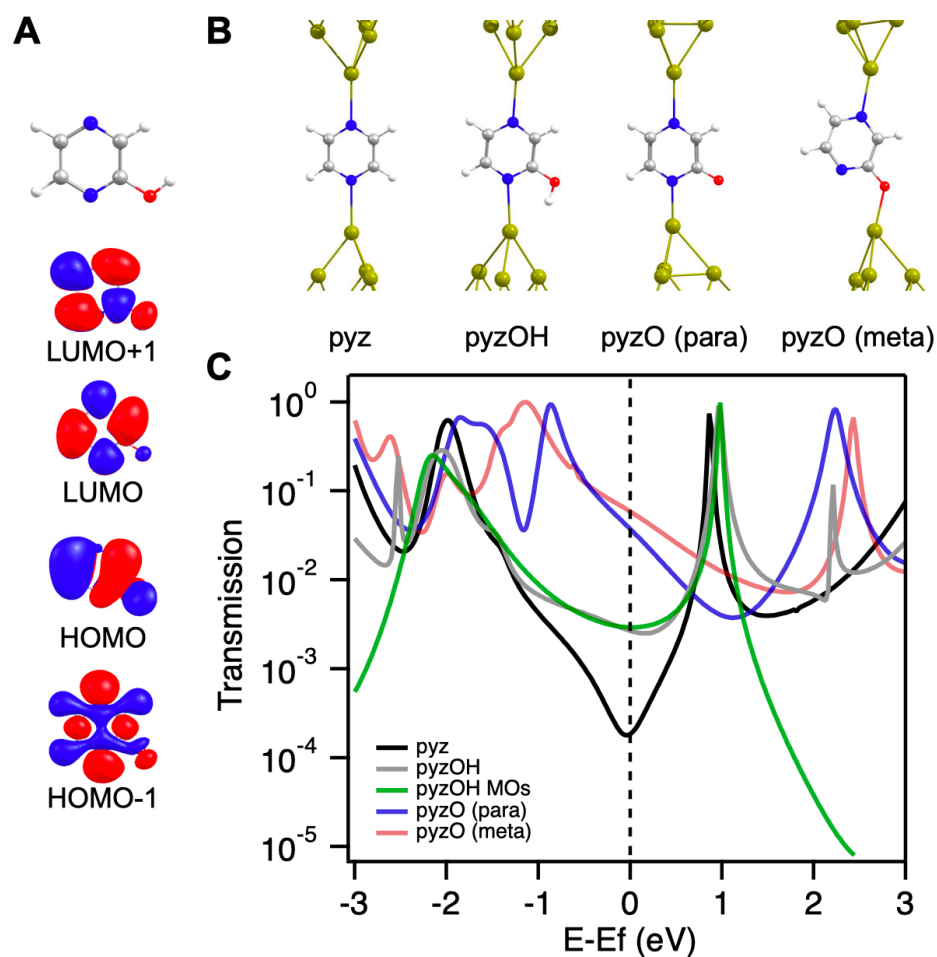


Figure 6.3. A) Frontier MOs of pyzOH at B3LYP/Def2-TZVP level of theory. B) Relaxed junction geometries from left to right of pyz, pyzOH, pyzO (para) and pyzO (meta) at the longest extension before Au rupture (5.7 Å, 5.3 Å, 5.1 Å and 5.5 Å respectively, reported from edge to edge of the apex Au atoms). C) Corresponding calculated transmission spectra for the pyz-based junction geometries shown above. Transmission calculated using Equation 1 considering the HOMO-1, HOMO and LUMO for pyzOH (green trace). The vertical dashed line indicates E_F .

To further modulate the QI, we deprotonate the OH group on the pyrazine ring and repeat the calculations of the vertical geometry and transmission as shown in Figure 6.3B (labeled pyzO para) and Figure 6.3C in blue. The HOMO and LUMO of the anion are shifted to higher energies as expected for the anion relative to the neutral molecule, which also causes the DQI feature to shift to higher energies, leading to a significantly higher transmission at E_F compared to the neutral pyzOH (grey). Importantly, the DFT-predicted transport through the para pyzO (blue) is about one order of magnitude higher than the neutral pyzOH. The charged pyzO also binds to the electrodes more strongly at ~ 2 eV (Figure 6.13) than the neutral pyz (Figure 6.6) or pyzOH (Figure 6.11), both with binding energies ~ 0.8 eV per Au-N bond. DFT results suggest that binding through the anionic O^- in the 3 position of the ring is also robust with a binding energy of ~ 2 eV (labeled pyzO meta in Figure 3B and Figure 6.13). From Figure 6.3C, we find that the transmission through pyzO via the meta pathway (red) is higher at E_F than the para pathway (blue).

Overall, the DFT results suggest that conductance through pyzOH can be turned on through deprotonation of the OH substituent. To experimentally test this strategy, we perform single molecule conductance measurements of pyzOH at various pH according to established protocols.²⁵ When protonated, the molecule exists in a tautomeric equilibrium between the enol (OH) and keto (=O) forms (Figure 6.4A). The conductance histogram from measurements recorded in the presence of pyzOH in neutral pH (shown in Figure 6.4B, gray) features a broad feature below $10^{-3} G_0$. This conductance is significantly below the expected range for molecules of this length, as shown in Figure 6.1. The feature is likely a result of dimer π - π stacking which has been widely reported in the literature.^{21, 137, 138} This

is supported by control measurements of 3-hydroxypyridine (pyOH), which lacks the second imine N. Conductance histograms of pyOH retain the conductance feature below $10^{-3} G_0$ as shown in Figure 6.16.

We now measure single molecule conductance signatures through deprotonated pyzO (Figure 6.4A) above pH 12 according to our established protocols.²⁵ In this environment, two distinct conductance peaks appear in the blue histogram in Figure 6.4B at $8.3 \times 10^{-3} G_0$ (peak 1) and $2.6 \times 10^{-3} G_0$ (peak 2) with a G1/G2 conductance ratio of ~ 3.2 . Measurements of pyzOH in acidic conditions (pH ~ 3) do not have these conductance features, but the addition of 1M NaOH base to the experiment restores conductance signatures (Figure 6.17C). This reversibility under changing pH confirms that the molecule is binding in its deprotonated form. The distinct conductance features in basic conditions are also clearly visible in the 2D histogram, in Figure 6.4C and agree with DFT calculated displacements in Figure 6.1 and 6.13.

To assign these peaks to binding geometries, we confirm that the deprotonated O can form bonds to gold in our junctions in basic pH. Prior measurements have documented the binding of O⁻ to undercoordinated Au upon deprotonation of carboxyl groups via pH and electrochemical methods.^{34, 109, 136, 164} We measure the conductance of pyO (left Figure 6.16, red trace) by dissolving pyOH into a pH 12 solution. The molecular signature shows a clear conductance peak in basic conditions. Notably, the conductance of the pyO peak is similar to peak G1 of pyzO. Both show an additional higher shoulder at ~ 1.5 times the conductance of the main peak when measured in solution, consistent with binding through a pyridine moiety. The histogram of pyO also has an additional higher shoulder at ~ 1.5

times the conductance of the main peak when measured in solution, consistent with binding through a pyridyl moiety (Figures 6.16 and 6.17).³³

Based on the similarity with these prior reports and transport calculated in Figure 6.3C, we assign the higher conducting peak of pyzO to the meta (N-O) channel where the molecule is bound through the oxygen at the 3 position. The lower conducting peak corresponds to binding through the para (N-N) pathway. Critically, this lower conductance peak occurs after additional pulling when the molecule can straighten in the junction, indicating that we have successfully turned on conductance through the para channel by inducing deprotonation of pyzOH through environmental pH.

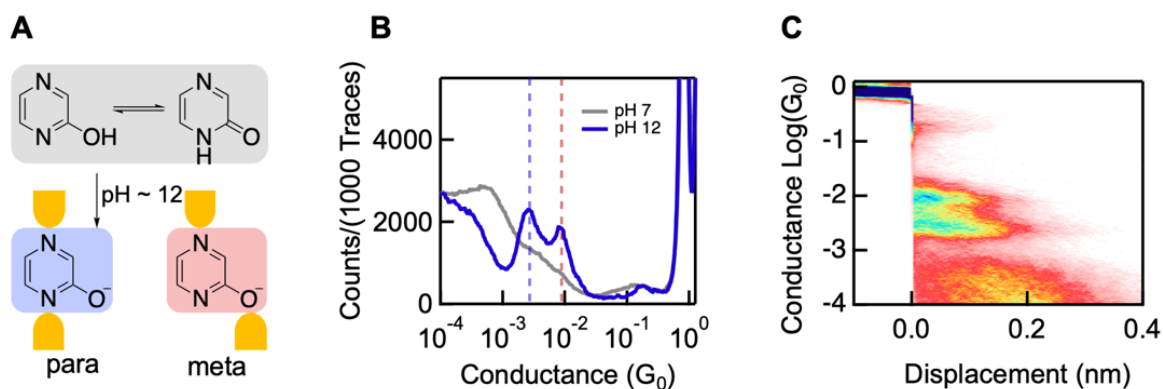


Figure 6.4. A) Molecular structures for pyzOH with predicted junction geometries through the para and meta pathways. B) 1D Conductance histogram of pyzOH measured in neutral conditions, pH ~ 7 (gray) and in basic conditions, pH ~ 12 (blue). C) 2D conductance histogram of pyzOH measured in basic conditions.

To summarize, the addition of the OH substituent to the meta position of the pyz ring modulates the DQI through the para channel. This synthetic modification coupled with deprotonation leads to an increase in conductance from null, or below the experimental limit of $\sim 10^{-6} G_0$ (Figure 6.2, green) to $\sim 2.6 \times 10^{-3} G_0$ as indicated by the blue dashed line in Figure 6.4B. Accounting for transport through the meta channel (red dashed line), we observe an overall conductance increase to $8.3 \times 10^{-3} G_0$ for pyzOH induced by pH.^{149, 165-169} This is significant for a molecule of this size ($\sim 4 \text{ \AA}$), with the conductance in the *on* state approaching $\sim 1\%$ of a fully open quantum channel.

6.4. Conclusion

In this work, we demonstrate QI between σ and π molecular orbitals which leads to distinct conductance phenomena in molecular junctions. This phenomenon is only possible in molecular junctions on the order of $\sim 5 \text{ \AA}$ where transport amplitudes across both types of MOs are comparable in magnitude. We show how modification of the benzene core alone can turn off conductance through the para channel by creating conditions for σ - π DQI. These insights suggest rules for how to synthetically engineer and tune short molecular systems to achieve junctions with desired QI features. Our work shows that the σ - π interference is sensitive to slight modifications in the molecular backbone due to reordering of the frontier MOs. Since frontier orbitals dominate transport, this slight change in the relative MO energies can lead to dramatic transport shifts. Having frontier σ and π orbitals also leads to additional sensitivity of the junction to mechanical modulation, as tilting the molecule alters the relative phase change through the σ and π system at the gold

links. We observe that molecular substituents can be leveraged to tune the symmetry of the π orbitals so that they become involved in transport and modulate QI features. Finally, our work shows that ionization through external pH control is a powerful way to modulate QI in molecular junctions. We demonstrate this experimentally by tuning DQI and the corresponding conductance through the para pathway in pyzOH via pH, resulting in junctions that switch between less than $0.001 G_0$ to $\sim 1\% G_0$. This work provides a platform for *in situ* manipulation of QI for the future engineering and design of molecular switching devices.

6.5. Experimental

Reagents (target molecules and solvents) were obtained commercially and used without further purification.

6.5.1. STMBJ Measurements

Break junction measurements were performed using a home-built STMBJ and experimental protocols established previously.^{24, 25} The Au tip and substrate are brought together forming a metallic contact. The junction is then stretched apart at 16 nm/s, while current is recorded under a constant bias of 500 mV. Measurements show steps at integer values of G_0 until the Au contact is broken, which correspond to the formation of Au contacts with integer number of Au atoms in the cross-section.²⁷ After the Au contact is broken a nano-gap is formed between the two Au electrodes which can interact with molecules via chemical linker groups. The measurement is repeated in the presence of target molecules in solution or deposited on the Au surface. At least 10,000 conductance traces showing the evolution of a junction as a function of displacement were compiled into histograms without data selection and normalized to enable comparison. Target molecules were dissolved in either 1,2,4-trichlorobenzene or H₂O, depending on solubility, and diluted to 1 mM concentrations. Measurements in H₂O were performed using a dropcast method as previously reported or in solution using a wax-coated tip.²⁵ The pH of the solution was adjusted using 1mM NaOH and 1mM HCl.

6.5.1. DFT Calculations

Density function theory (DFT) calculations for gas phase molecular orbitals were performed with Gaussian with PBE and B3LYP functionals and a Def2-TZVP basis set.^{119, 130, 131} Transport calculations were performed with FHI-aims and AITRANS with a PBE exchange correlation functional. A light level basis set was used for initial calculations to probe all junction geometries and final geometries were calculated with a tight level basis set.^{121, 122, 124} Pre-built Au(111) electrodes from the FHI-aims package were used. The Au₃₇ electrode consists of a gold pyramid with five layers and 35 atoms with two additional Au adatoms on the sides of pyramid. The molecule was first relaxed with Au₃₇ electrodes, frozen except for the molecule and four apex Au atoms on each electrode. The interaction (binding) energies between the electrode and molecule were calculated as the energy difference between the relaxed junction structure and the components of the junction relaxed separately (each electrode and the pyz molecule). Transmission across the junction as a function of energy at zero bias was calculated with non-equilibrium Green's Function using AITRANSS. Each Au electrode was then moved in or out in increments of 0.05 Å and the calculations are repeated.

6.6. Additional Data

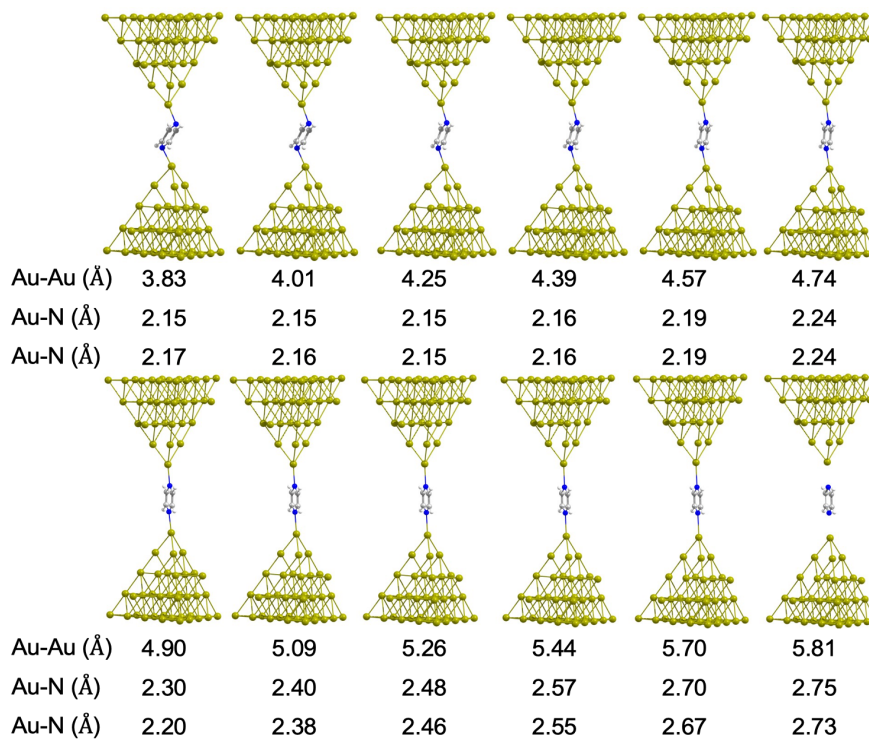


Figure 6.5. Pyz junction geometries and relevant junction lengths. Au-Au junction lengths are reported from edge to edge of the apex Au atoms. Au-N and Au-O bond lengths are reported from the center of the Au.

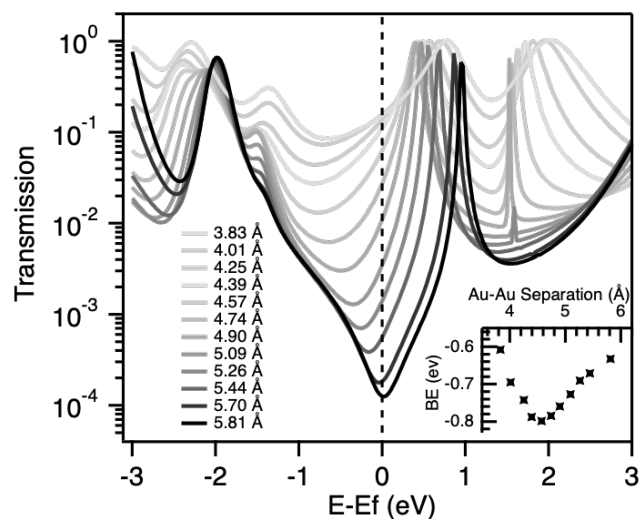


Figure 6.6. Transmission spectra and binding energy (inset) for all sampled geometries of pyz bridged between Au_{37} electrodes.

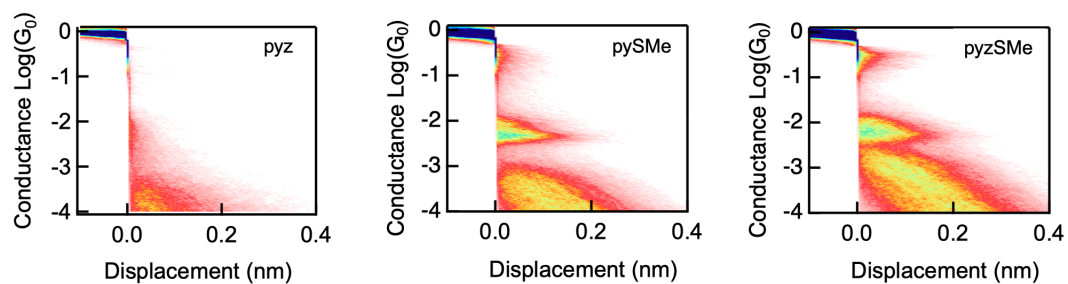


Figure 6.7. 2D conductance histograms of pyz, pySMe and pyzSMe (left to right).

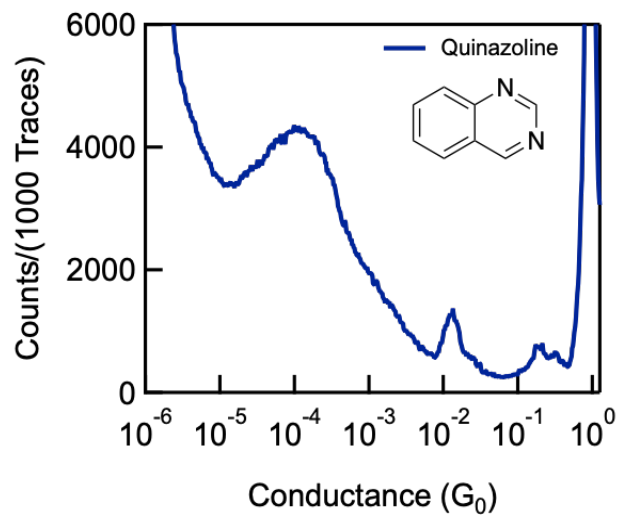


Figure 6.8. Conductance histogram of quinazoline, with N atoms in the 1, 3 positions (meta) of the ring. Measurements performed in a ~ 1 mM solution in 1,2,4-trichlorobenzene (TCB).

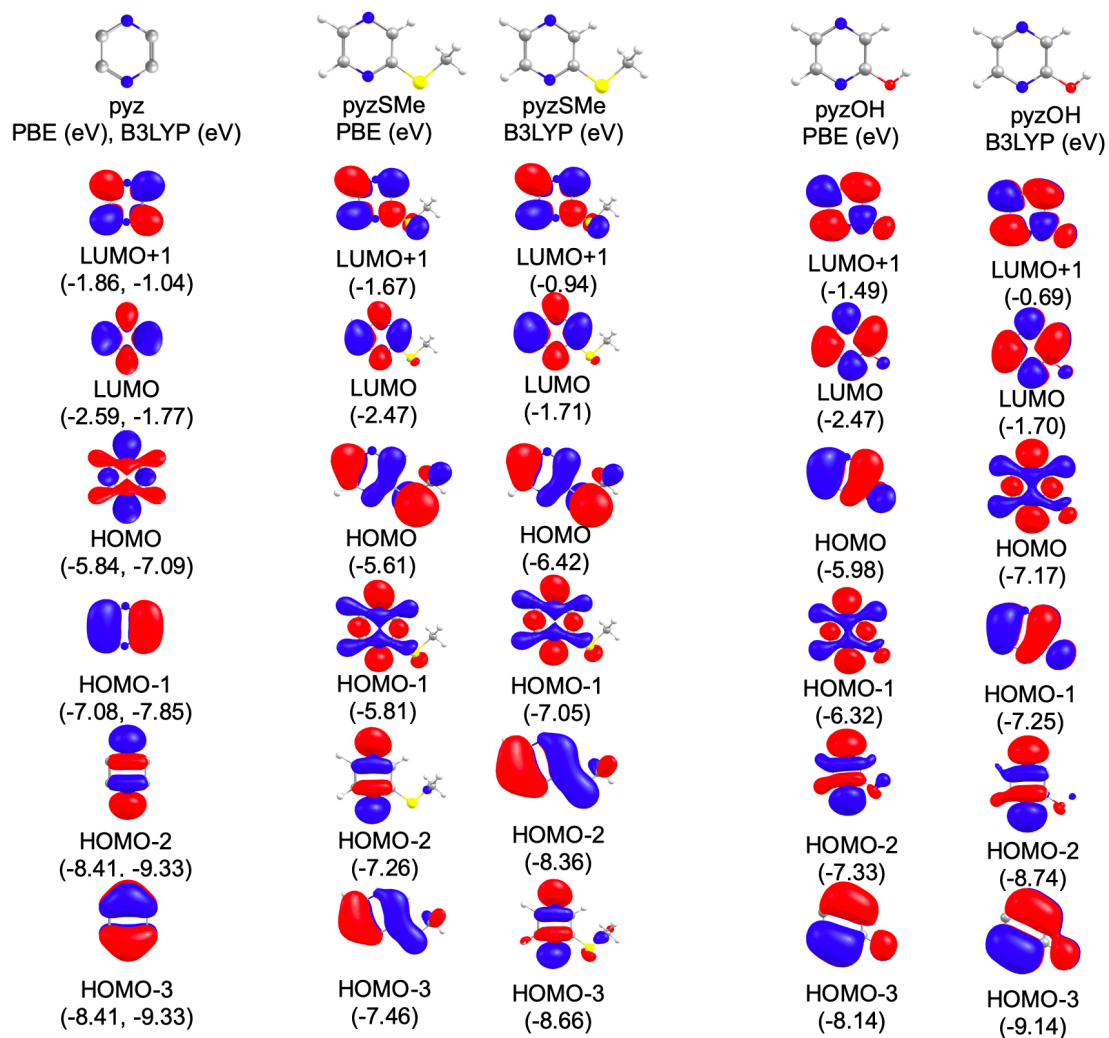


Figure 6.9. Frontier MOs of pyz and pyzOH at PBE and B3LYP level of theory with a Def2-TZVP basis set. Energies are reported in eV.

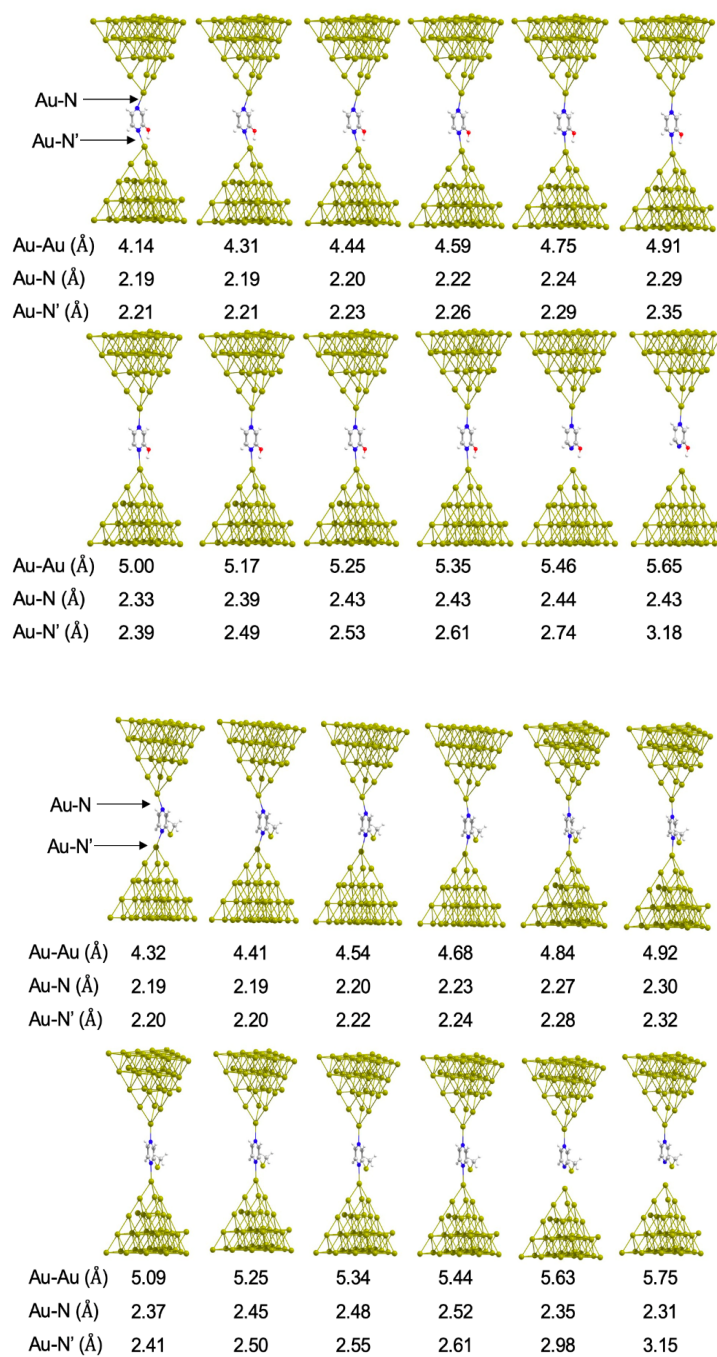


Figure 6.10. Junction geometries of pyzOH (top) and pyzSMe (top) and relevant junction lengths. Au-Au junction lengths are reported from edge to edge of the apex Au atoms. Au-N and Au-O bond lengths are reported from the center of the Au.

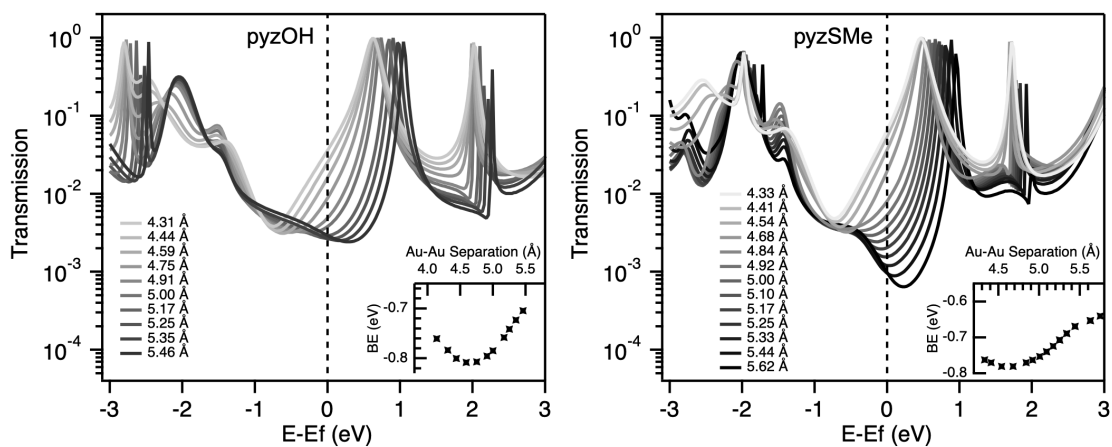


Figure 6.11. Transmission spectra and binding energy (inset) for all sampled geometries of pyzOH (left) and pyzSMe (right) bridged between Au_{37} electrodes.

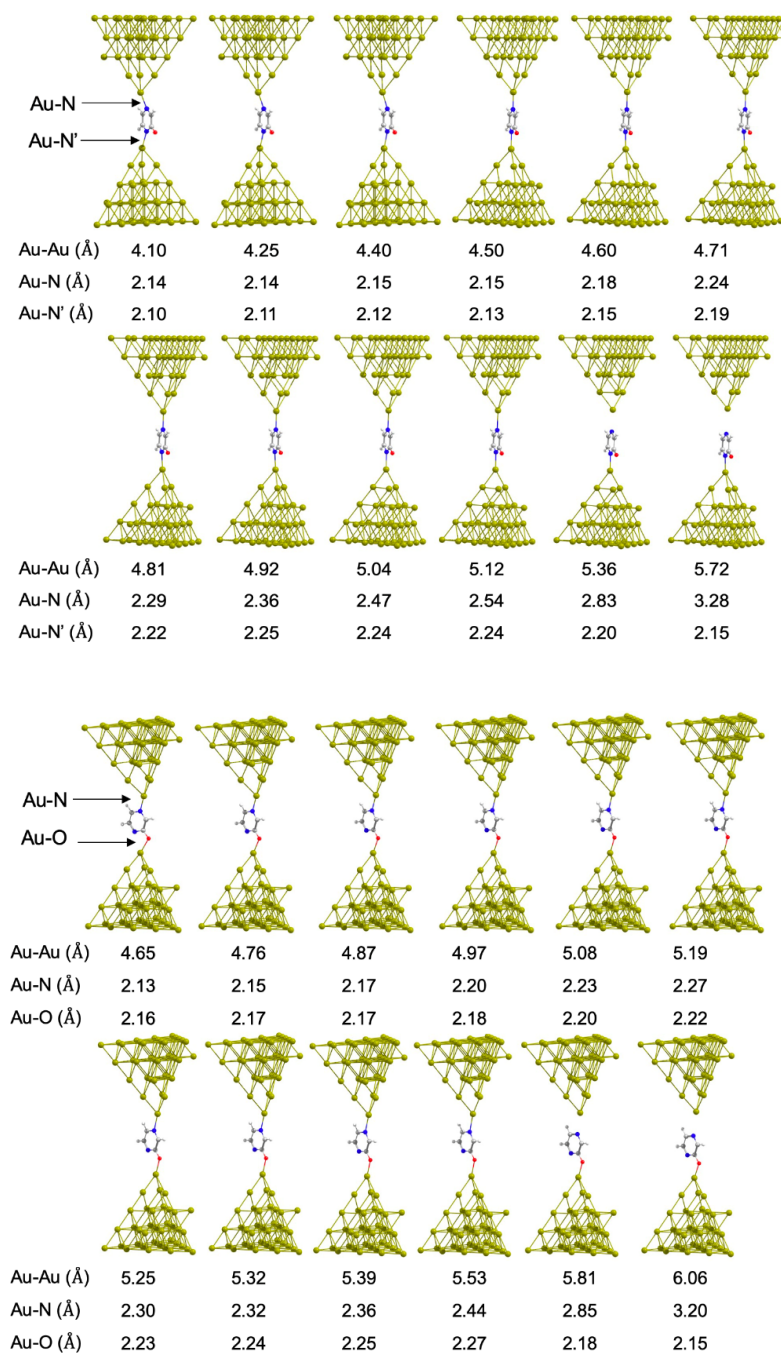


Figure 6.12. Junction geometries for pyzO para (top) and pyzO meta (top) and relevant junction lengths. Au-Au junction lengths are reported from edge to edge of the apex Au atoms. Au-N and Au-O bond lengths are reported from the center of the Au.

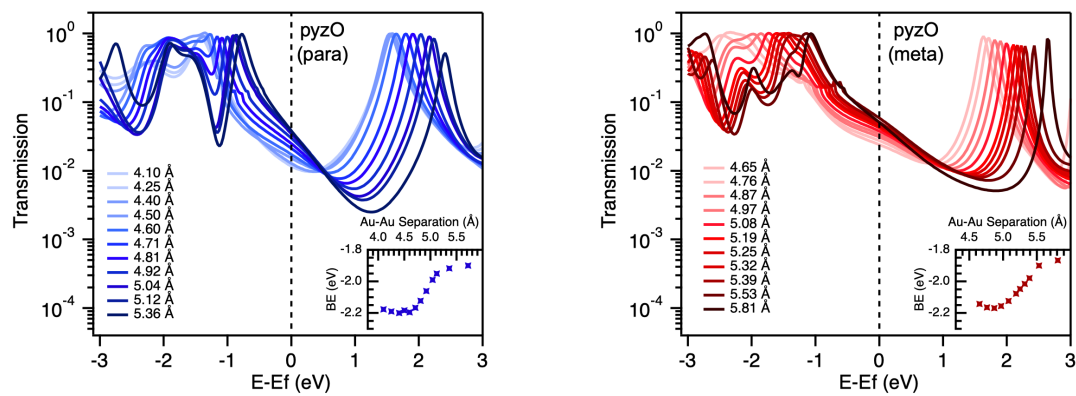


Figure 6.13. Transmission spectra and binding energy (inset) for all sampled geometries of pyzO para (left) and pyzO meta (right) bridged between Au₃₇ electrodes.

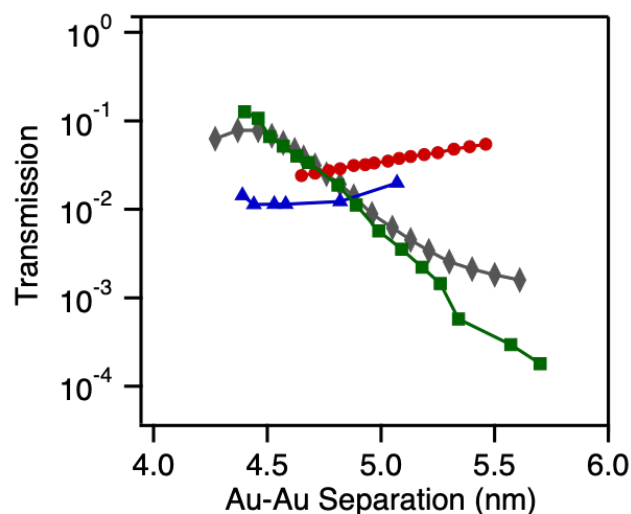


Figure 6.14. Calculated transmission at Fermi as a function of Au-Au distance, measured edge to edge, for pyz (green), pyzOH (gray), pyzO para (blue), pyzO meta (red).

The transmission at Fermi for all junction extensions is plotted for each molecule in Figure 6.14. Compared to the neutral molecules pyz (green) and pyzOH (gray), there is less change in transmission as a function of extension for the anion pyzO for both the para (blue) and meta (red) linked junctions. Additionally, the transmission through the meta channel is higher than the para channel at all calculated junction geometries.

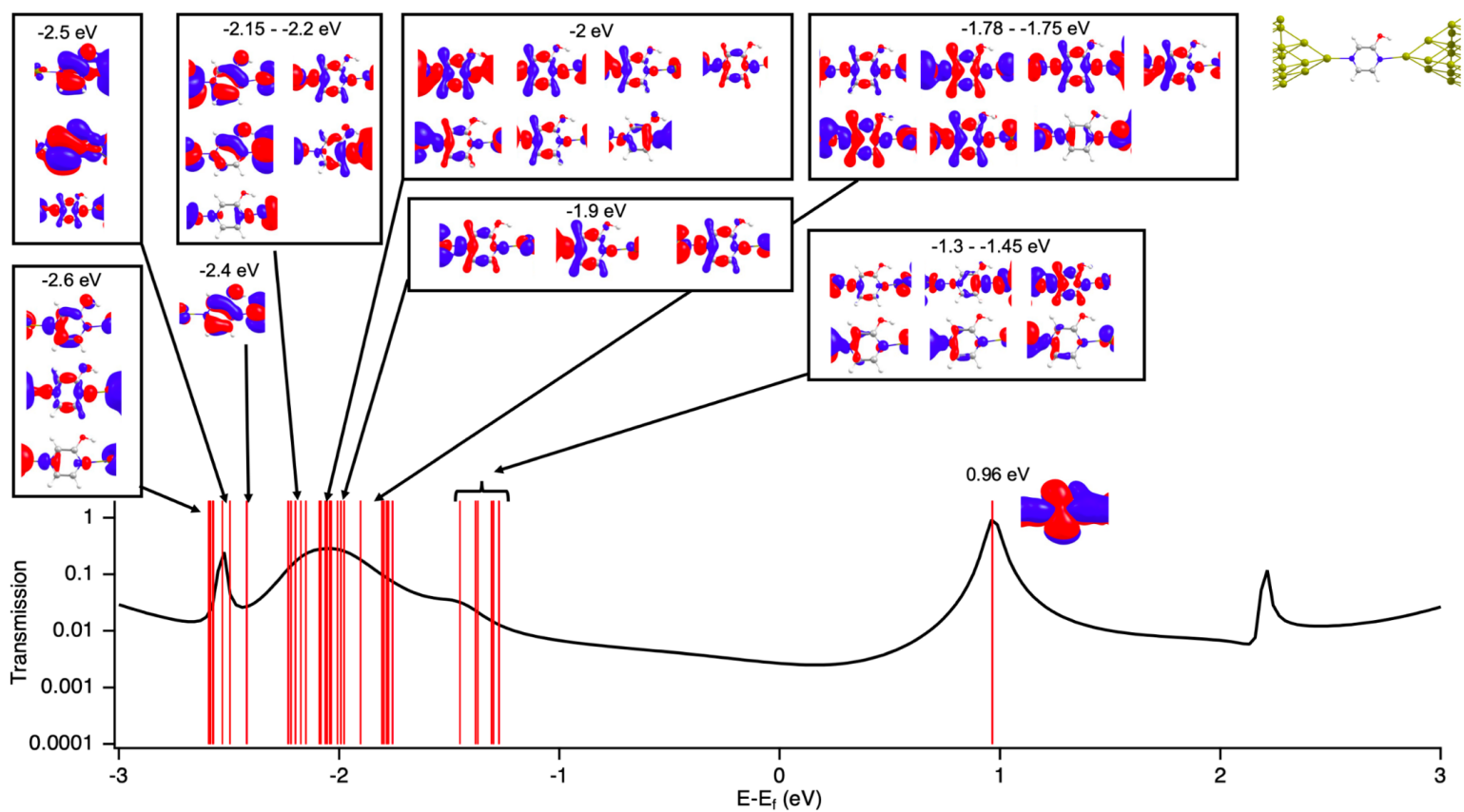


Figure 6.15. Isosurface plots of eigenchannels for the transmission of pyzOH bridged between two Au₃₇ electrodes with an Au-Au separation of 5.3 Å measured edge to edge (contour level 0.01).

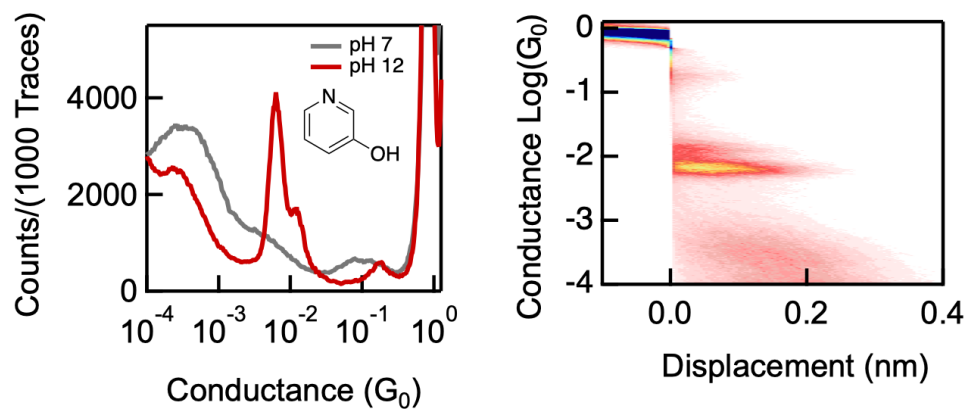


Figure 6.16. Conductance histogram for 3-hydroxypyridine (pyOH) in 1 mM aqueous solutions in pH \sim 7 (gray) and pH \sim 12 conditions (red) (right). 2D conductance histogram for pyzO (pyzOH measured in pH \sim 12 conditions (left)). Measurements were performed from H₂O solutions using the dropcast method.

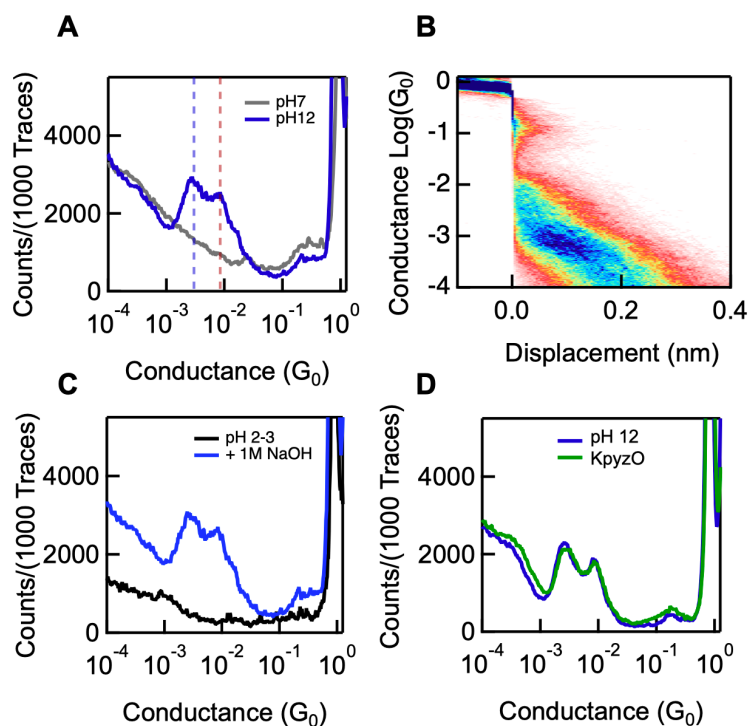


Figure 6.17. A) Single molecule conductance histogram of pyzOH in pH \sim 7 (gray) and pH \sim 12 conditions (blue), performed in H_2O solutions with a wax tip. B) 2D conductance histogram of pyzOH in pH \sim 7 conditions. C) Conductance histogram of pyzOH measurements in a H_2O solution with a wax-coated tip in acidic conditions (black) and after the addition of 30 μ L 1 mM NaOH. D) Conductance histogram of measurements of KpyzO, dropcast from a H_2O solution (green) compared to pyzO (pyzOH in basic conditions) (blue).

The potassium salt of pyzOH was prepared via the following: pyzOH and 1.1 equivalents of potassium hydroxide were stirred for two hours in ethanol. Off-white crystalline material was obtained from slow evaporation of the solvent which was then used for STMBJ measurement.

BIBLIOGRAPHY

LIST OF JOURNAL ABBREVIATIONS

Accounts of Chemical Research	Acc. Chem. Res.
ACS Applied Materials & Interfaces	ACS Appl. Mater. Interfaces
ACS Nano	ACS Nano
ACS Omega	ACS Omega
Acta Crystallographica Section B	Acta. Crystallogr. B.
Advanced Materials	Adv. Mater.
Advanced Materials Interfaces	Adv. Mater. Interfaces
Angewandte Chemie International Edition	Angew. Chem., Int. Ed.
Angewandte Chemie International Edition in English	Angew. Chem., Int. Ed. Engl.
Chemical Communications	Chem. Commun.
Chemical Reviews	Chem. Rev.
Chemical Science	Chem. Sci.
Chemical Society Reviews	Chem. Soc. Rev.
Chemistry – A European Journal	Chem. Eur. J.
Chemistry of Materials	Chem. Mater.
Computer Physics Communications	Comput. Phys. Commun.
Contemporary Physics	Comtemp. Phys.
Coordination Chemistry Reviews	Coord. Chem. Rev.
Dalton Transactions	Dalton Trans.
European Journal of Inorganic Chemistry	Eur. J. Inorg. Chem.

European Journal of Organic Chemistry	Eur. J. Org. Chem.
Fortschritte der Physik	Fortschir. Phys.
IBM Journal of Research and Development	IMB J. Res. Dev.
Inorganic Chemistry	Inorg. Chem.
Inorganic Chemistry Communications	Inorg. Chem. Commun.
Inorganic Chemistry Frontiers	Inorg. Chem. Front.
Inorganica Chimica Acta	Inorg. Chim. Acta.
Journal of Chemical Crystallography	J. Chem. Crystallogr.
Journal of Chemical Theory and Computation	J. Chem. Theory Comput.
Journal of Coordination Chemistry	J. Coord. Chem.
Journal of Magnetic Resonance (1969)	J. Magn. Reson.
Journal of Materials Chemistry	J. Mater. Chem.
Journal of Materials Chemistry C	J. Mater. Chem. C.
Journal of Organometallic Chemistry	J. Organomet. Chem.
Journal of Physics Condensed Matter	J. Condens. Matter Phys.
Journal of Solid State Chemistry	J. Solid State Chem.
Journal of the American Chemical Society	J. Am. Chem. Soc.
Journal of the Chemical Society (Resumed)	J. Chem. Soc.
Journal of the Chemical Society, Dalton Transactions	J. Chem. Soc., Dalton Trans.
Molecules	Molecules
Nano Letters	Nano Lett.
Nanoscale	Nanoscale

Nat Nanotechnol	Nat. Nanotechnol.
Nature	Nature
Nature Chemistry	Nat. Chem.
Nature Communications	Nat. Commun.
Nature Materials	Nat. Mater.
Nature Nanotechnology	Nat. Nanotechnol.
Nature Reviews Chemistry	Nat. Rev. Chem.
Nature Reviews Materials	Nat. Rev. Mater.
Nature Reviews Physics	Nat. Rev. Phys.
New Journal of Physics	New J. Phys.
Organometallics	Organometallics
Physical Chemistry Chemical Physics	Phy. Chem. Chem. Phys.
Physical Review B	Phys. Rev. B
Physical Review Letters	Phys. Rev. Lett.
Physics Letters A	Phys. Chem. A
Polyhedron	Polyhedron
Proceedings of the National Academy of Sciences	PNAS
Reviews of Modern Physics	Rev. Mod. Phys.
Science	Science
Science Advances	Sci. Adv.
Scientific Reports	Sci. Rep.
Synthesis	Synthesis

Tetrahedron Letters	Tetrahedron Lett.
The Journal of Chemical Physics	J. Chem. Phys.
The Journal of Physical Chemistry C	J. Phys. Chem. C
The Journal of Physical Chemistry Letters	J. Phys. Chem. Lett.
Zeitschrift für Technische Physik	Z. Tech. Phys.

REFERENCES

1. Nitzan, A.; Ratner, M. A., *Science* **2003**, *300* (5624), 1384-9.
2. Sun, L.; Diaz-Fernandez, Y. A.; Gschneidner, T. A.; Westerlund, F.; Lara-Avila, S.; Moth-Poulsen, K., *Chem. Soc. Rev.* **2014**, *43* (21), 7378-7411.
3. Evers, F.; Korytár, R.; Tewari, S.; van Ruitenbeek, J. M., *Rev. Mod. Phys.* **2020**, *92* (3), 035001.
4. Li, T.; Bandari, V. K.; Schmidt, O. G., *Adv. Mater.* **2022**, 2209088.
5. Park, Y. S.; Whalley, A. C.; Kamenetska, M.; Steigerwald, M. L.; Hybertsen, M. S.; Nuckolls, C.; Venkataraman, L., *J. Am. Chem. Soc.* **2007**, *129* (51), 15768-15769.
6. Su, T. A.; Neupane, M.; Steigerwald, M. L.; Venkataraman, L.; Nuckolls, C., *Nat. Rev. Mater.* **2016**, *1* (3), 16002.
7. Xin, N.; Guan, J.; Zhou, C.; Chen, X.; Gu, C.; Li, Y.; Ratner, M. A.; Nitzan, A.; Stoddart, J. F.; Guo, X., *Nat. Rev. Phys.* **2019**, *1* (3), 211-230.
8. Zhang, J. L.; Zhong, J. Q.; Lin, J. D.; Hu, W. P.; Wu, K.; Xu, G. Q.; Wee, A. T. S.; Chen, W., *Chemical Society Reviews* **2015**, *44* (10), 2998-3022.
9. Aragonès, A. C.; Aravena, D.; Cerdá, J. I.; Acís-Castillo, Z.; Li, H.; Real, J. A.; Sanz, F.; Hihath, J.; Ruiz, E.; Díez-Pérez, I., *Nano Lett.* **2016**, *16* (1), 218-226.
10. Jasper-Toennies, T.; Gruber, M.; Karan, S.; Jacob, H.; Tucek, F.; Berndt, R., *Nano Lett.* **2017**, *17* (11), 6613-6619.
11. Köbke, A.; Gutzeit, F.; Röhrich, F.; Schlimm, A.; Grunwald, J.; Tucek, F.; Studniarek, M.; Longo, D.; Choueikani, F.; Otero, E.; Ohresser, P.; Rohlf, S.; Johannsen, S.; Diekmann, F.; Rosnagel, K.; Weismann, A.; Jasper-Toennies, T.;

- Näther, C.; Herges, R.; Berndt, R.; Gruber, M., *Nature Nanotechnology* **2020**, *15* (1), 18-21.
12. Rocha, A. R.; García-suárez, V. M.; Bailey, S. W.; Lambert, C. J.; Ferrer, J.; Sanvito, S., *Nat. Mater.* **2005**, *4* (4), 335-339.
13. Wasielewski, M. R.; Forbes, M. D. E.; Frank, N. L.; Kowalski, K.; Scholes, G. D.; Yuen-Zhou, J.; Baldo, M. A.; Freedman, D. E.; Goldsmith, R. H.; Goodson, T.; Kirk, M. L.; McCusker, J. K.; Ogilvie, J. P.; Shultz, D. A.; Stoll, S.; Whaley, K. B., *Nature Reviews Chemistry* **2020**, *4* (9), 490-504.
14. Miller, J. S., *Extended Linear Chain Compounds*. Plenum Press, New York, 1982; Vol. 1-3.
15. Bera, J. K.; Dunbar, K. R., *Angew. Chem., Int. Ed.* **2002**, *41* (23), 4453-4457.
16. Blundell, S. J., *Comtemp. Phys.* **2007**, *48* (5), 275-290.
17. Gunasekaran, S.; Greenwald, J. E.; Venkataraman, L., *Nano Lett.* **2020**, *20* (4), 2843-2848.
18. Liu, S.-X.; Ismael, A. K.; Al-Jobory, A.; Lambert, C. J., *Acc. Chem. Res.* **2023**, *56* (3), 322-331.
19. Garner, M. H.; Li, H.; Chen, Y.; Su, T. A.; Shangguan, Z.; Paley, D. W.; Liu, T.; Ng, F.; Li, H.; Xiao, S.; Nuckolls, C.; Venkataraman, L.; Solomon, G. C., *Nature* **2018**, *558* (7710), 415-419.
20. Zhang, B.; Garner, M. H.; Li, L.; Campos, L. M.; Solomon, G. C.; Venkataraman, L., *Chem. Sci.* **2021**, *12* (30), 10299-10305.

21. Frisenda, R.; Janssen, V. A. E. C.; Grozema, F. C.; van der Zant, H. S. J.; Renaud, N., *Nat. Chem.* **2016**, *8* (12), 1099-1104.
22. Zhu, Y.; Zhou, Y.; Ren, L.; Ye, J.; Wang, H.; Liu, X.; Huang, R.; Liu, H.; Liu, J.; Shi, J.; Gao, P.; Hong, W., *Angew. Chem., Int. Ed.* **2023**, *62* (19), e202302693.
23. Xu, B.; Tao, N. J., *Science* **2003**, *301* (5637), 1221-1223.
24. Kamenetska, M.; Koentopp, M.; Whalley, A. C.; Park, Y. S.; Steigerwald, M. L.; Nuckolls, C.; Hybertsen, M. S.; Venkataraman, L., *Phys. Rev. Lett.* **2009**, *102* (12), 126803.
25. Pan, X.; Lawson, B.; Rustad, A. M.; Kamenetska, M., *Nano Lett.* **2020**, *20* (6), 4687-4692.
26. Landauer, R., *IMB J. Res. Dev.* **1957**, *1* (3), 223-231.
27. Yanson, A. I.; Bollinger, G. R.; van den Brom, H. E.; Agraït, N.; van Ruitenbeek, J. M., *Nature* **1998**, *395* (6704), 783-785.
28. Kaliginedi, V.; V. Rudnev, A.; Moreno-García, P.; Baghernejad, M.; Huang, C.; Hong, W.; Wandlowski, T., *Phy. Chem. Chem. Phys.* **2014**, *16* (43), 23529-23539.
29. McNeely, J.; Miller, N.; Pan, X.; Lawson, B.; Kamenetska, M., *J. Phys. Chem. C* **2020**, *124* (24), 13427-13433.
30. Fu, T.; Frommer, K.; Nuckolls, C.; Venkataraman, L., *J. Phys. Chem. Lett.* **2021**, *12* (44), 10802-10807.
31. Arroyo, C. R.; Leary, E.; Castellanos-Gómez, A.; Rubio-Bollinger, G.; González, M. T.; Agraït, N., *J. Am. Chem. Soc.* **2011**, *133* (36), 14313-14319.

32. Leary, E.; Zotti, L. A.; Miguel, D.; Márquez, I. R.; Palomino-Ruiz, L.; Cuerva, J. M.; Rubio-Bollinger, G.; González, M. T.; Agrait, N., *J. Phys. Chem. C* **2018**, *122* (6), 3211-3218.
33. Kamenetska, M.; Quek, S. Y.; Whalley, A. C.; Steigerwald, M. L.; Choi, H. J.; Louie, S. G.; Nuckolls, C.; Hybertsen, M. S.; Neaton, J. B.; Venkataraman, L., *J. Am. Chem. Soc.* **2010**, *132* (19), 6817-6821.
34. Chen, F.; Li, X.; Hihath, J.; Huang, Z.; Tao, N., *J. Am. Chem. Soc.* **2006**, *128* (49), 15874-15881.
35. van Veen, F. H.; Ornago, L.; van der Zant, H. S. J.; El Abbassi, M., *J. Phys. Chem. C* **2022**, *126* (20), 8801-8806.
36. Xiao; Xu; Tao, N. J., *Nano Lett.* **2004**, *4* (2), 267-271.
37. Quek, S. Y.; Venkataraman, L.; Choi, H. J.; Louie, S. G.; Hybertsen, M. S.; Neaton, J. B., *Nano Lett.* **2007**, *7* (11), 3477-3482.
38. O'Driscoll, L. J.; Bryce, M. R., *Nanoscale* **2021**, *13* (24), 10668-10711.
39. Higgins, S. J.; Nichols, R. J., *Polyhedron* **2018**, *140*, 25-34.
40. Berry, J. F.; Cotton, F. A.; Lei, P.; Lu, T.; Murillo, C. A., *Inorg. Chem.* **2003**, *42* (11), 3534-3539.
41. Hua, S.-A.; Cheng, M.-C.; Chen, C.-h.; Peng, S.-M., *Eur. J. Inorg. Chem.* **2015**, *2015* (15), 2498-2498.
42. Bock, S.; Al-Owaedi, O. A.; Eaves, S. G.; Milan, D. C.; Lemmer, M.; Skelton, B. W.; Osorio, H. M.; Nichols, R. J.; Higgins, S. J.; Cea, P.; Long, N. J.; Albrecht, T.; Martín, S.; Lambert, C. J.; Low, P. J., *Chem. Eur. J.* **2017**, *23* (9), 2133-2143.

43. Duan, P.; Liu, J.; Wang, J.-Y.; Chen, L.; Wang, F.; Zhang, Q.-C.; Hong, W.; Chen, Z.-N., *J. Mater. Chem. C* **2019**, *7* (24), 7259-7266.
44. Pal, A. N.; Li, D.; Sarkar, S.; Chakrabarti, S.; Vilan, A.; Kronik, L.; Smogunov, A.; Tal, O., *Nat. Commun.* **2019**, *10* (1), 5565.
45. Camarasa-Gómez, M.; Hernangómez-Pérez, D.; Inkpen, M. S.; Lovat, G.; Fung, E. D.; Roy, X.; Venkataraman, L.; Evers, F., *Nano Lett.* **2020**, *20* (9), 6381-6386.
46. Lawson, B.; Zahl, P.; Hybertsen, M. S.; Kamenetska, M., *J. Am. Chem. Soc.* **2022**, *144* (14), 6504-6515.
47. Rohlf, S.; Gruber, M.; Flöser, B. M.; Grunwald, J.; Jarausch, S.; Diekmann, F.; Kalläne, M.; Jasper-Toennies, T.; Buchholz, A.; Plass, W.; Berndt, R.; Tuczek, F.; Rossnagel, K., *J. Phys. Chem. Lett.* **2018**, *9* (7), 1491-1496.
48. Ossinger, S.; Naggert, H.; Kipgen, L.; Jasper-Toennies, T.; Rai, A.; Rudnik, J.; Nickel, F.; Arruda, L. M.; Bernien, M.; Kuch, W.; Berndt, R.; Tuczek, F., *J. Phys. Chem. C* **2017**, *121* (2), 1210-1219.
49. Knaak, T.; González, C.; Dappe, Y. J.; Harzmann, G. D.; Brandl, T.; Mayor, M.; Berndt, R.; Gruber, M., *J. Phys. Chem. C* **2019**, *123* (7), 4178-4185.
50. Rohlf, S.; Grunwald, J.; Jasper-Toennies, T.; Johannsen, S.; Diekmann, F.; Studniarek, M.; Berndt, R.; Tuczek, F.; Rossnagel, K.; Gruber, M., *J. Phys. Chem. C* **2019**, *123* (29), 17774-17780.
51. Miller, J. S.; Epstein, A. J., *One-dimensional inorganic complexes. Prog. Inorg. Chem.* 1976; Vol. 20.

52. Jang, K.; Jung, I. G.; Nam, H. J.; Jung, D.-Y.; Son, S. U., *J. Am. Chem. Soc.* **2009**, *131* (34), 12046-12047.
53. Chen, Y.; Li, K.; Lloyd, H. O.; Lu, W.; Chui, S. S.-Y.; Che, C.-M., *Angew. Chem., Int. Ed.* **2010**, *49* (51), 9968-9971.
54. Campbell, M. G.; Powers, D. C.; Raynaud, J.; Graham, M. J.; Xie, P.; Lee, E.; Ritter, T., *Nat. Chem.* **2011**, *3* (12), 949-953.
55. Campbell, M. G.; Zheng, S.-L.; Ritter, T., *Inorg. Chem.* **2013**, *52* (23), 13295-13297.
56. Chen, Y.; Cheng, G.; Li, K.; Shelar, D. P.; Lu, W.; Che, C.-M., *Chem. Sci.* **2014**, *5* (4), 1348-1353.
57. Cotton, F. A.; Dikarev, E. V.; Petrukhina, M. A., *J. Organomet. Chem.* **2000**, *596* (1), 130-135.
58. Pruchnik, F. P.; Jakimowicz, P.; Ciunik, Z.; Stanislawek, K.; Oro, L. A.; Tejel, C.; Ciriano, M. A., *Inorg. Chem. Commun.* **2001**, *4* (1), 19-22.
59. Krogmann, K., *Angew. Chem., Int. Ed. Engl.* **1969**, *8* (1), 35-42.
60. Alexandrov, E. V.; Virovets, A. V.; Blatov, V. A.; Peresypkina, E. V., *Chem. Rev.* **2015**, *115* (22), 12286-12319.
61. Wei, R.-M.; Cao, F.; Li, J.; Yang, L.; Han, Y.; Zhang, X.-L.; Zhang, Z.; Wang, X.-Y.; Song, Y., *Sci. Rep.* **2016**, *6* (1), 24372.
62. Guillet, J. L.; Bhowmick, I.; Shores, M. P.; Daley, C. J. A.; Gembicky, M.; Golen, J. A.; Rheingold, A. L.; Doerrer, L. H., *Inorg. Chem.* **2016**, *55* (16), 8099-8109.

63. Yamada, T.; Sadakiyo, M.; Kitagawa, H., *J. Am. Chem. Soc.* **2009**, *131* (9), 3144-3145.
64. Nimthong-Roldán, A.; Guillet, J. L.; McNeely, J.; Ozumerzifon, T. J.; Shores, M. P.; Golen, J. A.; Rheingold, A. L.; Doerrler, L. H., *Dalton Trans.* **2017**, *46* (17), 5546-5557.
65. Lu, J.; Yu, C.; Niu, T.; Paliwala, T.; Crisci, G.; Somosa, F.; Jacobson, A. J., *Inorg. Chem.* **1998**, *37* (18), 4637-4640.
66. Bogani, L.; Vindigni, A.; Sessoli, R.; Gatteschi, D., *J. Mater. Chem.* **2008**, *18* (40), 4750-4758.
67. Cassaro, R. A. A.; Reis, S. G.; Araujo, T. S.; Lahti, P. M.; Novak, M. A.; Vaz, M. G. F., *Inorg. Chem.* **2015**, *54* (19), 9381-9383.
68. Sun, H.-L.; Wang, Z.-M.; Gao, S., *Coord. Chem. Rev.* **2010**, *254* (9), 1081-1100.
69. Clérac, R.; Miyasaka, H.; Yamashita, M.; Coulon, C., *J. Am. Chem. Soc.* **2002**, *124* (43), 12837-12844.
70. Uemura, K.; Takamori, A., *Coord. Chem. Rev.* **2022**, *471*, 214736.
71. Pearson, R. G., *J. Am. Chem. Soc.* **1963**, *85* (22), 3533-3539.
72. Baddour, F. G.; Fiedler, S. R.; Shores, M. P.; Bacon, J. W.; Golen, J. A.; Rheingold, A. L.; Doerrler, L. H., *Inorg. Chem.* **2013**, *52* (23), 13562-13575.
73. Beach, S. A.; Doerrler, L. H., *Acc. Chem. Res.* **2018**, *51* (5), 1063-1072.
74. Beach, S. A.; Doerrler, L. H., *Accounts of Chemical Research* **2019**, *52* (9), 2756-2756.

75. Beach, S.; Zuckerman, L.; Portillo, R.; Shores, M.; Rheingold, A.; Doerr, L., *Inorg. Chim. Acta.* **2019**, *493*, 81-90.
76. Beach, S. A.; Guillet, J. L.; Lagueux, S. P.; Perfetti, M.; Livesay, B. N.; Shores, M. P.; Bacon, J. W.; Rheingold, A. L.; Arnold, P. L.; Doerr, L. H., *Chem. Commun.* **2020**, *56* (75), 11062-11065.
77. Dahl, E. W.; Baddour, F. G.; Fiedler, S. R.; Hoffert, W. A.; Shores, M. P.; Yee, G. T.; Djukic, J.-P.; Bacon, J. W.; Rheingold, A. L.; Doerr, L. H., *Chem. Sci.* **2012**, *3* (2), 602-609.
78. Baddour, F. G.; Fiedler, S. R.; Shores, M. P.; Golen, J. A.; Rheingold, A. L.; Doerr, L. H., *Inorg. Chem.* **2013**, *52* (9), 4926-4933.
79. Baddour, F. G. Platinum-Containing Heterobimetallic Lantern Complexes Prepared with Thiocarboxylates: Synthesis, Structural, and Magnetic Characterization and Synthesis Characterization of Magnetic Metal Oxide Nanoparticles. Boston University, 2013.
80. Sandoval-Olivares, Z.; Solis-Céspedes, E.; Páez-Hernández, D., *Inorg. Chem.* **2022**, *61* (3), 1401-1417.
81. Cotton, F. A.; Wilkinson, G.; Murillo, C. A.; Bochmann, M., *Advanced Inorganic Chemistry*. 6 ed.; Wiley, New York: 1999.
82. Guillet, J. Quasi 1D Chains of Pt-containing Heterobimetallic Lantern Complexes and Resultant Properties. Boston University, 2018.
83. Skipper, H. E.; May, C. V.; Rheingold, A. L.; Doerr, L. H.; Kamenetska, M., *J. Am. Chem. Soc.* **2021**, *143* (40), 16439-16447.

84. Evans, D. F., *J. Chem. Soc.* **1959**, (0), 2003-2005.
85. Little, B. F.; Long, G. J., *Inorg. Chem.* **1978**, *17* (12), 3401-3413.
86. Lemercier, G.; Mulliez, E.; Brouca-Cabarrecq, C.; Dahan, F.; Tuchagues, J.-P., *Inorg. Chem.* **2004**, *43* (6), 2105-2113.
87. Yergeshbayeva, S.; Hrudka, J. J.; Lengyel, J.; Erkasov, R.; Stoian, S. A.; Dragulescu-Andrasi, A.; Shatruck, M., *Inorg. Chem.* **2017**, *56* (18), 11096-11103.
88. Kelly, N. D.; Dutton, S. E., *Inorg. Chem.* **2020**, *59* (13), 9188-9195.
89. Yip, H.-K.; Cheng, L.-K.; Cheung, K.-K.; Che, C.-M., *J. Chem. Soc., Dalton Trans.* **1993**, (19), 2933-2938.
90. Baddour, F. G.; Kahn, M. I.; Golen, J. A.; Rheingold, A. L.; Doerrer, L. H., *Chem. Commun.* **2010**, *46* (27), 4968-4970.
91. Lloret, F.; Julve, M.; Cano, J.; Ruiz-García, R.; Pardo, E., *Inorg. Chim. Acta.* **2008**, *361* (12), 3432-3445.
92. Haddad, M. S.; Hendrickson, D. N.; Cannady, J. P.; Drago, R. S.; Bieksza, D. S., *J. Am. Chem. Soc.* **1979**, *101* (4), 898-906.
93. Kubelka, P.; Munk, F., *Z. Tech. Phys.* **1931**, *12*, 593-601.
94. Carlin, R. L., *Magnetochemistry*. Springer-Verlag, Berlin: 1986.
95. Hybertsen, M. S.; Venkataraman, L., *Acc. Chem. Res.* **2016**, *49* (3), 452-460.
96. Liu, K.; Wang, X.; Wang, F., *ACS Nano* **2008**, *2* (11), 2315-2323.
97. Yeh CY., W. C., Chen CH., Peng SM., Molecular Metal Wires Built from a Linear Metal Atom Chain Supported by Oligopyridylamido Ligands. In *Redox Systems Under Nano-Space Control*, Springer: Berlin, Heidelberg, 2006; pp 85-117.

98. Thiele, S.; Balestro, F.; Ballou, R.; Klyatskaya, S.; Ruben, M.; Wernsdorfer, W., *Science* **2014**, *344* (6188), 1135-1138.
99. Frisenda, R.; Harzmann, G. D.; Celis Gil, J. A.; Thijssen, J. M.; Mayor, M.; van der Zant, H. S. J., *Nano Lett.* **2016**, *16* (8), 4733-4737.
100. Karuppanan, S. K.; Martín-Rodríguez, A.; Ruiz, E.; Harding, P.; Harding, D. J.; Yu, X.; Tadich, A.; Cowie, B.; Qi, D.; Nijhuis, C. A., *Chem. Sci.* **2021**, *12*, 2381-2388.
101. Graham, M. J.; Zadrozny, J. M.; Fataftah, M. S.; Freedman, D. E., *Chemistry of Materials* **2017**, *29* (5), 1885-1897.
102. Hua, S.-A.; Cheng, M.-C.; Chen, C.-h.; Peng, S.-M., *Eur. J. Inorg. Chem.* **2015**, *2015* (15), 2510-2523.
103. Uemura, K.; Ito, D.; Pirillo, J.; Hijikata, Y.; Saeki, A., *ACS Omega* **2020**, *5* (47), 30502-30518.
104. Frei, M.; Aradhya, S. V.; Koentopp, M.; Hybertsen, M. S.; Venkataraman, L., *Nano Lett.* **2011**, *11* (4), 1518-1523.
105. Frei, M.; Aradhya, S. V.; Hybertsen, M. S.; Venkataraman, L., *J. Am. Chem. Soc.* **2012**, *134* (9), 4003-4006.
106. Xue, Y.; Li, X.; Li, H.; Zhang, W., *Nat. Commun.* **2014**, *5* (1), 4348.
107. Groom, C. R.; Bruno, I. J.; Lightfoot, M. P.; Ward, S. C., *Acta Crystallogr. B.* **2016**, *72* (2), 171-179.
108. Housecroft, C. E.; Sharpe, A. G., *Inorganic Chemistry*. 4 ed.; Pearson: 2012; p 235-236.

109. Ahn, S.; Aradhya, S. V.; Klausen, R. S.; Capozzi, B.; Roy, X.; Steigerwald, M. L.; Nuckolls, C.; Venkataraman, L., *Phy. Chem. Chem. Phys.* **2012**, *14* (40), 13841-13845.
110. Aradhya, S. V.; Frei, M.; Hybertsen, M. S.; Venkataraman, L., *Nat. Mater.* **2012**, *11* (10), 872-876.
111. Venkataraman, L.; Klare, J. E.; Tam, I. W.; Nuckolls, C.; Hybertsen, M. S.; Steigerwald, M. L., *Nano Lett.* **2006**, *6* (3), 458-462.
112. Li, C.; Pobelov, I.; Wandlowski, T.; Bagrets, A.; Arnold, A.; Evers, F., *J. Am. Chem. Soc.* **2008**, *130* (1), 318-326.
113. Häkkinen, H., *Nat. Chem.* **2012**, *4* (6), 443-455.
114. Quek, S. Y.; Kamenetska, M.; Steigerwald, M. L.; Choi, H. J.; Louie, S. G.; Hybertsen, M. S.; Neaton, J. B.; Venkataraman, L., *Nat. Nanotechnol.* **2009**, *4* (4), 230-234.
115. Roldan, D.; Kaliginedi, V.; Cobo, S.; Kolivoska, V.; Bucher, C.; Hong, W.; Royal, G.; Wandlowski, T., *J. Am. Chem. Soc.* **2013**, *135* (16), 5974-5977.
116. Venkataraman, L.; Klare, J. E.; Nuckolls, C.; Hybertsen, M. S.; Steigerwald, M. L., *Nature* **2006**, *442* (7105), 904-907.
117. Umakoshi, K.; Kinoshita, I.; Ichimura, A.; Ooi, S., *Inorg. Chem.* **1987**, *26* (21), 3551-3556.
118. Brandl, T.; El Abbassi, M.; Stefani, D.; Frisenda, R.; Harzmann, G. D.; van der Zant, H. S. J.; Mayor, M., *Eur. J. Org. Chem.* **2019**, *2019* (31-32), 5334-5343.

119. Frisch, M. J.; Trucks, G. W.; Schlegel, H. B.; Scuseria, G. E.; Robb, M. A.; Cheeseman, J. R.; Scalmani, G.; Barone, V.; Petersson, G. A.; Nakatsuji, H.; Li, X.; Caricato, M.; Marenich, A. V.; Bloino, J.; Janesko, B. G.; Gomperts, R.; Mennucci, B.; Hratchian, H. P.; Ortiz, J. V.; Izmaylov, A. F.; Sonnenberg, J. L.; Williams; Ding, F.; Lipparini, F.; Egidi, F.; Goings, J.; Peng, B.; Petrone, A.; Henderson, T.; Ranasinghe, D.; Zakrzewski, V. G.; Gao, J.; Rega, N.; Zheng, G.; Liang, W.; Hada, M.; Ehara, M.; Toyota, K.; Fukuda, R.; Hasegawa, J.; Ishida, M.; Nakajima, T.; Honda, Y.; Kitao, O.; Nakai, H.; Vreven, T.; Throssell, K.; Montgomery Jr., J. A.; Peralta, J. E.; Ogliaro, F.; Bearpark, M. J.; Heyd, J. J.; Brothers, E. N.; Kudin, K. N.; Staroverov, V. N.; Keith, T. A.; Kobayashi, R.; Normand, J.; Raghavachari, K.; Rendell, A. P.; Burant, J. C.; Iyengar, S. S.; Tomasi, J.; Cossi, M.; Millam, J. M.; Klene, M.; Adamo, C.; Cammi, R.; Ochterski, J. W.; Martin, R. L.; Morokuma, K.; Farkas, O.; Foresman, J. B.; Fox, D. J. *Gaussian 16 Rev. C.01*, Wallingford, CT, 2016.
120. V. Blum, R. G., F. Hanke, P. Havu, V. Havu, X. Ren, K. Reuter, M. Scheffler *The Fritz Haber Institute ab initio molecular simulations package (FHI-aims)*.
121. Blum, V.; Gehrke, R.; Hanke, F.; Havu, P.; Havu, V.; Ren, X.; Reuter, K.; Scheffler, M., *Comput. Phys. Commun.* **2009**, *180* (11), 2175-2196.
122. Ren, X.; Rinke, P.; Blum, V.; Wieferink, J.; Tkatchenko, A.; Sanfilippo, A.; Reuter, K.; Scheffler, M., *New J. Phys.* **2012**, *14* (5), 053020.
123. Wilhelm, J.; Walz, M.; Stendel, M.; Bagrets, A.; Evers, F., *Phy. Chem. Chem. Phys.* **2013**, *15* (18), 6684-6690.
124. Bagrets, A., *J. Chem. Theory Comput.* **2013**, *9* (6), 2801-2815.

125. Arnold, A.; Weigend, F.; Evers, F., *J. Chem. Phys.* **2007**, *126* (17), 174101.
126. Estrin, D. A.; Hamra, O. Y.; Paglieri, L.; Slep, L. D.; Olabe, J. A., *Inorg. Chem.* **1996**, *35* (23), 6832-6837.
127. Sur, S. K., *J. Magn. Reson.* **1989**, *82* (1), 169-173.
128. Millar, D.; Venkataraman, L.; Doerrler, L. H., *J. Phys. Chem. C* **2007**, *111* (47), 17635-17639.
129. Kamenetska, M.; Widawsky, J. R.; Dell'Angela, M.; Frei, M.; Venkataraman, L., *J. Chem. Phys.* **2017**, *146* (9), 092311.
130. Perdew, J. P.; Burke, K.; Ernzerhof, M., *Phys. Rev. Lett.* **1996**, *77* (18), 3865-3868.
131. Weigend, F.; Ahlrichs, R., *Phys. Chem. Chem. Phys.* **2005**, *7* (18), 3297-3305.
132. Pakula, R. J.; Berry, J. F., *Dalton Trans.* **2018**, *47* (39), 13887-13893.
133. Ajibade, P. A.; Kolawole, G. A.; O'Brien, P.; Raftery, J.; Helliwell, M., *J. Coord. Chem.* **2008**, *61* (3), 328-340.
134. Rappoport, D.; Furche, F., *J. Chem. Phys.* **2010**, *133* (13), 134105.
135. Perman, J. A.; Zaworotko, M. J., *J. Chem. Crystallogr.* **2009**, *39* (1), 78-82.
136. Martín, S.; Haiss, W.; Higgins, S.; Cea, P.; López, M. C.; Nichols, R. J., *J. Phys. Chem. C* **2008**, *112* (10), 3941-3948.
137. Wu, S.; González, M. T.; Huber, R.; Grunder, S.; Mayor, M.; Schönenberger, C.; Calame, M., *Nat. Nanotechnol.* **2008**, *3* (9), 569-574.

138. Martín, S.; Grace, I.; Bryce, M. R.; Wang, C.; Jitchati, R.; Batsanov, A. S.; Higgins, S. J.; Lambert, C. J.; Nichols, R. J., *J. Am. Chem. Soc.* **2010**, *132* (26), 9157-9164.
139. Al-Owaedi, O. A.; Bock, S.; Milan, D. C.; Oerthel, M.-C.; Inkpen, M. S.; Yufit, D. S.; Sobolev, A. N.; Long, N. J.; Albrecht, T.; Higgins, S. J.; Bryce, M. R.; Nichols, R. J.; Lambert, C. J.; Low, P. J., *Nanoscale* **2017**, *9* (28), 9902-9912.
140. Mayor, M.; von Hänisch, C.; Weber, H. B.; Reichert, J.; Beckmann, D., *Angew. Chem., Int. Ed.* **2002**, *41* (7), 1183-1186.
141. Tanaka, Y.; Kato, Y.; Sugimoto, K.; Kawano, R.; Tada, T.; Fujii, S.; Kiguchi, M.; Akita, M., *Chem. Sci.* **2021**, *12* (12), 4338-4344.
142. Mishchenko, A.; Zotti, L. A.; Vonlanthen, D.; Bürkle, M.; Pauly, F.; Cuevas, J. C.; Mayor, M.; Wandlowski, T., *J. Am. Chem. Soc.* **2011**, *133* (2), 184-187.
143. Hong, W.; Manrique, D. Z.; Moreno-García, P.; Gulcur, M.; Mishchenko, A.; Lambert, C. J.; Bryce, M. R.; Wandlowski, T., *J. Am. Chem. Soc.* **2012**, *134* (4), 2292-2304.
144. Ko, C.-H.; Huang, M.-J.; Fu, M.-D.; Chen, C.-h., *J. Am. Chem. Soc.* **2010**, *132* (2), 756-764.
145. Vladyka, A.; Perrin, M. L.; Overbeck, J.; Ferradás, R. R.; García-Suárez, V.; Gantenbein, M.; Brunner, J.; Mayor, M.; Ferrer, J.; Calame, M., *Nat. Commun.* **2019**, *10* (1), 262.

146. Hamill, J. M.; Ismael, A.; Al-Jobory, A.; Bennett, T. L. R.; Alshahrani, M.; Wang, X.; Akers-Douglas, M.; Wilkinson, L. A.; Robinson, B. J.; Long, N. J.; Lambert, C.; Albrecht, T., *J. Phys. Chem. C* **2023**, *127* (15), 7484-7491.
147. Moreno-García, P.; Gulcur, M.; Manrique, D. Z.; Pope, T.; Hong, W.; Kaliginedi, V.; Huang, C.; Batsanov, A. S.; Bryce, M. R.; Lambert, C.; Wandlowski, T., *J. Am. Chem. Soc.* **2013**, *135* (33), 12228-12240.
148. Manrique, D. Z.; Huang, C.; Baghernejad, M.; Zhao, X.; Al-Owaedi, O. A.; Sadeghi, H.; Kaliginedi, V.; Hong, W.; Gulcur, M.; Wandlowski, T.; Bryce, M. R.; Lambert, C. J., *Nat. Commun.* **2015**, *6* (1), 6389.
149. Greenwald, J. E.; Cameron, J.; Findlay, N. J.; Fu, T.; Gunasekaran, S.; Skabara, P. J.; Venkataraman, L., *Nat. Nanotechnol.* **2021**, *16* (3), 313-317.
150. Reznikova, K.; Hsu, C.; Schosser, W. M.; Gallego, A.; Beltako, K.; Pauly, F.; van der Zant, H. S. J.; Mayor, M., *J. Am. Chem. Soc.* **2021**, *143* (34), 13944-13951.
151. Darwish, N.; Díez-Pérez, I.; Guo, S.; Tao, N.; Gooding, J. J.; Paddon-Row, M. N., *J. Phys. Chem. C* **2012**, *116* (39), 21093-21097.
152. Yang, G.; Sangtarash, S.; Liu, Z.; Li, X.; Sadeghi, H.; Tan, Z.; Li, R.; Zheng, J.; Dong, X.; Liu, J.; Yang, Y.; Shi, J.; Xiao, Z.; Zhang, G.; Lambert, C.; Hong, W.; Zhang, D., *Chem. Sci.* **2017**, *8* (11), 7505-7509.
153. Lambert, C. J.; Liu, S.-X., *Chem. Eur. J.* **2018**, *24* (17), 4193-4201.
154. Huang, B.; Liu, X.; Yuan, Y.; Hong, Z.-W.; Zheng, J.-F.; Pei, L.-Q.; Shao, Y.; Li, J.-F.; Zhou, X.-S.; Chen, J.-Z.; Jin, S.; Mao, B.-W., *J. Am. Chem. Soc.* **2018**, *140* (50), 17685-17690.

155. Jiang, F.; Trupp, D. I.; Algethami, N.; Zheng, H.; He, W.; Alqorashi, A.; Zhu, C.; Tang, C.; Li, R.; Liu, J.; Sadeghi, H.; Shi, J.; Davidson, R.; Korb, M.; Sobolev, A. N.; Naher, M.; Sangtarash, S.; Low, P. J.; Hong, W.; Lambert, C. J., *Angew. Chem., Int. Ed.* **2019**, *58* (52), 18987-18993.
156. Tang, C.; Huang, L.; Sangtarash, S.; Noori, M.; Sadeghi, H.; Xia, H.; Hong, W., *J. Am. Chem. Soc.* **2021**, *143* (25), 9385-9392.
157. Yoshizawa, K.; Tada, T.; Staykov, A., *J. Am. Chem. Soc.* **2008**, *130* (29), 9406-9413.
158. Kaneko, S.; Takahashi, R.; Fujii, S.; Nishino, T.; Kiguchi, M., *Phy. Chem. Chem. Phys.* **2017**, *19* (15), 9843-9848.
159. Isshiki, Y.; Nishino, T.; Fujii, S., *J. Phys. Chem. C* **2021**, *125* (6), 3472-3479.
160. Borges, A.; Fung, E. D.; Ng, F.; Venkataraman, L.; Solomon, G. C., *J. Phys. Chem. Lett.* **2016**, *7* (23), 4825-4829.
161. Liu, Z.-F.; Neaton, J. B., *J. Chem. Phys.* **2014**, *141* (13).
162. Kim, T. K.; Liu, Z.-F.; Lee, C.; Neaton, J. B.; Venkataraman, L., *Proceedings of the National Academy of Sciences* **2014**, *111* (30), 10928-10932.
163. Sangtarash, S.; Vezzoli, A.; Sadeghi, H.; Ferri, N.; O'Brien, H. M.; Grace, I.; Bouffier, L.; Higgins, S. J.; Nichols, R. J.; Lambert, C. J., *Nanoscale* **2018**, *10* (6), 3060-3067.
164. Huang, J.; Grys, D.-B.; Griffiths, J.; de Nijs, B.; Kamp, M.; Lin, Q.; Baumber, J. J., *Sci. Adv.* **2021**, *7* (23), eabg1790.

165. Vazquez, H.; Skouta, R.; Schneebeli, S.; Kamenetska, M.; Breslow, R.; Venkataraman, L.; Hybertsen, M. S., *Nat. Nanotechnol.* **2012**, *7* (10), 663-667.
166. Bergfield, J. P.; Heitzer, H. M.; Van Dyck, C.; Marks, T. J.; Ratner, M. A., *ACS Nano* **2015**, *9* (6), 6412-6418.
167. Yin, X.; Zang, Y.; Zhu, L.; Low, J. Z.; Liu, Z.-F.; Cui, J.; Neaton, J. B.; Venkataraman, L.; Campos, L. M., *Sci. Adv.* **2017**, *3* (10), eaao2615.
168. Bai, J.; Daaoub, A.; Sangtarash, S.; Li, X.; Tang, Y.; Zou, Q.; Sadeghi, H.; Liu, S.; Huang, X.; Tan, Z.; Liu, J.; Yang, Y.; Shi, J.; Mészáros, G.; Chen, W.; Lambert, C.; Hong, W., *Nat. Mater.* **2019**, *18* (4), 364-369.
169. Yan, Z.; Li, X.; Li, Y.; Jia, C.; Xin, N.; Li, P.; Meng, L.; Zhang, M.; Chen, L.; Yang, J.; Wang, R.; Guo, X., *Sci. Adv.* **2022**, *8* (12), eabm3541.

CURRICULUM VITAE

Hannah E. Skipper
hskipper@bu.edu | 203-984-0152

Education

Doctor of Philosophy, Chemistry | Boston University, MA *Anticipated August 2023*
Dissertation: Chemical Design of Single Molecule Electronic Components and Quasi-1D Chains.

Bachelor of Arts | Skidmore College, NY May 2017

Research Experience

Doerrer Lab, Boston University | Boston, MA October 2018 – July 2023
Principle Investigator: Prof. Linda Doerrer, Dept. of Chemistry
Synthesized and characterized heterobimetallic lantern complexes and quasi-1D wires for electronic and magnetic studies.

Kamenetska Lab, Boston University | Boston, MA October 2018 – July 2023
Principle Investigator: Prof. Maria Kamenetska, Dept. Chemistry and Physics
Investigated single molecule conductance behavior of both inorganic and organic molecules using the Scanning Tunneling Microscopy Break Junction (STMBJ) technique and density functional theory (DFT) and transmission calculations.

Arnold Lab, Lawrence Berkeley National Lab | Berkeley, CA January – June 2022
Principle Investigator: Prof. Polly L. Arnold, Dept. of Chemistry
Synthesized a heterotertrametallic system with close lanthanide contacts for studying the coupling of f-orbital spins. Used air-free techniques and received training and experience with the handling of radioactive actinides.

Roca Lab, Skidmore College | Saratoga Springs, NY January 2014 – May 2017
Principle Investigator: Prof. Maryuri Roca, Dept. of Chemistry
Silver nanoparticle synthesis and development of novel procedures for the fabrication of colored silver nanoparticle films.

Employment

Research Scientist I, Curia (Formally AMRI) | Albany, NY June 2017 – May 2018
Analytical Technologies Department
Performed analysis of intermediates and target compounds.
Conducted and reviewed analytical tests in accordance with SOPs and cGMP procedures.

Reference Standards Intern, Curia | Albany, NY February 2017 – May 2017
Analytical Technologies Department
Maintained organization and inventory of reference standard samples and record keeping associated with active and inactive reference standards.
Prepared reference standard samples and documentation for shipments to customer and third-party sites.

Honors and Awards

Dept. of Energy and Office of Science Graduate Student Research (SCGSR) Fellowship
Lawrence Berkeley National Lab | Berkeley, CA (2022)

BUnano Cross-Disciplinary Fellowship
Boston University | Boston, NY (2019 – 2020)

Faculty Student Summer Research Grant Recipient
Skidmore College | Saratoga Springs, NY (2015, 2016)

Publications

Skipper, H. E.; Lawson, B. L.; Kamenetska, M., Assembly and Electron Transport Properties of Metal-Cyanide Containing Wires in Single Molecule Junctions. *In preparation* **2023**.

Skipper, H. E.; Valaydon-Pillay, A.; Rheingold, A. L.; Stoian, S.; Doerrer, L. H., Determination of Ligand Substituent Effects in Pt-Fe Heterobimetallic Lantern Complexes via ^{57}Fe Mössbauer Spectroscopy. *In preparation* **2023**

Skipper, H. E.; Lawson, B. L.; Pan, X.; Degtiareva, V.; Kamenetska, M., Manipulating Quantum Interference Between σ and π Orbitals in Single Molecule Junctions via Chemical Substitution and Environmental Control. *Under Review* **2023**.

Skipper, H. E.; May, C. V.; Rheingold, A. L.; Doerrer, L. H.; Kamenetska, M., Hard–Soft Chemistry Design Principles for Predictive Assembly of Single Molecule-Metal Junctions. *Journal of the American Chemical Society* **2021**, *143*, 16439-16447.

Trerayapiwat, K. J.; Kitadai, H.; Pazmany, V.; Lagueux, S. P.; **Skipper, H. E.**; Doerrer, L. H.; Ling, X.; Sharifzadeh, S., Vibrational Signature of Metallophilic Interactions in [Pt(terpy)Cl][Au(CN)₂]. *The Journal of Physical Chemistry C* **2021**, *125*, 22188-22194.

Roca, M.; **Skipper, H. E.**; Ndrianasy, J. R., Optical Properties of Nanocomposite Films: Size tuned vs. Shape-tuned Silver Nanoparticles. *American Journal of Nanomaterials*, **2019**, *7*, 22.

Presentations

Materials Research Society Meeting | San Francisco, CA, April 2023

Manipulating Quantum Interference in Single Molecule Junctions via Chemical Substitution and Environmental Control, **Hannah Skipper**, Brent Lawson, Xiaoyun Pan, Maria Kamenetska, Poster.

BU Chemistry Pchem Seminar | Boston, MA, November 2022

Hard-Soft Chemistry Design Principles for Predictive Assembly of Single Molecule-Metal Junctions.

American Chemical Society National Meeting | April 2021

Establishing design rules for robust coordination complexes on gold using single molecule conductance measurements, **Hannah Skipper**, Arnold L. Rheingold, Linda H. Doerrer, Maria Kamenetska, Contributed talk.

American Chemical Society National Meeting | San Francisco, CA, April 2017

Single vs Mixed Approaches to Form Silver Nanoparticle Films, **Hannah Skipper**, Maryuri Roca, Poster.

American Chemical Society National Meeting | San Diego, CA, March 2016

Synthesis of Silver Nanoparticle Films, **Hannah Skipper**, Maryuri Roca, Poster.

*Teaching Experience***Teaching Fellow, Chemistry Dept. Boston University** | Boston, MA

Intensive General Chemistry with Quantitative Analysis	Fall 2020, 2021
General Chemistry I	Fall 2019
General Chemistry and Quantitative Analytical Chemistry	Spring 2019
General Chemistry for Engineering Sciences	Fall 2018

Lab Assistant, Skidmore College | Saratoga Springs, NY

Analytical Chemistry Lab	Spring 2017
Physical Chemistry Lab	2015 – 2017